VISCOSITY STRUCTURE OF THE LITHOSPHERES OF GANYMEDE, CALLISTO, AND ENCELADUS, AND OF THE EARTH'S UPPER MANTLE

Thesis by

Quinn R. Passey

In Partial Fulfillment of the Requirements
for the Degree of
Doctor of Philosophy

California Institute of Technology
Pasadena, California

1982

(submitted April 12, 1982)

To my wife, Debbie

ACKNOWLEDGMENTS

It is my pleasure to thank Dr. E.M. Shoemaker for his support, advice and encouragement while acting as my advisor for the bulk of this thesis. Without his help, this thesis would never have been done. I am very grateful to Dr. K.E. Sieh for help and advice on the project concerning Lake Bonneville (Paper 5).

I thank my wife, Debbie, for being understanding during the times that I could not be home for supper, or when I was gone to Palomar Mountain in search of asteroids and lucre.

I also am thankful to my fellow graduate students for moral and scientific support and encouragement, among them Todd Clancy, Jim Friedson, Lucien Froidevaux, Randy Gladstone, Bruce Jakosky, David Jewitt, Jonathan Lunine, David Paige, Judy Pechmann, Carolyn Porco, Mike Summers, and Daniel Wenkert.

I thank Drs. Peter Goldreich, Andrew Ingersoll, Duane Muhleman, and Donald Burnett for advice concerning my academic career at Caltech. In addition, I am sincerely grateful to Dr. H.J. Melosh for advice and encouragement during my first year at Caltech, during which time he acted as my academic and research advisor.

This work would not have been completed as quickly without the assistance and cooperation G.E. Danielson, who allowed me access to the image display system and computer programs of the Wide Field/Planetary Camera Investigations Team for Space Telescope. He also supplied the magnetic tapes of the Voyager images required for the photoclinometry of the features on Ganymede, Callisto, and Enceladus; thanks also go to Carolyn Porco and Robert Deverill for programming assistance in conjunction with the photoclinometric profiles. Kay Edwards, of the USGS in Flagstaff, Arizona, assisted in the programming used in obtaining the initial photoclinometric profiles of craters on Ganymede.

I am extremely grateful to Gene and Carolyn Shoemaker, Ruth Wolfe, and Bill and Carol Breed for arranging for, or for providing, housing for my wife and me in Flagstaff, Arizona, during the summers of 1979 and 1980.

I am deeply appreciative to Drs. Thomas Ahrens, David Stevenson, Brad Hager, and Bruce Bills for many helpful discussions and suggestions concerning the work presented in this thesis. Dr. Bill McKinnon provided spirited discourses concerning the initial description and interpretation of the features on Ganymede and Callisto at the time when many of the basic ideas presented in this thesis were being formulated. I thank Jeff Plescia for sharing, in advance of publication, his detailed studies of crater density on Ganymede; also, he graciously provided the image of Enceladus, found in Paper 4.

The reviewers of the papers that make up this thesis provided critical reviews that greatly improved their content; for this I am appreciative to Drs. Ronald Greeley, M.D. Crittenden Jr., L.M. Cathles, and S.T. Crough.

Finally, I thank Ann Freeman, Kay Campbell, and Donna Lathrop for excellent secretarial assistance which reduced the amount of "red-tape" that I had to deal with.

This work was supported by NASA grants NSG-7316 and NAGW-138.

CONTENTS

ABSTRACT

Craterform and related features on Ganymede and Callisto include bowl-shaped craters, craters with nearly flat floors, craters with central peaks, craters with central pits, basins, crater palimpsests and penepalimpsests, and giant multiring systems of ridges and furrows. The large majority of all craters larger than 20 km diameter have a central pit. The pits are interpreted as formed by prompt collapse of transient central peaks. Most craters, in all size ranges, are highly flattened as a consequence of topographic relaxation by slow viscous or plastic flow.

Analysis of the global distribution of craters and multiring structures on Callisto reveal that the large multiring structures are concentrated in the leading hemisphere, whereas craters are depleted here. Calculations of model crater retention ages based on a sample of 2000 craters $\geq$ 30 km in diameter show that the mean age of Callisto's surface is between 4.0 and 4.2 Gy. Variations in the surface ages, derived from different diameter craters, suggests that larger craters are not retained from as early a period in time as were the smaller craters; this is in agreement with the results predicted by viscous relaxation theory where large wavelength features relax at a faster rate than do small wavelength features. Most of the variations in the observed distribution of craters can be explained satisfactorily by the effects due to the formation of multiring structures, and on the viscous relaxation of craters beneath an insulating regolith.

About 1000 topographic profiles of craters on Ganymede and Callisto were obtained by photoclinometry. Fresh craters on Ganymede and Callisto have depth-to-diameter ratios and rim height-to-diameter ratios similar to those of fresh lunar craters, but most craters are much shallower. Small craters have

not flattened or relaxed as much as have large craters; comparison of the crater profiles with the results from theoretical of crater relaxation studies in a viscous medium, allows determination of the viscosity at the surfaces of Ganymede and Callisto, and, also, determination of the viscosity gradient with depth. The derived mean surface viscosity for the lithospheres of Ganymede and Callisto is $1.0 \pm 0.5 \times 10^{26}$ poise. For Ganymede, the estimated thermal gradient at ~3.9 Gya was ≥ 8 K/km; the thermal gradient can be modelled as decreasing approximately exponentially with time, with an e-folding time of about 10^8 years; the estimated present thermal gradient is $\leq$ 2.0 K/km. For Callisto, the thermal gradient was ≥ 3 K/km at ~4.1 GYA and the decrease in the thermal gradient can be modelled as an exponential dropoff with an e-folding time between about 5×10^7 and 2×10^8 years; the estimated present thermal gradient on Callisto ≤ 1.5 K/km.

High resolution Voyager II images of Enceladus reveal that some regions on its surface are highly cratered; the most heavily cratered surfaces probably date back into a period of heavy bombardment. The forms of many of the craters, on Enceladus, are similar to those of fresh lunar craters, but many of the craters are much shallower in depth, and the floors of some craters are bowed up. Analysis of the forms of the flattened craters on Enceladus suggests that the viscosity at the top of the lithosphere, in the most heavily cratered regions, is between 10^{24} and 10^{25} poise. The exact time scale for the collapse of the craters is not known, but probably was between 100 My and 4 Gy. The flattened craters are located in regions in which the heat flow was (or is) higher than in the adjacent terrains. Because the temperature at the top of the lithosphere of Enceladus would be less than, or equal to that of Ganymede and Callisto, if it is covered by a thick regolith, and because the required viscosity, on Enceladus, is

one to two orders of magnitude less than for Ganymede and Callisto, it can be concluded that the lithospheric material, on Enceladus, is different from that of Ganymede and Callisto. Enceladus possibly has a mixture of ammonia ice and water ice in the lithosphere, whereas the lithospheres of Ganymede and Callisto are composed primarily of water ice.

New field measurements of elevation of Provo-level and Bonneville-level shoreline terraces, of Lake Bonneville, provide data for reanalysis of isostatic rebound in the Lake Bonneville basin. Analysis of the differential rebound between the Provo shoreline (maximum rebound of 43 m) and the Bonneville shoreline (maximum rebound of 69 m) requires that the latter be an equilibrium shoreline. From the new data, the best estimate of the upper limit of effective viscosity of the uppermost mantle, assuming a half-space model and a 2000 year time interval between the Bonneville and Provo shorelines, is 2×10^{19} N sec m^{-2} (2×10^{20} poise). In addition, comparison of shoreline rebound profiles, for both shorelines, with theoretical plate flexure models indicates that the mean flexural rigidity of the Basin and Range lithosphere in this region is 1×10^{23} N m, or slightly less.

PAPER 1

CRATERS AND BASINS ON GANYMEDE AND CALLISTO: MORPHOLGICAL INDICATORS OF CRUSTAL EVOLUTION

by QUINN R. PASSEY

and

E.M. SHOEMAKER

Chapter 12 in *THE SATELLITES OF JUPITER*

ABSTRACT

Craterform and related features on Ganymede and Callisto include bowl-shaped craters, craters with nearly flat floors, craters with central peaks, craters with central pits, basins, crater palimpsests and penepalimpsests, and giant multiring systems of ridges and furrows. The large majority of all craters larger than 20 km diameter have a central pit. The pits are interpreted as formed by prompt collapse of transient central peaks. Most craters, in all size ranges, are highly flattened as a consequence of topographic relaxation by slow viscous or plastic flow.

During early heavy bombardment, the lithospheres of Ganymede and Callisto were sufficiently thin, owing to the combined effect of impact heating and heat flow from the deep interior, to prevent retention of any recognizable craters. The loss of these craters occurred as a consequence of relatively rapid viscous relaxation of individual craters, smothering of groups of highly flattened craters beneath ejecta deposits, and regional effects of multiring structures. The oldest retained craters are relatively small (less than 10 km diameter) and occur in the polar region of Callisto and near the antapex of motion of each satellite. As the lithosphere of each satellite cooled and thickened, crater retentivity spread as a "wave" from the polar regions and antapex toward the apex; at any given location, progressively larger craters were retained with the passage of time. The asymmetric pattern of the thickening and stiffening of the lithosphere, inferred from the pattern of retention of the craters, probably reflects asymmetric development of an insulating regolith and the regional effects of large impact structures.

INTRODUCTION

One of the more startling discoveries of the Voyager missions is the host of craters and related features on Ganymede and Callisto. As the densities of these two largest satellites of Jupiter strongly suggest that they are made up of about one-quarter to one-half H_2O, it was widely supposed that their crusts are composed largely of ice I. Detailed spectrophotometry, moreover, has confirmed that H_20 ice is an important constituent of the surfaces of these two bodies (Clark, 1980). The extent to which these icy crusts might preserve observable topographic relief and a decipherable geologic record was largely a matter of conjecture prior to the Voyager missions. The remarkable revelation from the Voyager television pictures is that the cratering record on both Ganymede and Callisto appears to extend back to the period of late heavy bombardment, about 4 billion years before the present (Smith et al., 1979 a,b).

A second fact immediately evident from the Voyager pictures is that the forms of the ancient craters have been greatly modified, as might be expected from major topographic features formed in ice. The oldest craters are invariably extremely flattened (Shoemaker and Passey, 1979). Relaxation of topographic relief on Ganymede and Callisto by viscous flow or creep was first suggested by Johnson and McGetchin (1973). Their suggestion is basically confirmed by the Voyager evidence; broad features of the topography have flattened or have disappeared, while small features such as secondary craters and the hummocks of crater rim deposits are preserved, as predicted by viscous relaxation theory.

Although Ganymede and Callisto are similar in size and bulk density, the surfaces of these two bodies are significantly different. Callisto's surface consists essentially of a single type of heavily cratered terrain which evidently dates from

a period of heavy bombardment. Ganymede's surface, on the other hand, consists of two very distinct types of terrain, 1) an ancient heavily cratered terrain, and 2) a younger grooved terrain (Smith et al, 1979 a,b). Slightly less than half the surface of Ganymede is ancient cratered terrain and more than half is grooved terrain. The ancient cratered terrain of Ganymede is similar to the cratered terrain of Callisto except that the mean crater density on Ganymede is only about half as great.

Craters and related features on Ganymede are remarkably similar to those on Callisto, but the morphology of most craters on Ganymede and Callisto differ in important respects from similar sized craters on the Moon, Mars, and Mercury. These differences appear to be due, in part, to the contrast in physical properties between the icy satellites and the rocky surfaces of the Moon and terrestrial planets that affect the initial form the the craters as well as to the slow relaxation of topographic relief on the icy satellites. Despite these differences, it is clear that the craters on Ganymede and Callisto are closely related in origin to the vast majority of craters on the Moon, Mars and Mercury. Ray craters on Ganymede and Callisto, in particular, resemble ray craters on the Moon, both in crater form and in the pattern of the rays. Relationships of rim deposits and secondary craters observed around large relatively fresh craters and basins on Ganymede leave little room for doubt that almost all of the observed craters are either of primary or secondary impact origin. The collision of comet nuclei has been suggested to be primarily responsible for the formation of the ray craters on Ganymede and Callisto (Shoemaker and Wolfe, 1982).

A number of first order conclusions about Ganymede and Callisto may be obtained directly from a careful study of the forms and relations of their numerous craters. For example, many 10 km craters have extremely subdued

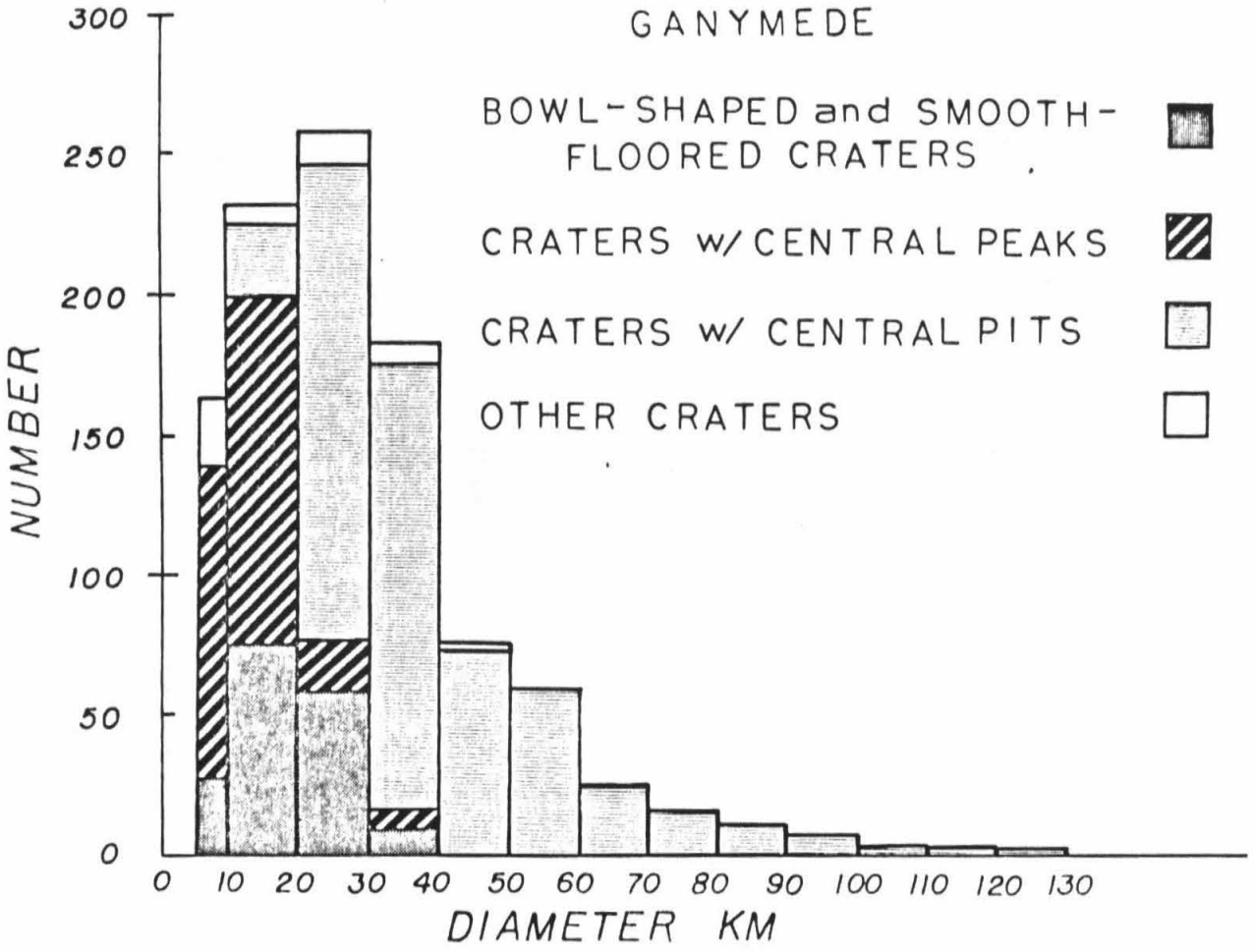

FIGURE 1 - Size-frequency distribution of different morphologic classes of craters on Ganymede. The decrease in the number of craters less than 20 km in diameter is due to the limited number of high resolution images. The category *other craters* represents craters which, owing to low resolution or obscuring by reseau marks could not be classified.

relief. The flattening or relaxation of these craters implies very steep thermal gradients or much higher surface temperatures at an early period in the history of both satellites. Many large craters, initially formed on the ancient cratered terrain of Ganymede, have flattened to the degree that the craters are no longer recognizable, but their former presence is indicated by distinctive high albedo patches termed palimpsests. On the other hand, there are also large craters that extend in size up to basins (diameter ~150 km) that were formed relatively early in the cratering history and which have not disappeared. The preservation of the basins indicates that there was a large decrease in thermal gradient and corresponding increase in lithosphere thickness after the 10 km craters had flattened. In this chapter we will first survey the morphologic characteristics of craters and palimpsests on Ganymede and Callisto; then we will explore what might be ascertained from the observations of the craters about the crustal properties of these two icy bodies and, especially, about the evolution of their crustal properties with time.

MORPHOLOGY OF CRATERS AND RELATED FEATURES

For purposes of description we have divided the craters and related features on Ganymede and Callisto into several morphological categories. These include 1) bowl-shaped craters, 2) smooth-floored craters, 3) craters with central peaks, 4) craters with central pits, 5) chain craters on Callisto, 6) the Gilgamesh and Western Equatorial Basins on Ganymede, 7) crater palimpsests and penepalimpsests, 8) multiring structures on Callisto, and 9) the Galileo Regio rimmed furrow system on Ganymede.

Bowl-shaped Craters

The smallest craters discernible on Ganymede are simple bowl-shaped craters, generally with resolved raised rims. The diameters of bowl-shaped

craters range from less than 5 km to approximately 20 km. Essentially all craters smaller than about 5 km in diameter appear to fall into the bowl-shaped category. This may be partially due, however, to the limiting resolution of the imaging system. Craters and other features on Ganymede smaller than 5 km in diameter are less than ten pixels across in the highest resolution images; details in the crater floors cannot be resolved with this limited number of pixels. Approximately 20 percent of craters 5 to 10 km in diameter and 30 percent of craters 10 to 20 km in diameter are bowl-shaped (Fig. 1). Simple craters larger than 20 km in diameter appear to be flat-floored or to have convex floors rather than bowl shapes.

Average depth-to-diameter ratios for fresh appearing bowl-shaped craters, that are approximately 10 km in diameter, are 1:6 to 1:12. (Depths are measured from the crater rims.) The height of the rim crest above the surrounding surface generally is less than about 300 meters; for very fresh craters, the rim height may exceed 500 meters. These depths and heights were derived from photoclinometric crater profiles (see Watson, 1968; Bonner and Schmall, 1973) and from shadow measurements and probably have errors of the order of ± 100 meters.

Most of the bowl-shaped craters probably are of primary impact origin, but many craters also occur in swarms around much larger craters and palimpsests. By analogy with crater swarms observed on the Moon and Mercury, the swarm craters are inferred to be secondary craters related to the ejection of material from the much larger primary craters. On Ganymede, the ratio of the diameter of the largest secondary craters to the diameter of the central primary crater is about 1:15, comparable to that observed on the Moon (Shoemaker, 1966). Prominent resolved secondary crater swarms are associ-

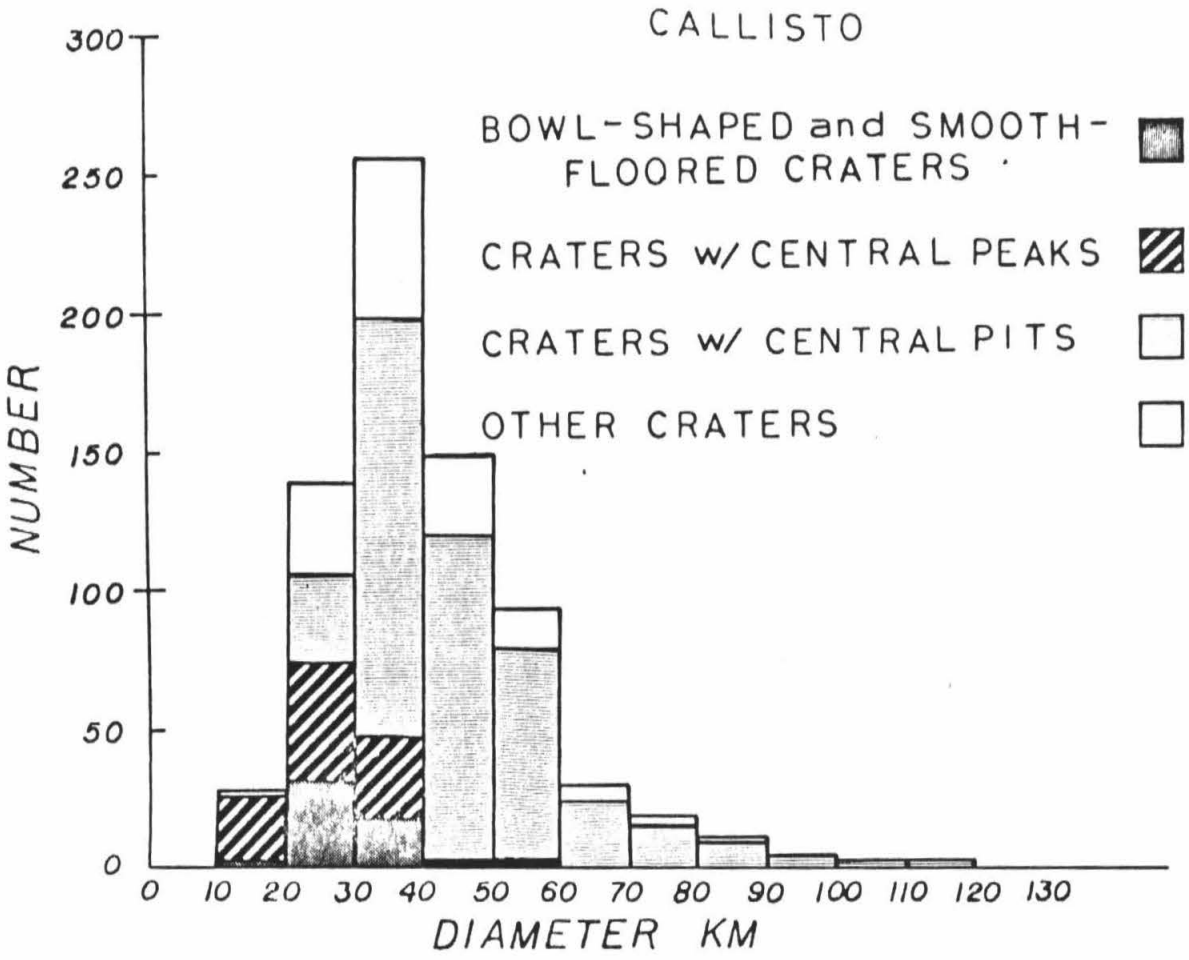

FIGURE 2 - Size-frequency distribution of different morphologic classes of craters on Callisto. The decrease in the number of craters less than 30 km in diameter is due to the limited number of high resolution images. The category *other craters* represents craters which, owing to image smear or low resolution, could not be classified.

ated with most craters larger than about 70 km in diameter. The largest secondary craters occur as far as three primary crater diameters beyond the rim of the primary crater.

On Callisto, craters smaller than about 15 km in diameter are difficult to categorize owing to the limited resolution of the Voyager images of Callisto. Probably many of these craters are bowl-shaped, as on Ganymede.

Smooth-floored Craters

We designate craters with flat or slightly convex floors that do not exhibit either a central peak or central pit as smooth-floored craters. Generally, the smooth-floored craters are larger than the bowl-shaped craters. The transition from bowl shape (or concave floors) to smooth nearly level floors occurs at crater diameters in the range 15 to 20 km. The diameter for which this transition occurs probably reflects physical properties of the crusts of Ganymede and Callisto at the times the craters formed. The smooth-floored craters range in diameter from approximately 20 to 40 km. About 20 percent of Ganymedian craters 20 to 30 km in diameter have smooth-floors, compared to only 5 percent of craters 30 to 40 km in diameter (Fig. 1).

Photoclinometric crater profiles show that many smooth-floored craters on Ganymede are distinctly convex or bowed-up in the center (Fig. 3). Theoretical studies of the collapse of craters by slow viscous flow have been carried out by Danes (1962, ;1965) and Scott (1967). Danes' work indicates that collapse of craters in a medium of uniform viscosity includes both an overall flattening of the crater and a bowing-up of the floor, the time dependence of which varies with the viscosity. Experimental studies by Scott (1967) of the collapse of crater-like forms in asphalt verified the time dependence of the flattening of the craters predicted by the viscous flow equations of Haskell (1935). A slight

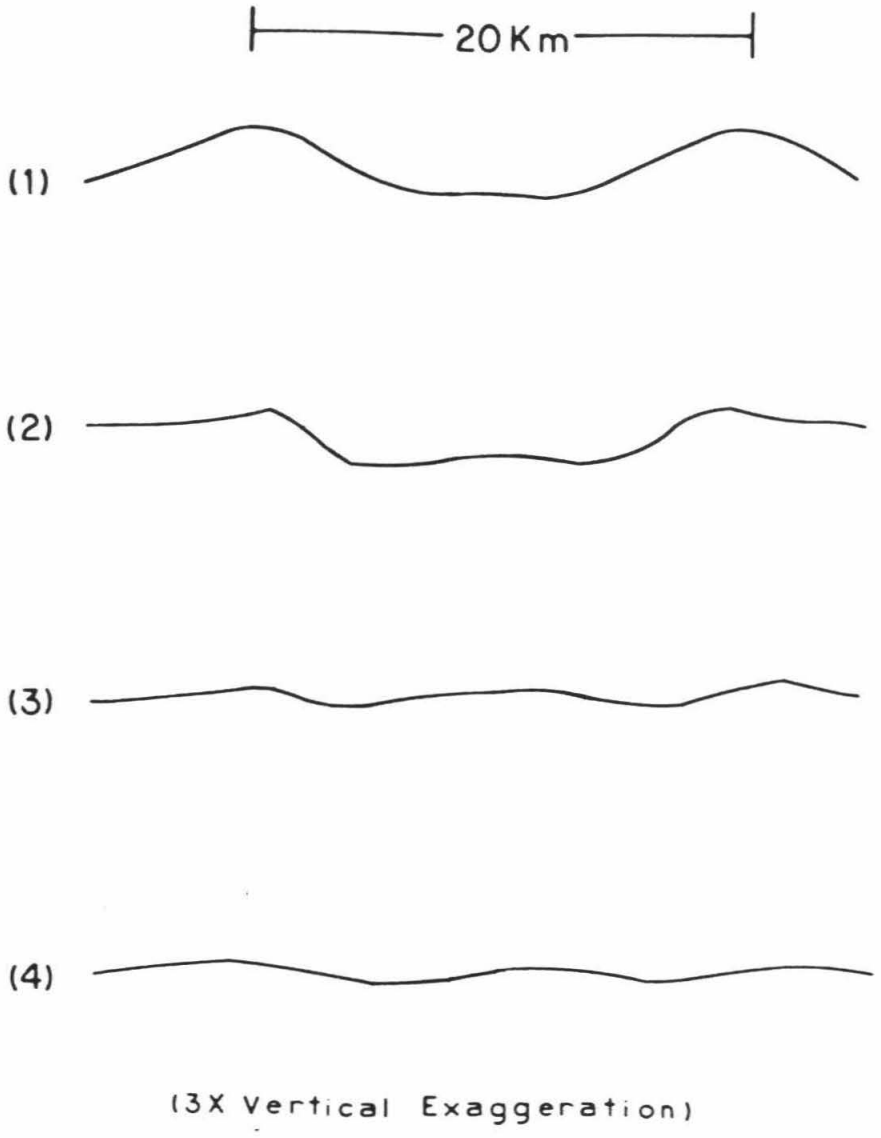

FIGURE 3 - Photoclinometric profiles of four craters on Ganymede with diameters of approximately 20 km. Profile (1) is of a crater located in grooved terrain of the Harpagia Sulci; the other three profiles are for craters located within the ancient cratered terrain of the Nicholson Regio.

bowing-up of the floor was observed in these experiments which, however, may have been due to an increase of viscosity near the surface of the experimental model. A vertical gradient of viscosity (viscosity decreasing with depth) clearly will enhance the phenomenon of bowing-up of the crater floor.

The average degree of bowing-up in the center is greater for craters located within the ancient cratered terrain than for craters within the younger grooved terrain of Ganymede (Shoemaker and Passey, 1979). Within grooved terrain, depth-to-diameter ratios for smooth-floored craters 20 km in diameter are from 1:6 to 1:20. Depth-to-diameter ratios for similar craters located in the ancient cratered terrain is from 1:6 to 1:80. Depths of the craters were measured from the rim crests. Maximum height of the crater rim above the surrounding surface is between 200 and 300 meters for fresh smooth-floored craters; for degraded craters, the rim heights are substantially less.

Smooth-floored craters on Callisto range from about 18 km to 40 km in diameter. Smooth-floored craters comprise approximately 30 percent of craters 20 to 30 km in diameter and about 8 percent of craters 30 to 40 km in diameter (Fig. 2). No photoclinometric profiles have been obtained for craters on Callisto at the time of the writing of this chapter. Measurements of shadow lengths near the terminator, however, reveal that these craters are also anomalously shallow compared to fresh craters of similar size on the Moon. Depth-to-diameter ratios for smooth-floored craters 20 to 40 km in diameter range from about 1:15 to 1:45. Maximum depth below the crater rim, for smooth-floored craters on Callisto, is about 2 km.

Craters with central peaks

On Ganymede, craters which display a central peak are common in the diameter range of 5 to 35 km. No craters with diameters larger than 35 km have

been found to have a central peak. This observation is in contrast with craters on the Moon, where the majority of fresh craters larger than 25 km in diameter and essentially all craters larger than 55 km in diameter have central peaks (Pike, 1975). On Mercury, a majority of craters larger than 40 km in diameter exhibit a central peak (Gault et al., 1975; Cintala et al., 1977). Approximately 70 percent of Ganymedian craters 5 to 10 km in diameter, 50 percent of craters 10 to 20 km in diameter, 7 percent of craters 20 to 30 km in diameter, and 3 percent of craters 30 to 40 km in diameter have central peaks (Fig. 1). Although the diameter range of craters with central peaks overlaps the diameter range of smooth-floored craters, the smooth-floored craters tend to comprise a larger proportion of craters 20 to 30 km in diameter than do craters with central peak.

Central peaks range in basal diameter from about 1 km, for small craters, to approximately 5 km in larger craters. The maximum heights of the peaks are approximately 700 meters, as indicated from shadow measurements. The resolution of these craters is insufficient to show details in the central peaks. Collapsed terrace walls are associated with craters with central peaks. The widths of the resolved terraces vary from roughly 1 to 4 km. The smallest crater with a central peak that exhibits a resolved terraced wall is about 10 km in diameter.

On Callisto, craters with distinct central peaks have been found within the size range of from 11 to about 40 km in diameter. Approximately 40 percent of craters 20 to 30 km in diameter and about 15 percent of craters 30 to 40 km in diameter have central peaks (Fig. 2). Depth-to-diameter ratios for craters 30 km in diameter, with central peaks, range from about 1:10 to 1:30. primary craters of the same size.

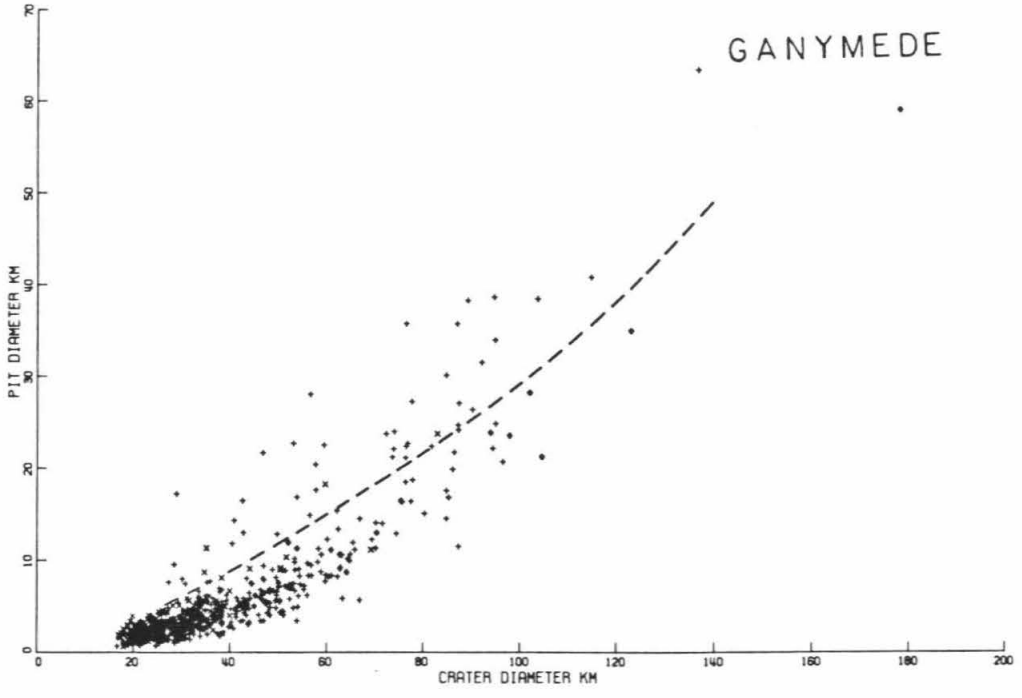

FIGURE 4 - Diameter of central pit versus crater diameter for 640 craters on Ganymede. Those craters which fall above the broken line are recognizably younger than those below this line. Ray craters generally have the smallest central pit diameter, for a given crater diameter, and fall at the lower boundary of the distribution.

Craters with central pits

Craters which have a central depression or pit are abundant on both the ancient cratered terrain and on the grooved terrain on Ganymede. These craters range in diameter from 16 km to more than 120 km. Approximately 25 percent of craters 10 to 20 km in diameter, 60 percent of craters 20 to 30 km in diameter and about 90 percent of 30 to 40 km diameter craters have central pits. Essentially all craters larger than 40 km in diameter have a central pit. From figure 1, it may be seen that craters with central peaks are replaced by craters with central pits at roughly 20 km crater diameter. It is apparent, from the highest resolution Voyager images of Ganymede, that most, if not all craters with central pits also have collapsed terraced walls. The width of the identifiable terrace zones range from about 1 to 7 km.

The diameter of the central pit is positively correlated with the crater diameter, as shown in figures 4 and 5. (See also Boyce, 1980.) From the distribution of the pit diameter versus the crater diameter, the relationship appears to be curvilinear. Using the data for ray craters and craters with high albedo rims, the best fit exponential relationship for pit diameter versus crater diameter for Ganymedian craters is

$$d = 1.9 \exp (.023\ D) \qquad (1)$$

where d is the diameter of the central pit, and D is the crater diameter.

The diameter of the pit relative to the diameter of the crater is also dependent upon the age of the crater. For a given crater diameter, recognizably older craters have central pits with diameters that are larger than the central pits in recognizably younger craters. The smallest pits, for a given crater size, are generally encountered in ray craters (Fig. 6d). Differences in the pit size, as a func-

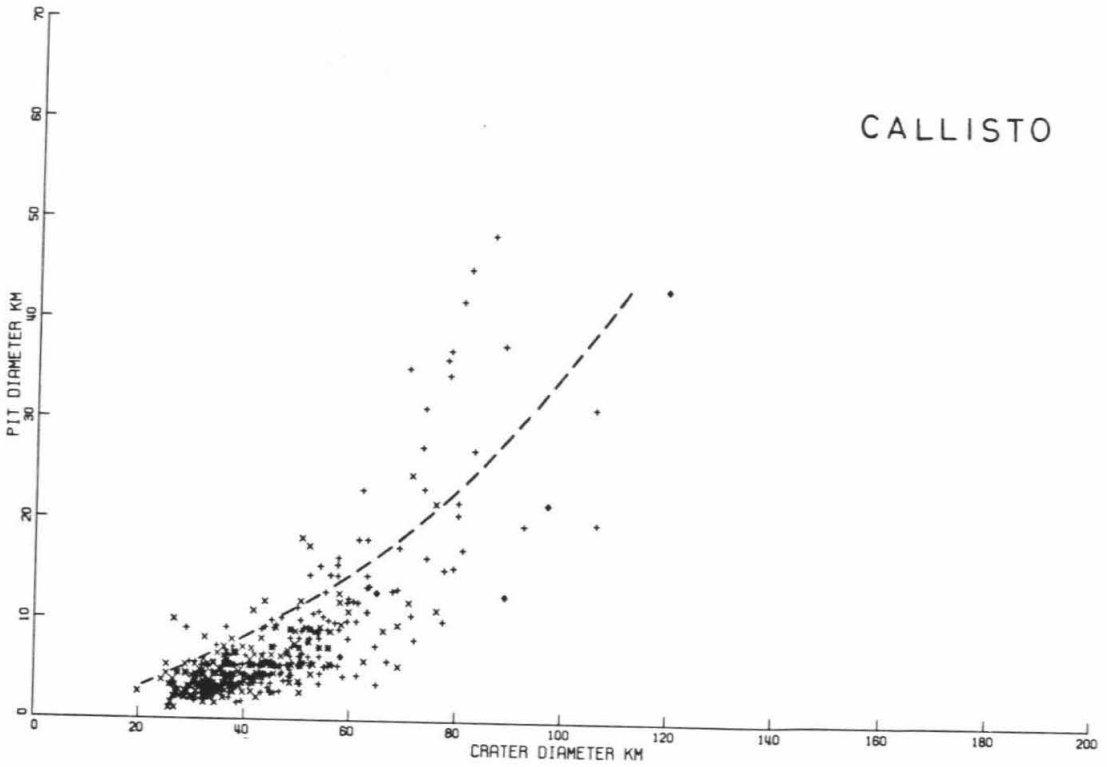

FIGURE 5 - Diameter of central pit versus crater diameter for about 450 craters on Callisto. Craters which fall above the broken line are recognizably older than those below this line; ray craters generally are located at the lower boundary of the distribution.

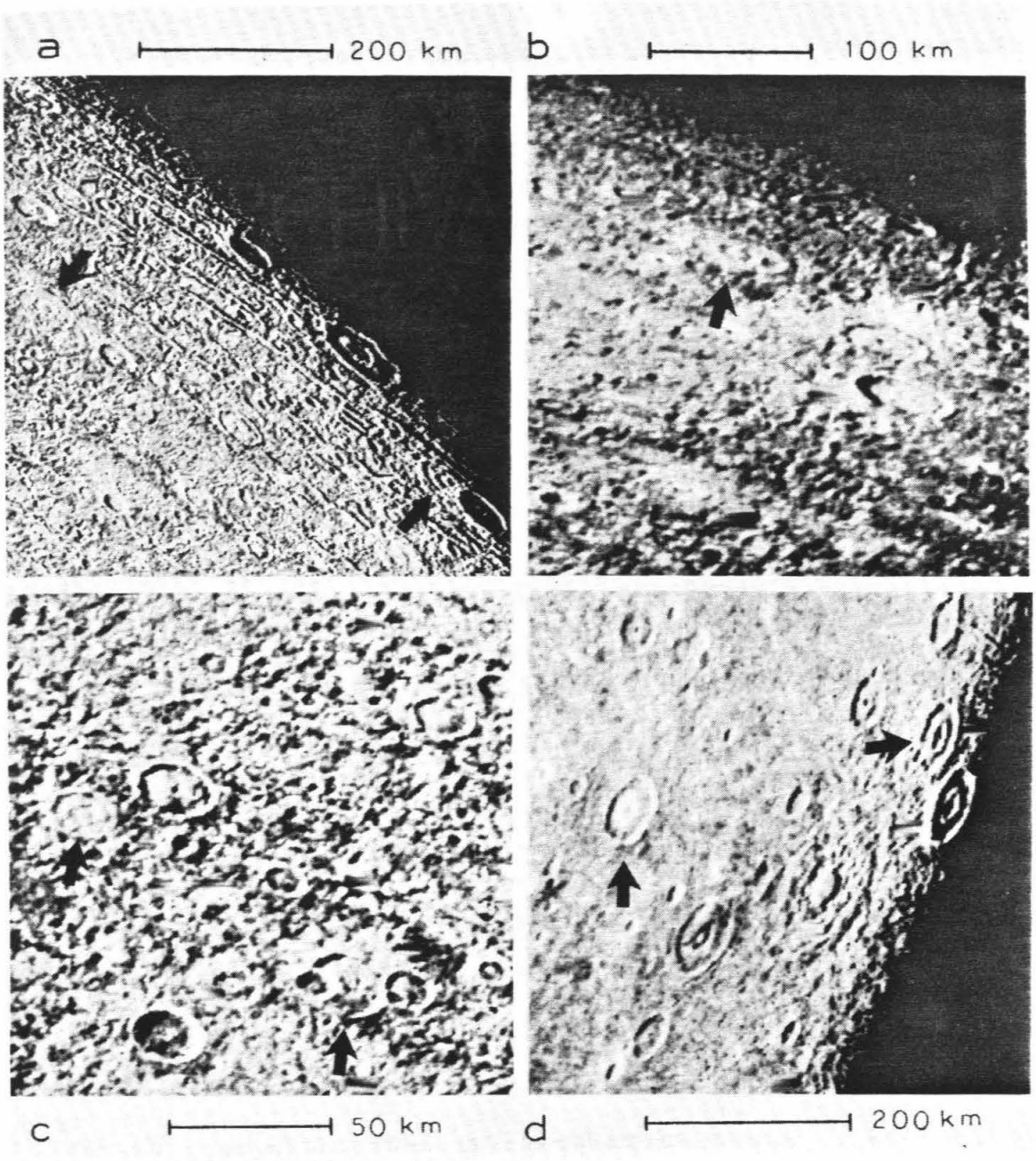

FIGURE 6 - Voyager II images of several craters that have anomalously large central pits. The topographic relief of the craters marked by arrows in 6a-c is more subdued than that of other craters of the same size, which indicates greater age. In figure 6d, the arrow on the left marks a ray crater which has a smaller pit than does the crater on the right of closely similar size. A Type II penepalimpsest, 166 km in diameter, is also visible in 6d to the right and below the center of the frame (FDS 20636.50, 20636.44, 20636.59, and 20631.33)

tion of crater age, probably are related to differences in crustal properties at the different times that the craters were formed. All of the craters that have anomalously large pits on Ganymede (pits much larger than predicted by eq.(1) are located in the ancient cratered terrain.

Profiles of craters with central pits (Fig. 7) reveal that although the pits are depressions, they generally are surrounded by a raised rim. The depth of the pit below this rim is, in most cases, less than 1 km. In large pits, the pit floors are bowed-up in much the same manner as are the crater floors. Among the pits we have measured so far, the floors of the largest pits appear to be very near the level of the crater floors outside of the pits. Measured depth-to-diameter ratios of Ganymedian craters with central pits that are 30 to 50 km in diameter range from 1:9 to 1:30, for craters in grooved terrain. Depth-to-diameter ratios for similar craters within the ancient cratered terrain range from about 1:12 to 1:85. The height of the crater rim above the level of the surrounding surface varies from a few hundred meters (or less) to about 2 km.

Whereas most Ganymedian craters larger than 40 km in diameter exhibit a single central pit, one crater, centered at 54° N latitude and 192° W longitude, appears to have a small pit centered within a larger central pit. The diameter of this crater is 115 km; the relatively large rimmed central pit is 50 km in diameter and the small pit at the center is 4.5 km in diameter. This crater is located in grooved terrain and has bright rays.

Craters with central pits are also common on Callisto. These craters range in diameter from 18 to approximately 160 km. About 25 percent of craters 20 to 30 km in diameter and about 80 percent of craters 30 to 40 km in diameter have central pits. Essentially all craters larger than about 40 km in diameter have a central pit (Fig. 2). Crater depths up to 3 km below the crater rims have been

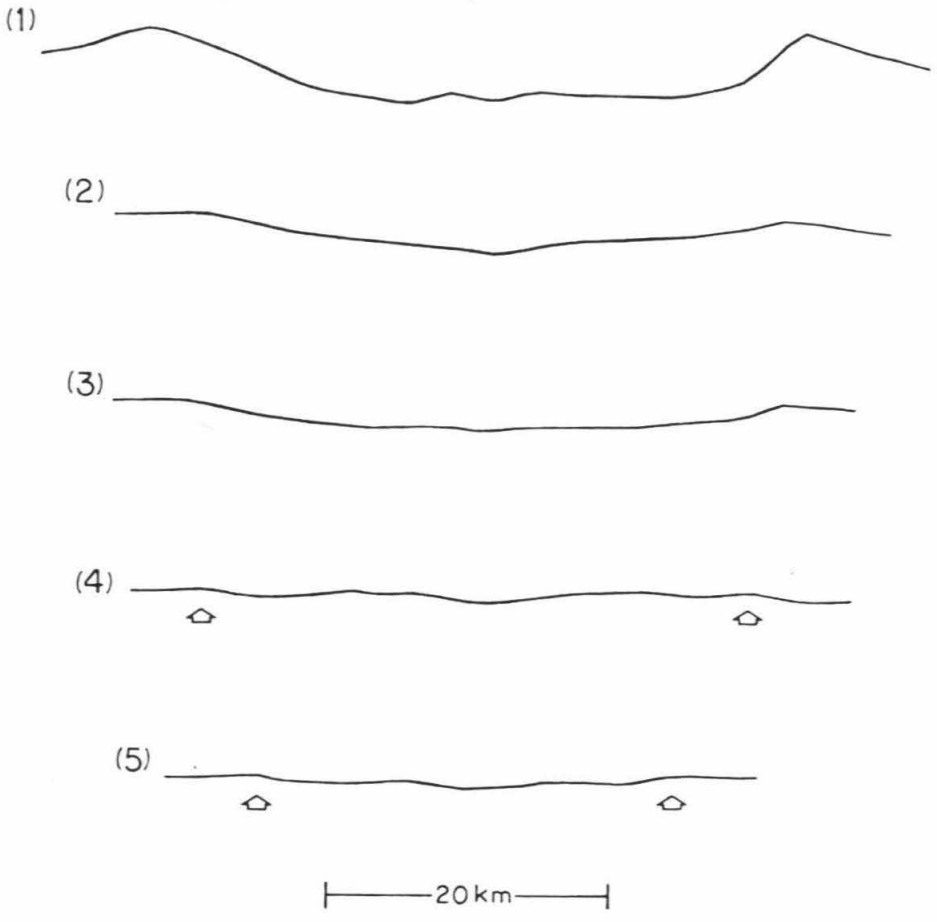

FIGURE 7 - Photoclinometric profiles of five craters with central pits on Ganymede that illustrate various degrees of topographic relaxation. The arrows in profiles (4) and (5) mark the crater rims in these extremely flattened craters. Note that, in the flattened craters, the relative size of the central pit is much larger than in the less relaxed craters (profiles 1,2, and 3). In profile (1), taken from a crater with a bright rim deposit, the central pit has an unusually high rim. This high rim may be the remnant of a partially collapsed central peak. The vertical scale is the same as the horizontal scale for these profiles.

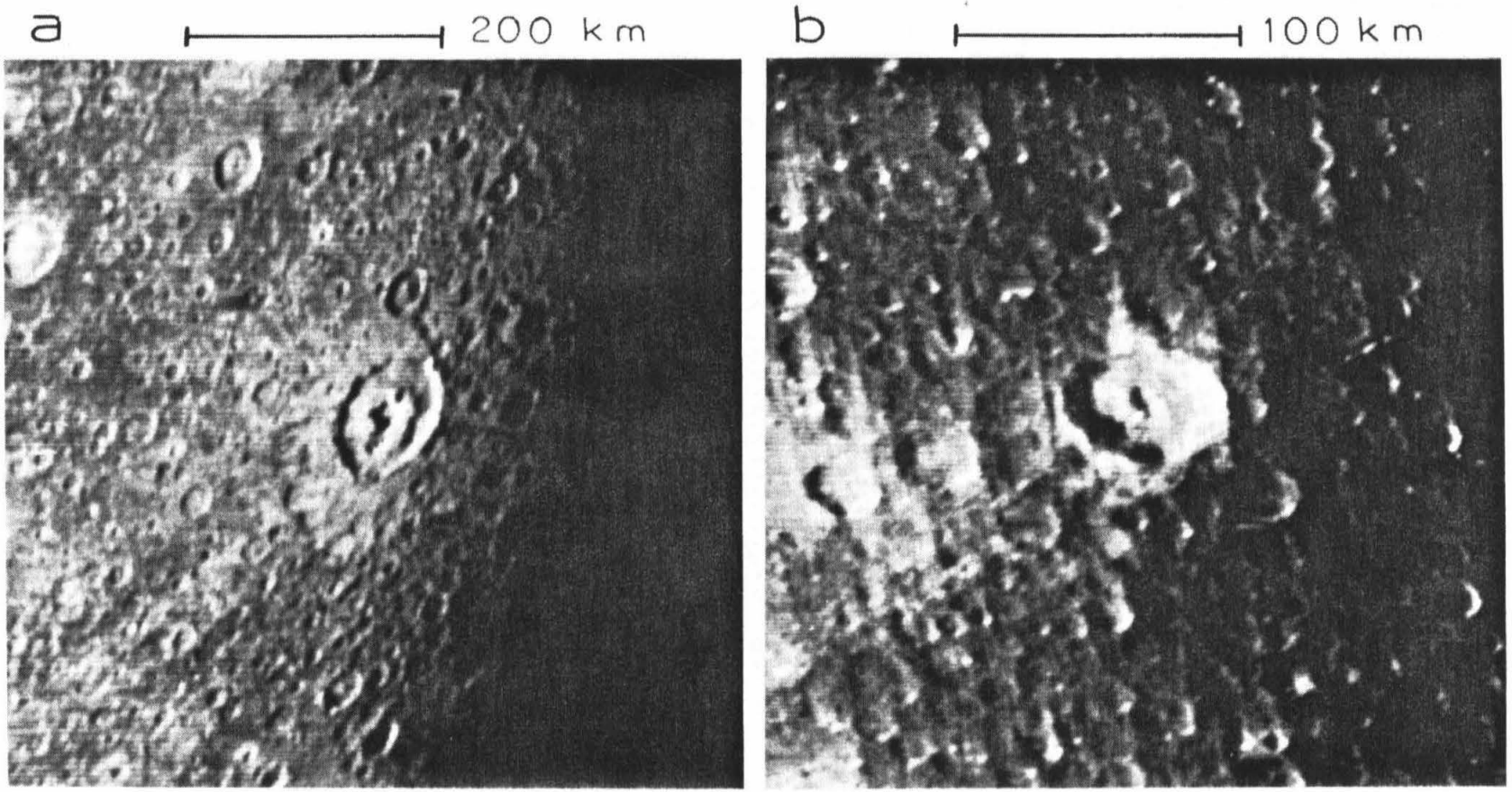

FIGURE 8 - Voyager I images of two craters on Callisto with strongly modified central pits. The pit illustrated in 8a appears to be modified either by superposed craters or by unusually extensive and irregular collapse. The form of the central pit in 8b appears to have been influenced by faulting, which extends beyond the confines of the crater rim; considerable enlargement of this pit appears to have occurred along the trend of the fault (FDS 16421.27 and 16426.36).

calculated from shadow measurements.

As in the case on Ganymede, the diameter of the central pit is positively correlated with the crater diameter on Callisto, and a curvilinear fit to the data is suggested when comparing pit diameter to crater diameter, particularly for the largest craters (Fig. 5). On Callisto, however, there is a larger spread in pit diameters for craters larger than 60 km in diameter, as compared to Ganymedian craters of this size. The smallest pits for a given crater size appear to be associated with the fresh apppearing ray craters. The best fit of an exponential function for the pit diameter versus the crater diameter for ray craters and craters with bright rim deposits on Callisto is

$$d = 1.45 \exp (.028\ D) \qquad (2)$$

where d and D are, respectively, the pit diameter and the crater diameter.

Most central pits on both Callisto and Ganymede are circular, but, some have irregular shapes (Fig. 8).

Chain craters on Callisto

Several relatively large chains of craters (catena) have been identified on Callisto. These are almost certainly chains of secondary craters related to large basins that have disappeared either by prompt collapse or by slow relaxation. Crater chains up to about 700 km in length have been found, and up to 27 craters are recognized in the longer crater chains. It is difficult to relate a given crater chain to the site of a former basin, but assuming that the crater chains are oriented radially to the source of impacting ejecta, sites can be suggested. Crater chains at about 50° N latitude and 350° W longitude (Fig. 9b) and at 12° S latitude and 13° W longitude (Fig. 9d) may be related to Valhalla. The sites of the original primary basins associated with the other crater chains are not yet

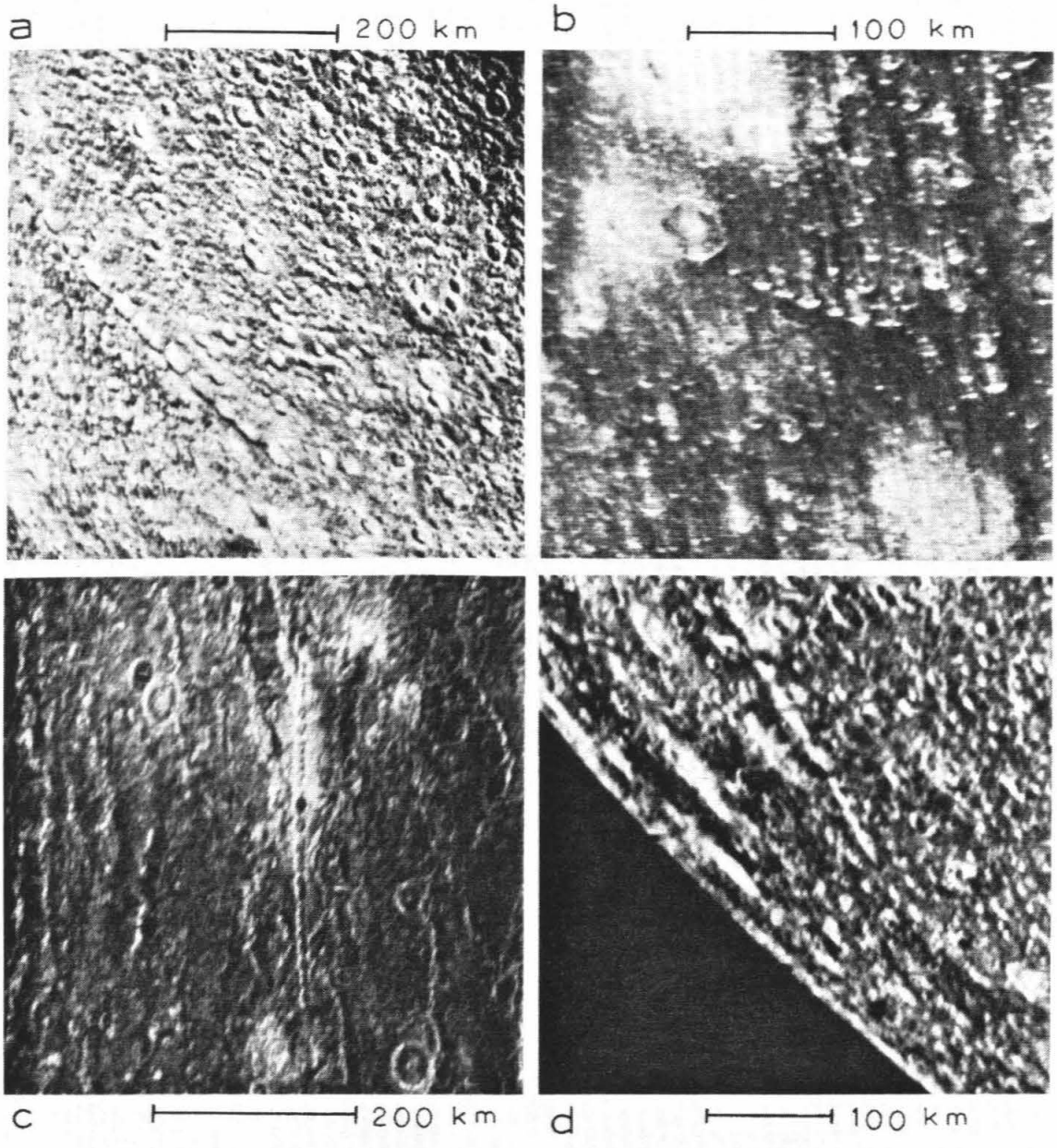

FIGURE 9 - Voyager I images of four large crater chains on Callisto. The diameters of the individual craters within a given chain are fairly uniform (FDS 16428.19, 16426.10, 16424.32, and 16424.26).

TABLE I - Prominent Crater Chains on Callisto

#	Lat.[1]	Long.[1]	No. of Craters	Chain length (km)[2]	Largest crater diameter[3] (km)	Smallest crater diameter[3] (km)
1	+67	57	14	700	31	24
2	+50	350	6	110	25	18
3	+32	347	27	370	17	15
4	-12	13	9	225	20	14
5	-18	343	10	175	10	8

[1] From U.S. Geological Survey Map I-1239, 1979.

[2] Lengths ± 10%.

[3] Diameters are generally ± 2 km.

identified.

The chain craters generally are circular in shape. In some cases, individual craters overlap substantially, and in other cases, they are completely separated (Fig. 9). Diameters of recognizable craters in a given chain are within ± 15 percent of the mean for the chain. The observed range in crater diameters, for craters from different chains, is from about 8 to 30 km.

Most chain craters about 20 km in diameter have central peaks, whereas most chain craters 30 to 35 km in diameter have a slight central depression, possibly a central pit. The morphology of large craters in secondary crater chains is basically the same as for primary craters of the same size. Thus any isolated secondary craters larger than 10-15 km in diameter are not expected to be morphologically distinguishable from primary craters of the same size.

Gilgamesh and Western Equatorial Basins on Ganymede

One fresh relatively unmodified basin, Gilgamesh, is found on Ganymede; it is located within grooved terrain (centered at 59° S, 123° W). The floor of the conspicuous central depression is relatively smooth and flat and is approximately 150 km in diameter (Fig. 10). Several small peaks are arranged in an arc in the center of the floor; the diameter of the arc is about 50 km. Faint radial lineations also appear to be present on the floor (Fig. 10c). A poorly defined rim, approximately 175 km in diameter, with an approximate average height of 1/2 km bounds the central depression. This depression evidently corresponds to the central pit of the impact basin.

A rugged hilly-to-mountainous region surrounds the central depression and extends radially for approximately 500 km. Individual features of the relief have an angular or blocky appearance; the heights of the individual blocky mas-

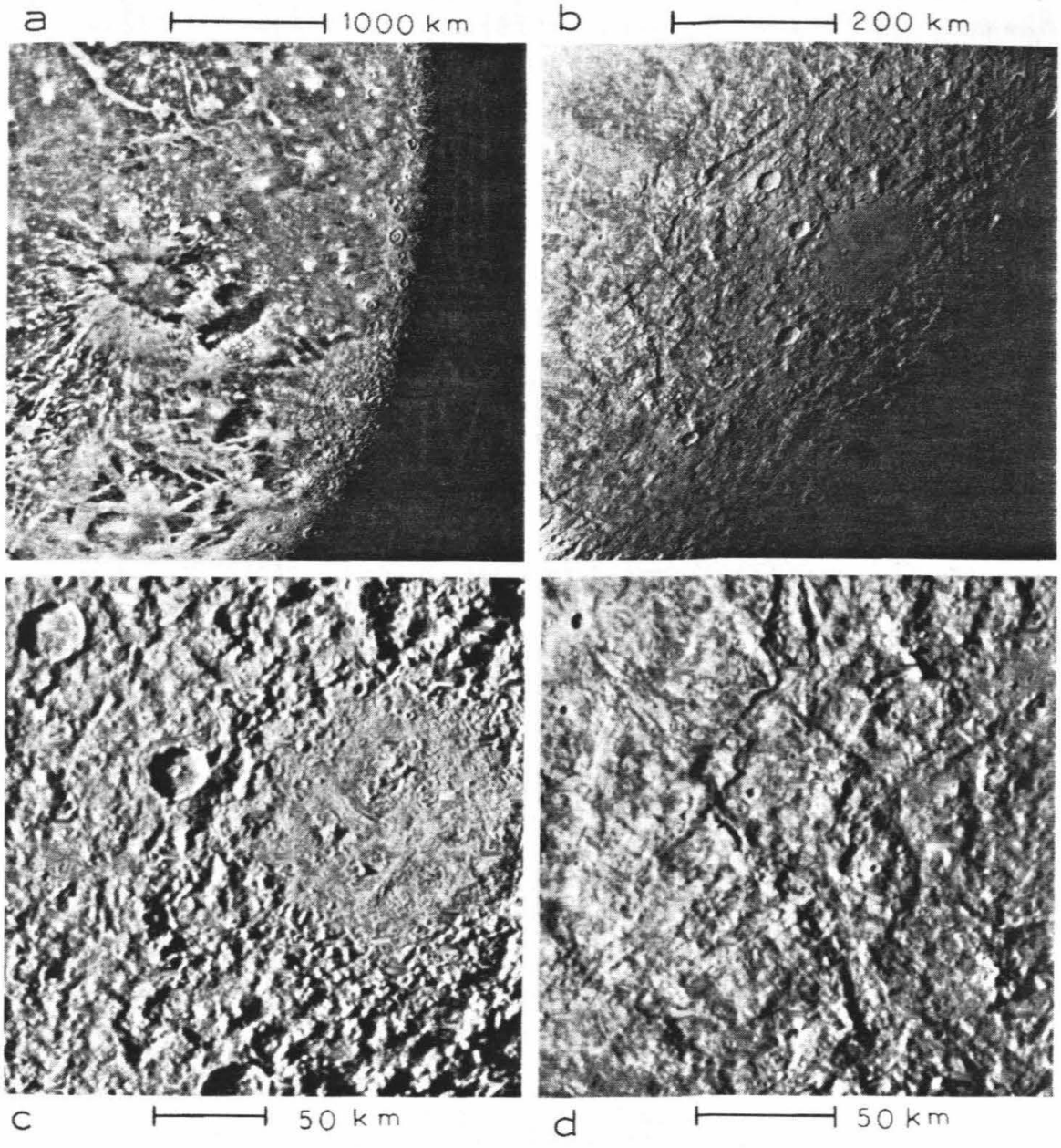

FIGURE 10 - Voyager II images of Gilgamesh, the least topographically relaxed basin on Ganymede. The diameter of the relatively smooth basin floor is about 150 km; the ill-defined rim is about 175 km in diameter. A high resolution image of the basin (10c) reveals radial lineations as well as a roughly arcuate group of central peaks. Gilgamesh is surrounded by a rugged region of blocky to irregular relief about 1000 km in diameter; this region probably corresponds to a continuous ejecta blanket. Inward facing concentric scarps can be seen in this region. Figure 10d shows a high resolution image of one of these scarps where its trace apparently cuts across a 20 km diameter crater (just below the center of the frame). Since this crater postdates the formation of the Gilgamesh basin and emplacement of the ejecta rim, the extension of the scarp across this crater is probably a result of renewed movement, possibly due to settling of the ejecta deposit along the fault that produced the scarp (FDS 20639.04, 20638.14, and 20639.15).

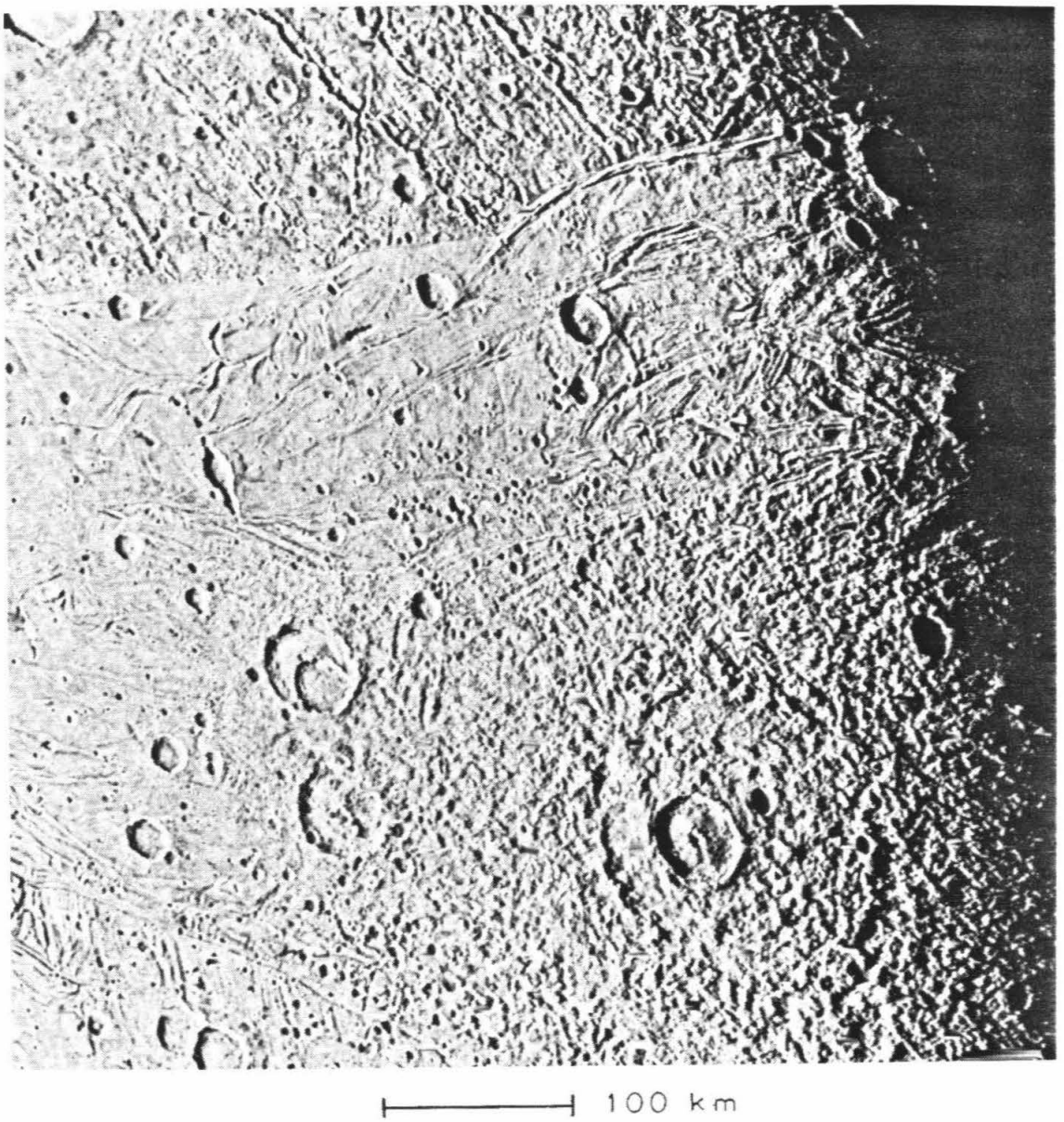

FIGURE 11 - Voyager II image of the Western Equatorial Basin on Ganymede (lower right part of the frame). This basin is somewhat similar to Gilgamesh but is slightly larger and has much more subdued relief. The diameter of the basin rim is 183 km; the basin is surrounded by a hummocky rim deposit about 530 km in diameter. Prominent secondary craters and crater chains extend beyond the recognizable rim deposit and are superposed on grooved terrain (FDS 20638.39).

sifs are 1/2 km to 1-1/2 km. Several inward facing concentric scarps occur within the outer blocky annulus. The scarps are discontinuous in circumferential extent and have heights from less than 1 km to about 1-1/2 km. The most prominent scarp, at about 275 km radius, is considered by Shoemaker et al. (1982) to mark the rim of the Gilgamesh basin.

A great swarm of secondary craters and crater chains surrounds the Gilgamesh basin. These craters extend from a radial distance of about 400 km to about 750 km from the center of the basin. The diameters of most secondary craters are less than 5 km, but some craters up to about 15 km in diameter are present in the swarm.

A second basin, slightly larger than the central depression of Gilgamesh, but greatly flattened by viscous relaxation, occurs on grooved terrain centered at 7° S latitude and 115° W longitude (Fig. 11). The center of this basin is relatively flat but appears rough, owing to ejecta deposits of craters which postdate this basin. The diameter of this central region is about 185 km. A well-defined rim or scarp surrounds the central region; the height of this rim is less than 600 meters. a rim deposit, composed of low hills and hummocks, surrounds the central basin and extends radially to about 265 km; the relief within the rim deposit is generally less than 400 meters. A swarm of secondary craters surrounds this basin; secondary craters can be found from a radial distance of about 150 to 450 km from the center of the basin. The maximum diameter of the secondary craters is about 10 km.

Crater Palimpsests

A crater palimpsest is a roughly circular spot of high albedo that marks the site of a former crater and its rim deposit (Smith et al., 1979b) (see Figs. 12 & 13). At low resolution, palimpsests are relatively featureless. Except for

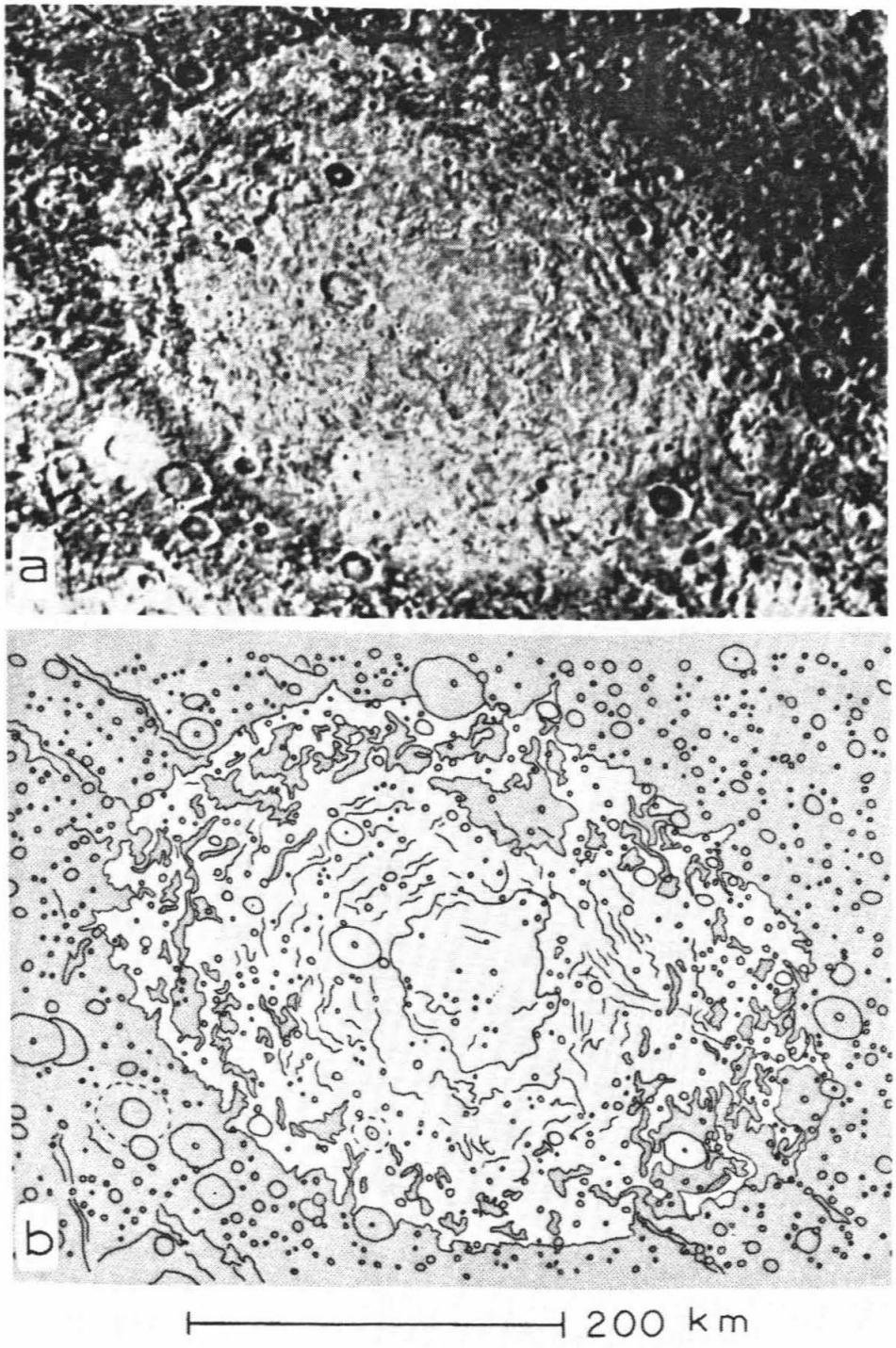

FIGURE 12 - Voyager II image and sketch map of a large palimpsest in the Galileo Regio of Ganymede. The palimpsest is divisible into three distinct zones: 1) a relatively smooth central region about 100 km in diameter , which is roughly circular and is bounded by a very gentle irregular topographic step (shown with a nearly continuous solid line near center of map), 2) a uniform high-albedo annulus with small semi-concentric ridges or hummocks, and 3) an outer annulus which is mottled in albedo. Vestiges of the pre-palimpsest rimmed furrow system extend within the palimpsest. Secondary craters probably are represented among the abundant small craters illustrated in the sketch map; proceeding out from the center, the region of highest density of small craters, begins in the annulus of mottled albedo (beyond approximately 100 km from the center) and extends beyond the palimpsest. Areas of relatively low albedo are shaded on the sketch map; craters and pits are outlined with solid lines; short irregular solid lines represent subdued ridges; furrows are shown with paired line; the limit of bright ejecta around two craters is shown with dashed lines (FDS 20638.29).

TABLE II -Crater Palimpsests on Ganymede

#	Latitude[1]	Longitude[1]	Palimpsest Diameter[2](km)	Diameter of Central Structure[2] (km)	Terrain Type[3]
1	+22	184	335	128	G
2	+19	197	228	---	AC
3	+10	215	370	---	AC
4	+ 6	209	334	---	AC
5	+ 9	203	240	---	AC
6	+ 4	202	306	---	AC
7	+ 8	195	137	---	AC
8	-11	220	211	132	AC
9	+40	160	169	---	AC
10	+38	154	152	---	AC
11	+36	153	196	---	AC
12	+29	146	188	---	AC
13	+19	129	319	186	AC
14	+ 9	141	256	---	AC
15	+11	352	183	---	AC
16	+ 6	353	179	---	AC
17	- 1	356	167	---	AC
18	-17	339	116	58 (34)	AC
19	+10	354	173	---	AC
20	+10	359	102	---	AC
21	+10	358	79	---	AC
22	- 9	15	123	---	AC

[1] From U.S. Geological Survey Map I-1242, 1979.

[2] All measurements ± 10%.

[3] AC= Ancient cratered terrain; G= Grooved Terrain

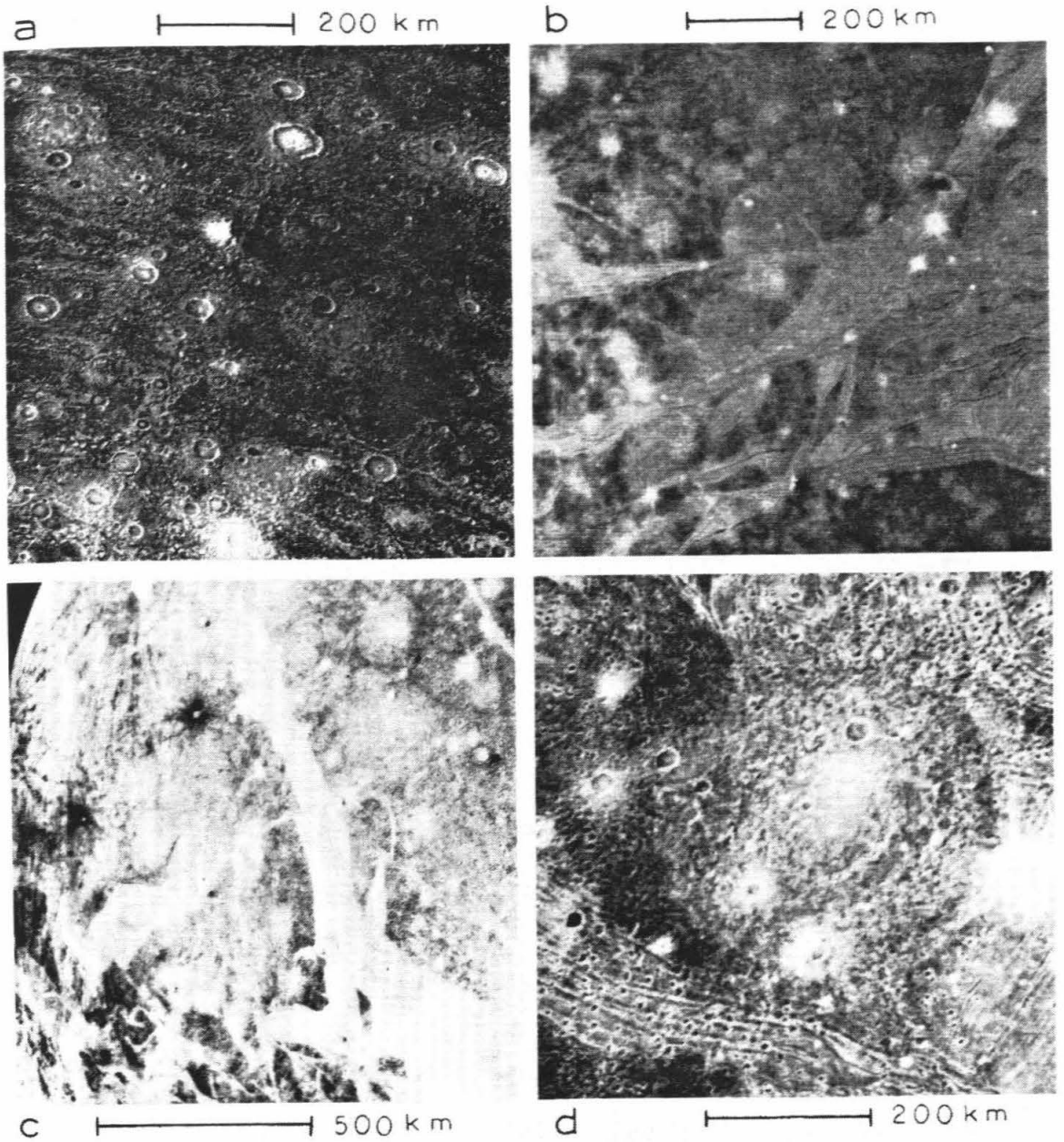

FIGURE 13 - Voyager I and II images of several palimpsests. Figure 13a shows six palimpsests with diameters less than 200 km located in the Galileo Regio. Younger grooved terrain units have cut across the palimpsest in 13b. The region of Marius Regio in 13c is about half occupied by palimpsests. With the exception of the palimpsest in 13d, all of the palimpsests are found within the ancient cratered terrain, and appear to be older than the formation of the grooved terrain (FDS 20636.59, 16402.22, 20631.17, and 20635.37).

TABLE III - Possible Crater Palimpsests on Ganymede

#	Latitude[1]	Longitude[1]	Palimpsest Diameter[2](km)	Diameter of Central Structure[2](km)	Terrain Type[3]
1	+25	195	235	---	AC
2	-10	211	168	---	AC
3	+37	145	215	---	AC
4	+22	149	156	---	AC
5	- 5	217	436	---	AC
6	+32	9	131	---	AC
7	-11	8	127	---	AC
8	- 3	322	125	70 (36)	AC
9	- 9	342	94	---	AC
10	- 2	342	75	---	AC
11	+28	135	138	---	AC
12	-10	319	155	---	AC

1 From U.S. Geological Survey Map I-1242, 1979.

2 All measurements ± 10%.

3 AC=Ancient cratered terrain; G=Grooved Terrain.

secondary craters and traces of hummocks in the rim deposit, they retain almost none of the original relief of the crater or its rim. In a few instances, a smooth central area can be defined in high resolution pictures of large palimpsests (Fig. 12). We infer that this smooth area corresponds approximately to the floor of the original crater. Where the smooth area can be recognized, the diameter of the palimpsest is about two to four times the diameter the the central smooth area. Swarms of small secondary craters occur near the outer boundary of large palimpsests. The relationship of the secondary craters to the palimpsests suggests that the outer boundary corresponds approximately to the limit of continuous ejecta (Smith et al., 1979b).

Three distinct concentric zones can be recognized from high resolution pictures of one of the largest palimpsests (Fig. 12). The central smooth region is essentially featureless and is at nearly the same elevation as the surrounding terrain. A very gentle irregular discontinuous topographic step surrounds this central region. A zone of uniform albedo extends about one central-area diameter beyond this step, and this zone is characterized by a semiconcentric fabric of very low ridges or hummocks, that have an average radial spacing of approximately 5 km. Beyond this zone, the palimpsest becomes discontinuous and mottled in albedo.

Vestiges of a pre-palimpsest rimmed furrow system can be recognized in this outermost zone. Extremely faint lineations, along the trends of the rimmed furrows are also visible in the central and intermediate zones as well. The outer boundary of the palimpsest is demarcated by the contrast in albedo between the palimpsest and the surrounding ancient cratered terrain. The transition in albedo generally occurs in less than 5 km.

TABLE IV - Crater Palimpsests and Possible Palimpsests on Callisto

#	Latitude[1]	Longitude[1]	Diameter (km)[2]	Remarks
1	+42	2	156	
2	+46	348	121	
3	- 5	5	206	
4	- 5	348	169	
5	- 7	337	94	
6	-12	38	93	
7	- 2	25	286	
8	+59	346	87	
9	+11	57	571	Valhalla
10	+80	10	102	
11	+30	39	230	Asgard
12	- 6	247	417	
13	-11	234	272	
14	-19	249	118	
15	-41	224	94	

[1] From U.S. Geological Survey Map I-1239, 1979.

[2] All measurements ± 10%.

A total of 22 readily recognized palimpsests have been identified on Ganymede (Table II). Their outer diameters range from 80 to 335 km. In addition, there are twelve palimpsests that are identified with less certainty, with diameters up to 440 km (Table III). All but one (Fig. 13d) of the palimpsests listed are located on ancient cratered terrain.

Palimpsests on Callisto are less obvious than those on Ganymede; the albedo contrast with the surrounding terrain is less than for Ganymedian palimpsests and the outer boundaries of palimpsests on Callisto are more diffuse and irregular. Table IV gives coordinates and diameters for 15 palimpsests and possible palimpsests. The palimpsest outer diameters range from about 80 to 570 km. The resolution of the images of Callisto is insufficient to define morphological zones within these palimpsests. The two largest palimpsests occupy the central regions of two great multiring structures, Valhalla and Asgard (Figs. 16 & 17).

Penepalimpsests

In addition to palimpsests, there are a number of features on Ganymede which are more or less transitional in form between craters and palimpsests. These features have diverse topographic and albedo characteristics but all have vestiges of crater rims or other topographic features of the rim deposits. Evidently they represent ancient craters which have nearly disappeared by viscous relaxation or creep. Here we will group these features together under the category of penepalimpsests (almost palimpsests). In contrast with the palimpsests, most penepalimpsests occur on grooved terrain, rather than the ancient cratered terrain. For the purpose of description, they can be broadly grouped into two categories. The first category (type I) consists essentially of extremely relaxed craters. The second category (type II) comprises more complex structures with a low central dome surrounded by annuli of complicated

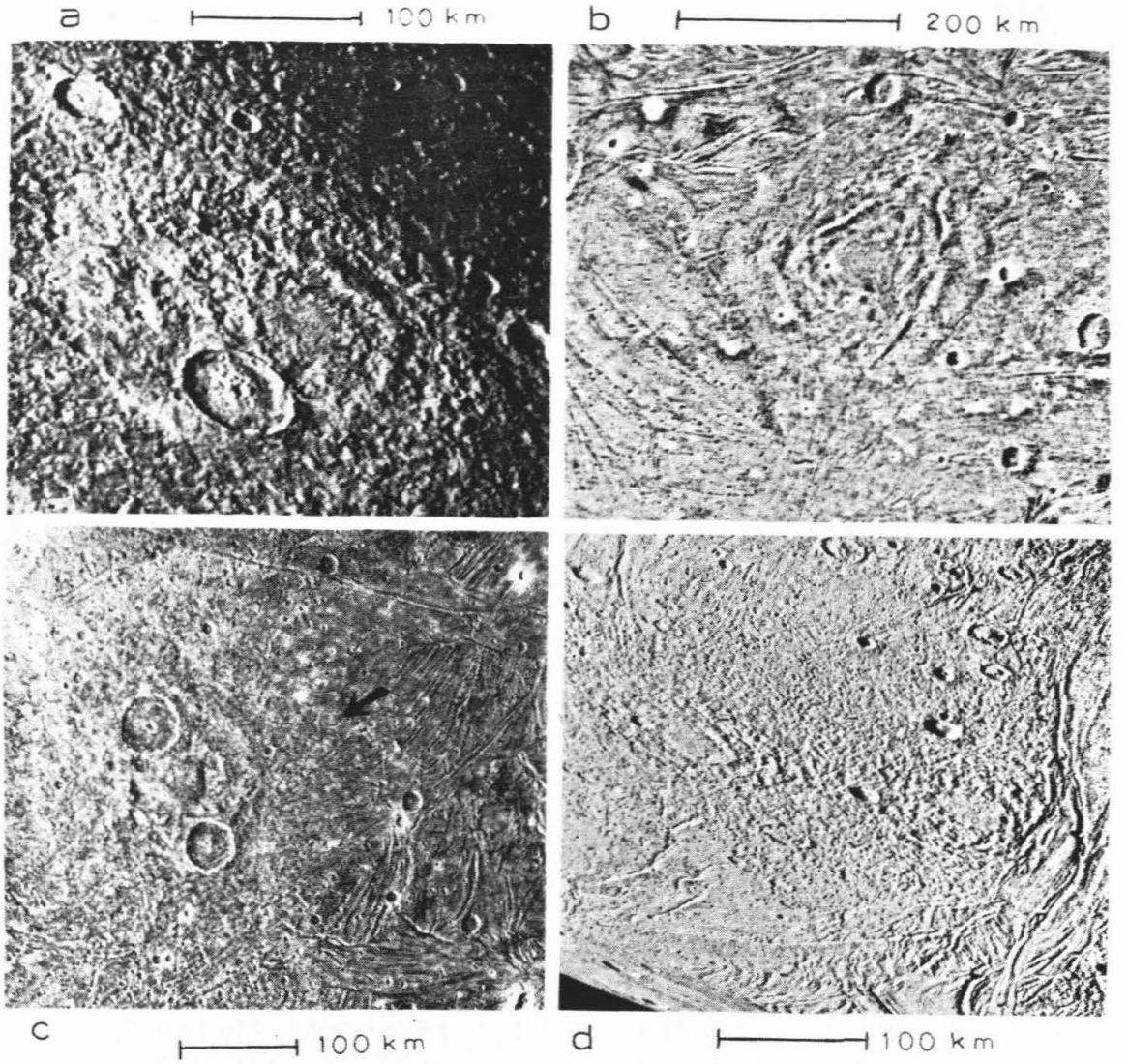

FIGURE 14 - Voyager I and II images of four Type I penepalimpsests; see text for description. The initial crater relief of all of these features has nearly disappeared, presumably due to viscous flow or creep within Ganymede's crust. The arrow in figure 14c marks the approximate outer limit of the burial of grooves by the continuous ejecta blanket of the ~140 km diameter penepalimpsest (left of frame center) (FDS 20638.31, 16405.30, 20639.53, and 20640.31).

but very subdued relief.

Type I penepalimpsests.-- A variety of features are grouped in this category. One feature (type I-a, Table V) in the ancient cratered terrain of the Galileo Regio (Fig. 14a) closely resembles the palimpsests of this region except that distinct vestiges of the original crater rim are preserved. Surrounding the rim is a roughly circular area of high albedo, about twice the diameter of the crater rim, which is similar to the intermediate and outer zones of the palimpsests.

Three features (type I-b, Table V), one in ancient cratered terrain and two in grooved terrain, are characterized by a wreath of low semi-concentric ridges surrounding a central smooth region. An outer zone 1 1/2 to 2 times the diameter of the wreath, is relatively smooth but also contains very subdued semiconcentric ridges. Where formed on the grooved terrain there is no conspicuous contrast in albedo between the penepalimpsest and the surrounding surface. In the example illustrated in figure 14b, the outer zone is 260 km in diameter; by means of a photoclinometric profile, the entire feature has been shown by Squyres (1980) to be a topographic dome about 2 1/2 km high. Prominent swarms of secondary craters extend northeast and southwest from this penepalimpsest.

One penepalimpsest (type I-c, Table V) is a highly flattened basin that occurs within grooved terrain (Fig. 14c). Its relief appears comparable to the type I-a penepalimpsest that lies in the ancient cratered terrain, but because the type I-c penepalimpsest lies in a region of intrinsically higher albedo, there is no evident contrast in albedo between the area immediately surrounding the collapsed basin and the neighboring terrain. A central circular ridge 71 km in diameter is surrounded by an outer very subdued raised rim 138 km in diameter. Local sharp relief is found along the rim. Grooves and ridges in the grooved

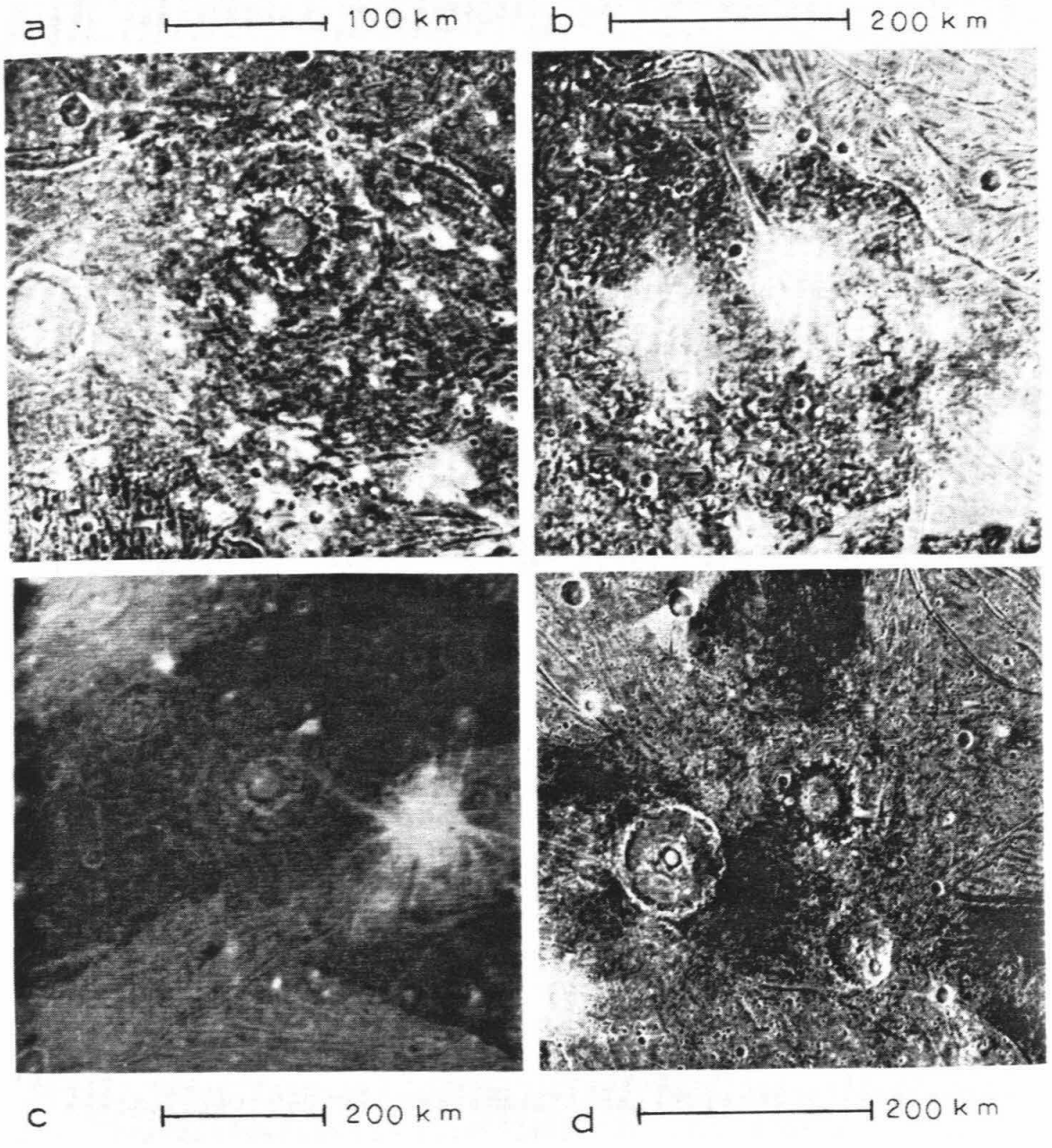

FIGURE 15 - Voyager I and II images of several Type II penepalimpsests. All have a circular central area of high albedo which is surrounded by an annulus of low albedo with radial light streaks. Two concentric ridges surround this central area. The inner ridge corresponds to the rim of an unusually large central pit, and the outer ridge corresponds to the original crater rim. In some cases, as shown in figures (15a) and (15c), the outer rim is bright; as shown in figures (15b) and (15d), however, the ridge which corresponds to the initial crater rim is not always bright (FDS 20637.41, 20635.49, 16402.12, and 20637.23).

terrain are obliterated to a distance of about 150 km from the center of the penepalimpsest. We interpret the slightly elevated rim as the original rim of the basin and the inner circular ridge as the rim of a huge flattened central pit. The rim deposit of this basin extends to the limit of obliteration of grooves in the grooved terrain. Abundant secondary craters associated with this flattened basin extend from a radial distance of about 150 km (just beyond the rim deposit) to about 200 km. The maximum diameter of the secondary craters is about 7 km.

Two penepalimpsests on grooved terrain (type I-d, Table V) are characterized by a large central smooth area encompassed by a broad annulus of subdued short semiconcentric ridges and irregular hummocks (Fig. 14d). In each case, the width of the annulus is roughly the same as the diameter of the central smooth region. The smooth region evidently corresponds to the initial crater floor and the annulus to the original crater rim deposit. Apparently because these penepalimpsests occur in the relatively high albedo grooved terrain, there is no contrast in albedo between the rim deposit and the grooved terrain. Each of these penepalimpsests is superposed on and is younger than some grooved terrain units. One of these penepalimpsests, however, is also older than one unit of grooved terrain which transects the rim deposit (Fig. 14d). This latter penepalimpsest, therefore, was formed during the period of the grooved terrain formation.

Type II penepalimpsests.-- Five unusual craterform features are included here under the category of penepalimpsest, although a separate designation might be appropriate. They are large highly relaxed craters, approaching basins in size, that are characterized by unusually large irregular central pits (Fig. 15). In the center of each central pit is a circular area of high albedo that appears to

TABLE V - Penepalimpsests on Ganymede

#	Lat.[1]	Long.[1]	Penepalimpsest Diameter[2] (km)	Diam. Initial Crater (km)	Diam. Central Structure (km)	Penepalimpsest Type[3]	Terrain Type[4]
1	+22	119	266	144	---	I-a	AC
2	-16	120	139	---	---	I-b	G
3	+36	328	260	---	---	I-b	G
4	- 3	323	125	70	---	I-b	AC
5	-36	137	300	138	71	I-c	G
6	-69	265	183	64	---	I-d	G
7	-70	280	171	60	---	I-d	G
8	-28	169	---	103	52 (25)[5]	II	G
9	-14	132	---	127	66 (32)[5]	II	G
10	+ 4	173	---	142	81 (30)[5]	II	AC
11	+36	2	---	149	85 (40)[5]	II	AC
12	-12	102	---	166	90 (38)[5]	II	G

1 From U.S. Geological Survey Map I-1242, 1979.

2 All measurements ± 10% due to uncertainty in penepalimpsest boundary.

3 Refer to text for discussion of penepalimpsest type.

4 AC= Ancient cratered terrain; G= Grooved terrain.

5 Diameter of high albedo central dome.

have the form of a broad topographic dome. Each dome is about half the diameter of the central pit. It has been suggested that the high albedo dome may be an icy diapir (Malin, 1980) or the result of the freezing of a central lake which was produced at the time the crater was formed (Croft, 1980). Surrounding the dome, but within the pit walls, is an annulus of low albedo marked with roughly radial light streaks. The enclosing central pit walls have high albedo. Considerable relief is preserved in the central parts of these penepalimpsests but the outer crater rim is extremely subdued.

Two of the Type II penepalimpsests occur on ancient cratered terrain (Fig. 15c) and three on grooved terrain (Figs. 15a,d). No distinct areas of high albedo surrounding the relaxed craters have been recognized either on grooved terrain or on the ancient cratered terrain.

Multiring structures on Callisto

Several systems of multiple concentric ridges occur on Callisto. Eight have been found (Table VI); they fall into two size categories, 1) diameter of the outer ridge ring larger than 500 km, and 2) diameter of outer ridge ring less than 200 km. None has been found with an outer diameter between 200 and 500 km.

The largest multiring structure, Valhalla, has concentric ridges out to approximately 2000 km from the center (Fig. 16c). A central bright palimpsest occupies a region nearly 600 km in diameter. In the center of the palimpsest is a circular, relatively smooth area approximately 350 km in diameter. The superposed crater density on the palimpsest is roughly one-fourth of the crater density of the surrounding surface of Callisto. The innermost concentric ridge occurs at a radius of about 200 km; hence the palimpsest overlaps the inner ridges over a radial distance of about 100 km.

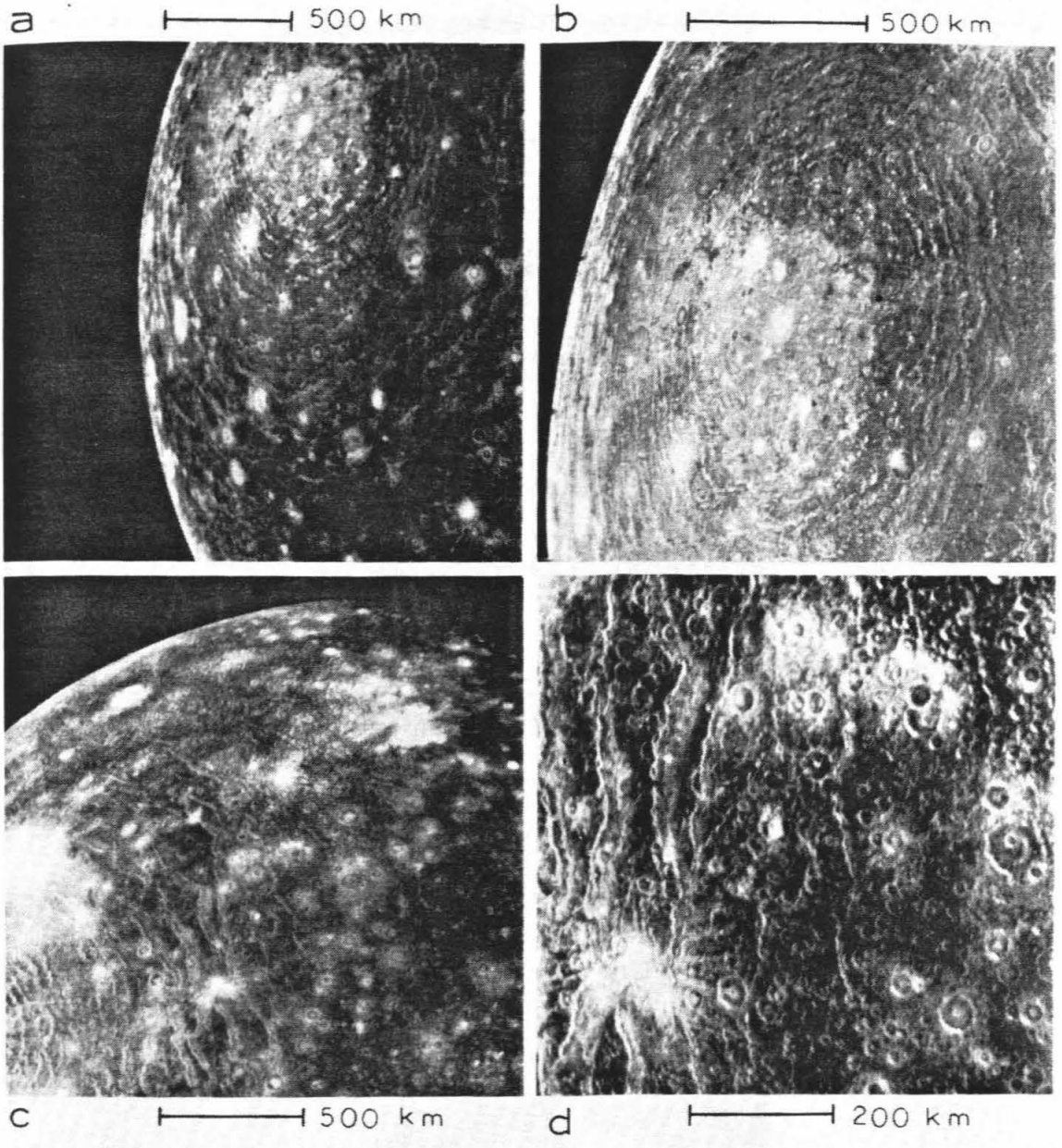

FIGURE 16 - Voyager I images of Valhalla, the largest multiring structure on Callisto. The center of the structure is occupied by a high albedo palimpsest 600 km in diameter (16b). Ridges occur up to approximately 200 km from the center of the feature, as shown in 16c. The individual ridges in the ring system appear to be flat-topped, as shown in 16d. (Note that the illumination is from the left and not from the right). Some images reveal troughs in the tops of the ridges (FDS 16418.42, 16422.11, 16418.58, and 16424.46).

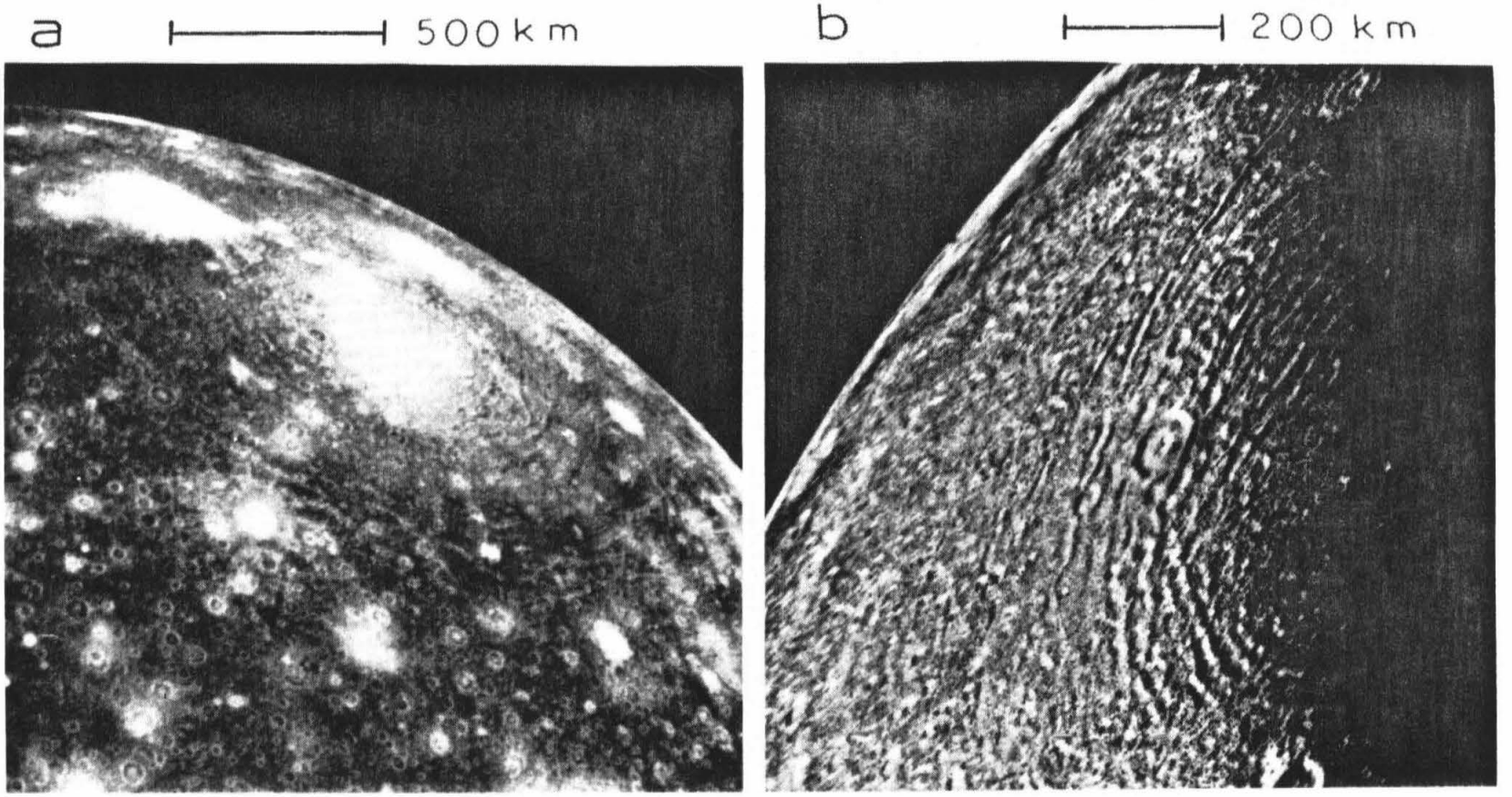

FIGURE 17 - Voyager I and II images of Asgard, the second largest multiring system on Callisto. This structure is very similar to Valhalla but is only about 1500 km in diameter. The center is occupied by a palimpsest and the ring ridges appear flat-topped. As is the case with Valhalla, the spacing of the ridges is closest near the center of the ring system (FDS 20606.21, and 16428.09).

In detail, the individual ridges in this multiring system are irregular in plan and are discontinuous in circumferential extent. Maximum length of the individual ridge arcs is approximately 700 km; most ridges are between 200 and 500 km in length. Distance between the ridges varies from approximately 20 to 30 km, for the inner ridges, to roughly 50 to 100 km, for the outer ridges.

On average, the ridges are about 15 km wide, and they appear to be flat-topped (Fig. 16d). In a few places, however, a central groove or furrow is resolved within the ridge (McKinnon and Melosh, in press). It is difficult to determine the heights of the ridges of the Valhalla multiring system, owing to the proximity of Valhalla to the subsolar point at the time the pictures were obtained. Comparison with ridges of the Asgard multiring system, the heights of which can be determined by shadows, suggests that the ridge heights in the Valhalla system are less than 1 km above the surrounding surfaces.

The second largest multiring system on Callisto, Asgard, has concentric ridges out to 600 km from the center of the system (Fig. 17). The center of this system is occupied by a palimpsest about 230 km in diameter. The innermost concentric ridges are located approximately 80 km from the center. The spacing between the inner ridges is 20 to 30 km, and between the outer ridges generally 50 to 60 km. The heights of most ridges are between 500 and 1000 meters above the inter-ridge surfaces.

A third relatively large multiring structure is centered at about 53° S and 36° W (Fig. 18d). The outermost ridges are at roughly 450 km from the center and the innermost ridges recognizable in the available low resolution images occur at a radius of about 70 km. Coverage of this feature by Voyager pictures is limited and details within this system are not resolved. Albedo characteristics of the center of the ring structure are obscured by rays from the very large ray

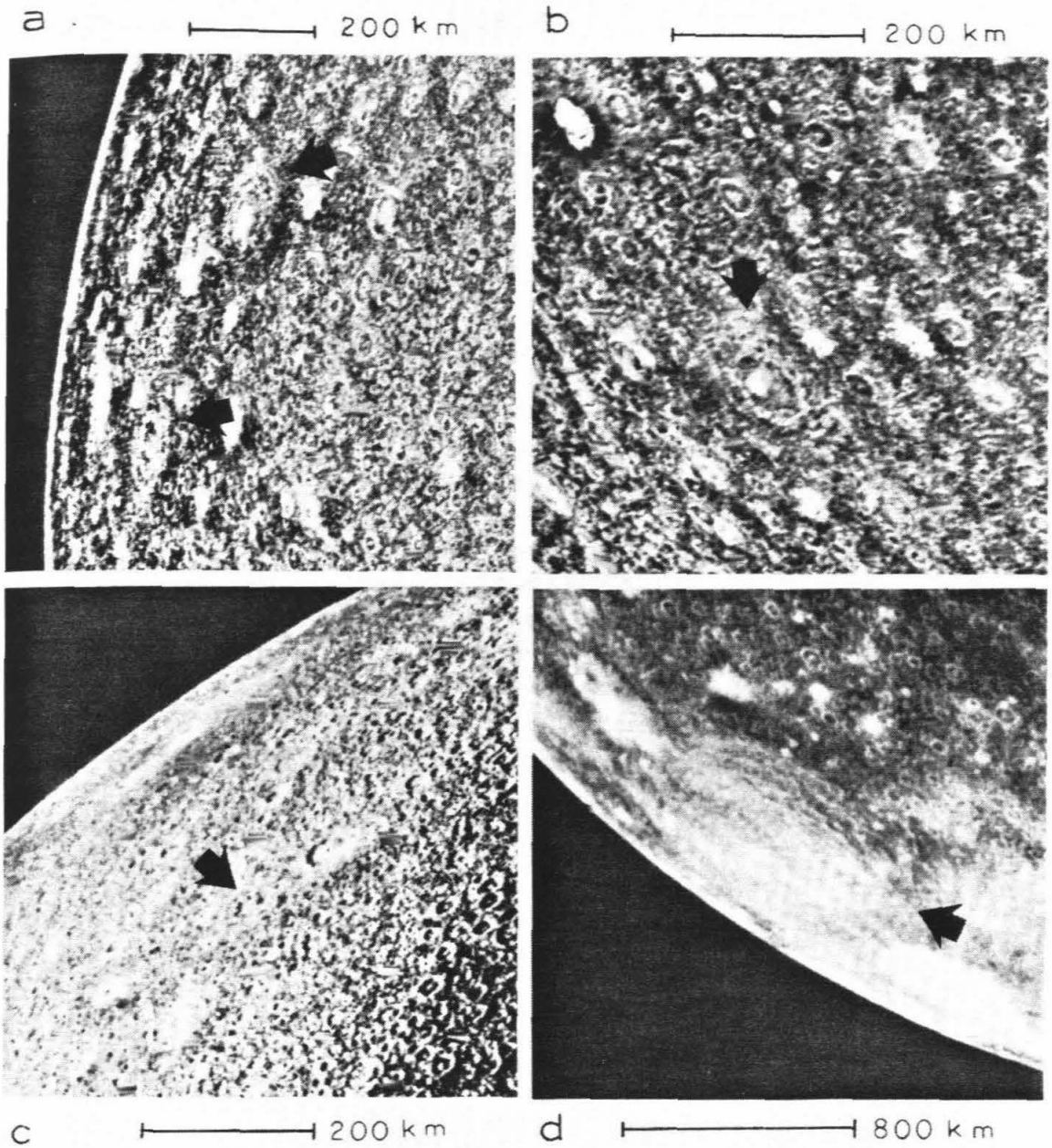

FIGURE 18 - Voyager I and II images covering five multiring structures on Callisto. Four of these multiring structures are smaller than 200 km in diameter (18 abc) and the spacing of their ring sets is about 5 to 10 km. Alfr (top central) and Loni are shown in 18a, Grimr in 18b, and an unnamed structure in in 18c. An unnamed large multiring system which has a diameter of about 900 km is shown in 18d (FDS 20617.21, 20616.53, 20619.36, and 16418.14).

TABLE VI- Multiring structures on Callisto

#	Lat.[1]	Long.[1]	Outer Ring Diameter[2] (km)	Inner Ring Diameter[2] (km)	Ring Spacing Inner	Ring Spacing Outer	Name
1	+11	57	4000	400	30	50-100	Valhalla
2	+30	139	1640	163	20-30	50-60	Asgard
3	-53	36	920	130	15	30	Unnamed
4	+45	138	500	?	?	?	Unnamed
5	- 9	222	163	80	7-9	-----	Alfr
6	- 3	215	123	25	10	-----	Loni
7	+42	213	180	96	5	-----	Grimr
8	-41	262	71	35	?	?	Unnamed

[1] From U.S. Geological Survey Map I-1239, 1979.

[2] All measurements ± 10%.

crater, Adlinda, to the southeast.

Another large multiring structure overlaps with Asgard and is centered approximately 45° N latitude and 138° W longitude. Its outer diameter is approximately 500 km.

Four small multiring structures with outer diameters less than 200 km are Alfr and Loni (Fig. 18a), Grimr (Fig. 18b), and one unnamed structure (Fig. 18c). The number of individual circumferential ridges varies from three to more than six. The spacing between ridges is less than 10 km. The heights of the ridges cannot be accurately obtained because of the location of these structures with respect to the terminator at the times they were imaged.

One of the small multiring structures (Fig. 18c) may be analogous to the Type II penepalimpsests of Ganymede. The resolution of this feature on Callisto is too low, however, for close comparison with penepalimpsests on Ganymede.

Galileo Regio rimmed furrow system

A system of rimmed furrows (Smith et al., 1979b) occurs throughout the greatest region of ancient cratered terrain on Ganymede, known as the Galileo Regio (Fig. 19). This system extends over an area of more than 10^7 km^2, an area greater than the United States, and can be found in many polygons of ancient cratered terrain that are separated from the Galileo Regio by grooved terrain. The system is more than 2000 km across in the direction normal to the trend of the furrow; the area covered by the preserved remnants of this system must be only a fraction of the area of the original system. The rimmed furrow system is so large that it was difficult to determine with certainty, at first, whether the average trends of the furrows follow small circles or great circles on the Galileo Regio. They do follow small circles on the Galileo Regio and on other

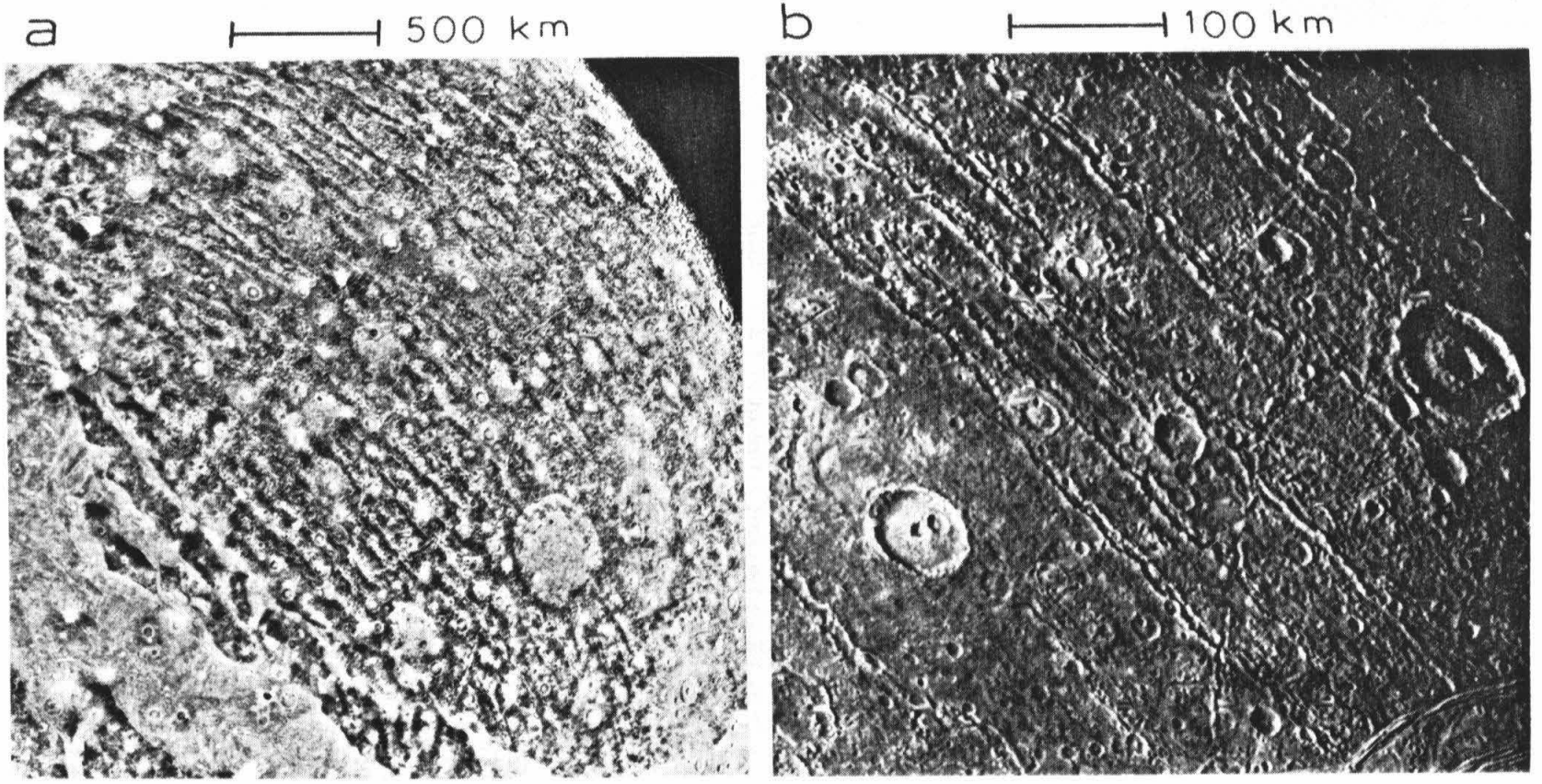

FIGURE 19 - Voyager II images of the Galileo Regio rimmed furrow system. The furrows are older than most features on the Galileo Regio and they have a curvilinear trend (19a). The furrows are about 10 km wide and spaced about 50 km apart on the Galileo Regio (19b) (FDS 20631.11, and 20638.35).

major segments of ancient cratered terrain south and west of Galileo Regio. The center of the concentric system of small circles is about 20° S latitude and 165° W longitude, where about half of a faint poorly defined palimpsest is preserved on the ancient cratered terrain. The southern half of the palimpsest is replaced by grooved and reticulate terrain. The palimpsest, about 500 km in diameter, is surprisingly small compared to the size of the rimmed furrow system. The original crater may have been smaller than the central depression of Gilgamesh. As the furrows are older than the vast majority of craters on the ancient cratered terrain, it is perhaps not so surprising that so small an original crater gave rise to the ring system. The lithosphere of Ganymede probably was very thin at the time the furrows were formed (McKinnon and Melosh, 1981).

Segments of the rimmed furrow system found on polygons of ancient cratered terrain between the latitudes of 10° S and 42° N, and longitudes 180° and 225° W appear to be displaced left laterally and possibly slightly rotated with respect to the part of the system in Galileo Regio. This displacement complicates the problem of defining the exact center of the system, as the center of curvature of the furrows on the Galileo Regio (Smith et al., 1979b) is about 20° southwest of the center of the palimpsest.

Individual rimmed furrows on the Galileo Regio are approximately 10 km wide and hundreds of kilometers long (Fig. 19b). The depths of the furrows are estimated to be a few hundred meters and the rims of the furrows rise about 100 meters above the surrounding surface. On the Galileo Regio, the furrows are relatively uniformly spaced about every 50 km, but they are more closely spaced where well preserved near the center of the system northwest of the central palimpsest. Where age relations are determinable, the furrows almost invariably predate recognizable craters and palimpsests on Galileo Regio. Elsewhere, a few

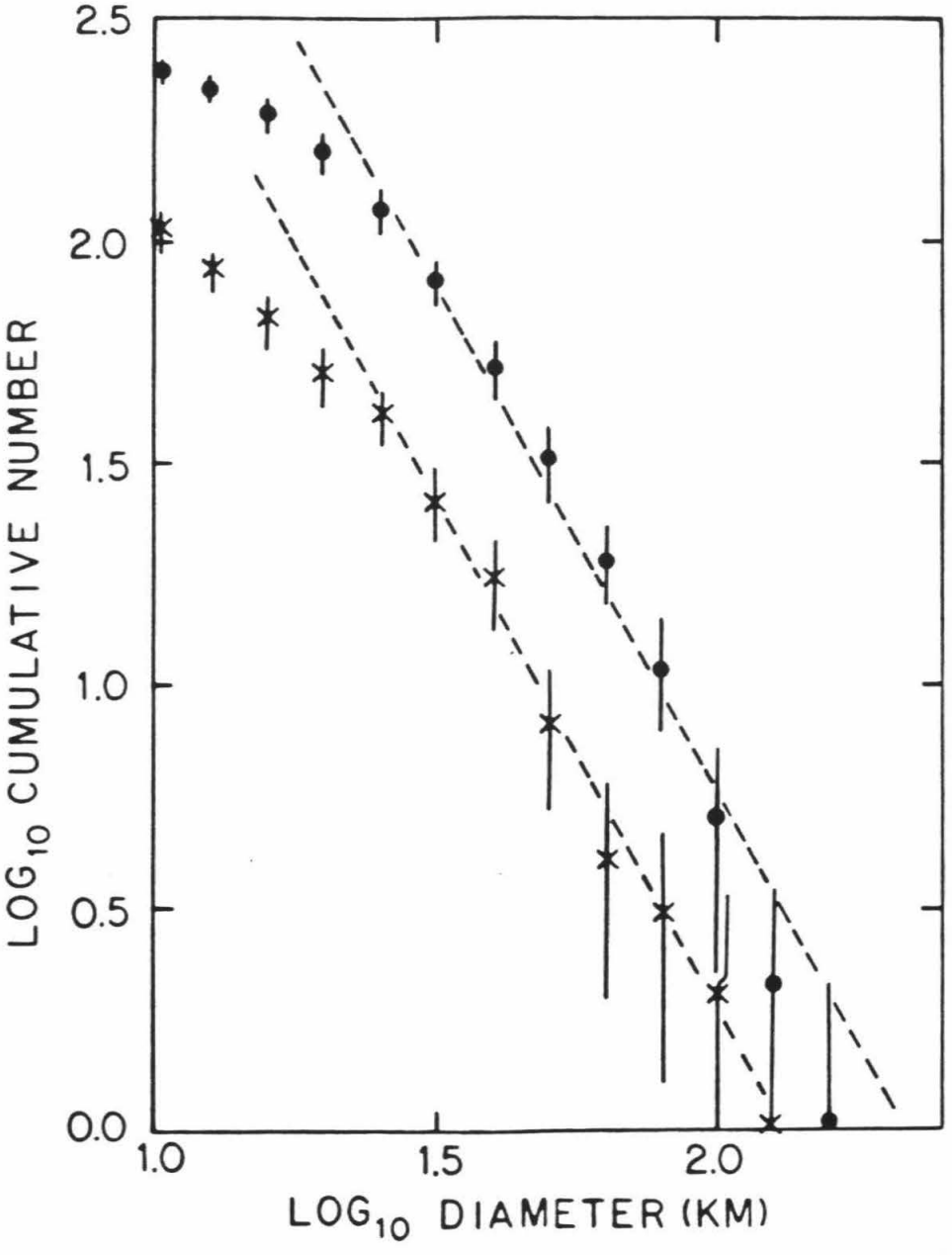

FIGURE 20 - Cumulative size-frequency distribution of bright ray craters on Ganymede. Frequencies of bright ray craters observed in the high resolution Voyager I pictures are shown by *X's* ; the combined frequencies derived from both the Voyager I and Voyager II coverage are shown with solid circles. Error bars are ± one standard deviation. The dashed lines have a slope of -2.2, and fit the observations within one standard deviation down to 25 km diameter. The break in the slope at 25 km ($Log_{10} = 1.4$) crater diameter is interpreted to be the result of incomplete counts at relatively small crater diameters.

craters appear to be cut by the furrows.

Ray craters

Both bright ray and dark ray craters occur on Ganymede. Forty-three dark ray craters have been found; the diameters of these craters range from less than 4 km to 60 km (Conca, in press). Roughly two-thirds of the identified dark ray craters are located on grooved terrain; this may be due, in part to the greater ease in identifying dark ejecta and rays on the relatively high albedo grooved terrain.

Craters on Ganymede with bright rim deposits or rays range in diameter from a few kilometers to 155 km; over 110 such craters larger than 25 km in diameter have been identified (Fig. 20). The mean frequency of craters larger than 25 km in diameter with bright rim deposits or rays on grooved terrain is 3.3 craters per $10^6\ km^2$; for similar craters on ancient cratered terrain, the frequency is 2.3 craters per $10^6\ km^2$. We interpret the 1/3 lower frequency of craters with bright rim deposits or rays on ancient cratered terrain to be the result of differential retention times for rays on these two surfaces. Bright rim deposits and rays on the ancient cratered terrain are apparently darkened 40% faster than those of the grooved terrain. The darkening is probably due to the gradual addition of meteoritic debris to the surface, to the concentration of this debris as a lag deposit where net ablation of ice is taking place, and where rays are thin, to the gardening of the surface by small impact craters that mix the ray material with the underlying darker regolith.

On Callisto, no craters with dark rays have been found. Craters with bright rim deposits or rays are more abundant than on Ganymede. The maximum diameter of craters with bright rims and rays on Callisto is about 120 km; the mean frequency of craters larger than 25 km in diameter, is about 4.2 craters per $10^6\ km^2$. The craters with bright rim deposits or rays on both Ganymede

and Callisto generally exhibit the least topographic relaxation.

CRUSTAL EVOLUTION OF GANYMEDE AND CALLISTO

We turn now to an interpretation of the crater record on Ganymede and Callisto and to the implications of the observed forms of the craters with respect to the thermal histories of these two bodies. To do this it will be necessary to make use of information on spatial frequency (density) of craters and of deductions by Shoemaker and Wolfe (this volume) on the rates of cratering over time for these two bodies.

It is crucial to bear two points in mind in interpreting the crater record on these giant icy satellites. First, it is manifest from the varying degrees of topographic relaxation of the observed craters, especially on the most densely cratered terrains, and from the existence of palimpsests that craters have disappeared, either by prompt collapse or slow viscous flow or creep on both Ganymede and Callisto. In assigning ages to terrains on the basis of crater density, ages for all terrains that contain palimpsests must be regarded as *crater retention ages*. As viscous relaxation is a function of crater size, it is also clear that for a given surface the crater retention age can vary with the size of the craters counted. Moreover, if surfaces are preserved that reflect different thermal histories for different regions of the lithosphere, it is evident that the size distribution of the preserved craters can vary. We shall see that there are dramatic differences in size distribution as a function of both position on the satellite and age of the crater population.

Second, because the orbital velocity of each Galilean satellite is roughly 45 to 60 percent as high as the average encounter velocity of extra-Jovian bodies with the orbit of the satellite, there is a very strong gradient in cratering rate from the apex of orbital motion to the antapex (Shoemaker and Wolfe, this volume). At the present time, the ratio of the cratering rate at the apex to the rate at the

antapex, from impact of comet nuclei, is about 9.6 on Callisto and about 14.9 on Ganymede. These ratios depend, to some extent, on the populations of impacting bodies but certainly have always been greater than 3 on all the Galilean satellites. Hence, it is essential to take account of the position of the satellite in interpreting both absolute and relative ages from crater densities. It turns out that regions with comparatively low crater densities near the antapices of Ganymede and Callisto have some of the highest crater retention ages (based on the model of Shoemaker and Wolfe, this volume) for the surfaces of each satellite.

Evolution of ancient cratered terrain

One of the earliest recognizable features preserved on the leading hemisphere of Ganymede is the Galileo Regio rimmed furrow system. As shown by McKinnon and Melosh (1981), the characteristics of the rimmed furrow system provide clues about the thickness of the lithosphere at the time the furrows were formed. The furrows are interpreted by them as graben; if the dips of normal faults bounding these graben are close to 60° , as is typical for many normal faults, they intersect at an average depth of about 10 km. This may be taken as an estimate of the thickness of the Ganymedian lithosphere at the time the furrows were formed. The dip of the faults might be steeper and the lithosphere thicker, but from the theory of multiring structures of Melosh and McKinnon (1978), the lithosphere of the Galileo Regio was no thicker than the average spacing between the furrows, about 50 km. Hence, the low latitude lithosphere in the leading hemisphere of Ganymede was probably between 10 and 50 km thick at the time the furrows formed, perhaps closer to the 10 km rather than 50 km limit.

It is of interest to inquire as to how this lithosphere came into being. What happened prior to the impact that produced the multiring system? One conceivable scenario is that Ganymede was resurfaced by a global event, perhaps a satellite-wide extrusion of water associated with final melting or differentiation of a hydrous mantle a short time before the rimmed furrows formed. The lithosphere could then be envisioned simply as a layer refrozen since that event. The crater record on the ancient cratered terrain, however, suggests that this did not occur. On the basis of the cratering time scale and model of Shoemaker and Wolfe (this volume), the crater retention ages of parts of the crust in the trailing hemisphere of Ganymede are substantially greater than on the Galileo Regio in the leading hemisphere.

From detailed studies of the crater densities by J.B. Plescia it was found that, although the mean density of 10 km and larger craters on the ancient cratered terrain varies slightly with distance from the apex of orbital motion (Table VII), the variation in density is not nearly as great as predicted for a surface of a single age. If only craters larger than 30 km are considered, there is a larger difference in crater density between areas near the apex and areas near the antapex, but the difference is still much less than predicted. One possible way to explain a more uniform distribution of craters than predicted is to suppose that the rotation of Ganymede was not always synchronous with its orbital motion during part of the decipherable history of cratering. If several stable positions were possible when the rotation was locked, differences in cratering rate over the surface might have been averaged out. Alternatively, it might be supposed that the lithosphere of Ganymede was sufficiently decoupled from the rocky core so that even though the core may always have been tidally locked, the lithosphere was free to slip relative to the core. The size-frequency distribu-

TABLE VII- Estimated 10 km crater retention ages for the ancient cratered terrain on Ganymede

Distance from mean apex of orbital motion	Observed crater density [1] (per 10^6 km^2)	Derived satellite wide mean crater density [2] (per 10^6 km^2)	Calculated crater retention age of surface [3] (Gy)
20° - 40°	290	171	3.80
40° - 60°	258	170	3.80
60° - 80°	271	212	3.84
80° - 100°	245	245	3.87
100° - 120°	270	373	3.93
120° - 140°	188	392	3.94

[1] Crater densities for each range of distance from the apex have been obtained by averaging the results of detailed crater counts by J.B. Plescia.

[2] The satellite wide mean density $\bar{F}$ obtained from

$$\bar{F}_{10} = \frac{F_{10}(\beta)}{[1 + \cos \beta(\delta - 1)/(\delta + 1)]} ,$$

where $F_{10}(\beta)$ is the observed integral crater density to 10 km diameter at distance β from the mean apex of orbital motion, $\bar{F}_{10}$ is the corresponding satellite-wide mean density to 10 km diameter equivalent to the crater density at $\beta = 90°$, and $\delta = 9.55$ is the ratio of the cratering rate at the apex to the cratering rate at the antapex for Ganymede (Shoemaker and Wolfe, this volume).

[3] Crater retention ages greater than 500 my are calculated from

$$\bar{F}_{10}(t) = \left[\frac{R_o \exp \lambda(t - 3.3 \text{ Gy})}{\lambda} + \frac{(1.15 \times 10^{-8})\ t}{\text{yr}} + 5.70 \right] \frac{\text{craters} \geq 10 \text{ km dia}}{10^6 \text{ km}^2} ,$$

where $\bar{F}_{10}(t)$ is the mean crater density to 10 km crater diameter on a surface formed at time t, $\lambda = \ln 2/t_{1/2}$, $t_{1/2} = 10^8$ years, and the exponential component of the cratering rate at 3.3 Gy, R_o, is 2.63×10^{-8} yr^{-1} (Shoemaker and Wolfe, this volume).

tion of craters on the ancient cratered terrain, however, provides direct evidence that the lithosphere was, in fact, approximately fixed with respect to the mean apex during essentially all of the recorded cratering history. On average, the crater-size distribution is steeper in the trailing hemisphere than in the leading hemisphere. The ratio of small craters to large craters is higher in the trailing hemisphere than in the leading hemisphere, as would be expected if the trailing hemisphere were older and the crust were everywhere stiffening with time.

The observed distribution of crater densities on the ancient cratered terrain of Ganymede indicates that the crater retention ages of the trailing hemisphere are higher than on the Galileo Regio (in the leading hemisphere). The range in crater retention ages on the ancient cratered terrain can be estimated from the cratering time scale presented by Shoemaker and Wolfe (this volume). Mean crater retention ages increase systematically with increasing distance form the apex of motion (Table VII). The range of model ages at 10 km crater diameter is 140 my ± 30 my. As neither the apex nor the antapex of Ganymede was imaged at high enough resolution for studies of crater density, the full range of crater retention ages is not known but probably is somewhat greater. The rimmed furrow system on the Galileo Regio evidently is somewhat younger than the 10 km crater retention age of the surface it cuts, about 3.8 Gy. The mean 10 km crater retention age of the Nicholson Regio and nearby polygons of cratered terrain in the trailing hemisphere is about 3.9 Gy. The calculated difference in age depends chiefly on the adopted rate of decay of cratering rate during heavy bombardment (modelled by Shoemaker and Wolfe after the decay rate obtained for the Moon) and is relatively insensitive to errors in the absolute calibration of the cratering time scale.

A similar picture emerges from the study of the crater distribution on Callisto, except that the crater retention ages over the surface of Callisto are systematically higher than on Ganymede. The distribution of large impact structures on Callisto is strikingly nonuniform. The four largest multiring structures (Valhalla, Asgard, and two unnamed structures) are all located in the leading hemisphere. The center of the Valhalla palimpsest is within 40° of the apex, and the center of Asgard is within 55° . Craters larger than 60 km in diameter are 2.2 times as abundant in areas counted near the apex as they are near the antapex (Table VIII); for craters larger than 25 km in diameter as well as those larger than 10 km in diameter, the density of craters near the apex is about the same as at the antapex. Hence, the size distribution of craters near the apex has a lower slope than the size distribution near the antapex.

If the orientation of the crust of Callisto remained fixed relative to the mean apex of orbital motion and if the crust were everywhere the same age and all craters produced were still preserved, then the ratio of crater density in the region sampled near the apex to the density near the antapex should be about 9.6, in contrast to the observed ratios of 2.2 at 60 km, and about 1 at 25 and 10 km crater diameters. We interpret the observations as showing that the crust of Callisto was, in fact, fixed relative to the apex during the period of recorded cratering history, and that the crust has a spatially varying set of crater retention ages (Table VIII). With the exception of the polar region and local areas that we suspect are former palimpsests, the crater retention ages at 60 km crater diameter tend to become greater as the antapex is approached. At 25 km crater diameter this trend is even stronger. All of the 25 km crater retention ages are higher than the 60 km crater retention ages, and the difference is greatest on the oldest surfaces, near the antapex. The difference in crater retention age

TABLE VIII - Estimated 25 km and 60 km crater retention ages for various locations on the surface of Callisto.

Distance from mean apex of orbital motion	Observed density of 25 km craters (per 10^6 km^2)	Calculated 25 km crater retention age of surface[1] (Gy)	Observed density of 60 km craters (per 10^6 km^2)	Calculated 60 km crater retention age of surface[1] (Gy)
40°	97	4.08	10.7	4.04
65°	98	4.09	9.0	4.04
78°	96	4.12	9.8	4.07
81° [2]	124	4.16	12.1	4.10
91° [3]	107	4.16	5.9	4.02
121° [4]	75	4.17	4.3	4.04
123° [4]	78	4.19	2.1	3.94
140°	112	4.29	4.4	4.09
143°	106	4.29	3.9	4.08
167°	103	4.34	4.8	4.17
38° Valhalla palimpsest	49	3.96	3.6	3.85
54° Asgard	70	4.04	10.0	4.04

[1] Values of mean crater density used in calculating the crater retention ages are obtained from

$$\bar{F}_i = \frac{F_i(\beta)}{[1 + \cos \beta(\delta - 1)/(\delta + 1)]} ,$$

where $F_i(\beta)$ is the observed integral crater density to diameter i at distance β from the apex, $\bar{F}_i$ is the corresponding satellite-wide mean density to diameter i equivalent to the crater density at $\beta = 90°$, and $\delta = 9.6$ is the ratio of the cratering rate at the apex to the cratering rate at the antapex for Callisto. To obtain the equivalent satellite-wide mean crater density at 10 km, $\bar{F}_{10}$, from integral crater densities at 25 and 60 km, the size-frequency distribution of craters produced over any given interval of time is assumed to be given by

$$\bar{F}_{10} = \bar{F}_i \left(\frac{10}{i}\right)^{\gamma} ,$$

where γ, the size index, is -2.2 (Shoemaker and Wolfe, this volume). Crater retention ages greater than 500 my are calculated from

$$\bar{F}_{10}(t) = 0.52 \left[\frac{R_o \exp \lambda (t - 3.3\ \text{Gy})}{\lambda} + \frac{(1.15 \times 10^{-8})\ t}{\text{yr}} + 5.70 \right] \frac{\text{craters} \geq 10\ \text{km diameter}}{10^6\ \text{km}^2} ,$$

where $\bar{F}_{10}(t)$ is the satellite-wide mean crater density to 10 km crater diameter on a surface formed at time t, $\lambda = \ln 2/t_{1/2}$, $t_{1/2} = 10^8$ years, and the coefficients of the exponential component of the cratering rate at 3.3 Gy, R_o, is 2.63×10^{-8} yr^{-1} (Shoemaker and Wolfe, this volume).

[2] Center of area counted is at 78° north latitude.

[3] Center of area counted is at 80° north latitude.

[4] Area counted probably includes a the site of a former palimpsest.

between the apex and the antapex is about 100 my at 60 km crater diameter and 200 my at 25 km crater diameter. Unfortunately, the resolution of Voyager images is inadequate to obtain an accurate regional distribution of crater densities to 10 km diameter.

The observed distribution of craters and calculated crater retention ages on the heavily cratered terrain of Ganymede and Callisto follows a pattern that would be expected if craters have disappeared by viscous flow or creep or by prompt collapse and disruption of the lithosphere, and if the retention of craters is, itself, partly but not entirely a function of the cratering history. As the oldest crater retention ages are observed near the antapex, on both Ganymede and Callisto, this indicates that the lithosphere became thick and stiff enough to retain craters earlier near the antapex than near the apex. The implication of this relationship is that the local bombardment history has influenced the cooling of the lithosphere. As the cratering rate declined during heavy bombardment, the region of the antapex, where the cratering rate at any given time was much lower than in the leading hemisphere, became cool and stiff enough to support 10 km and larger craters earlier than near the apex. At any given location, the lithosphere first stiffened sufficiently to support small craters and then became capable of retaining larger craters.

The primary effect of late bombardment on the lithospheric temperature of each satellite probably arose from the production of an insulating regolith due to pulverization and gardening of the surface by small craters. For an equilibrium population of craters, one might expect a globally uniform mean thickness of regolith. The relative uniform latitudinal distribution of relaxed craters, however, indicates that the regolith must have been thermally annealed at its base (Shoemaker et al., 1982). If a time of the order of 10^5 years or longer was

required for annealing to occur, however, then the mean thickness of the effective insulating layer would have been proportional to the local cratering rate during heavy bombardment. Hence, the top of the lithosphere would have been cooler near the antapex than at the apex.

Another factor which leads to younger crater retention ages in the leading hemisphere is the higher rate of production of multiring structures in the leading hemisphere. Observed crater densities are relatively low throughout a fairly large fraction of the areas of the Valhalla and Asgard multiring structures on Callisto. Earlier production of multiring structures on the thin early lithosphere may have lead to similar regional suppression of the density of recognizable preexisting craters. The distribution of this suppression effect over the satellite should have followed the spatial variation of cratering rate, leading to a more uniform final distribution of retained crater density and a gradient of crater retention ages increasing toward the antapex.

A third factor enhances the abundance of small craters at the antapex, but we judge this effect to be subordinate to the differences in of stiffening of the crust with time. Distant secondary craters associated with large craters and basins excavated on the leading hemisphere will be produced on the trailing hemisphere. The occurrence of secondary crater chains shows that many secondaries 10 km in diameter and some up to 30 km in diameter can be formed, at least during the late stage of heavy bombardment. It is less clear that equally large secondaries were produced at an earlier stage when the lithosphere was very thin. As many more large craters and basins are formed in the leading than in the trailing hemisphere, the number of distant secondaries produced in the trailing hemisphere will be disproportionately large in comparison with the number of both small and large primaries formed there. This probably

leads to significant overestimation of crater retention ages at 10 km diameter over the entire surface and especially near the antapex, but the effect is probably small at 25 km crater diameter, and essentially vanishes for larger craters.

Detailed examination of the local variation of crater density on Ganymede and Callisto provides direct evidence on the manner in which early-formed craters disappeared. On the recognizable palimpsests, the crater density (at crater sizes greater than the largest associated secondary craters) generally is less than on adjacent ancient cratered terrain. Typically, nearly all earlier craters are obliterated in the area covered by each palimpsest, even though 70 to 90 percent of the area of the palimpsest evidently corresponds to an ejecta blanket. The reason for this efficient obliteration is that nearly all of the pre-palimpsest craters were either small enough to begin with or had flattened by viscous flow or creep to sufficiently low relief that the remaining relief was smothered by a comparatively thin ejecta deposit. On Ganymede, the palimpsests are fairly abundant. A large area of ancient cratered terrain in the Marius Regio is about one-half occupied by palimpsests (Fig. 13c). The mean area occupied by recognizable palimpsests on the ancient cratered terrain of Ganymede is roughly estimated at 25 percent. Although less easily mapped, palimpsests cover a roughly comparable fraction of the surface of Callisto.

Between the recognizable palimpsests on Ganymede and Callisto, there are also local areas where the crater densities are lower than the regional mean by an amount greater than would be expected by chance. Some of these areas on Callisto are recognizable by their low crater abundances listed in Table VIII, and similar areas of local low crater abundance have been found by Plescia on Ganymede. In some cases the occurrence of small palimpsests or large craters in the areas counted is responsible for the low crater abundance, but in other

cases there is no obvious cause. As the albedo contrast between a palimpsest and the surrounding surface evidently fades with time, it seems likely that many areas of anomalously low crater abundance (perhaps 10 to 20 percent of the ancient cratered terrains) correspond to former palimpsests. If one pushes the cratering history back far enough, of course, all parts of the surface probably were occupied at one time or another by palimpsests.

Our picture of the early evolution of the lithospheres of Ganymede and Callisto can be summarized as follows. During early heavy bombardment, the heating of the lithosphere by the combination of impact generation of an insulating regolith and heat flow from the deep interior was sufficient to prevent retention of any recognizable craters. As the bombardment rate and heat production by radioactivity waned, the upper part of the lithosphere of each satellite cooled to the point where craters large enough to be recognized in the Voyager images were retained. The earliest retained craters on each satellite are relatively small (less than 10 km diameter) and occur either in the polar regions or near the antapex. Crater retention then spread in a "wave" toward the apex. At any given distance from the apex, progressively larger craters were retained with the passage of time. In detail, the loss of craters was a stochastic process. Individual craters first flattened by flow or creep, and then groups of craters were smothered beneath ejecta deposits. Large early craters that penetrated the shallow asthenosphere probably flattened almost immediately after they were formed. At early times, when the lithosphere was very thin ($\leq$ 10 km thick), extensive regions probably were resurfaced by the formation of multiring structures.

We have not found any evidence that flooding of the surface by water was an important part of the early evolution of the lithospheres of Ganymede or Callisto nor any evidence that a major fraction of the mantle of either satellite was

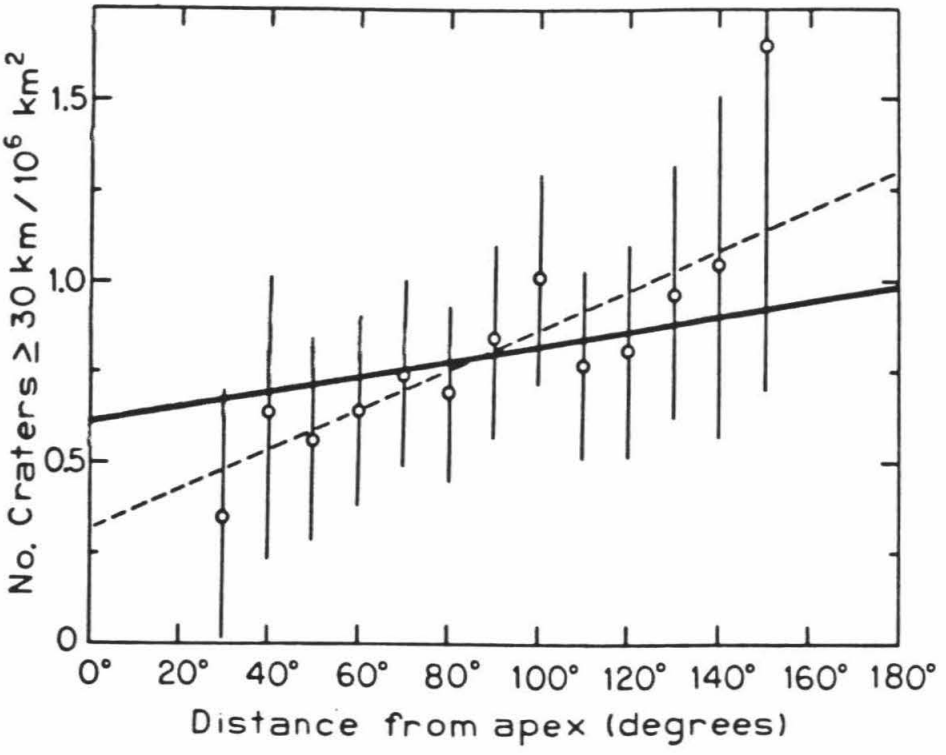

FIGURE 21 - Density of ray craters equal to or greater than 30 km diameter as a function of distance from the apex (0° N, 90° W) on Ganymede. A total of 84 ray craters is used in the construction of this graph. The crater densities are averaged over 20° intervals. The increase in density from the apex indicates that the ratio of the rate of ray removal to rate of production is higher in the leading hemisphere than in the trailing hemisphere. The broken line is a linear least-squares fit to the points plotted, weighted according to the number of points in each distance bin. The fit is

$$\frac{\textit{No. Craters} \geq 30\ km}{10^6\ km^2} = 0.3063 + 0.0056\ (\textit{distance in degrees})$$

with a correlation coefficient (r^2) of 0.58.

The heavy solid line marks the limiting slope assuming that the ratio of ray crater production rate at the apex to the production rate at the antapex, as estimated by Shoemaker and Wolfe, is 9.6, and that ray erasure is due entirely to gardening of the surface by small projectiles on circular orbits (see text for discussion).

liquid at any one time during its decipherable history. Owing to combined heating by impact and radioactivity, the shallow thermal gradients on both satellites probably were steep enough to lead to convection of solid ice within their deeper interiors very early in their histories. In all likelihood, Ganymede and Callisto differentiated during or shortly after accretion; no more than a small fraction of water may have been present at a given moment during this differentiation (Schubert et al., in press). It should be noted that thermal history calculations for Ganymede and Callisto that ignore heating by impact both during accretion and possible intense heavy bombardment by projectiles external to the Jovian system after accretion, probably are unrealistic.

Record of ray craters

As on the Moon, the ray craters on Ganymede and Callisto are the youngest features recognized on each satellite. The rays are superimposed on craters that lack rays and on all the recognized types of terrain. The rays must fade with time and disappear, evidently as a consequence of processes that influence the average albedo of material exposed locally at the surface. Presumably, nearly all primary craters large enough to be resolved on the Voyager pictures had associated rays when they were first formed. These rays are bright for about 99% of the newly formed craters on Ganymede and essentially 100% of the craters on Callisto.

On Ganymede, the density of bright ray craters larger than 30 km in diameter ranges from about 0.3 per 10^6 km^2 in the leading hemisphere to about 1.1 per 10^6 km^2 in the trailing hemisphere (Fig. 21). The observed densities correspond to ray retention ages of less than 500 million years in the leading hemisphere, on the basis of the bombardment model and the cratering timescale of Shoemaker and Wolfe (this volume); for the trailing hemisphere, the mean ray

retention age is about 2 billion years. On Callisto, the density distribution of ray craters is less clearly related to distance from the apex. If anything, there is a trend of declining density with increasing distance from the apex, but considerable scatter is found in this trend (Fig. 22). The mean density of ray craters in the leading hemisphere of Callisto is higher than that observed anywhere on Ganymede. Ray retention ages on Callisto range from 1.1 billion years in the leading hemisphere, to about 3.7 billion years near the antapex. Although the crater rays on Callisto are retained for a longer period of time than rays on Ganymede, they are generally much fainter. Both the albedo of the rays on Callisto and the contrast in albedo between the rays and the adjacent surface is less than for rays on Ganymede.

The densities and regional variation of density of ray craters on the satellites reflect a balance between the rate of production of ray craters and the rate at which rays disappear. If the rate of ray erasure were everywhere constant, then the ray retention ages would be spatially uniform and density would reflect the crater production rate. In this case, ray craters would be most abundant at the apex of both satellites, and Ganymede would have more ray craters than Callisto, contrary to what is observed.

A range of ray retention ages increasing systematically with distance from the apex would be expected on Ganymede and Callisto, if the fading and disappearance of rays were due entirely to the local production of small impact craters that result in gardening of the surface and contamination of the regolith with dark debris. If the small particles that produce the gardening and contamination of the surfaces had a distribution of orbits like those of the larger bodies that produce the ray craters, and if the ratio of the flux of small particles to the flux of the larger bodies did not change with time, then the rate at

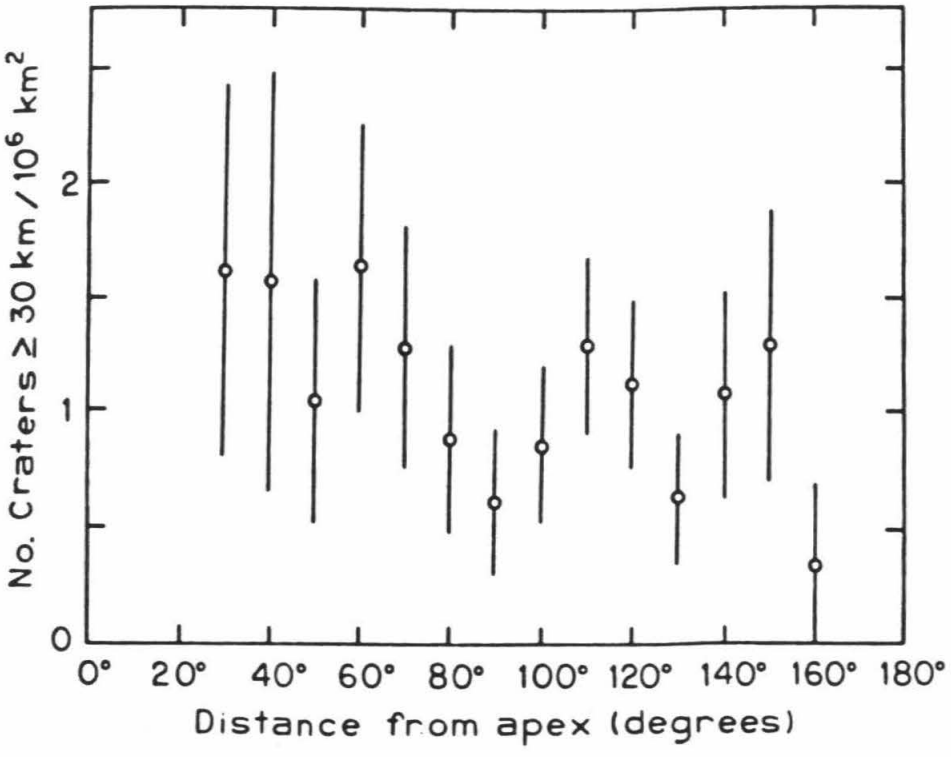

FIGURE 22 - Density of ray craters equal to or greater than 30 km in diameter as a function of distance from the apex on Callisto. A total of 79 ray craters is used in the construction of this graph. The crater densities are averaged over 20° intervals. In contrast to the relation found on Ganymede (Fig. 21) there is an irregular trend to lower crater densities toward the antapex.

which rays fade would be proportional to the rate at which they are produced. In this case the density of ray craters would be spatially uniform on each satellite and it would be the same on both Ganymede and Callisto. These conditions are closer but still contrary to observation.

If small particles that result in gardening and contamination tend to be on less eccentric orbits than the orbits of the ray crater producing bodies, the difference in the impact rates between the apex and antapex will be greater for the small particles than for the larger bodies. In this case, the ratio of ray removal rate to the ray production rate will be higher at the apex than at the antapex and an increasing density of ray craters toward the antapex would be predicted, as found on Ganymede. Moreover, the rate of ray removal would be higher on Ganymede than on Callisto, which would lead to a higher ray crater density on Callisto, as observed. If gardening by small craters were the only cause of ray fading and disappearance, however, a gradient of increasing ray crater density toward the antapex should also be found on Callisto. As such a gradient is not found, gardening by small craters and contamination of the surface by impacting debris cannot be the only process of ray erasure.

Assuming the impacting bodies are all on heliocentric orbits, there is a limit to the gradient in ray crater density between the apex and antapex that can be accounted for by the difference in orbits between the small particles and the larger ray crater producing bodies. The maximum possible gradient (ray crater density increasing toward the antapex) would result if all the small impacting particles were on orbits nearly identical with that of Jupiter. The Poynting-Robertson effect will tend to circularize the orbits of small Jupiter-crossing particles, but they cannot be driven to coincide with Jupiter's orbit. The ratio, U , of encounter velocity with Jupiter's sphere of influence to the orbital velocity of

Jupiter is given, in the limit of a circular orbit, by

$$U = [\, 2\,(\,1 - \cos i\,) + 4 / 9\, e_o^2\,]^{1/2} \qquad (3)$$

where i = inclination of small particle orbits to orbit plane of Jupiter, and $e_o = 0.046_4$ is the average eccentricity of Jupiter (see appendix 1, of Shoemaker and Wolfe, this volume). Most of the impacting small particles probably are derived from disintegration of short period comets and they will tend to inherit the orbital inclination of the respective parent comets. Hence the small particle swarm should have about the same mean inclination as the short period comets, about 10.6° ; the limiting value of U , then, from eq. (3) is 0.18_7 . From the equations presented by Shoemaker and Wolfe (this volume), at $U = 0.18_7$, the ratio, δ_s of the small particle cratering rate at the apex to the rate at the antapex is 26.7, on Ganymede. The ratio, σ , between ray crater density at the apex and at the antapex is given by $\sigma = \delta_l / \delta_s$, where δ_l is the ratio of ray crater production rate between the apex and antapex. Adopting $\delta_l = 14.9$, as estimated by Shoemaker and Wolfe, we find $\sigma = 0.56$. This corresponds to a gradient of increasing ray crater density toward the antapex somewhat less steep than the least squares fit to the observations form Ganymede (Fig. 21), but, within the counting errors, it is consistent with the observations. Using $\sigma = 0.36$, which is the best fit to the observations when the the two points with the greatest uncertainty are neglected, and using the limiting value $\delta_s = 26.7$, the maximum value of δ_l suggested by the small crater gardening model of ray removal is 5.3. This low value of δ_l would correspond to a distribution of orbits for the large impacting bodies dominated by long period comets rather than a distribution dominated by short period comets postulated by Shoemaker and Wolfe.

For the small crater gardening model of ray removal, the ratio, C_r , of mean ray crater density on Ganymede to the mean ray crater density on Callisto is

given by $C_r = C_p / \varepsilon$ where C_p is the ratio of production of ray craters on Ganymede to the production on Callisto and ε is the ratio of production of small craters on Ganymede to the production on Callisto. From the equations given by Shoemaker and Wolfe (this volume) it can be shown that ε is given by

$$\varepsilon = \left(\frac{1 + S_g^2 / U^2}{1 + S_c^2 / U^2} \right) \left(\frac{S_g^2 + S_{ge}^2 + U^2}{S_c^2 + S_{ce}^2 + U^2} \right)^{2\lambda/3.4} \qquad (4)$$

where $S_g^2 = 1.38_9$ is the square of the dimensionless escape velocity from Jupiter at the orbit of Ganymede (ratio of the escape velocity from Jupiter at the orbit of Ganymede to the orbital velocity of Jupiter), $S_{ge}^2 = 0.044_0$ is the square of the dimensionless escape velocity from Ganymede, $S_c^2 = 0.790_4$ is the square of the dimensionless escape velocity from Jupiter at the orbit of Callisto, and $S_{ce}^2 = 0.034_9$ is the square of the dimensionless escape velocity from Callisto, and $-\lambda$ is the size index for small craters, provisionally taken to be 2.9 (Shoemaker et al., 1982). Introducing $U = 0.18_7$, the lower limiting value for small particles, we find the maximum value of ε is 2.7_5. If $2.3 / 1.2_3 = 1.8_7$ found for large crater production by Shoemaker and Wolfe, is adopted for C_p , then the lower limiting value of C_r is found to be $1.8_7 / 2.7_5 = 0.68$. The observed value of C_r for craters on ancient cratered terrain down to 25 km diameter is $3.3 \times 10^{-6}\ km^{-2} / 4.8 \times 10^{-6}\ km^2 = 0.69$, in close agreement with the ratio predicted by Shoemaker and Wolfe (1982).

If gardening by small craters is the primary process of ray removal on Ganymede, another process or set of processes must be dominant on the trailing hemisphere of Callisto. Ablation of the surface, leading to residual concentration of dark silicates, is one possibility. Development of a lag deposit of dark material might occur through slow sublimation of ice or from differential sputtering of ice and silicates under bombardment of the trailing hemisphere of

Callisto by the co-rotating plasma in the Jovian magnetosphere. Direct evidence of the influence of sublimation due to insolation is found on Ganymede, where bright rays are seen to be generally much fainter at low latitudes than at high latitudes. The slow transfer of H_2O from low latitude to high latitude has been treated from a theoretical standpoint by Purves and Pilcher (1980) and may account for the polar shrouds found on Ganymede. What remains to be accounted for, however, is the absence of similar shrouds on Callisto. Differential sputtering, which has been invoked by Conca (1981) to explain an observed strong concentration of dark ray craters on the trailing hemispheres of Ganymede, may also be a promising mechanism to explain the loss of bright rays on the trailing hemisphere of Callisto. In particular, sputtering may be partly responsible for an apparent low surface density of fine particles on the trailing hemisphere of Callisto indicated by polarization observations (Dollfus et al., 1980). The role of both sublimation and sputtering in ray removal may be greater on Callisto than on Ganymede, because of the lower rates of cratering on Callisto.

The distribution of craters with bright rim deposits on Ganymede appears to be independent of distance from the apex, but the observations of density are scattered. The retention ages of bright rims on Ganymede range from about 800 million years in the leading hemisphere to about 3.5 billion years in the trailing hemisphere; the corresponding crater densities range from about 2.1 to 3.0 craters larger than 30 km in diameter per $10^6\ km^2$ in the leading hemisphere, to about 1.6 to 2.6 craters per $10^6\ km^2$ in the trailing hemisphere. On Callisto, the density of craters with bright rim deposits decreases systematically with increasing distance from the apex (Fig. 23). The retention ages for bright rims range from 3.2 billion years in the leading hemisphere to 3.7 billion years

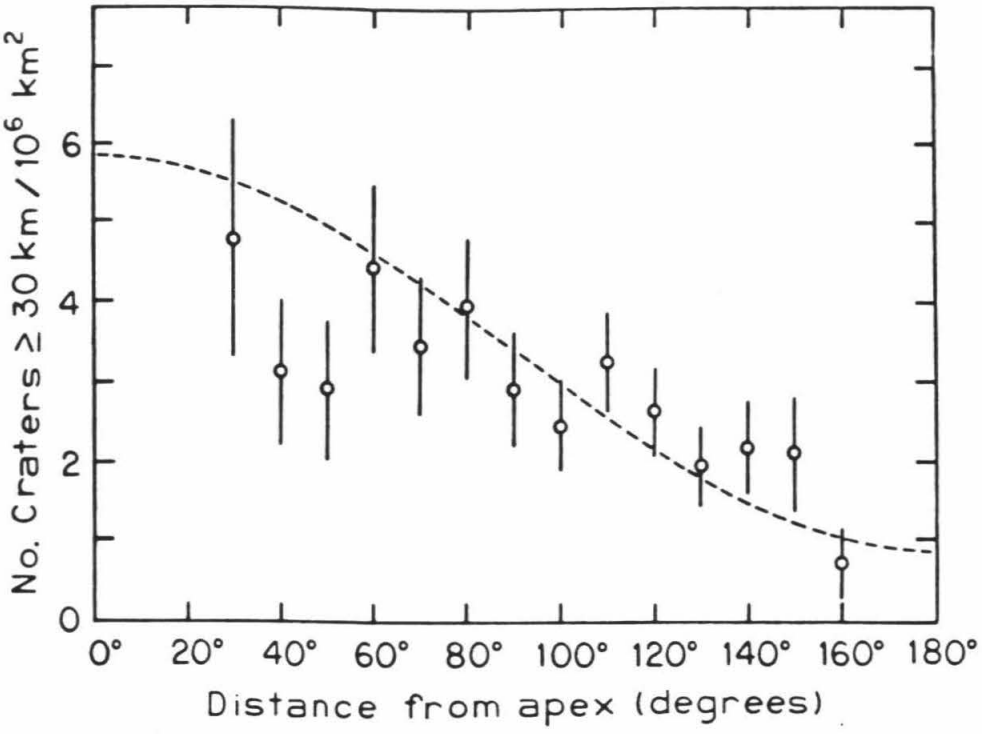

FIGURE 23 - Density of craters equal to or larger than 30 km in diameter with bright rim deposits as a function of distance from the apex on Callisto. The crater densities are averaged over 20° intervals. A total of 219 craters is used in the construction of this graph. The decrease in crater density toward the antapex is the trend predicted if the retention time of bright rims is relatively uniform as is shown by the broken line (based on the model of Shoemaker and Wolfe, this volume). This suggests that bright rim deposits are not primarily darkened by meteoroid impact, which has a very large variation in rate as a function of distance form the apex. An additional process, whose rate is independent of distance from the apex, such as the slow ablation of ice by insolation, is required to explain the darkening of the rim deposits.

in the trailing hemisphere. Thus the spatial variation of density of craters with bright rims on Callisto follows approximately, but not precisely, the distribution that would be predicted if the retention time for bright rims were everywhere the same. It is clear that the processes which remove or darken rays work somewhat differently with respect to the albedo of the continuous ejecta deposits. The rim deposits remain noticeably bright long after rays have disappeared, and, on Callisto, the darkening of the rims is not proportional to the small crater gardening rate or to the influx of dark contaminating debris. The very slow ablation of ice, due to insolation, especially at low latitudes, may be an important cause of darkening of the crater rim deposits.

Thermal history of the lithosphere of Ganymede

If the timescale is known, the observed topographic relaxation of a crater, whose initial form is known, in a material whose properties are also known can, in principle, be made to yield information bearing on the subsurface thermal regime. It should be possible to infer the variation of thermal gradient with time by analysis of the relief of many craters of different ages and different sizes. A different but related approach to determination of thermal history based on crater size statistics, has been taken by Phillips and Malin (1980). There are several difficulties in the rigorous application of these concepts to Ganymede and Callisto. First, the relevant physical properties of ice at the very low temperatures of the surfaces of Ganymede and Callisto are unmeasured. The mechanisms of flow or creep of ice at these temperatures have been inferred on theoretical grounds (Goodman et al., 1981) but are unverified. Moreover, there is direct evidence that, at least at the surface, the ice is impure; the composition, abundance, and effect of these impurities on the flow of ice is unknown. Secondly, while it is possible to make estimates of the ages of surfaces by

crater counting, it is difficult to date any but the largest individual craters. Hence we are reduced to looking at the distribution of crater shapes on dated surfaces and arriving at the answer by statistical arguments. Finally, the temperature and correlated physical properties vary not only as a function of depth at a given site but also as a function of time. This last circumstance merely raises practical problems of computation rather than any fundamental obstacle.

Here we shall attempt to leap over these rather formidable hurdles with some very rough approximations. We do so in the spirit of an exploratory foray to see if the broad outlines of lithospheric thermal history might be ascertained.

We start with the analysis by Danes (1965) of the relaxation of a crater in a Newtonian viscous fluid whose viscosity is uniform in both space and time. At relatively high temperatures, ice behaves nearly like an ideal plastic solid rather than a viscous fluid, but for our present exploration purposes the approximation of a Newtonian viscous fluid may be satisfactory; it has the great advantage of mathmatical tractability. The "viscosities" which we will derive must be regarded as effective viscosities. Furthermore, they must be regarded as very crude estimates of the average effective viscosity from the surface to depths that are not well defined and also they must be regarded as averaged over time. The most serious defect in our application here of Danes' solution for crater relaxation to craters on Ganymede and Callisto probably lies in the failure to account for very strong vertical gradients in effective viscosity that must exist at any time during the evolution of the lithosphere.

Danes' solution for crater relaxation can be reduced to a series of theoretical profiles at various e-folding times. Profiles obtained by photoclinometry can then be compared with the computed profiles to determine the approximate e-

folding degree of relaxation, r . If we can set appropriate bounds to the time interval, Δt , over which the observed relaxation occurred, the characteristic e-folding time, τ , is given by

$$\tau = \Delta t \; / \; r \tag{5}$$

The effective viscosity, η_{eff} , can then be estimated (Danes, 1965) from

$$\eta_{eff} = \frac{1}{1.605} \rho \, \tau \, g \, (D \; / 2) \tag{6}$$

where ρ is the density of the lithosphere, g is the acceleration of gravity of the satellite, and D is the crater diameter (all units are cgs). For purposes of comparing the results obtained from craters of different sizes we will adopt the mean depth, h , to which the estimate of η_{eff} applies, as $h = D \; / \; 2$. In a separate paper, we will show that our use of this assumption here gives results similar to the case in which the viscosity decreases exponentially with depth, corresponding to the situation in which heat flow is uniform with depth.

Next, we will assume that the Arrhenius relation for the temperature dependence of viscosity (Shaw, 1972)

$$\eta = \eta_o \exp \left[\; T^* \left(\frac{1}{T} - \frac{1}{T_o} \right) \right] \tag{7}$$

where T is the temperature of the medium, T_o is the reference temperature for which the viscosity is n_o , and T^* is an "activation" temperature, is applicable to the material of the lithospheres of Ganymede and Callisto. Two values of T^* are used here; both values are based on an effective viscosity of 10^{14} poise at 270 K as a reference. Assuming that the effective viscosity of ice at 130 K is 10^{25} poise, T^* is 6.28 x 10^3 K; for a viscosity of 10^{26} poise at 130 K the corresponding value for T^* is 6.85 x 10^3 K. Various formulae that have been used to estimate the effective viscosity of ice yield values close to 10^{25} poise at 130 K (e.g. Reynolds and Cassen, 1979). The competence of Ganymede's lithosphere to support large

craters at a late stage of thermal evolution, however, suggests that 10^{26} poise is a better estimate for effective viscosity at the surface of the lithosphere. The values derived for the activation temperature are fairly typical. For comparison, the viscosity of the upper 100 km of the earth's crust has been estimated to be in excess of 10^{25} poise (Gordon, 1967; McKenzie, 1967) Therefore, the viscous behavior ice at very low temperatures (130 K) is very much rocklike.

The estimated thermal gradient, $\Delta T / h$, will be taken as

$$\Delta T / h = (T - T_s) / h \qquad (8)$$

where T_s is a representative surface temperature and T is the calculated temperature of the lithosphere at depth h . The annealing temperature at the base of the regolith is estimated by Shoemaker et al. (1982) to be 130K. Here we will adopt 130K as the global temperature at the top of the lithosphere.

The most difficult step in applying equations (5) through (8) is to obtain an appropriate estimate of Δt . From evidence presented earlier, we adopt the model that the lithosphere, at any given place was relatively thin at the time the oldest preserved craters were formed and that the thermal gradient decreased monotonically with time. Stochastic changes in the thermal regime associated with the individual larger craters will be ignored for this first analysis. As the thermal gradient was decreasing rapidly during the earliest part of the crater record, Δt will simply be taken as the difference in age between craters that reveal, by their degree of topographic relaxation, a substantial change in the thermal gradient. The success of this procedure depends on the fact that the characteristic relaxation time depends linearly on η_{eff} and that η_{eff} depends exponentially on T . Hence, with a steadily declining mean T, most of the observed relaxation occurs early in the history of a given crater. If sufficient

determinations of $\Delta T / h$, distributed over time, are obtained for a given region, more precise estimates of Δt can be found, utilizing the first derived thermal history; an improved thermal history is then obtained by iteration. This refinement, however, is nor warranted for the very crude estimates presented here.

To illustrate the method, we have taken observations from photoclinometric profiles of craters on the ancient cratered terrain of the Nicholson Regio and the adjacent grooved terrain of the Harpagia Sulci. This region is in the trailing hemisphere of Ganymede and includes areas with some of the highest observed crater retention ages on the satellite. Crater retention ages of the oldest (most flattened) craters at 10 km, 20 km, and 60 km on the Nicholson Regio and the age of the most flattened 20 km diameter craters on the Harpagia Sulci are from unpublished crater densities by J. B. Plescia. Ages for the oldest ray craters on the Nicholson Regio are taken from ray crater densities shown in figure 21. These various estimates of the ages of the observed craters together with the observed values of crater relaxation, τ , (from the comparison of photoclinometric profiles with the theoretical profiles of Danes) and the derived value of T, η_{eff} , and $\Delta T / h$ are listed in Table IX.

As the thermal gradient was declining fairly rapidly with time, especially near the beginning of the preserved crater record, the time at which the calculated viscosities and thermal gradients most nearly apply probably is fairly close to the time of origin of the respective craters. For example, the thermal gradient on the Nicholson Regio is estimated at 5.5 to 6.7 K/ km at a time close to 3.94 Gy; the thermal gradient declined to about 0.17 to 0.40 K/ km by about 2.0 Gy. As given in Table IX, there is one anomaly in an otherwise simple picture of monotonic decrease of thermal gradient with time. The calculated gradient at

the time of retention of the oldest 60 km crater on the Nicholson Regio (t_o = 3.76 Gy) appears too low. This anomaly almost certainly is an artifact of the assumptions used; our estimate of Δt for collapse of this crater may be several times too long. The values of η_{eff} and $\Delta T / h$ must be considered very rough estimates. Although the absolute values may be considerably in error, the sequence or historical trend of η_{eff} and $\Delta T / h$ is highly significant.

The thermal gradient in the Nicholson Regio apparently decreased by an order of magnitude in the time interval from about 4.0 Gy to 2.0 Gy. The early decay in the derived thermal gradients rather closely follows the estimated decay in cratering rate, dropping by about half every 10^8 years during late heavy bombardment. Following heavy bombardment, the decay of the thermal gradient apparently slowed considerably.

A quantitative assessment of impact heating shows that the derived drop in thermal gradient between 3.94 and 3.86 Gy or at later times cannot be due simply to a decrease in heating by impact at those times. The cratering rate at 3.94 Gy is about 400 craters equal to or larger than 10 km diameter per $10^6\ km^2$ per 10^8 years. The area, A , covered by these craters is

$$A = \frac{\gamma \pi N}{4} \int_{D_{max}}^{10\ km} D^{(\gamma+1)}\ dD \qquad (9)$$

where the size index γ =-2.2 (Shoemaker and Wolfe, this volume), N = 6.3 x $10^4\ km^{-2.2}$ per $10^6\ km^2$ and D_{max} , the diameter of the largest crater formed, is 150 km. Integration of equation (9) yields an area of craters formed in 10^8 years of 1.4 x $10^5\ km^2$, or only 14% of the surface. Integration to 1 km crater diameter, a size at which heating of the lithosphere would be very ineffective, would merely double the area covered. The cumulative energy, E , delivered to the surface by projectiles forming craters 10 km in diameter and larger per

$10^6\ km^2$ per 10^8 years is

$$E = \frac{\gamma N}{K_n^s} \int_{D_{max}}^{10\ km} D^{(\gamma + s - 1)}\ dD \qquad (10)$$

where K_n is a scaling constant relating the diameter of a crater to the kinetic energy of the projectile, W, and s is the inverse scaling exponent,

$$D = K_n\ W^{(1/s)} \qquad (11)$$

Adopting K_n = 0.125 km $(kt\ TNT)^{-1/3.4}$ and s = 3.4 (Shoemaker and Wolfe, this volume), we obtain E = 2.3 x 10^{30} ergs, and the power per unit area is 0.07 erg $cm^{-2}\ sec^{-1}$. This may be compared to the drop in power per unit area implied by the drop in thermal gradient between 3.94 and 3.86 Gy. The mean thermal conductivity coefficient of the lithospheric ice (temperatures from 120 to 190 K) is estimated from measurements summarized by Hobbs (1974) at about 4 watts $m^{-1}\ K^{-1}$. Hence the change in heat flow corresponding to a change in thermal gradient of 3.7 K km^{-1} is 4 watts $K^{-1}\ m^{-1}$ x 3.7 x $10^{-3}\ km^{-1}$ which is equal to 15 x 10^{-3} watts m^{-2} or 15 ergs cm^{-2} sec^{-1}. The total rate of delivery of impact energy to the surface of Ganymede at 3.94 Gy is 200 times less than the derived change in heat flow between 3.94 and 3.86 Gy. Even if as much as 50 percent of the impact energy were retained as heat in the lithosphere, heating associated with craters forming at 3.94 Gy could not account for more than a few parts per thousand of the total heat flow at that time.

It is clear that the thermal gradients on Ganymede, from the time of the earliest crater retention ages, must be controlled by heat flowing from the deep (sublithosphere) interior of the satellite. If the correlation of crater retention ages with proximity to the antapex is related directly to the gradient in cratering rate, the distribution of crater retention ages probably reflects an indirect

effect such as regional variation in the temperature at the top of the lithosphere due to a gradient in thickness of insulating regolith.

A remote possibility remains that the asymmetric cooling and thickening of the lithosphere after 4 Gy may partly reflect asymmetric impact heating of Ganymede at a time very close to its accretion. The trailing hemisphere of Ganymede probably never was heated as much as the leading hemisphere, during the early stages of heavy bombardment. If the early flux of projectiles arriving from outside the Jovian system were sufficiently intense, then the gradient in crater retention ages on the ancient cratered terrain might reflect an early pattern of impact heating of the entire body.

A history similar to that obtained for Ganymede is applicable to Callisto. The distribution of crater retention ages, increasing toward the antapex, may partly be a reflection of asymmetric regolith development and also partly the result of asymmetric production of multiring structures on the thin early crust. Crater retention ages (at 25 km crater diameter) extend back to 4.3 Gy (based on a uniform half-life of the cratering rate of 10^8 years).

The greater overall crater retention age of the lithosphere of Callisto, as compared with Ganymede, probably is attributable to two causes, 1) a lower abundance of radioactive heat sources per unit surface area (cf Cassen et al., 1980), and 2) less total heating by impact during accretion and early heavy bombardment.

A comment is in order on the absolute values of the derived thermal gradients in Table IX. If we assume that the lithosphere-asthenosphere boundary occurs at η_{eff} of about 10^{18} poise, comparable to the boundary on earth, the temperature of the boundary, from eq (7) is about 190 K. The thermal gradient of 6.7 K km^{-1} at about 3.9 Gy suggests a lithosphere thickness of (190-120)/ 6.7

km = 10 km. This is close to the lower limiting thickness estimated for the lithosphere of the Galileo Regio, at a probably comparable stage of thermal evolution. Hence, we consider the derived thermal gradient on the Nicholson Regio for 3.94 Gy to be a realistic estimate. The derived gradient for times less than 3 Gy probably are too low, however. The heat flow implied by these gradients is much lower than the equilibrium heat flow expected from plausible abundances of radioactive elements in the rocky core of Ganymede (cf. Cassen et al., 1980). The discrepancy is probably due mainly to our failure to take account of the changing influences of the regolith as both the cratering rate and heat flow declined. As the heat flow decreased, the top of the lithosphere probably cooled significantly.

The survival of the central depression of the Gilgamesh Basin is also a problem of considerable interest. From crater densities given in Shoemaker et al. (1982), the model age of the basin is ~3.5 Gy. The effective viscosity averaged over time, required to preserve the depression at its present degree of topographic relaxation is about 10^{25} poise, at a depth comparable to the diameter of the central depression. This high viscosity (which implies a lithosphere thickness of 300 km or more) would not be expected at low latitudes. The derived thermal gradient for this latitude (using 110 K as the mean temperature at the top of the lithosphere, is roughly consistent with the derived late stage thermal gradients at the low latitudes of the Nicholson Regio. However, if we use the present global heat flow on Ganymede suggested by Cassen et al. (1980) for equilibrium with a current level of radioactivity from a chondritic abundance of radioactive elements in the rocky core, the present thickness obtained for the lithosphere below Gilgamesh would be only 80 km.

TABLE IX - Effective lithospheric viscosites and thermal gradients of Ganymede

Crater	Age (Gy)	r	Δ t (Gy)	τ (Gy)	Effective viscosity (poise)	Thermal gradient[1] (1) deg/km	(2) deg/km
Most flattened 10 km crater in Nicholson Regio	3.94	50	0.08	.0016	2.0×10^{21}	5.5	6.7
Most flattened 20 km crater[2] in Nicholson Regio	3.86	50	0.10	.0020	5.0×10^{21}	2.4	3.0
Most flattened 60 km crater in Nicholson Regio	3.76	50	0.15	.0030	2.3×10^{22}	0.6	0.8
Most flattened 20 km crater[3] in Harpagia Sulci	3.61	6.5	1.6	.25	6.2×10^{23}	0.8	1.4
48 km crater with bright rim deposit in Harpagia Sulci[4]	(2.0)	1.0	0.4	.4	2.4×10^{24}	0.17	0.40
123 km crater with rays on Nicholson Regio	1.6	(6.5)	1.6	.25	3.8×10^{24}	0.04	0.14
Gilgamesh Basin[5] (175 km diameter)	3.5	(10)	3.5	.35	7.7×10^{24}	0.23	0.30
		(40)		.09	1.9×10^{24}	0.28	0.35

1 Gradient (1) based on assumption that the viscosity of ice at 120 K is 10^{25} poise, and gradient (2) based on assumption that the viscosity of ice at 120 K is 10^{26} poise.

2 From profile 4, figure 3.

3 From profile 1, figure 3.

4 From profile 1, figure 7.

5 Thermal gradients calculated for Gilgamesh are based on a mean surface temperature of 100 K at 60° latitude rather than 120 K used in calculating the other gradients.

Origin of central pits

The global abundance of craters with central pits on Ganymede and Callisto exceeds, by far, the abundance of similar craters on any of the terrestrial planets. Craters with central pits identified on Mars (Wood et al., 1979; Hodges et al., 1980) and craters with "peak-rings" on Mercury and the Moon, probably are analogous to the craters with central pits on Ganymede and Callisto. The origin of the central pits and peak-rings has been a subject of debate. We note that craters with central pits on Ganymede and Callisto have terraced walls. On the Moon, there is nearly a one-to-one correspondence between the presence of a central peak and the presence of terraced walls, for fresh craters up to 100 km diameter. The terraces are very probably produced by prompt collapse along the crater walls. Thus the development of a central peak appears to be strongly correlated with and probably is a consequence of prompt collapse of the crater walls. Our observation that craters with central peaks make up most craters 5 to 20 km in diameter, whereas craters with central pits make up a majority of craters larger than 20 km in diameter on Ganymede and Callisto, suggests that, in craters larger than 20 km, central pits have replaced the central peaks. In other words the circumstantial evidence is very suggestive that central pits have formed by collapse of an initial central peak. High resolution images of Ganymede reveal a number of central peaks which appear to have a small pit at the summit or a pit with an anomalously high rim. We interpret these features as examples of partially collapsed central peaks.

Taking a central peak to be a simple conical solid with a basal radius of approximately 1/7 the crater radius, and a maximum peak height of the order of 1 km (in agreement with the observations of peaks in 20-30 km diameter craters), the stress due to the load of the peak at the level of the crater floor is

$$Stress = \frac{1/3\ \pi \rho R^2 H g}{\pi R^2} = 1/3\ \rho H g \qquad (12)$$

where R is the basal radius of the peak, H is the height, g is gravity, and ρ is the density of the material in the peak. Substituting a value of 1 km for H and the density of ice I of 0.9 g cm^{-3} (the peak may actually consist of metastable higher pressure phases produced by shock) in eq (12) yields a stress of 4.3 bars. This may be compared with the ultimate strength of ice. In the temperature range of 0° C to −10° C the strength of ice I varies from about 14 to 50 bars (Voitkovskii, 1962). Even if the central peaks consisted of warm ice, one might expect much larger peaks than those observed to have been preserved. Therefore, for our model of collapse to be physically valid, the strength of the material within and beneath a central peak must be many times less than the strength of pure warm ice.

A possible clue to the implied very low strength of the material beneath the central peaks is provided by an experiment reported by Shoemaker et al.(1963). In this experiment, fragments were recovered from an iron projectile fired at hypervelocity into sandstone. As shown by metallography, the temperature of the fragments remained below the melting point of the iron, but certain surfaces of the fragments were coated with a quenched iron melt. The melt was produced by frictional heating of the shear surfaces along which the projectile was pulled apart. Similar frictional heating along shear surfaces in relatively strongly shocked ice in the central peaks of craters on Ganymede and Callisto may well have produced abundant thin veins and veinlets of water. Lubrication of the shear surfaces by water would greatly reduce the bulk strength of the peak and deep-seated material underlying the peak.

We suggest that all central pits in the craters on Ganymede and Callisto are formed by prompt collapse of a transient central peak. A central pit in the

Prairie Flat crater, produced by detonation of 500 tons of TNT, evidently was formed in this manner (Roddy, 1976; Roddy et al., 1977; and D. J. Roddy, personal communication, 1980). When a transient peak is formed whose basal load is much greater than the instantaneous strength of the strongly shocked (and partially melted) subjacent ice, the collapse of the peak is comparable to a case of very low velocity impact. A crater with a raised rim is formed which is roughly similar to craters produced by true impact. We do not suggest, however, that any of the material of the peak was necessarily lofted into space above the surface of the satellite or that the peak went through more than one up-down oscillation (cf Murray, 1980).

The occurrence of craters with anomalously large central pits is clearly related to their age. In all cases, they probably formed when the lithosphere was relatively thin. A good example is the 60 km highly flattened crater on the Nicholson Regio (Table IX), which has a 29 km diameter central pit. If the base of the lithosphere occurs at η_{eff} of about 10^{18} poise, with a corresponding temperature of about 190 K, then the depth to the base of the lithosphere indicated by the thermal gradient given in Table IX is about 70 km. We consider the thermal gradient derived from this crater to be too low by more than a factor of 2, however, and the correct thickness of the lithosphere probably was closer to 35 km. The diameter of the crater, in other words, is nearly twice the probable depth to the asthenosphere at the time this crater formed. Assuming the transient cavity produced had a depth of $1/5\ D$ = 12 km, the uplift of the central peak probably formed a dome in the underlying asthenosphere of the order of 12 km. Hence, the depth to the asthenosphere beneath the transient peak was (35-12) km = 23 km, somewhat less than the anomalous diameter of the central pit. As the effective viscosity of material at a depth comparable to the diameter

of the pit may influence the flow as the pit is formed, it appears reasonable that the proximity of the asthenosphere influenced the growth of this anomalously large central pit.

Acknowledgments.-- We would like to thank W. B. McKinnon for spirited discourses concerning the description and interpretation of features on Ganymede and Callisto. We are especially indebted to Jeffrey B. Plescia for sharing with us in advance of publication, his detailed studies of crater densities on Ganymede. We would also like to thank Ronald Greeley for a helpful review of this chapter.

REFERENCES CITED

Bonner, W.J.,and Schmall, R.A., (1973) A photometric technique for determining planetary slopes from orbital photographs, *U.S. Geol. Survey Prof. Paper 812-A*, 16 p.

Boyce, J.M., (1980) Basin peak-ring spacing on Ganymede and Callisto: Implications for the origin of central peaks and peak-rings, *NASA TM 81776* p. 339-342.

Cassen, P., Peale, S.J., and Reynolds, R.T., (1980) On the comparative evolution of Ganymede and Callisto, *Icarus*, *41* p. 232-239.

Cintala, M.J., Wood, C.A., Head, J.A., and Mutch, T.A., (1977) Interplanetary comparisons of fresh crater morphology: Preliminary results, Lunar Science VII, p. 181-183.

Clark, R.N., (1980) Spectroscopic studies of water and water/regolith mixtures on planetary surfaces at low temperature, PhD Thesis, Univ. Hawaii, January, 1980, 337 p.

Conca, J., (1981) Dark ray craters on Ganymede, Proc. Lunar Planet. Sci. 12, p. 1599-1606.

Croft, S.K., (1980) On the origin of pit craters, Poster presentation at IAU Colloquium No. 57, May 13-16, 1980, Kailua-Kona, Hawaii.

Danes, Z.F., (1962) Isostatic compensation of Lunar craters, Research Institute Univ. Puget Sound, Tacoma, Washington, RIR-GP-62-1, 11 p.

---------, (1965) Rebound processes in large craters, U.S. Geol. Survey Astrogeol. Stud. Annu. Prog. Rept. July 1, 1964 to July 1, 1965, Part A: Lunar and Planetary Investigations, Nov. 1965, p. 81-100.

Davies, M.E., (1980) Coordinates of features on the Galilean satellites, Poster presentation at IAU Colloquium No. 57, May 13-16, 1980, Kailua-Kona, Hawaii.

Dollfus, A., Mandeville, J.C., and Geake, J.E., (1980) Regolith and cratering on Callisto, Presented at IAU Colloquium No. 57, May 13-16, 1980, Kailua-Kona, Hawaii.

Gault, D.D., Guest, J.E., Murray, J.B., Dzurisin, D., and Malin, M.C., (1975) Some comparisons of impact craters on Mercury and the Moon, *Jour. Geophys. Res. 80*, p. 2444-2460.

Goodman, D.J., Frost, H.J., and Ashby, M.F., (1981) The plasticity of polycrystalline ice, *Philosophical Mag. A, 43*, p. 665-695.

Gordon, R.B., (1967) Thermally activated processes in the Earth: Creep and seismic attenuation, *Geophys. Jour., 14*, p. 33-43.

Haskell, N.A., (1935) The motion of a viscous fluid under a surface load, *Physics, 6*, p.265-269.

Hobbs, P.V., (1974) **Ice Physics,** Clarendon Press, Oxford, 837 p.

Hodges, C.A., Shew, N.B., and Clow, Gary, (1980) Distribution of central pit craters on Mars, (Abstract) Lunar and Planetary Science XI, p. 450-452.

Johnson, T.V., and McGetchin, T.R., (1973) Topography on satellite surfaces and the shape of asteroids, *Icarus, 18*, p. 612-620.

Malin, M.C., (1980) Fables in Ganymede tectonics from morphologic studies, Presented at IAU Colloquium No. 57, May 13-16, 1980, Kailua-Kona, Hawaii.

McKenzie, D.P. (1967) The viscosity of the Mantle, *Geophys. J., 14* p. 297-305.

McKinnon, W.B.,and Melosh, H.J., (in press) Evolution of planetary lithospheres: Evidence from multiringed basins on Ganymede and Callisto, *Icarus*.

Melosh, H.J., and McKinnon, W.B., (1978) The mechanics of ringed basin formation, *Geophys. Res. Lett.*, *5*, p. 985-988.

Murray, J.B., (1980) Oscillating peak model of basin and crater formation, *The Moon and Planets*, *22*, p. 269-291.

Phillips, R.J., and Malin, M.C., (1980) Ganymede: A relationship between thermal history and crater statistics, *Science*, *210*, p. 185-187.

Pike, R.J., (1975) Size-morphology relations of Lunar craters: Discussion, *Modern Geology*, *5*, p. 169-173.

Purves, N., and Pilcher, C.B., (1980) Thermal migration of water on the Galilean satellites, *Icarus*, *43*, p. 51-55

Reynolds, R.T., and Cassen, P.M., (1979) On the internal structure of the major satellites of the outer planets, *Geophys. Res. Letters*, *6*, p. 121-124

Roddy, D.J., (1976) High-explosive cratering analogs for bowl-shaped, central uplift, and multiring impact craters, *Proc. Lunar Sci. Conf. 7th*, p. 3027-3065.

Roddy, D.J., Ullrich, G.W., Sauer, F.M., and Jones, G.H.S., (1977) Cratering motions and structural deformation in the rim of the Prairie Flat multiring explosion crater, *Proc. Lunar Sci. Conf. 8th*, p. 3389-3407.

Schubert, G., Stevenson, D.J., and Ellsworth, K, Internal structure of the Galilean satellites, submitted to *Icarus*.

Scott, R.F., (1967) Viscous flow of craters, *Icarus*, *7*, p. 139-148.

Shaw, H.R., (1972) Viscosities of magmatic silicate liquids: An empirical method of prediction, *Am. Jour. Sci., 272*, p. 870-893.

Shoemaker, E.M., (1966) Preliminary analysis of the fine structure of the lunar surface in Mare Cognitum, in *The Nature of the Lunar Surface; Proceedings of the 1965 IAU-NASA Symposium*, Hess, W.N., Menzel, D.H., and O'Keefe, J.A., eds., John Hopkins Press, p. 23-78.

Shoemaker, E.M., Gault, D.E., Moore, H.J., and Lugn, R.V., (1963) Hypervelocity impact of steel into Coconino Sandstone, *Am. Jour. Sci., 261*, p. 668-682.

Shoemaker, E.M., and Passey, Q.R., (1979) Tectonic history of Ganymede, *(Abstract) EOS, 60*, p. 869.

Shoemaker, E.M.,and Wolfe, R.F., (1982) Cratering time scales for the Galilean satellites, in **The Satellites of Jupiter,** D. Morrison, ed., University of Arizona Press, Tucson.

Smith, B.A., Soderblom, L.A., Johnson, T.V., Ingersoll, A.P., Collins, S.A., Shoemaker, E.M., Hunt, G.E., Masursky, H., Carr, M.H., Davies, M.E., Cook, A.F. II, Boyce, J., Danielson, G.E., Owen, T., Sagan, C., Beebe, R.F., Veverka, J., Strom, R.G., McCauley, J.F., Morrison, D., Briggs, G.A., and Suomi, V.E., (1979a) The Jupiter system through the eyes of Voyager 1, *Science, 204*, p. 951-972.

Smith, B.A., Soderblom, L.A., Beebe, R., Boyce, J., Briggs, G., Carr, M., Collins, S.A., Cook, A.F. II, Danielson, G.E., Davies, M.E., Hunt, G.E., Ingersoll, A., Johnson, T.V., Masursky H., McCauley, J., Morrison, D., Owen, T., Sagan, C., Shoemaker, E.M., Strom, R., Suomi, V.E., and Veverka, J., (1979b) The Galilean satellites and Jupiter: Voyager 2 imaging science results, *Science, 206*, p. 927-950.

Squyres, S.W., (1980a) Surface temperatures and retention of H_2O frost on Ganymede and Callisto, *Icarus*, *44*, p. 502-510.

---------, (1980b) Water vulcanism on Ganymede?, presented at IAU Colloquium No. 57, May 13-16, 1980, Kailua-Kona, Hawaii.

Strom, R.G., Woronow, A., and Gurnis, M., (1980) Crater populations on Ganymede and Callisto, presented at IAU Colloquium No. 57, May 13-17, 1980, Kailua-Kona, Hawaii.

Voitkovskii, K.F., (1962) The mechanical properties of ice, Translated from Russian by The American Meteorological Society and The Artic Inst. of North America, Air Force Cambridge Research Laboratories, Bedford, Mass., 92 p.

Watson, K., (1968) Photoclinometry from spacecraft images, *U. S. Geol. Survey Prof. Paper 599-B*, 10 p.

Wood, C.A., Head, J.W., and Cintala, M.J., (1978) Interior morphology of fresh Martian craters: The effects of target characteristics, in *Proc. Lunar Planet. Sci. Conf. 9th*, p. 3691-3709.

PAPER 2
VARIATIONS IN CRATER DENSITY MODEL SURFACES AGES ON CALLISTO

by QUINN R. PASSEY

Submitted to *ICARUS*

ABSTRACT

Analysis of the global distribution of craters and multiring structures on Callisto reveals that the large multiring structures are concentrated in the leading hemisphere, whereas craters are depleted there. There is a slight increase in crater density toward the poles but no significant surface age dependence on latitude exists. Calculations of model crater retention ages based on a sample of 2000 craters ≥ 30 km in diameter show that the mean age of Callisto's surface is between 4.0 and 4.2 Gy; some areas in the leading hemisphere are about 300 MY younger than some areas in the trailing hemisphere. The model age of a given surface area is dependent upon the diameter of the craters counted; generally, larger craters yield ages that are younger than those derived from smaller craters. The interpretation of this is that larger craters are not retained from as early a period in time as were the smaller craters; this is in agreement with the results predicted by viscous relaxation theory where large wavelength features relax at a faster rate than do small wavelength features.

Several proposed models that probably can explain the regional differences in crater densities and crater retention ages include: the disruption of the lithosphere by the formation of large multiring structures and palimpsests, the burial of pre-existing craters by heated ejecta deposits (thus increasing the rate at which they will viscously flatten), the formation of a temporary "hot spot" beneath a large impact structure, and the loss of craters resulting from the thermal effects induced by a veneer of insulating regolith. Most of the variations in the observed distribution of craters can be explained satisfactorily by the effects due to the formation of multiring structures, and on the production of an insulating regolith.

INTRODUCTION

In 1979 Voyagers I and II encountered Callisto, the second largest of the Galilean satellites; relatively high resolution images were returned of much of its surface. The images revealed that Callisto's surface is heavily cratered, and that the craters are similar to craters observed on the Moon and Mercury, displaying raised rims, ejecta deposits and commonly bright rays (Passey and Shoemaker,1982; Smith et al.,1979ab). By analogy with craters on the Moon, there is little doubt that the vast majority of craters on Callisto are either of primary or secondary impact origin. Despite the similarities, one important structural difference between the craters on Callisto and those on the Moon, is the presence of a rimmed central pit in essentially all craters larger than about 40 km in diameter. In this paper, the global distribution of craters on the surface of Callisto is analysed, and surface ages are inferred by utilizing the cratering time scale proposed by Shoemaker and Wolfe (1982). Specific processes that may have been responsible for the regional variation in crater density and surface ages are also discussed.

Several large multiring structures are also visible on Callisto; these features exhibit morphologies strikingly different from the multiring basins on the Moon. Although the morphology of the multiple ring structures on Callisto is remotely similar to those of lunar multiring basins, the centers of these structures are not currently occupied by a topographic basin surrounded by a raised rim; rather, the centers of the multiring structures on Callisto are often occupied by a circular high albedo feature, with little or no topographic expression. Despite the lack of a central basin, these features are inferred to be of impact origin (Smith et al., 1979a,1979b; Passey and Shoemaker, 1982). Other features that are found on Callisto (and Ganymede), and are assumed to be of impact origin,

TABLE I- Multiring structures on Callisto

#	Lat.[1]	Long.[1]	Outer Ring Diameter[2] (km)	Inner Ring Diameter[2] (km)	Name
1	+11	57	4000	400	Valhalla
2	+30	139	1640	163	Asgard
3	-53	36	920	130	Unnamed
4	+45	138	500	?	Unnamed
5	- 9	222	163	80	Alfr
6	- 3	215	123	25	Loni
7	+42	213	180	96	Grimr
8	-41	262	71	35	Unnamed

[1] From U.S. Geological Survey Map I-1239, 1979.

[2] All measurements ± 10%.

are crater palimpsests - roughly circular spots with albedos slightly higher than the surrounding terrain (Smith et al., 1979b); it should be noted that, by definition, a palimpsest does not retain any vestige of the original crater rim, and features with vestiges of the original crater are referred to as highly flattened craters, rather than as palimpsests. Palimpsests can be found in many locations on the surface of Callisto, and are interpreted to be the remnant scars of craters and basins that have flattened beyond recognition; the flattening apparently is due primarily to the viscous or plastic flow of material in the icy lithosphere of Callisto (Passey and Shoemaker, 1982).

DISTRIBUTION OF IMPACT FEATURES

Multiring Structures

The distribution of large multiring structures on Callisto is highly nonuniform (Figure 1)(Passey and Shoemaker, 1980). The four largest and apparently youngest structures, Valhalla, Asgard and two unnamed structures, are located in the leading hemisphere; these features range in outer diameter from about 500 km to about 4000 km (Table I); the outer diameter is based on the outermost ring in the system. Several multiring structures can be found in the trailing hemisphere, but all of these have outer diameters less than 200 km. (For descriptions of the morphology and possible formation mechanisms of these multiring structures, see Passey and Shoemaker, 1982; Melosh, 1982; McKinnon and Melosh, 1981; and Hale, 1981).

Because the orbital velocity of Callisto, of 8.1 km sec^{-1}, is 0.45 times the rms encounter speed of impacting projectiles at Callisto's orbit (Shoemaker and Wolfe, 1982), the present cratering rate on Callisto is not globally uniform. The present flux of impacting bodies at Callisto's apex of orbital motion (0° N, 90° W) is $\sim$5 times the flux at the antapex. Moreover, the rms impact velocity at the

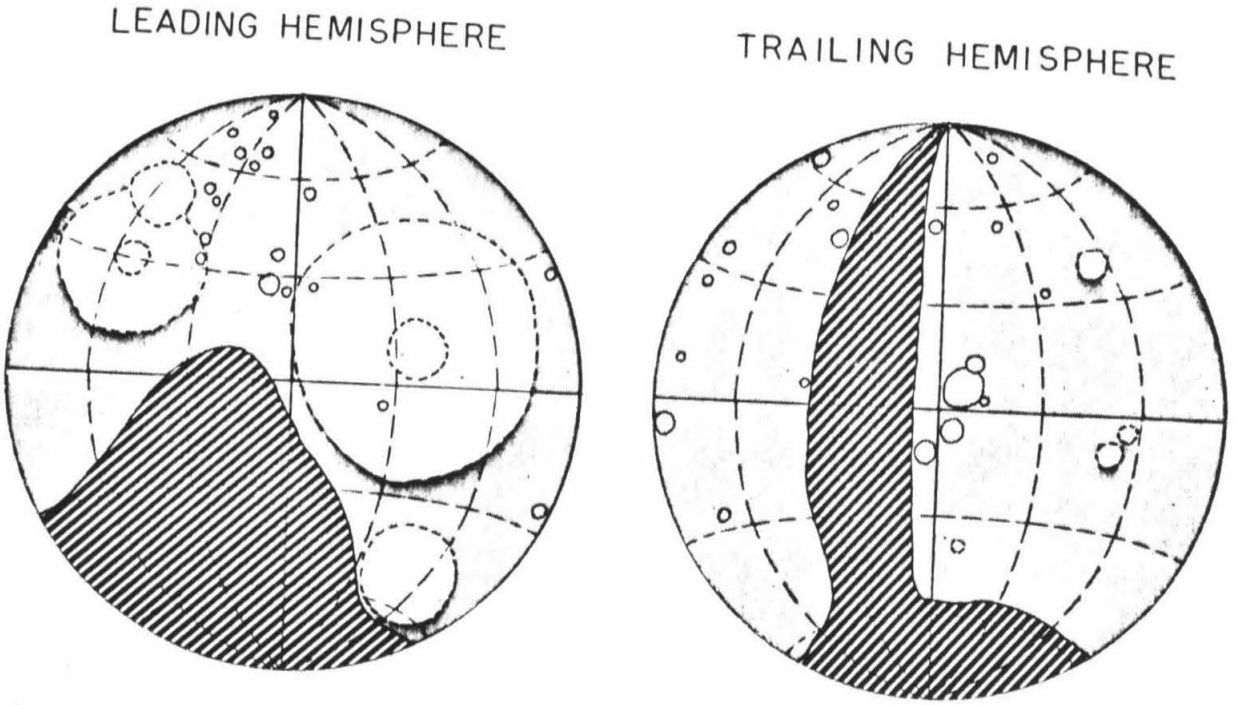

FIGURE 1 – Orthographic projections of the leading and trailing hemispheres of Callisto showing the distribution and approximate size of eight multiring structures (no stipple pattern). Also shown are large impact craters (shaded circles). Areas of the surface that were not imaged at sufficient resolution to identify these features are shown by the heavy diagonal pattern. The center point in the leading hemisphere is 0° N , 90° W.

apex is about twice the rms impact velocity at the antapex. Adopting a size index of -2.2 for the craters produced (Shoemaker and Wolfe, 1982), yields a cratering rate at the apex about 10 times the cratering rate at the antapex. A similar large difference in cratering rate between apex and antapex of orbital motion is found for any source of impacting projectiles external to the Jovian system but bound to the sun. Hence, the observed asymmetric global distribution of the large multiring structures suggests that the impacting bodies that formed these structures were external to the Jovian system, and that Callisto has been tidally locked in its rotation from the period extending from, at least, the time of the formation of the large multiring structures.

Craters

Relatively high resolution images (better than 5 km/lp) were obtained for approximately 53% of the surface of Callisto. Although about 80% of the surface was imaged at somewhat lower resolution, only the highest resolution (better than 5 km/lp) coverage will be used for statistical purposes in this paper. From these high resolution images, position and diameter were determined for more than 2200 craters ≥ 25 km in diameter; the latitude and longitude of each crater were obtained using the network of control points established by Davies and Katayama (1980). The survey is believed to be complete for crater diameters ≥ 30 km for the 53% of the surface of Callisto imaged at high resolution.

Figure 2 shows the observed local density of craters $\geq$ 30 km in diameter at a spatial resolution of 10° latitude by 10° longitude (except near the poles where the highest latitude bin include latitudes 60° - 90°). Large areas of relatively low crater density correspond to the large multiring structures, where the density of craters $\geq$ 30 km in diameter is less than 30 craters per 10^6 km^2. The average number of craters per 10° bin is approximately 10.

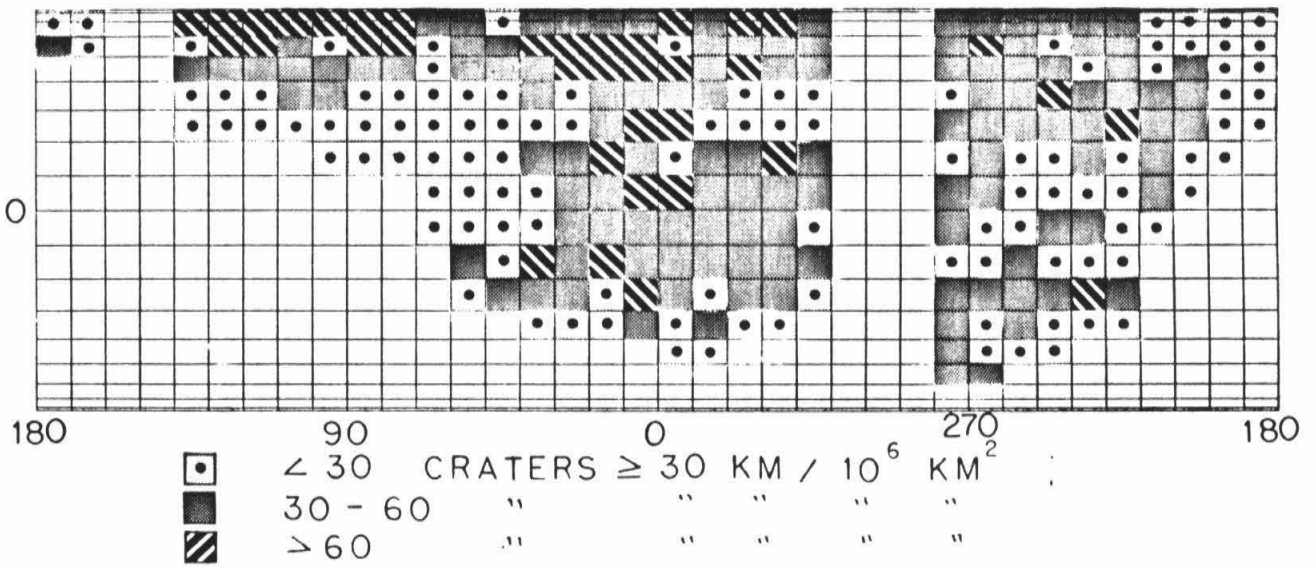

FIGURE 2 – Cylindrical equal area map of Callisto showing the density of craters ≥ 30 km in diameter per 10^6 km^2 . The unshaded areas were not included because of relatively low resolution images of these areas.

Detailed analysis of the crater distribution on the largest multiring structure, Valhalla (Figure 3), reveals that the crater density on the region occupied by this structure is not radially uniform (Figure 4) The central region of Valhalla is occupied by a roughly circular palimpsest about 300 km in radius (Passey and Shoemaker, 1982). The outer boundary of the palimpsest is interpreted to represent the outer limit of a continuous ejecta deposit surrounding a, now flattened, central basin; but the palimpsest may just represent the original basin. This is based on analysis of palimpsests and penepalimpsests on Ganymede (Passey and Shoemaker, 1982). The density of craters ≥ 25 km in diameter is fairly uniform over the palimpsest at about 20 craters per 10^6 km^2; beyond the central palimpsest, the crater density systematically increases until the outermost ring is reached, at a radial distance of about 1800 km. Beyond 1800 km the crater density is more or less uniform at about 65 craters per 10^6 km^2.

Most areas of highest observed crater density on Callisto are located in the leading hemisphere and tend to be concentrated at high latitude. The observed latitudinal dependence (Figure 5) is undoubtedly influenced by the locations of the multiring structures. Excluding the multiring structures, the average crater density is slightly higher in the leading hemisphere than in the trailing hemisphere. Figure 6 shows the distribution of craters as a function of distance from the apex. A marked low crater density less than 60° from the apex is primarily due to the locations of the Asgard and Valhalla multiring structures. Beyond 60° from the apex, the density of craters ≥ 30 km in diameter declines as the antapex is approached (180° from the apex). A linear least squares fit to craters ≥ 30 km in diameter beyond, 60° from the apex, yields

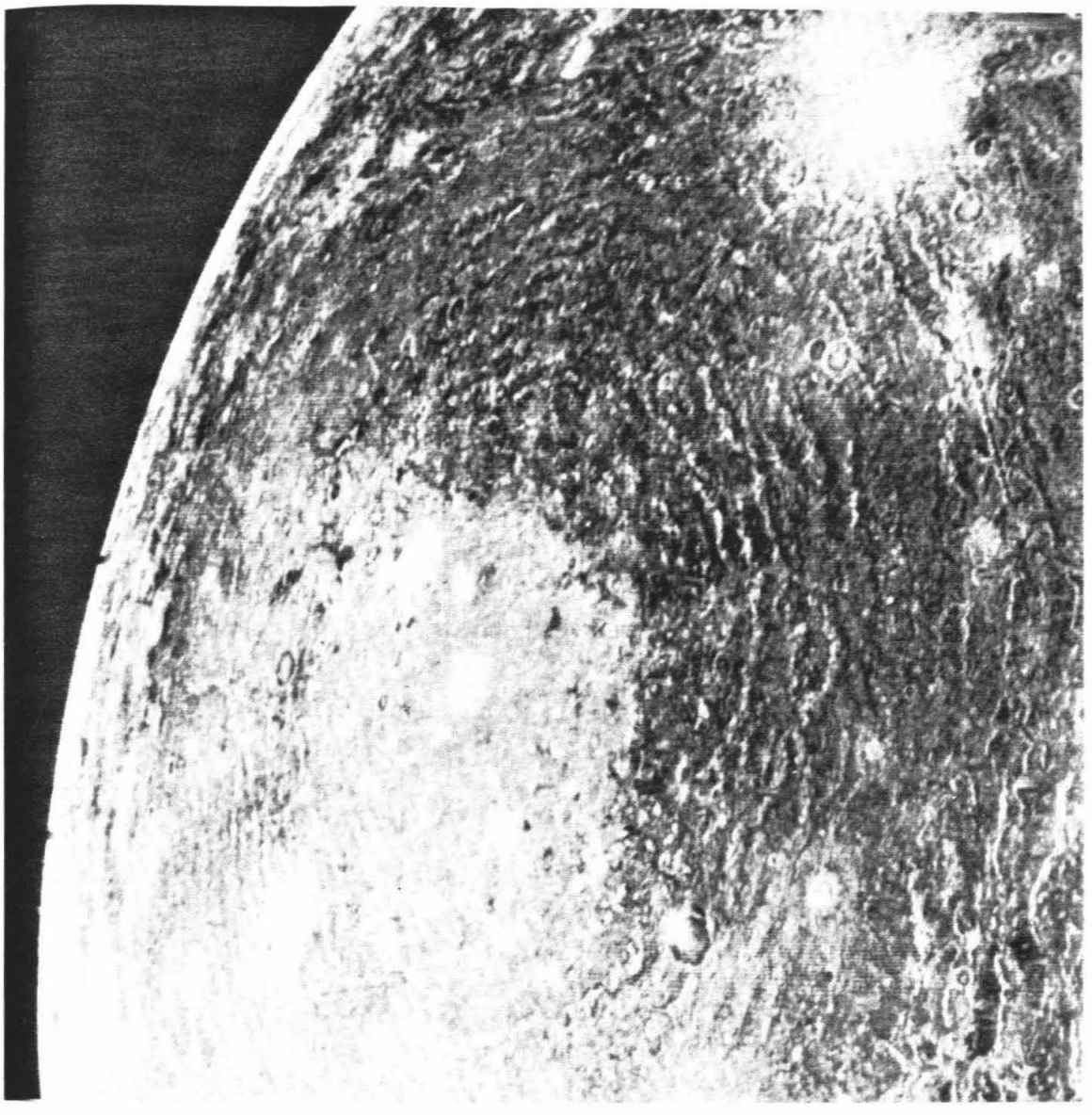

FIGURE 3 – Voyager I image of Valhalla, the largest multiring structure on Callisto. Note that the central region is occupied by a palimpsest ~600 km in diameter.

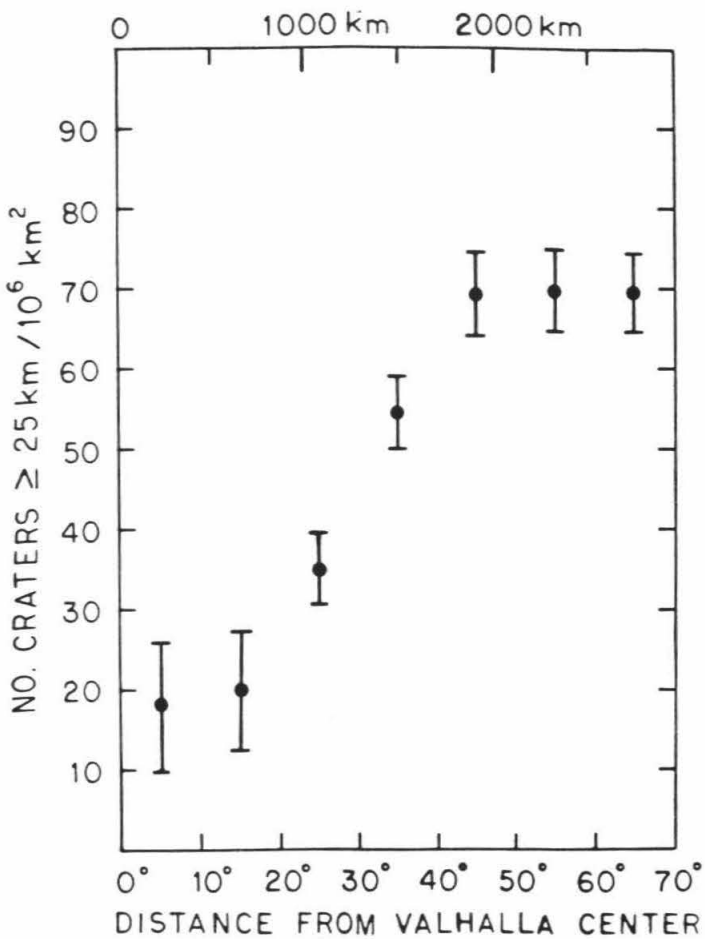

FIGURE 4 – Density of craters ≥ 25 km in diameter as a function of distance from the center of the Valhalla multiring structure. Note that the density is approximately a linear function of distance in the region between about 300 km and 1800 km. The Valhalla palimpsest occupies the region < 300 km and the outer ring sets are located at about 1800 km from the center.

$$N(30) = -0.128\,\beta + 57.2 \quad (1)$$

where $N(30)$ is the number of craters $\geq$ 30 km in diameter per 10^6 km^2, and β is the distance from the apex (in degrees), with a correlation coefficient r^2 of 0.47. For craters $\geq$ 40 km in diameter, the fit is

$$N(40) = -0.136\,\beta + 37.8 \quad (2)$$

with r^2 of 0.72; for craters $\geq$ 50 km in diameter, the fit is

$$N(50) = -0.056\,\beta + 18.3 \quad (3)$$

with r^2 of 0.46, and for craters $\geq$ 60 km in diameter, the fit is

$$N(60) = -0.030\,\beta + 8.9 \quad (4)$$

with r^2 of .34. The observed decreasing gradient in crater density toward the antapex is much less steep than would be observed if the entire surface of Callisto were of a single age, and if the cratering rate from apex to antapex varied according to the model of Shoemaker and Wolfe (1982). The observed ratio of the crater density for craters $\geq$ 30 km in diameter, at $\beta = 90°$ to that at $\beta = 180°$ is 1.3:1; the predicted ratio for a surface of globally uniform age is 5.3:1 (this assumes that the cratering rate at the apex is 9.6 times the cratering rate at the antapex). The slope, α, of the predicted distribution, for craters $\geq$ 30 km in diameter, averaged over $\beta = 60°$ to 180° is $\alpha(30) = -0.45$, which is much steeper than the slope of -0.128 observed; the other average predicted slopes for the other crater diameters are $\alpha(40) = -0.27$, $\alpha(50) = -0.10$, and $\alpha(60) = -0.050$. These slopes are approximately twice the slopes observed in (2), (3), and (4), respectively. It is important to note that the ratio of the cratering rate at the apex to that at the antapex of 9.6:1 (Shoemaker and Wolfe, 1982), refers to the present estimated flux of impacting bodies. Assuming that the present flux of impacting bodies is a good representation of the flux 4 Gya, then the ratio of

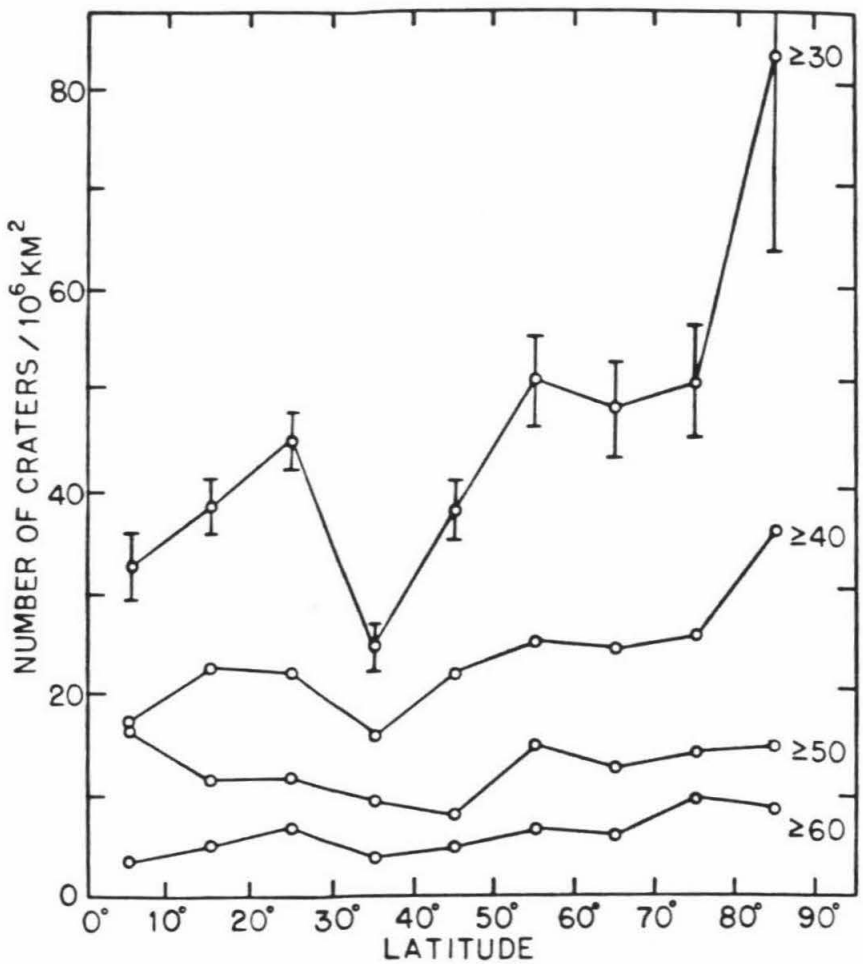

FIGURE 5 – Latitudinal dependence of crater density on Callisto for various diameter samples (e.g. ≤ 30 km, etc). The drop in density at 30° to 50° latitude is primarily due to the location of the Valhalla and Asgard multiring structures. There appears to be a significant increase in crater densities, at all diameters, but much of this may be due to the location of the multiring structures, of low crater density.

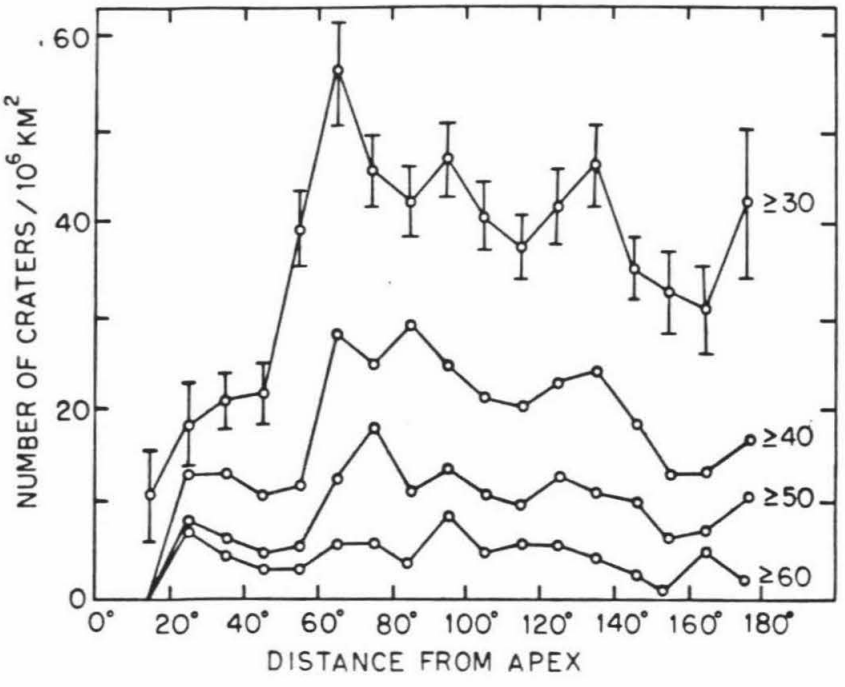

FIGURE 6 – Distribution of crater densities as a function of angular distance from the apex of orbital motion (0° N, 90° W). The decrease in density < 60° from the apex is clearly due to the locations of Valhalla and Asgard. Beyond 60°, there is a decrease in crater density toward the antapex.

9.6:1 should be valid for the observed crater record on Callisto. Based on this model, the oldest surfaces are found in the trailing hemisphere near the antapex of orbital motion even though the crater densities at these locations are not necessarily the highest; the ages are the oldest because of the much lower model cratering rate near the antapex. The derived difference in the cratering rate at Callisto's apex versus the cratering rate at the antapex is based on the assumption that 70% of the impacting bodies are in long period comet orbits, and 30% are objects on short period comet orbits (Shoemaker and Wolfe, 1982). The minimum difference in the cratering rate at the antapex versus the antapex exists if it is assumed that all of the impacting bodies are in long period comet orbits (i.e. a higher encounter velocity with Callisto). For this case, the ratio of the cratering rate at the apex to the cratering rate at the antapex would be about 3:1.

DISTRIBUTION OF MODEL AGES

If we accept the cratering model of Shoemaker and Wolfe (1982), and assume that the ratio of the present cratering rate at the apex to that at the antapex, of 9.6:1, can be extended back into the period of heavy bombardment, and if we assume that Callisto has been tidally locked throughout its preserved cratering history, then the crater densities shown in Figure 2 can be transformed to model surface ages. The distribution of determined model ages based on craters $\geq$ 30 km in diameter is shown in Figure 7. For the coverage shown in Figure 7, about 2% of the surface has model ages less than 3.8 Gy, 26% is between 3.8 and 4.0 Gy, 60% is between 4.0 and 4.2 Gy, and 13% is between 4.2 and 4.4 Gy. From this model, the best estimate of the absolute ages of the Valhalla and Asgard multiring structures are 3.96 $\pm$ 0.12 Gy and 4.04 $\pm$ 0.14 Gy, respectively.

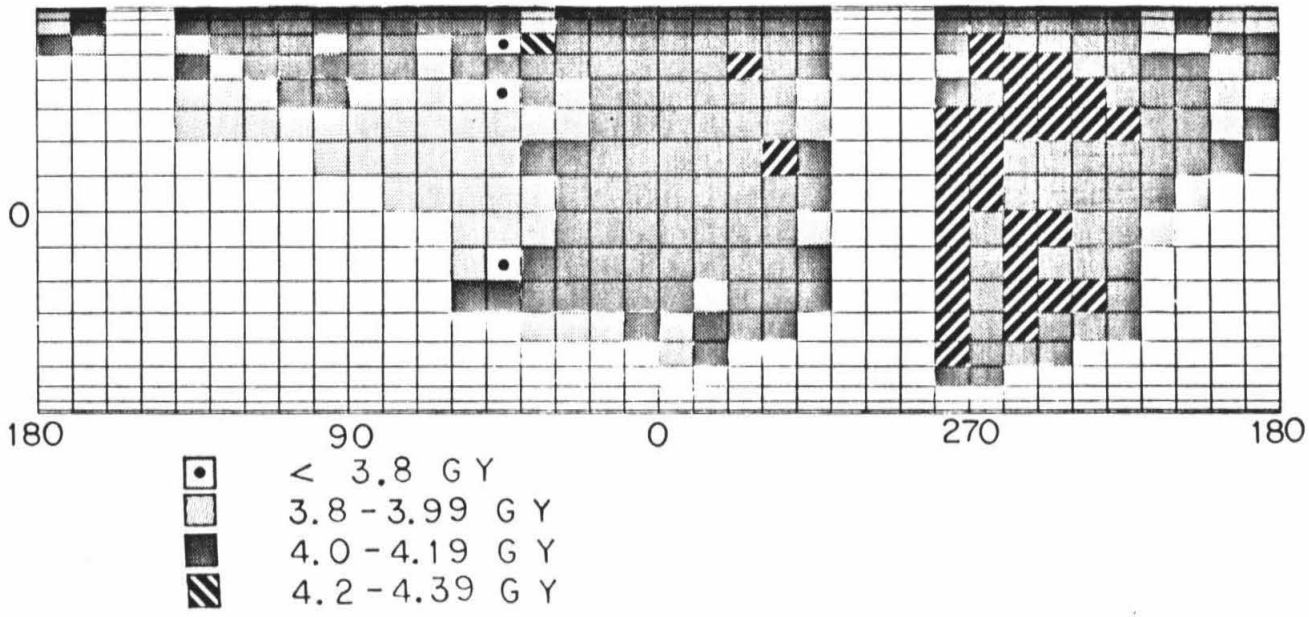

FIGURE 7 – Cylindrical equal area map of Callisto showing the model crater retention ages of regions of the surface from craters ≥ 30 km in diameter. The ages shown assume the cratering time scale proposed by Shoemaker and Wolfe (1982). These ages also assume that the cratering rate at the apex is 9.6 times the cratering rate at the antapex.

Using the limiting ratio for cratering rate at the apex versus that at the antapex, of ~3:1 (for impacting bodies external to the Jovian system), the distribution of calculated model ages is shown in Figure 8. For this model, 27% of the included coverage of Callisto's surface is between 3.8 and 4.0 Gy, 67% is between 4.0 and 4.2 Gy, and 6 % is between 4.2 and 4.4 Gy, based on the density of craters ≥ 30 km in diameter. As is observed in Figure 8, the age of Callisto's surface (excluding the large multiring structures) is more nearly globally uniform for this model but areas near the antapex are still slightly older. For this case (where the cratering rate at the apex is 3 times that at the antapex) the predicted ratio of crater density, for a globally uniform age surface, at $\beta = 90°$ to that at $\beta = 180°$ is 2.0:1, in comparison with the observed ratio of 1.3:1. The predicted slope at averaged over $\beta = 60°$ to 180°, for craters ≥ 30 km in diameter, is -0.229. This is still quite a bit steeper than the -0.128 observed.

On the other hand, if most of the impacting bodies were on short period comet orbits or were Jupiter planetesimals, the ratio of the cratering rate at the apex as compared to the cratering rate at the antapex would be much greater than 9.6:1, and the difference between the model surface age at the apex to that at the antapex would increase. Thus, the observed distribution of craters is most easily explained if most of the impacting bodies were on long period orbits (assuming that Callisto has remained tidally locked and that the bodies are not internal to the Jovian system).

CRATER RETENTIVITY OF CALLISTO'S LITHOSPHERE

On Ganymede it has been observed that craters ≤ 10 km in diameter are extremely flattened (Passey and Shoemaker, 1982); detailed studies of crater relaxation indicate that in order for these relatively small craters to collapse, steep viscosity and thermal gradients must have existed at one time (Passey and

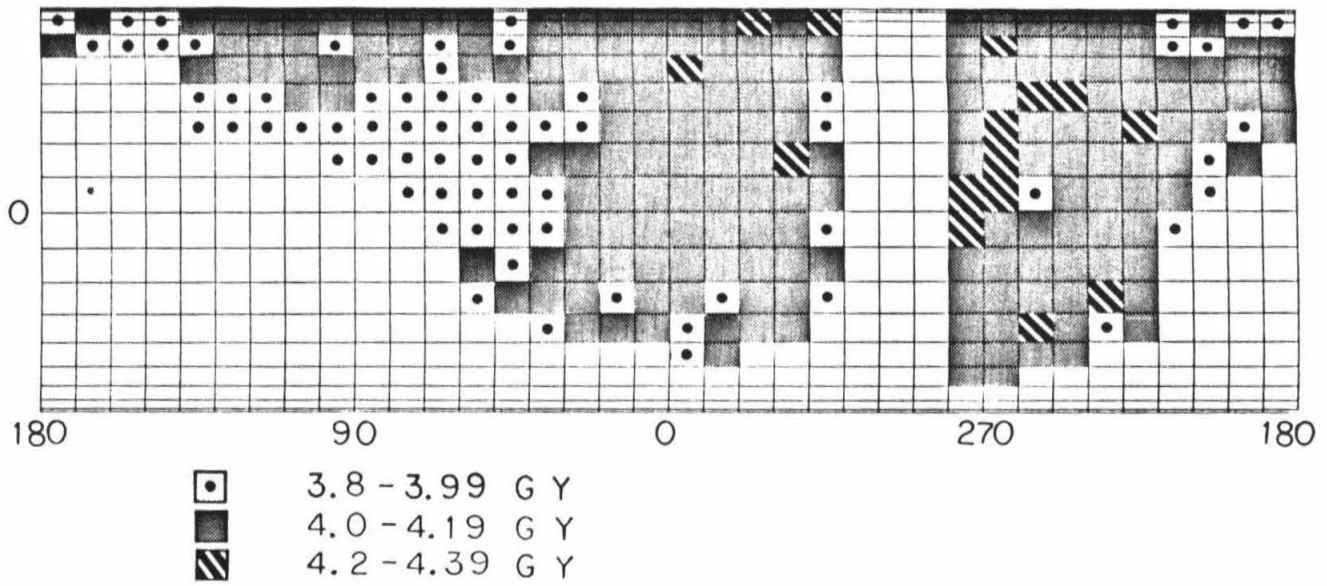

FIGURE 8 – Same as for Figure 7 except that these ages assume that the cratering rate at the apex is ~3 times that at the antapex, as is discussed in the text.

Shoemaker, in preparation). Extending the derived thermal gradients into the interior of Ganymede suggests that, approximately 4 Gya, the mechanical crust or lithosphere was, possibly, 10 km thick. Based on this observation on Ganymede, it was proposed that the lithosphere of Callisto was, also, at one time early in its history, quite thin (< 20 km thick). Crater relaxation studies indicate that a lithosphere < 20 km thick would be too thin to retain moderate sized craters (diameters ≥ 20 km) over geologic time; but the icy lithosphere would cool and thicken, with time, due to a reduction in heating from impact and radiogenic sources. Because the viscosity of ice is a strong function of temperature, with the viscosity decreasing exponentially with increasing temperature, the rate of crater flattening by viscous flow would also be reduced with time. With a decreasing thermal gradient in the lithosphere, at any given location, progressively larger craters could be retained against viscous collapse as time passed.

When discussing the ages of the surfaces as dated from the spatial density of superposed impact craters, it is important to note the diameter range of the craters used in the age determination. Because small wavelength features (i.e. ≤ 10 km diameter craters) flatten viscously at a much slower rate than long wavelength features (i.e. craters ≥ 50 km diameter), the ages derived from the smaller craters could be higher than the ages derived from the larger craters; this would be the case if many of the oldest larger craters, that are the same age as the oldest smaller craters, have flattened beyond recognition and are not included in the crater counts and the age determinations. Thus crater size must be specified when discussing *crater retention ages*; a crater retention age derived from craters ≥ 25 km diameter could be greater than the crater retention age derived from craters ≥ 50 km in diameter.

Size distribution of craters

To obtain meaningful and comparable crater retention ages derived from populations of different diameter craters, one must know the size distribution of impacting bodies. From three independent calculations, (1) statistics of bright ray craters on Ganymede (Passey and Shoemaker, 1982), (2) the size distribution of present day Jupiter crossing comet nuclei (Shoemaker and Wolfe, 1982), and (3) the size distribution of craters on the grooved terrain on Ganymede (Shoemaker and Wolfe, 1982), it was found that the size distribution of impacting objects from the present through ~3.8 Gya, to first order, follows a simple power law distribution with the exponential size index = -2.2. In that the original crater topography of many of the largest impact craters has possibly flattened beyond recognition, as is the case for the palimpsests, it is not possible to unambiguously determine a size index for craters on surfaces that contain palimpsests (i.e. the heavily cratered terrains of Ganymede and Callisto) using the present day record of craters. On the other hand, there has not been significant, if any, loss of craters on the grooved terrain on Ganymede, and this terrain dates back to the late stages of heavy bombardment (Shoemaker et al., 1982).

It should be noted here that Woronow and Strom (1981, 1982) suggest that the population of impacting bodies on Ganymede and Callisto is inherently devoid of large impactors and that craters have not relaxed completely away. They also argue that "as yet definitive examples of palimpsests analogous to those on Ganymede have not been found on Callisto" (Woronow and Strom, 1981). Figure 9 show examples of palimpsests on Ganymede and analogous features on Callisto in similar resolution images. Although the palimpsests on Callisto are generally more diffuse and irregular than those of Ganymede, the

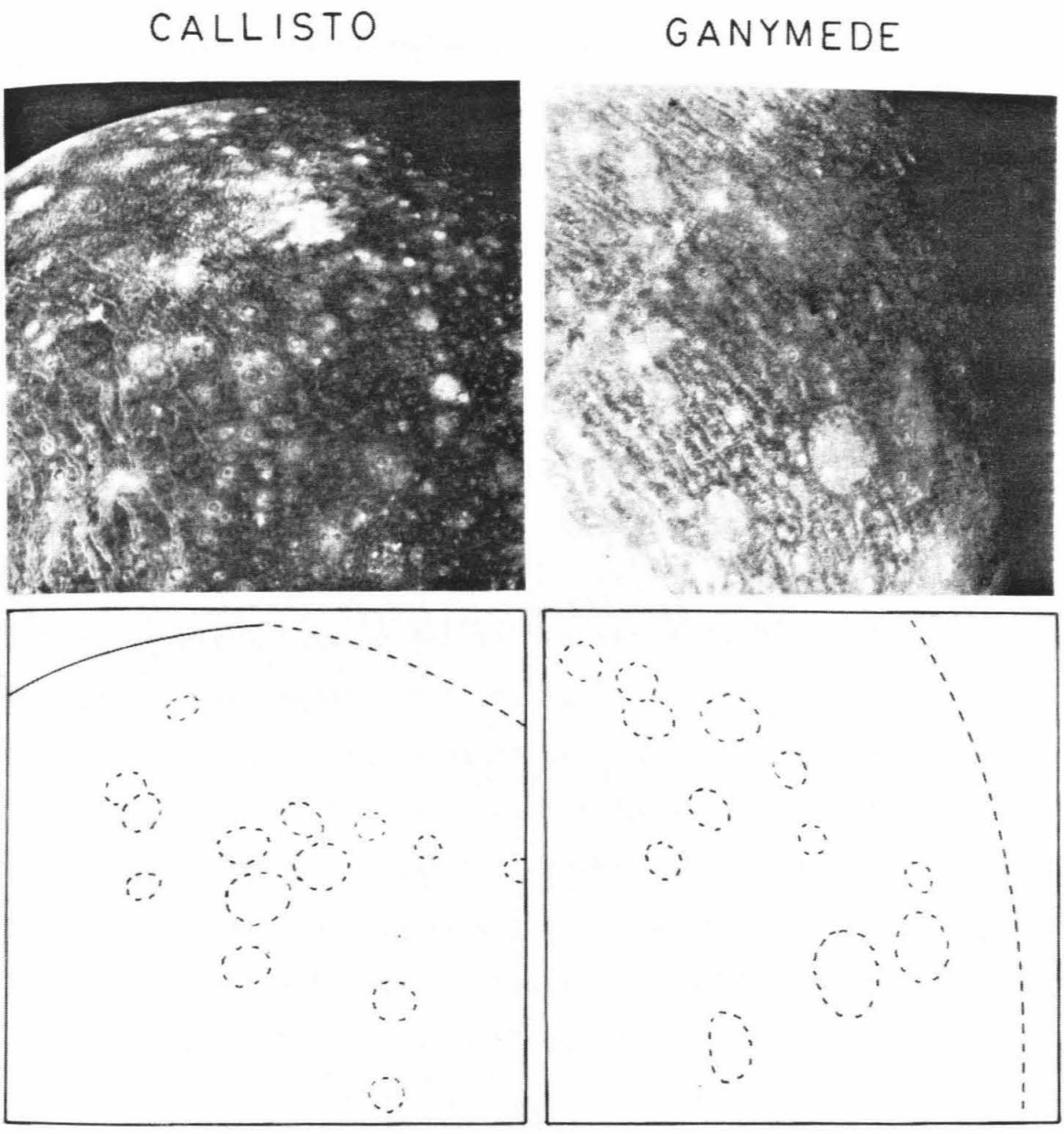

FIGURE 9 – Palimpsests on Ganymede and Callisto are shown here. On Callisto several conspicuous high albedo patches, which are interpreted as palimpsests, are visible; these are marked in the accompanying sketch map. The image of Ganymede, at similar resolution, shows several palimpsests within the Galileo Regio. The palimpsests on Callisto are generally more subdued than those on Ganymede, but nevertheless are present (FDS 16418.54, 20631.11).

higher albedo patches are present. One easily recognized palimpsest on Callisto is the one located at the center of the Valhalla multiring structure (Figure 3).

Woronow and Strom (1981) have correctly shown that if one applies a lunar highlands-like size-frequency distribution of craters to Callisto and allows for the complete relaxation of some of the largest craters, one can match the observed size-frequency distribution of craters on Callisto, but the spatial distribution of the preserved craters will be dissimilar to that observed. They conclude from this that the observed crater population on Callisto did not result directly from a lunar highlands crater size distribution. This is indeed the case; the size distribution of impacting bodies on the Galilean satellites is definitely not the same as for the lunar highlands. The observed cumulative size-frequency distribution for craters that are less than 3.8 Gy old (i.e. those craters on the grooved terrain of Ganymede) is a power function with an exponential slope of -2.2 (Shoemaker et al., 1982). The average exponent for the lunar highland size distribution used by Woronow and Strom (1981) in their analysis is much less than this, ($\sim$-1.42 for craters 7 km to 112 km in diameter (Woronow, 1978)); it is not surprising, therefore, that a lunar highlands size distribution cannot explain the observed spatial distribution of craters on Callisto, even with the complete relaxation of some of the largest craters. The problem is to determine if a simple power law distribution with an exponential size index of -2.2 can result in the observed spatial distribution of craters observed on Callisto, if the oldest and largest craters of this distribution are allowed to flatten beyond recognition. It is important to note that there is considerable scatter in the the densities of craters observed over Callisto's surface (Figures 2, 5, and 6), and that some of this scatter is possibly due to regions where craters have been lost (as is probable in the region surrounding the Valhalla multiring struc-

ture).

Without detailed modelling of the spatial distribution of craters, as was done by Woronow and Strom (1981), it is difficult to make any definite statements, from the observed distribution of crater sizes, about what the size distribution of impacting objects was prior to ~3.8 Gya, if it is accepted that many of the oldest large craters have flattened beyond recognition. Extending the observed size distribution for the craters on the grooved terrain of Ganymede (and for the bright ray craters) backward in time is probably the best estimate without proposing an *ad hoc* size distribution for the earlier impacting bodies. In this paper it will be assumed that the size index of -2.2 can be extended back to include all of the preserved cratering record. This assumption allows for the direct comparison of retention ages for craters of various diameters. This, in turn, provides a method for estimating the amount of time it takes a given diameter crater to flatten beyond recognition.

Crater retention for various diameter crater populations

The calculated model ages from various diameter crater populations as a function of distance from the apex (β) are shown in Figures 10 and 11. These figures were constructed assuming that the ratio of the cratering rate at the apex versus the cratering rate at the antapex is 9.6:1 . As the diameter of the smallest crater in a given crater population increases (e.g. $\geq$ 30 km versus $\geq$ 50 km), the corresponding *crater retention age* generally decreases. Again, these ages refer to the age at which the surface began retaining craters, of a given diameter range, to the present. For the lithosphere near the antapex, the model crater retention age based on craters with diameters $\geq$ 10 km is 4.4 Gy; the model crater retention age determined from craters $\geq$ 30 km in diameter is 4.3 Gy, 4.2 Gy for craters $\geq$ 70 km in diameter and 4.1 Gy for craters $\geq$ 100 km in

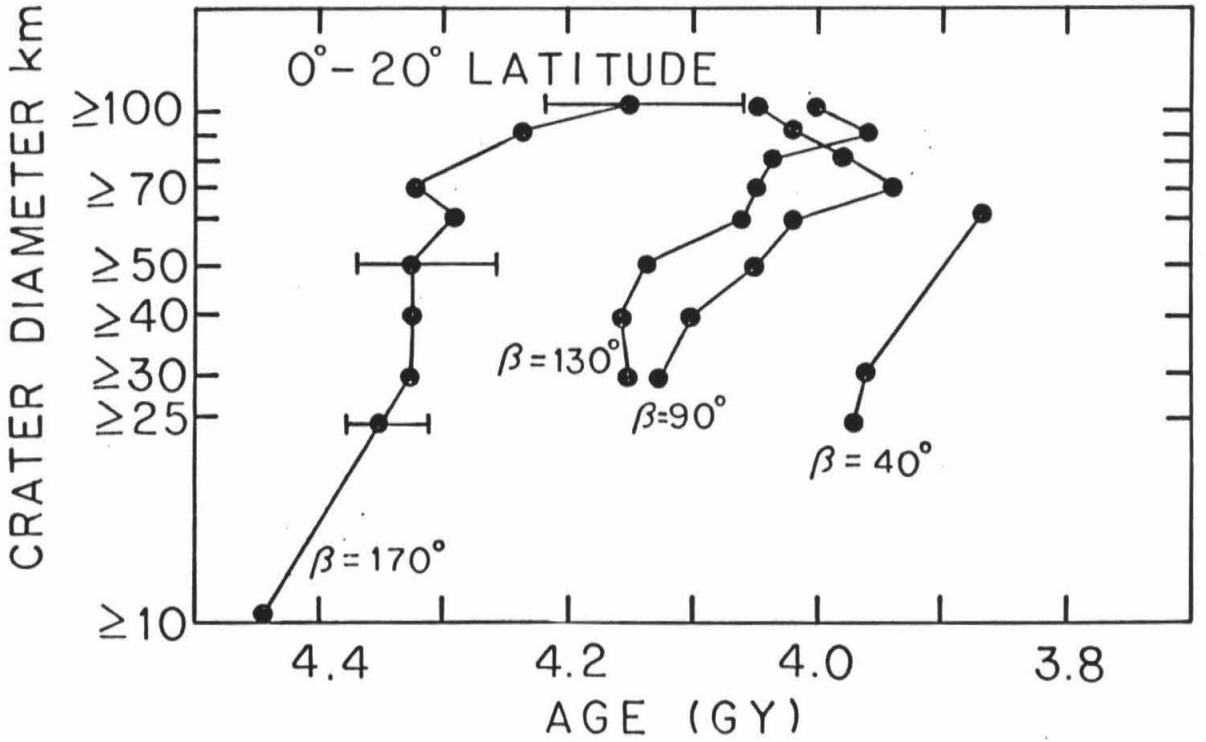

FIGURE 10 – Crater retention ages for various diameter crater populations in the 0° to 20° latitude band. β is the distance from the apex. Note that the model ages generally decline as larger diameter craters are used for the age determinations. This is interpreted as indicating that the larger craters were not retained in Callisto's lithosphere as early as were the smaller craters. The crater size index used here is -2.2, and the cratering rate at the apex was assumed to be 9.6 times that at the antapex.

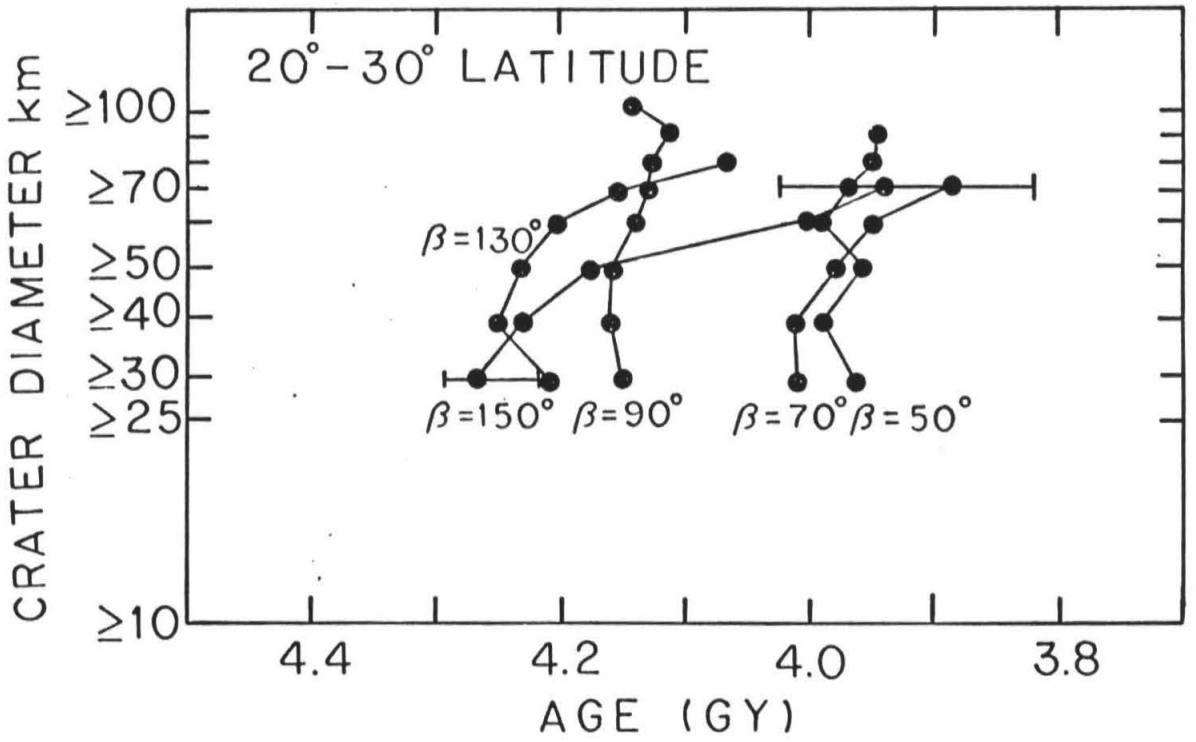

FIGURE 11 – Same as for Figure 10 except that this figure is for the 20° to 30° latitude band. The difference in age for the different diameter populations is not a pronounced as in Figure 10.

diameter. Near the apex, the crater retention ages based on craters with diameters ≥ 30 km is 4.00 Gy, 3.95 for craters ≥ 70 km in diameter and 3.90 Gy for craters ≥ 100 km in diameter. The model ages suggest that the lithosphere of Callisto could support craters ≥ 30 km in diameter approximately 300 My earlier near the antapex than near the apex; for craters ≥ 100 km in diameter, the difference in the crater retention ages between the apex and antapex is approximately 200 My. This implies that although the cooling of the lithosphere was delayed at the apex, when it did cool enough to retain craters, it cooled and thickened at a more rapid rate than at the antapex. Probably by ~3.7 Gy, the properties of the lithosphere of Callisto were more nearly globally uniform. From this time forward, craters in excess of about 200 km in diameter should still be recognizable; but, none have formed since that time. Note that at around 4.0 Gy the lithosphere in the leading hemisphere ($\beta < 90°$) would not retain craters ≥ 100 km in diameter as is indicated by 100 km crater retention ages of less than 4.0 Gy; this is the approximate time of the formation of the Valhalla multiring structure (basin diameter > 300 km) and none of the original topography of the central basin remains. If an impact of this magnitude occurred after about 3.7 Gya, at least remnants of the original basin relief probably would be preserved today. For comparison, the ~550 km diameter Gilgamesh basin on Ganymede is approximately 3.5 Gy old, and it has retained much of its original topographic relief (Shoemaker et al., 1982).

Although there is an observed increase in crater density toward the poles (Figure 5), most of this effect is a result of including the regions occupied by the multiring structures, of low crater density. In order to study any latitudinal dependence of crater density not related to the crater depleted multiring structures, it is necessary to look at regions well away from the Valhalla and Asgard

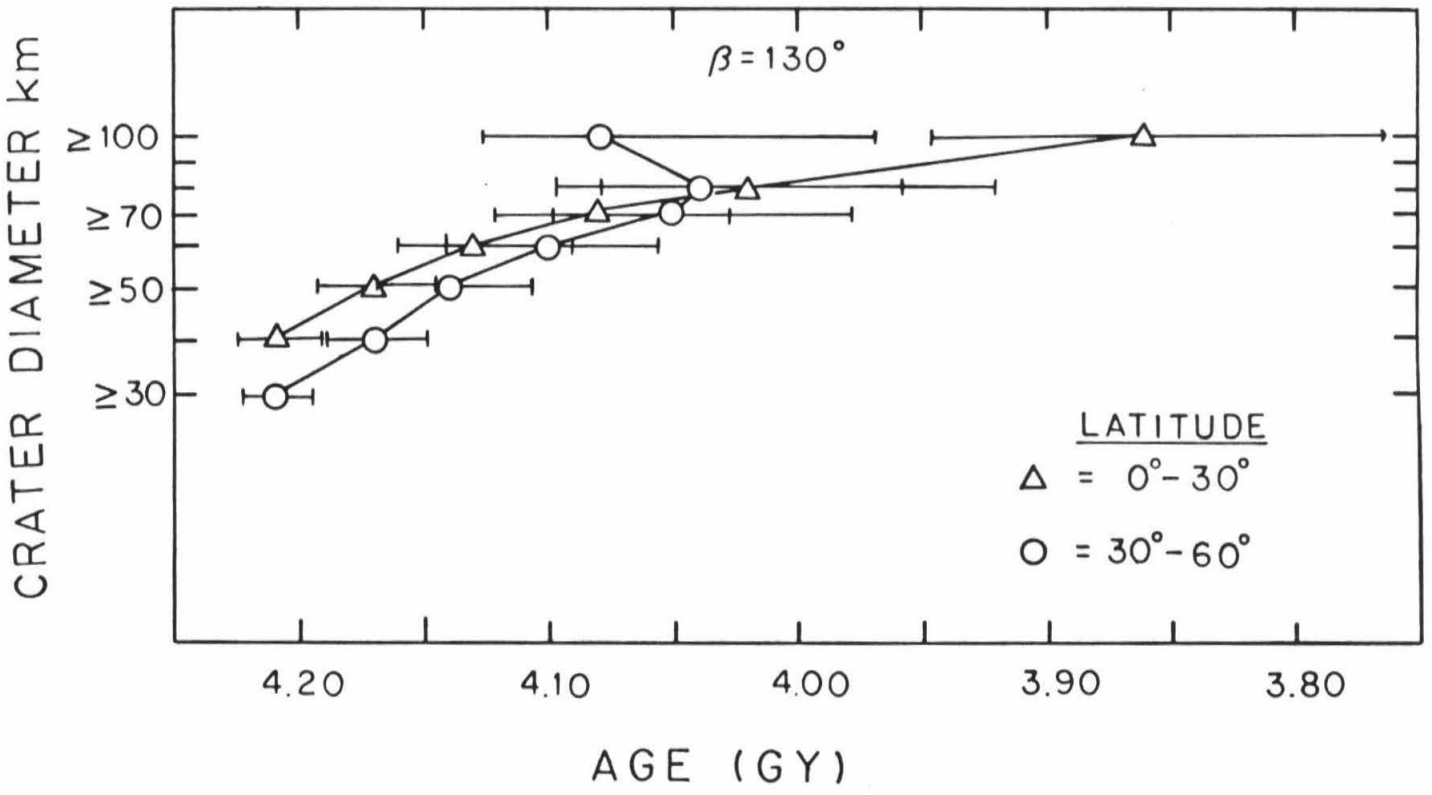

FIGURE 12 – Crater retention ages for various diameter crater populations for two different latitude bins is shown here. With the exception of the largest crater diameters, the crater retention ages appear to have no distinct latitudinal dependence. The craters used for this figure are all between 120° and 140° (i.e. β = 130°) from the apex; this was chosen to avoid the effect from any multiring structure.

structures. Ideally it would be best to look at regions at the poles and compare them to regions near the equator, but both of the polar regions are ~90° from the apex of orbital motion (β=90°), and the corresponding equatorial regions at β = 90°, for which high resolution coverage exists, is well within the region occupied by the Valhalla structure, and will be depleted in crater density. Thus, in order to look at latitudinal age variations, it is necessary to compare areas (at a given β) that do not include the extreme polar regions, with areas (at the same β) but located at equatorial latitudes. For this, regions that are 130° (120° to 140°) from the apex were chosen because these regions are well beyond the effects of the multiring structures (Figure 12); the ages of the surface between 0° to 30° latitude are not significantly different than the ages of the surface between 30° to 60° latitude, except for craters ≥ 100 km in diameter, and even for these craters the difference is not very significant. Crater retention ages of surfaces 60° to 90° latitude are not shown because no surface with β = 130° exists at latitudes higher than ~60° latitude. Areas with values of β less than ~130° from the apex will all be influenced by the Valhalla multiring structure at low latitudes, and areas with β greater than ~130° from the apex, have a smaller possible range in latitude covered.

POSSIBLE CRATER REMOVING MECHANISMS

It has been shown that Callisto's surface, which is made up of only one major type of terrain (in contrast to Ganymede which has at least two significantly different types of terrain), has a great diversity in both crater density and model crater retention ages. Possible explanations for the observed regional variations in crater density and model age include (1) regional variation in the cooling history of the lithosphere, (2) the formation of large multiring structures and palimpsests that locally reduce the crater density by smothering craters

beneath ejecta, or by introducing possible temporary thermal perturbations in the lithosphere, and (3) the thermal effects of an insulating regolith. Each of these will be discussed in detail in the following sections in light of the data that have been already presented.

Formation of large multiring structures

Large multiring structures result in the lowering of the local crater density over a region much larger than is occupied by the basin and its ejecta deposit (i.e. the central palimpsest). Even though the entire structure is, presumably, of a single age, some mechanism has resulted in a variation in crater density, of a factor of three, from the center of this structure to its outer ring sets. Secondary cratering cannot directly explain this phenomenon because, as is found with craters on the Moon, the number of secondary craters falls off with increasing distance from the center of the primary crater (Shoemaker, 1962); the opposite of what is observed.

Basin and continuous ejecta deposit

Assuming that the Valhalla multiring structure is the result of a very large impact, a large topographic basin must have been present, at one time, at its center; any pre-existing craters immediately beneath the impact would be obliterated during the basin excavation stage. Huge amounts of lithospheric material would be thrown out, and much of this would fall back as an ejecta deposit, just beyond the basin rim. Any pre-existing craters in the region of the continuous ejecta deposit would probably be completely burried by this deposit. If the Valhalla palimpsest represents the region occupied by both the original basin and its continuous ejecta deposit, then any visible evidence for pre-existing craters in this region should have been completely destroyed or burried. The observation that the lowest crater densities are found near the center

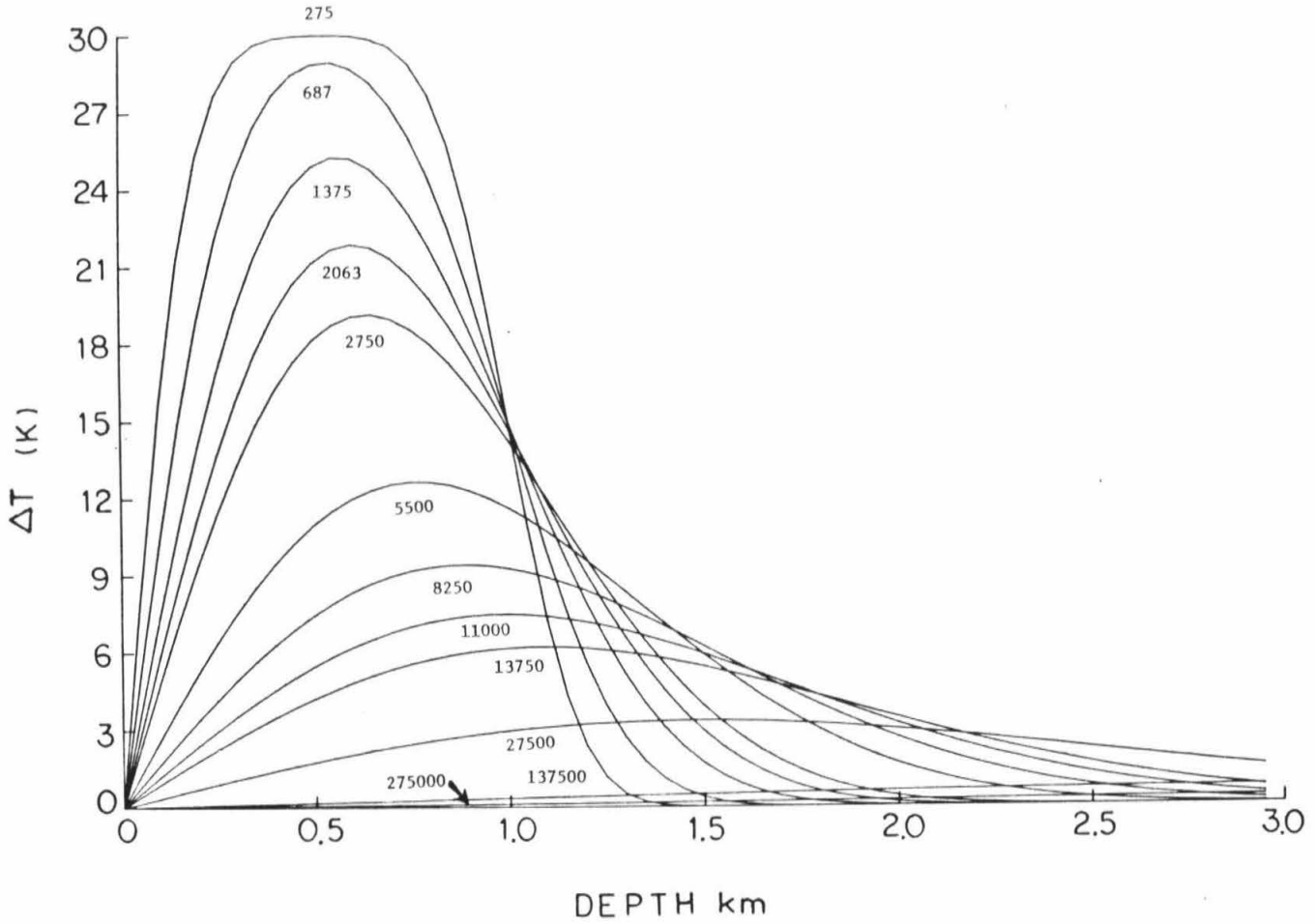

FIGURE 13 – The theoretical one-dimensional heat flow from a 1 km thick heated ejecta deposit, at initial temperature of 30K above the underlying lithosphere (ΔT = 30K), is shown in this figure. The different curves are for different times, in years, after the deposition of the ejecta. The top surface of the ejecta deposit (Depth = 0) was maintained at ΔT = 0. The lithosphere is depths > 1.0 km.

of the Valhalla structure and on the central palimpsest (Figure 4), supports the idea that these craters represent post-Valhalla impacts, and that any pre-Valhalla impact craters have been destroyed or burried. This mechanism adequately explains the observed low density of craters near the center of the Valhalla structure, but fails to explain the gradational increase in crater density with increasing radial distance from the center out to ~1800 km.

Thermal perturbations induced by large impacts

Because the viscosity of water ice (presumably the predominant material in the lithosphere of Callisto) is a strong function of temperature, and because viscous relaxation of crater relief has probably played an important role in the surface evolution of Callisto, the thermal effects induced by large impacts will now be studied in an attempt to explain the observed distribution of craters over the Valhalla structure.

Most of the lithospheric material excavated during the formation of the Valhalla basin was probably shock heated. The deposition of this heated material on the surface would result in the raising of the temperature and the resulting lower effective viscosity at the top of the underlying lithosphere, until the temperature of the ejecta equilibrated with that of the surrounding terrain. If it is assumed that the heated ejecta is ~1 km thick and that the mean temperature of the ejecta is ~30K warmer than the underlying lithosphere, then the cooling of the ejecta deposit and of the underlying material can be calculated (Jaeger, 1961). The history of the temperature profile in a heated ejecta deposit and underlying bedrock is shown in Figure 13; this figure was constructed assuming that the thermal diffusivity for ice is 0.0115 cm^2 sec^{-1} (Carslaw and Jaeger, 1959), and that the free surface, at $D=0$, was maintained at $\Delta T=0$, where D is the depth below the top of the ejecta deposit, and ΔT is the temperature

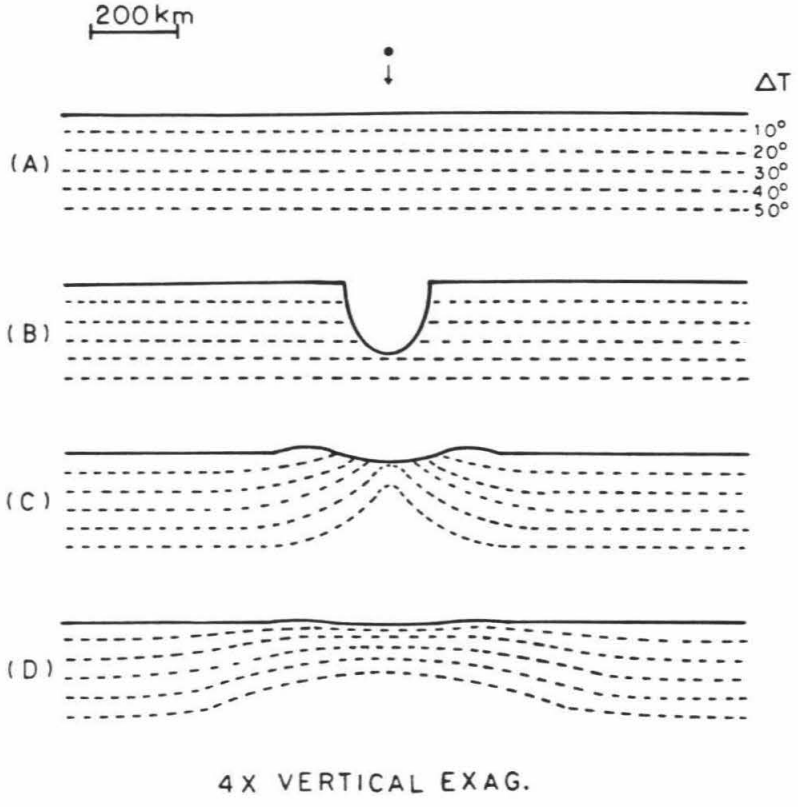

FIGURE 14 – Schematic diagram of how the formation of an impact basin the size of Valhalla might have resulted in the formation of a temporary "hot spot". (a) For this figure it is assumed that the thermal gradient was ~1 K/km; the values of the isotherms would be doubled if the thermal gradient were 2 K/km; (b) an original basin 200 km in diameter would have a transient cavity approximately 40 km deep; (c) the basin would immediately collapse from the transient cavity stage and the diameter would be enlarged by the collapse of the basin walls (new diameter assumed to be ~300 km). This rapid collapse would result in the bowing up of the isotherms directly beneath the basin and the production of a temporary "hot spot". (d) After a given time, the "hot spot" would cool by heat loss at the top of the lithosphere, thus approaching the thermal conditions in the lithosphere that existed prior to the impact.

difference above the equilibrium temperature (i.e. the temperature due to insolation). For this example, it would take ~275,000 years before the ejecta blanket would cool to near the equilibration temperature $\Delta T = 0$. The top ~2 km of the underlying lithosphere would experience a temperature increase of between 3 and 10 K, that would last approximately 10^5 years. Using an average ΔT of 5K would result in a lowering of the viscosity at the top of the icy lithosphere of approximately one order of magnitude. This, in turn, would result in an increase in the rate of topographic relaxation of pre-existing craters beneath the ejecta, of ~10 times during the 10^5 year period, until the ejecta temperature reaches equilibrium. Thus, any craters covered by the ejecta that were not completely burried, would tend to disappear by relatively rapid viscous relaxation of topography. This mechanism would be most effective near the center of the Valhalla structure within the region of the central palimpsest.

Examination of the lateral (radially outward) heating resulting from the emplacement of a warm ejecta deposit, that is ~1 km thick, indicates that this mechanism is insufficient to result in significant heating of the surrounding terrain to affect the rate of relaxation of any craters beyond beyond the edge of the continuous ejecta deposit (palimpsest).

Possibly the Valhalla impact resulted in the formation of a temporary "hot spot" in Callisto's lithosphere, as is illustrated in Figure 14. Because no topographic basin is currently preserved at the center of the Valhalla, it is plausible to imagine that very soon after the transient cavity was formed, it immediately collapsed to near its present state. The collapse may have taken much longer, but if most of the collapse occurred within a few thousand years after formation, the collapse would result in the temporary updoming of the isotherms (as shown in Figure 14c); this is because a few thousand years is a much shorter

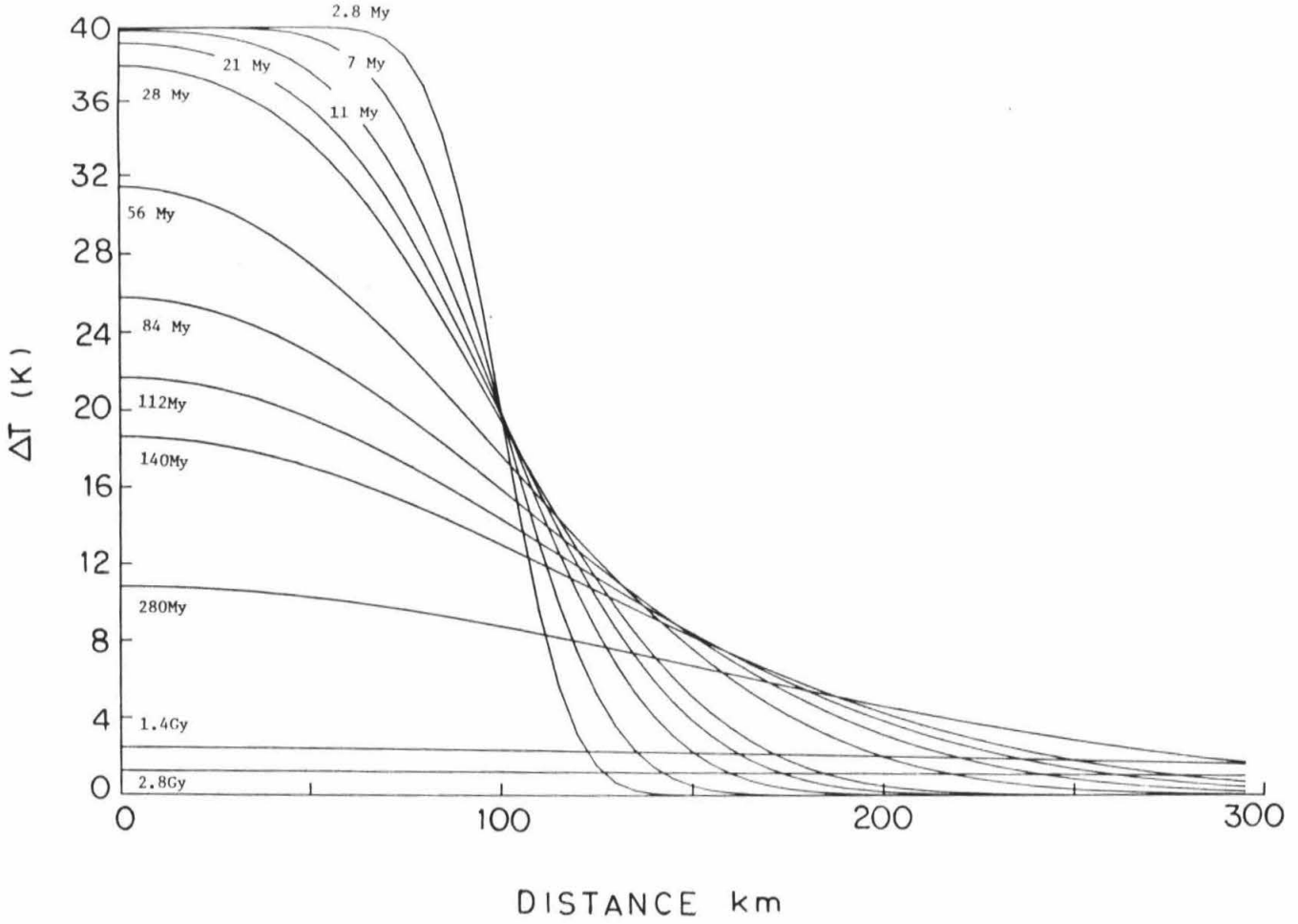

FIGURE 15 – The theoretical one dimensional heat flow from an infinitely long hot cylinder is shown in this figure as a function of the time, in years. The initial radius of the cylinder is assumed to be 100 km, and the initial temperature is 40K above the surrounding lithosphere.

time period than is required for the raised isotherms to equilibrate. If the material within the transient cavity was substantially shock heated, as it must have been, then the upbowing of the isotherms would be enhanced. In either case, relatively warm ice would be located near the surface until the lithosphere could equilibrate.

To see if the upbowing of the isotherms can result in a significant reduction in the density of craters on Valhalla, the following thermal model will be studied. As a limiting case, the upbowed isotherms will be modelled as a vertical cylinder (Lovering, 1935; Mundry, 1968); for this limiting case we will look only at the one dimensional lateral heating and ignore the heat loss through radiation at the surface and by convection at the base of the lithosphere (i.e. an infinite hot column)(Figure 15). Assuming that this column has an initial temperature 40K above the surrounding lithosphere (in agreement with Figure 14c), and that the diameter is 200 km (corresponding to a original basin diameter of ~400 km), then by ~300 My, the lithosphere, out to a distance of ~250 km from the center (i.e. within the the current palimpsest), would experience a temperature increase of about 10K. The lithosphere beyond about 300 km from the center of the original impact basin (beyond the palimpsest) would be relatively unaffected. If it is assumed that the Valhalla palimpsest (~600 km diameter) represents the original basin then the region affected by the upbowing of the isotherms would be within about 900 km from the center of the basin, but the time scale for cooling would be much longer (i.e. by a factor of 9). Thus, even though this mechanism can affect regions beyond the original basin and ejecta deposit, it fails to affect regions out to ~1800 km from the center, as is observed in the crater densities (Figure 4); the efficacy of this model would be severely reduced if surface radiation and convection within an asthenosphere were

included.

A possible deep subsurface effect that might be more significant would be the lateral transport of heat by convection in the asthenosphere beneath a hot spot formed at the time of the Valhalla impact. If a permanent hot spot were established in the lithosphere above a convection plume, by whatever mechanism, then the thermal gradient in the entire region surrounding the hot spot would be increased. If the rate of the convection were slow in comparison to the rate of heat conduction to the surface, then the lateral heating away from a concentrated hot spot would not be significant over radial distances much greater than the thickness of the conducting plate (lithosphere); for Callisto, the thickness of the lithosphere at the time Valhalla formed has been estimated to be between 20 and 50 km thick (McKinnon and Melosh, 1980), and, thus, the radial conduction of heat away from the hot spot would be effective over a region approximately 50 to 100 km from the edge of the hot spot. If, on the other hand, the rate of asthenospheric convection was fast in comparison to the rate of heat conduction to the surface, then the size of the hot spot would be larger because of the spreading out of the plume at the base of the lithosphere, but the thermal gradient in the hot spot would be less than for a smaller hot spot in order to conserve the net heat flux from the deep interior; so the effective lateral heating could be approximately the same as for the concentrated hot spot. In either case, the magnitude of the radial heating is probably too low by an order of magnitude to explain the apparent loss of craters at a radial distance of about 1800 km from the center of Valhalla.

Formation of a regolith

Another very important by-product of both primary and secondary cratering is the production of a regolith (Shoemaker et al, 1982). The effect of an

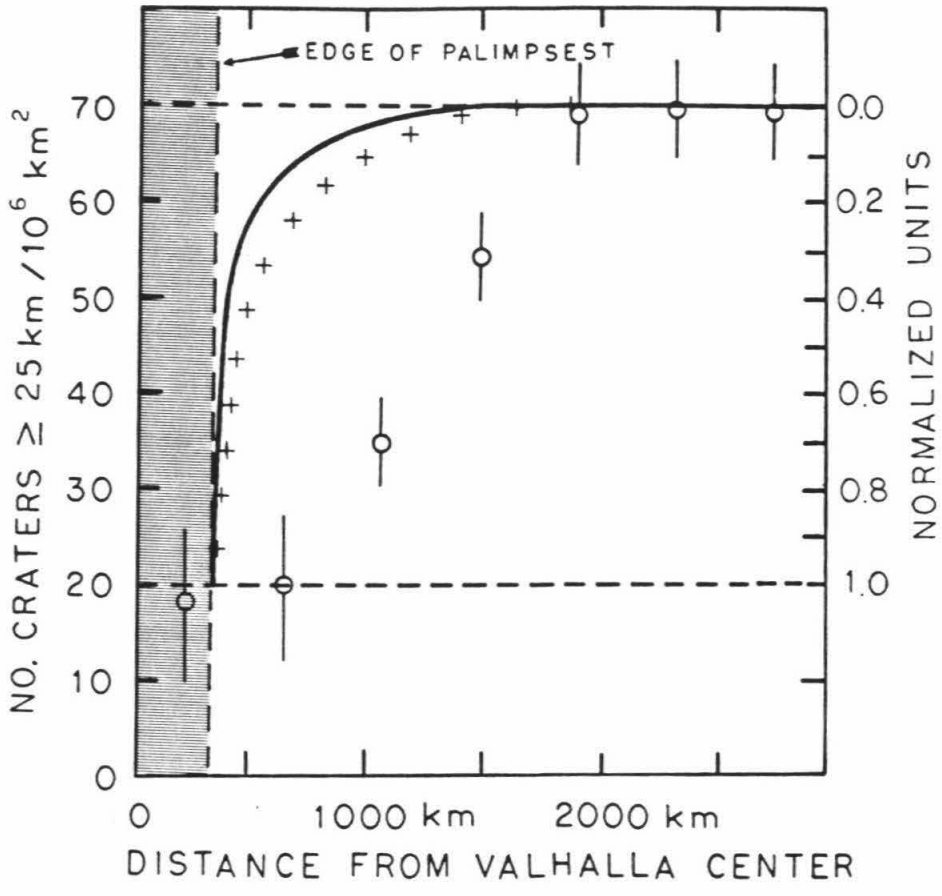

FIGURE 16 – The frequency distribution of secondary craters, beyond the Valhalla palimpsest, is shown by the +'s (refer to the right hand scale), modeled after that found around the lunar crater Copernicus (Shoemaker, 1962). If it is assumed that the thickness of the regolith produced by the secondaries is proportional to the spatial density of secondary craters, then the regolith thickness, beyond the Valhalla palimpsest, as a function of distance is illustrated by the heavy solid line (refer to the right hand scale); also shown by the open circles are the data for the distribution of craters within the region occupied by the Valhalla multiring structure (refer to the left hand scale) (see Figure 4).

insulating regolith on the rate of crater relaxation is much like that of the emplacement of warm ejecta deposits except that the net effect is more enduring. The physical and thermal properties of an icy regolith probably are similar to those of the silicate regolith found on the Moon (Shoemaker et al., 1982); if so, then the thermal conductivity of the icy regolith probably is several orders of magnitude less than for the solid icy lithosphere. Heat flow measurements within the lunar regolith, done during the Apollo 15 and 17 missions, indicate that the regolith conductivity is between 1.5×10^{-4} and 3×10^{-4} W cm^{-1} K^{-1} (Langseth, Keihm, and Chute, 1973). These values are approximately 2 to 3 orders of magnitude less than for solid rock. The thermal gradient in the regolith must be inversely proportional to the conductivities K under conditions of equilibrium heat flow, (e.g. if K(Lithosphere)/K(Regolith) = 10^3, a thermal gradient of 1 K/km in the lithosphere would correspond to a thermal gradient of ~ 1000 K/km in the regolith). If the thermal gradient on Callisto ~4.0 billion years ago was several degrees per km in the lithosphere, a regolith a few meters thick will result in a rise in temperature from the top to the base of the regolith of, possibly, several tens of degrees, depending on the thickness of the regolith. Moreover, this rise in temperature at the top of the subsurface solid lithosphere will lower the viscosity at that point as much as two orders of magnitude from what it would be if no regolith was present (Passey and Shoemaker, in preparation). This will result in a much more rapid rate of flattening of craters than would be predicted if no regolith layer were present.

An attempt to quantify the effect of a regolith layer in explaining the observed distribution of crater densities on the Valhalla multiring structure (Figure 4) follows. The basic assumptions used here include (1) the thickness of the regolith is proportional to the spatial density of secondary craters, (2) the

distribution of secondary craters surrounding the Valhalla palimpsest is similar to that surrounding lunar craters, (3) the density distribution of pre-Valhalla craters within the region now occupied by the Valhalla multiring structure was uniform, and (4) the spatial density of post-Valhalla craters is uniform over this structure and the density is the same as observed on the Valhalla palimpsest.

Modelling the frequency distribution of secondary craters around the Valhalla palimpsest (> 300 km from the center of the structure) after that observed beyond the continuous ejecta deposit of Copernicus, on the Moon (Shoemaker, 1962) results in the pattern shown by the crosses (+) in Figure 16. Correcting the secondary crater frequency to a spatial crater density, and assuming that the mean thickness of the freshly formed regolith, averaged over the area covered, is proportional to the crater density, the predicted new regolith thickness as a function of range from the Valhalla palimpsest is shown by the heavy solid line in Figure 16. From the original basin rim to about 300 km from the center, the region was buried completely by a warmed ejecta deposit and is shown by the shaded region. Beyond the continuous ejecta blanket, secondary craters are always distributed in rays. The rays cover progressively less surface area as distance from the crater or basin increases; hence, although the mean thickness of the new regolith decreases, the actual thickness does not change much, but the proportion of the surface covered goes down. Because the data presented in Figure 4 are averaged over relatively large annuli within the Valhalla structure, the spatial resolution is not sufficient to resolve the rays and secondary craters; so, even though the actual thickness of the new regolith remains about the same, because of the decreasing area covered by the new regolith, the problem will be treated here as if the effective thickness of the regolith decreases with increasing radial distance (as shown by the heavy solid

line in Figure 16).

In order to measure any quantitative effect of an insulating regolith, we must determine the thermal properties of such a regolith. Studies of the thermal inertia of the surface of Callisto and Ganymede (Hansen, 1973; Morrison and Cruikshank, 1973) reveal that the uppermost surface layer has an extremely low thermal inertia. This layer has been interpreted as consisting of loosely stacked fine particulate material. Calculations of the conductivity K of this uppermost layer by Hansen (1973) indicate a value of 4 μW cm^{-1} K^{-1}; using K = 2 to 4 x 10^{-2} W cm^{-1} K^{-1} for solid ice (Carslaw and Jaeger, 1959), the ratio of the conductivity of the uppermost regolith, K(R) to that of the lithosphere, K(L), is approximately $10^{-4} : 1$.

As is discussed in Shoemaker et al. (1982), it is reasonable to expect that the conductivity of an icy regolith increases with depth, owing to decrease of pore space, increase in density, and cementation of grains. The increase of conductivity with depth was observed in the case of lunar regolith (Langseth et al., 1973). The measured conductivity of the lunar regolith is several orders of magnitude less than for bedrock, and this difference in thermal conduction probably exists even near the base of the regolith; this is probably not the case with an icy regolith, however. Shoemaker et al. (1982) have pointed out that the survival of many craters on Ganymede at equatorial latitudes precludes a regolith that is similar to the lunar regolith in all respects; this is because a very thick regolith at equatorial latitudes would produce a temperature offset across a regolith that would result in the lowering of the effective viscosity of the near surface lithosphere to the degree that no craters > 10 km in diameter would be preserved against complete relaxation by viscous flow in the lithosphere. They suggest that the depth to the base of the effective regolith is controlled by an

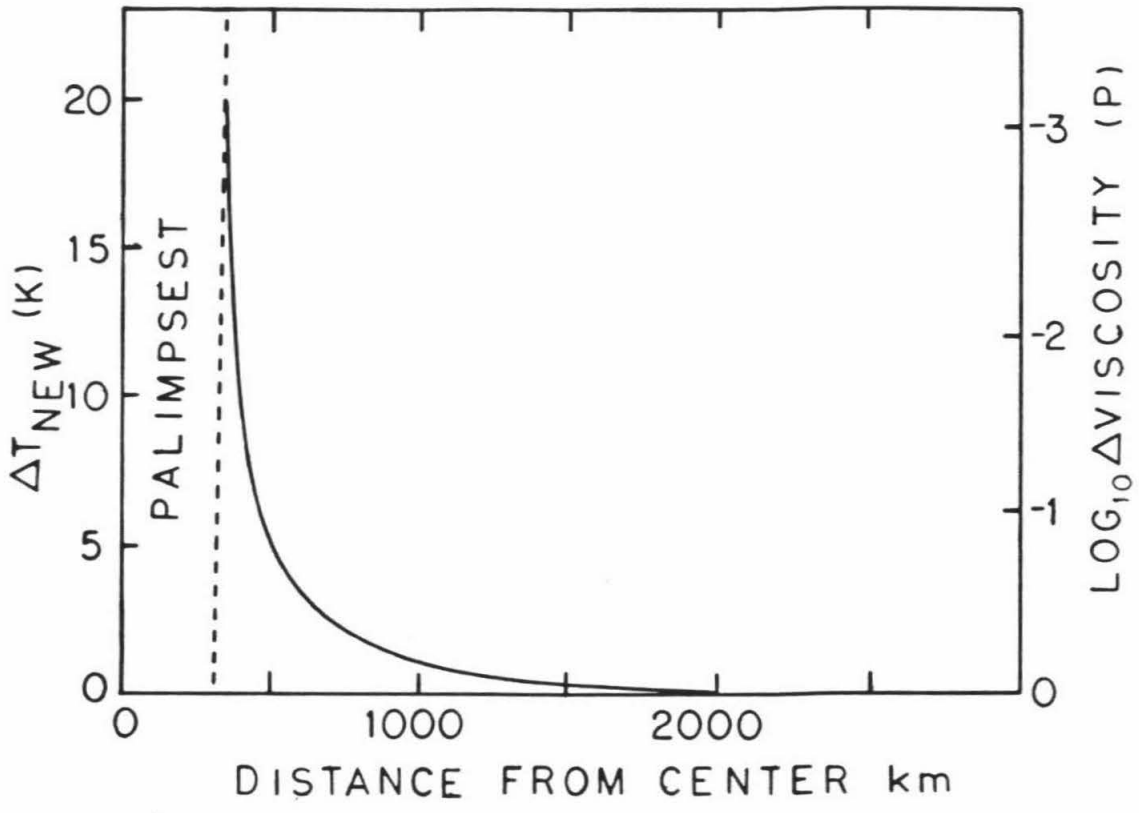

FIGURE 17 – The change in temperature ΔT_{NEW} due to the presence of an insulating regolith is shown as a function of the distance from the center of Valhalla. Also shown is the change in viscosity at the top of the lithosphere. The new regolith is assumed to have an additional thickness Δh of 20 meters, a thermal conductivity of 2×10^{-3} that for the lithosphere, and a thermal gradient in the lithosphere, at this time, of 2 K/km.

isotherm rather than the depth to the ungardened bedrock. Where the temperature at the base of a regolith layer exceeds this threshold temperature, the ice would tend to sublime near the base and be redeposited at higher cooler levels. Thus, the thickness of an insulating regolith could be controlled by this process of thermal annealing (Morrison and Cruikshank, 1973), with the thermal conductivity of the annealed regolith being essentially that of the ungardened lithosphere or bedrock. The deeper annealed regolith then becomes "bedrock". Shoemaker et al. (1982) suggest that the annealing temperature for an icy regolith is ~130 K; this in accordance with analysis of the transport of water vapor as a function of temperature by Purves and Pilcher (1980) and Squyres (1980).

For the regolith model considered here, it is assumed that a regolith exists on the lithosphere at the time of the formation of Valhalla; this pre-Valhalla regolith will be assumed to be thick enough to be thermally annealed at the base. A simple two layer model for the pre-Valhalla regolith will be used here; the top layer is assumed to have a conductivity 10^{-4} that of polycrystalline ice, in agreement with thermal inertia measurement of Ganymede by Hansen (1973), and the lower layer is assumed to have a conductivity 2×10^{-3} that of solid ice. The temperature offset ΔT across the regolith can be expressed as

$$\Delta T = \frac{\delta T}{\delta Z}[10^4 h_u + 5\times10^2 (h - h_u)] \qquad (5)$$

where h is the total thickness of the unannealed regolith, h_u is the thickness of the upper layer, and $\delta T / \delta Z$ is the thermal gradient in the lithosphere at the time of the formation of Valhalla; from studies of the relaxation of craters on Callisto, the value for $\delta T / \delta Z$ is ~2 K/km (Passey and Shoemaker, in preparation).

Two possible cases for the thickness and ΔT across the pre-Valhalla regolith

exist. For the first case (Case 1), the regolith is assumed to be thermally annealed at a depth corresponding to the 130K isotherm when Valhalla formed; thus

$$\Delta T = (Annealing\ temperature) - (Surface\ temperature) = 130-120 = 10K.$$

Using $\delta T/\delta Z$ = 2 K/km, the thickness h would be ~6 meters. For the second case (Case 2), the regolith is assumed to be thermally annealed at a depth that corresponded to the 130K isotherm when $\delta T/\delta Z$ was much higher at a time in the past than at formation of Valhalla (i.e. a fossil isotherm); for this case, the temperature offset across the regolith (ΔT) would probably be between 2.5 and 10 K, the lower limit is based on a thermal gradient of ~5 K/km with only the top (0.5 meter thick) layer of the regolith preserved. For case 2, the total thickness h of the pre-Valhalla regolith is from 0.5 to 6 meters.

We now need to consider what effect the formation of a new regolith on a pre-existing regolith would have on the temperature at the top of the lithosphere. If we assume that the effective thickness of the new regolith, formed by Valhalla secondaries, thins with increasing distance from the center of Valhalla (Figure 16), then the additional temperature offset across the new regolith ΔT_{NEW} will also decrease with increasing distance. Assuming that the new regolith can be approximated by a two layer model, it is possible to estimate the additional temperature offset. The formation of the new regolith will involve the mixing up of, at least the top layer, of the pre-Valhalla regolith, and assuming that the thickness of the top low thermal conductivity layer remains constant, the formation of a new regolith on a pre-existing one can be simply modelled as an increase in thickness of the lower layer; this increase will be designated as Δh. If the increase in regolith thickness Δh, due to secondary cratering from Valhalla, is ~

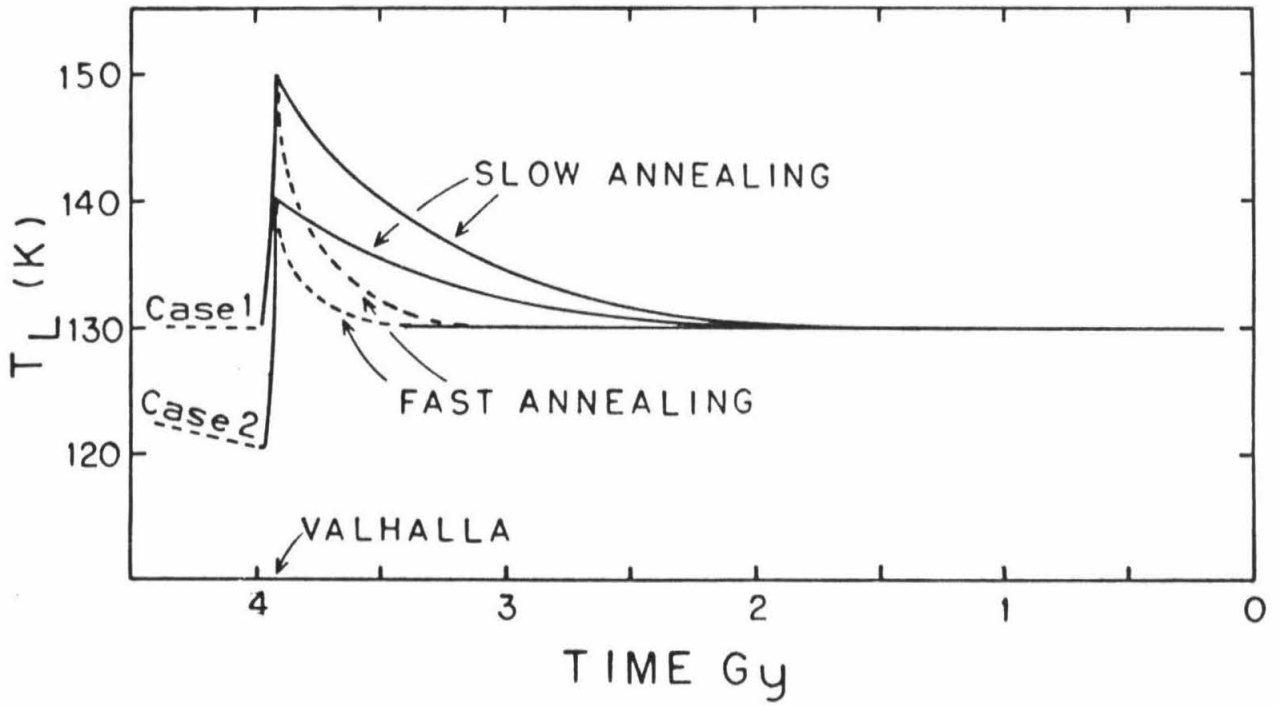

FIGURE 18 – Possible histories of the temperature at the top of the lithosphere, beneath the Valhalla structure, is shown here for two different cases for the pre-Valhalla regolith. See the text for the discussion of the two cases. Also shown are two cooling curves for the lithospheres assuming that the rate of thermal annealing at the base of the regolith is "fast" and "slow", respectively for the two cases; no quantitative assessment for the annealing rates is used here. For the case of "slow" annealing, the temperature at the top of the lithosphere will be maintained relatively high for considerable time; the "fast" annealing is probably the more realistic of the two choices, however.

20 meters, then this corresponds to ΔT_{NEW} = 20K, using $\delta T / \delta Z$ = 2 K/km; similarly Δh = 5 meters would correspond to ΔT_{NEW} = 5K.

Using the mean regolith thickness averaged over the area covered, the additional temperature offset across the new regolith ΔT_{NEW}, as a function of distance, follows the heavy solid line in Figure 16; using Δh = 20 meters, the temperature offset ΔT_{NEW} across the new regolith over the Valhalla structure is shown in Figure 17, in addition to the corresponding change in viscosity at the top of the lithosphere (based on a temperature viscosity relationship discussed in Passey and Shoemaker, in preparation). Although the additional temperature offset at a distance of ~ 1000 km from the center of Valhalla is only a few degrees K, because of the exponential dependence of the viscosity on temperature, the mean change in viscosity at the top of the lithosphere can be significant at that distance. By lowering the viscosity at the top of the lithosphere by a factor of 10, the rate of crater flattening will also increase by a factor of 10. Thus, the observed decrease in crater density with increasing distance from the center of Valhalla might reflect the nonuniform loss of craters, by relatively rapid viscous relaxation; craters near the outer edge of this structure (~ 1800 km from the center) do not have a significant offset in temperature and, thus, craters located here will not relax as rapidly.

For the case of the pre-Valhalla regolith annealed at a depth corresponding to the 130K isotherm (case 1), there will be a race against time to collapse the craters before the regolith is thermally reequilibrated by reannealing (Figure 19). the effectiveness of the crater relaxation mechanism in explaining the distribution of craters on Valhalla, will depend on the rate of crater relaxation versus the rate of regolith annealing. For the case of the annealed "fossil" isotherm (case 2), the production of the new regolith will, again, temporarily raise

the temperature at the top of the lithosphere by a given amount, but in this case, the final equilibration temperature at the top of the lithosphere could be higher than it was before the formation of Valhalla; thus, the craters within this region will continue to flatten at rates considerably in excess of the rates before Valhalla was formed (Figure 18).

If the viscous relaxation of craters within the Valhalla structure has been important, it would be expected than this effect should show up in selective erasure of the larger pre-Valhalla craters. It is observed that the craters in this region have a steeper cumulative size index than do craters on Ganymede's grooved terrain (-2.6 compared to -2.2 for the grooved terrain); this indicates a possible loss of some of the larger craters, but it is difficult to assess the loss of large craters as compared to the preservation of small craters near the center of this structure because the regions near the center are near the subsolar point, and small craters ($\leq$ 15 km) are difficult to identify.

It is, therefore, proposed that the observed decrease in crater density toward the center of the Valhalla structure might be a result of the flattening of craters, by viscous relaxation of topography, to a point where the relief is too low for recognition. Most of the loss of craters, however, should occur within ~ 1000 km from the center of Valhalla. Regions of local flooding, described by Remsberg (1981), could also substantially lower the crater density on Valhalla (possibly by ~10% to ~30%); this is because the regions of flooding are primarily located between ~ 500 and ~ 1500 km from the center of Valhalla, and the flooded zones occupy between 10 and 30 percent of this area. Thus, the decrease in craters within Valhalla probably reflects (1) mechanical obliteration beneath the original basin, (2) burial beneath the continuous ejecta deposit, (3) viscous relaxation of craters beneath a newly formed insulating regolith, and (4)

the flooding of regions adjacent to the ring scarps.

As is discussed by Shoemaker et al. (1982) the regolith on the leading hemisphere of Ganymede would be thicker at any given time than that on the trailing hemisphere because of the higher production of primary craters and resultant higher rate of regolith production; this would also probably be true for Callisto. This implies that if the heat flow is globally uniform, then at any given time and latitude, the temperature at the top of the lithosphere could be higher in the leading hemisphere, and thus the viscosity lower, than at a corresponding latitude on the trailing hemisphere. If there is already an equilibrium regolith, the effect depends on the rate of regolith buildup on newly formed craters. This tends to make the rate of crater loss proportional to crater production, and would result in a more nearly uniform crater retention over different longitudes, so long as the thermal gradient is high enough; but there should be significant latitude dependence. This effect could result in the rough global distribution of model ages for Callisto's surface shown in Figures 7 and 8 where the crater retention ages of leading hemisphere are maintained younger by more rapid flattening and loss of craters in a lithosphere that is warmer as a result of a thicker insulating regolith.

SUMMARY AND CONCULSIONS

From the analysis of over 2200 craters ≥ 25 km in diameter, it is revealed that the surface of Callisto is not uniformly cratered. In the leading hemisphere, there is a concentration of the large multiring structures, as well as an overall depletion of craters; the depletion of craters is primarily due to the locations of the multiring structures which are relatively young and, thus, have low densities of superposed craters. The highest crater densities, however, are found in the leading hemisphere, but in regions not covered by the multiring

structures.

Application of a cratering model proposed by Shoemaker and Wolfe (1982) to the derived crater densities, suggests that the age of most of Callisto's surface is between 4.0 and 4.2 Gy. The large multiring structures are among the youngest features with ages ranging from 3.9 to 4.1 Gy; the oldest areas of Callisto's surface, based on statistics of craters ≥ 30 km in diameter, are between 4.2 and 4.4 Gy, and are located near the antapex of orbital motion.

The distribution of crater densities and model ages of surface regions on Callisto can be explained, primarily by two mechanisms: (1) the effects resulting from the formation of multiring structures (this exists regardless of the cause), and, (2) independently, the general production of an insulating regolith will have a global effect resulting in the faster relaxation of craters in the leading hemisphere. The other mechanisms discussed in this paper can be accounted for within mechanism (1).

REFERENCES CITED

Carslaw, H.S., and Jaeger, J.C. (1959) **Conduction of Heat in Solids,** Clarendon Press:Oxford, 510 p.

Davies, M.E., and Katayama, F.Y. (1980) Coordinates of features on the Galilean satellites, The Rand Corp., P-6479, June 1980, 37 p.

Hale, W.S. (1981) The Valhalla ring system on Callisto (abstract) *EOS, 62*, p. 318.

Hansen, O.L. (1973) Ten-micron eclipse observation of Io, Europa, and Ganymede *Icarus, 18*, p. 237-246.

Jaeger, J.C. (1961) The cooling of irregularly shaped igneous bodies, *Am. Jour. Sci., 259*, p. 721-734.

Langseth, M.G., Keihm, S.J., and Chute, L.L. (1973) Heat flow experiment, *Apollo 17 Preliminary Sci. Rept., NASA SP-330*, p. 9-1 to 9-24.

Lovering, T.S. (1935) Theory of heat conduction applied to geological problems, *Bull. Geol. Soc. America, 46*, p. 69-94.

McKinnon, W.B., and Melosh, H.J. (1980) Evolution of planetary lithospheres: Evidence from multiringed basins on Ganymede and Callisto, *Icarus, 44*, p. 454-471.

Melosh, H.J. (1982) A simple mechanical model of Valhalla basin, Callisto, *Jour. Geophys. Res., 87*, p. 1880-1890.

Melosh, H.J., and McKinnon, W.B., (1978) The mechanics of ringed basin formation, *Geophys. Res. Lett., 5*, p. 985-988.

Morrison, D., and Cruikshank, D.P. (1973) Thermal properties of the Galilean satellites, *Icarus, 18* , p. 224-236.

Mundry, V.E. (1968) Über die Abkehlung magmatischer Korper, *Geol. Jb.*, *85*, p. 755-766.

Passey, Q.R., and Shoemaker, E.M. (1980) Global distribution of craters and multiring structures on Callisto (abstract) *Bull. Amer. Astron. Soc.*, *12*, p. 712.

---------- (1981) Regional variation of crater density and model ages of Callisto's crust,(abstract) *Lunar and Planetary Science XII*, p. 816-818.

---------- (1982) Craters and basins on Ganymede and Callisto: Morphological indicators of crustal evolution, in **The Satellites of Jupiter,** D. Morrison ed., University of Arizona Press, Tucson.

---------- (in preparation) Thermal evolution of the lithospheres of Ganymede and Callisto.

Purves, N., and Pilcher, C.B., (1980) Thermal migration of water on the Galilean satellites, *Icarus*, *43*, p. 51-55

Remsberg, A.R. (1981) A structural analysis of Valhalla basin, Callisto (abstract), *Lunar and Planetary Science XII*, p. 874-876.

Schubert, G., Stevenson, D.J., and Ellsworth, K, Internal structure of the Galilean satellites, submitted to *Icarus*.

Shoemaker, E.M. (1962) Interpretation of lunar craters, *in*, *Physics and Astronomy of the Moon*, Z. Kopal (ed.), Academic Press: New York, p. 283-359.

Shoemaker, E.M., Lucchita, B., Wilhelms, D., Plescia, J.B., and Squyres, S.W., (1982) The Geology of Ganymede, in **The Satellites of Jupiter,** D. Morrison ed., University of Arizona Press, Tucson.

Shoemaker, E.M., and Wolfe, R.F. (1982) Cratering time scales for the Galilean Satellites, in **The Satellites of Jupiter,** D. Morrison ed., University of Arizona

Press, Tucson.

Smith, B.A., Soderblom, L.A., Johnson, T.V., Ingersoll, A.P., Collins, S.A., Shoemaker, E.M., Hunt, G.E., Masursky, H., Carr, M.H., Davies, M.E., Cook, A.F. II, Boyce, J., Danielson, G.E., Owen, T., Sagan, C., Beebe, R.F., Veverka, J., Strom, R.G., McCauley, J.F., Morrison, D., Briggs, G.A., and Suomi, V.E., (1979a) The Jupiter system through the eyes of Voyager 1, *Science*, *204*, p. 951-972.

Smith, B.A., Soderblom, L.A., Beebe, R., Boyce, J., Briggs, G., Carr, M., Collins, S.A., Cook, A.F. II, Danielson, G.E., Davies, M.E., Hunt, G.E., Ingersoll, A., Johnson, T.V., Masursky H., McCauley, J., Morrison, D., Owen, T., Sagan, C., Shoemaker, E.M., Strom, R., Suomi, V.E., and Veverka, J., (1979b) The Galilean satellites and Jupiter: Voyager 2 imaging science results, *Science*, *206*, p. 927-950.

Squyres, S.W. (1980) Surface temperatures and retention of H_2O frost on Ganymede and Callisto, *Icarus*, *44*, p. 502-510.

Woronow, A. (1978) A general cratering-history model and its implications for the Lunar highlands, *Icarus*, *34*, p. 76-88.

Woronow, A., and Strom, R.G. (1981) Limits on large-crater production and obliteration on Callisto, *Geophys. Res. Letters*, *8*, p. 891-894.

---------- (1982) Interpreting the cratering record from Mercury to Ganymede, in **The Satellites of Jupiter,** D. Morrison ed., University of Arizona Press, Tucson.

PAPER 3
THERMAL EVOLUTION OF THE LITHOSPHERES OF GANYMEDE AND CALLISTO

by QUINN R. PASSEY

Submitted to *JOURNAL OF GEOPHYSICAL RESEARCH*

ABSTRACT

About 1000 topographic profiles of craters on Ganymede and Callisto were obtained by photoclinometry. Fresh craters on Ganymede and Callisto have depth-to-diameter ratios and rim height-to-diameter ratios similar to those of fresh lunar craters. Most craters on these planet-like bodies, however, are much shallower than fresh craters on the Moon of similar size. The floors of many craters, moreover, are bowed-up in the center, indicative of viscous relaxation in a medium where the effective viscosity is uniform or decreases with depth. Small craters have not flattened or relaxed as much as have large craters; comparison of the crater profiles with the results from calculation of crater relaxation in a viscous medium allows determination of the viscosity at the surfaces of Ganymede and Callisto, and also determination of the viscosity gradient with depth. The derived mean surface viscosity for the lithospheres of Ganymede and Callisto is $1.0 \pm 0.5 \times 10^{26}$ poise. Combining the statistics for craters exhibiting various states of relaxation, with a proposed cratering time scale, the time dependence of the viscosity gradient is obtained. The viscosity gradients can then be converted, by means of a model for the physical properties of ice, to thermal gradients, the time dependence of which is also known. For Ganymede, the estimated thermal gradient at ~3.9 Gya was $\geq$ 8 K/km; the thermal gradient can be modelled as decreasing approximately exponentially with time, with an e-folding time of about 10^8 years; the estimated present thermal gradient is $\leq$ 2.0 K/km. For Callisto, the thermal gradient was $\geq$ 3 K/km at ~4.1 GYA and the decrease in the thermal gradient can be modelled as an exponential dropoff with an e-folding time between about 5×10^7 and 2×10^8 years; the estimated present thermal gradient on Callisto is $\leq$ 1.5 K/km.

INTRODUCTION

Prior to the Voyager I and II spacecraft encounters with Ganymede and Callisto, there was considerable speculation about their surface appearance. It had been suggested that the lithospheres of these two planet-like bodies were composed chiefly of ice and that the topographic relief would be subdued because of flow of the ice (Johnson and McGetchin, 1973; Parmentier and Head, 1979). The first high resolution images revealed that the surfaces of both Ganymede and Callisto are heavily cratered; certain features of the craters are similar to features of lunar craters but most craters are much shallower than lunar craters of similar size (Smith et al., 1979a); also, in contrast to craters on the Moon, most craters larger than about 20 km in diameter exhibit a well defined central pit (Passey and Shoemaker, 1982).

Callisto's surface consists almost entirely of heavily cratered terrain with a lower albedo than is found on most other icy satellites. Ganymede's surface, on the other hand, is divided into two very distinct types of terrain, a relatively low albedo heavily cratered terrain, and younger higher albedo grooved and smooth terrains that transect the dark heavily cratered terrain. The average spatial density of craters on the grooved and smooth terrain, here referred to simply as grooved terrain, is much less than on the dark heavily cratered terrain. Large circular to irregular spots with slightly higher albedo than the surrounding surface occur on the dark cratered terrains of both Ganymede and Callisto; these spots, termed palimpsests, are interpreted as the remnant rim and floor deposits of ancient craters where the original topography of the craters has long since flattened away either by prompt collapse or by viscous flow or creep (Smith et al., 1979b). Other features that appear to be transitional in topographic expression between a crater and a palimpsest are found on Ganymede

and have been termed penepalimpsests (almost palimpsests) (Passey and Shoemaker, 1982).

Topographic profiles of craters on Ganymede, obtained by photoclinometric methods, reveal that not only are many craters shallower than lunar craters of similar size, but that a majority of the craters also display a bowed-up floor (Shoemaker and Passey, 1979; Passey and Shoemaker, 1982). The bowing up of the crater floor is indicative of viscous relaxation of a crater in a medium of constant viscosity (Danes, 1962, 1965) or in a medium where viscosity decreases with depth (Parmentier and Head, 1981).

In order to study the topographic relaxation, about 1000 photoclinometric profiles were obtained of craters on Ganymede and Callisto. It is possible to quantify the viscous behavior of the icy lithospheres of Ganymede and Callisto from the statistics of the crater profiles by means of the theory for crater relaxation in a viscous medium. First we will present statistics on maximum depth-to-diameter ratios, rim heights, and degree of relaxation and/or bowing up of the crater floor. Next we calculate various models of crater relaxation with the aid of a proposed cratering time scale and the time dependent viscous behavior of the lithospheres is derived for Ganymede and Callisto by comparison of the statistics of the observed degree of relaxation with the results from the theoretical models. Finally, thermal histories of Ganymede and Callisto are presented; the time scale used for these thermal histories is that derived by Shoemaker and Wolfe (1982) but the thermal histories can easily be obtained for other cratering time scales.

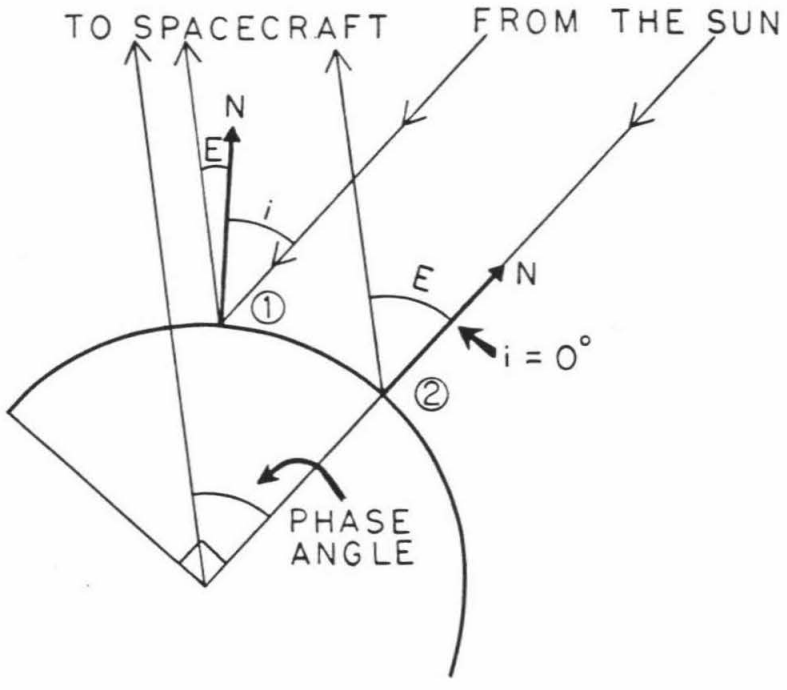

FIGURE 1 - Geometry used for photometric slope determination. See text for discussion.

TOPOGRAPHY OF CRATERS

Determination of topography by photoclinometric method

In order to study the flattening of craters and basins on Ganymede and Callisto, information is required about the present topographic relief of these features. The images of these bodies obtained by the Voyager I and II spacecraft do not permit useful stereoscopic determination of topographic relief. Crater depths can be determined from shadow measurements only in limited regions near the terminator; another method, therefore, must be used to determine topographic relief for most of the features on these satellites. Using the technique of photoclinometry, it is possible to obtain the needed data (Bonner and Schmall, 1973; Watson, 1968). The successful application of this method requires that the photometric function of the surface material be known.

Photometric studies of Ganymede and Callisto by Squyres and Veverka (1981) indicate that the photometric function can be represented adequately by a Lommel-Seeliger function; the form of this function is

$$I = \frac{C\,\mu_o}{(\mu_o + \mu)} \qquad (1)$$

where I is the intensity of the reflected radiation, C is a constant, $\mu_o = \cos(i)$, and $\mu = \cos(E)$, where i is the angle between the incident radiation and the surface normal, and E is the emission angle; Figure 1 shows the simplified geometric relationships between these quantities for two locations within the same phase plane on a spherical surface. Knowing the average values for i, E, and the phase angle for a given location, the value of the constant C can be calculated using the observed intensity I obtained from Voyager images. Within an area of uniform albedo, the intensity observed from a given picture element (pixel) can be related to the average absolute of slope of the area within that

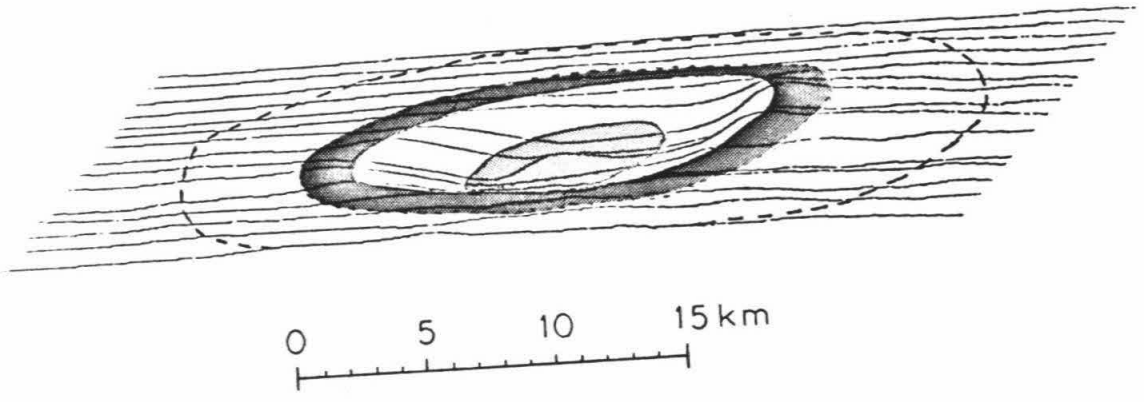

FIGURE 2 - Fifteen profiles of different cross-sections across a 13 km diameter crater (71° S, 152° W) were arranged to produce this 3-dimensional projection. The inner shaded region indicates the approximate floor of the crater. Note the presence of the central peak ~800 meters high. The outer shaded region marks the outer flank of the crater rim; the outer edge of the bright ejecta deposit, associated with this crater, is shown by the outermost broken line.

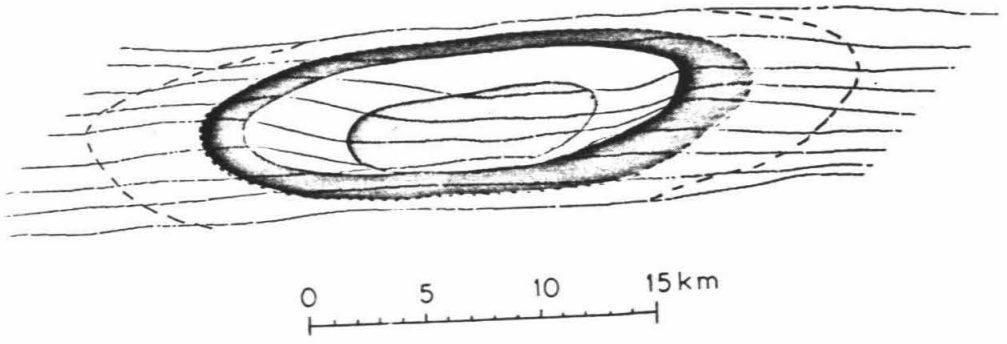

FIGURE 3 - Same as for Figure 2 except that this composite is from nine separate cross-sectional profiles of a crater 19 km in diameter (65° S, 144° W) The floor of this crater appears relatively flat.

pixel (the absolute slope is the component of slope in the phase plane). The function (1) was be assumed to be the photometric function for Ganymede and Callisto in the construction of all of the photoclinometric profiles presented in this paper. From a string of adjacent pixels, two-dimensional topographic profiles can be constructed as discussed by Squyres (1981). It is also possible to construct 3-dimensional projections of craters by offsetting several 2-dimensional profiles from different cross-sections of the crater, as shown in Figures 2 and 3. These profiles are of two fresh craters on grooved terrain that exhibit bright ejecta deposits. The crater shown in Figure 2 has well developed central peak approximately 800 meters high; the crater shown in Figure 3 displays a relatively flat floor.

The accuracy of the profiles obtained by this method is primarily a function of the accuracy of the determination of the constant C; the intensity (I), emission angle (E), incident angle (i), and phase angle are all well constrained by the camera calibration and by the viewing geometry of the surface of interest. Two independent tests for the accuracy of the value determined for C exist. The first test is the comparison of the crater depth derived from shadow measurements from the shadowed side of a given crater d_1, with the crater depth derived by photoclinometry from the opposite illuminated side d_2, as is shown in Figure 4a. By this method it was found that the depths determined by photoclinometry are within ± 25% of the shadow depths within a 95% confidence interval. The second test for accuracy comes from the observed symmetry (or asymmetry) between the two halves of the crater profile, as is shown in Figure 4b. The two halves of the profiles are constructed from different portions of the photometric function curve, because one rim is facing into the sun while the other is facing away, and if the two halves are reasonably symmetric, then the

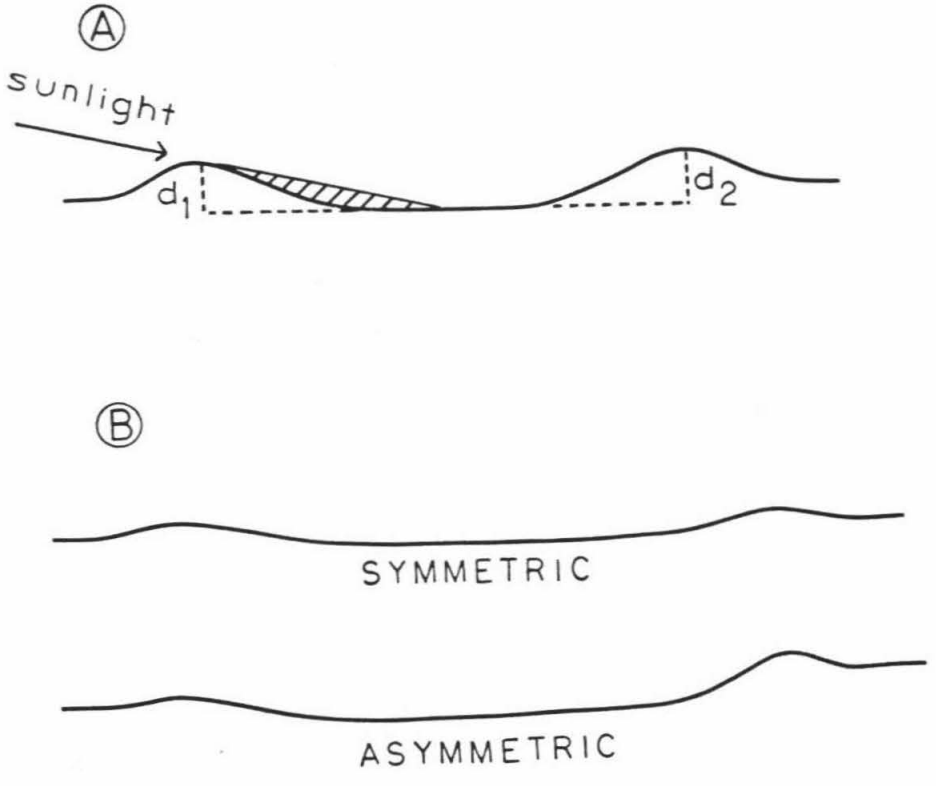

FIGURE 4 - (A) Test of accuracy of photoclinometric profile is possible when one inner wall of the crater is in shadow while the other is illuminated. The depth of the crater determined by shadow measurements (d_1) can be directly compared to the depth determined from the photoclinometric profile from the other side (d_2). (B) A second test for the accuracy of the photoclinometric profiles is in the symmetry of the two crater halves as is discussed in the text.

TABLE I - Sample of crater profiles*

LOCATION	CRATER DIAMETER 0-10	10-20	20-30	30-40	40-50	> 50 km	TOTAL
GANYMEDE							
Cratered Terrain	48	104	95 (101)	44 (50)	25 (30)	14 (30)	330 (363)
Grooved Terrain	129	175	82	49	19	26 (28)	480 (482)
CALLISTO	0	6	34	44	26	43	153

* The numbers in parentheses include several features for which useful photoclinometric profiles could not be obtained due to their extremely flattened topography and albedo contrasts with the surround plains. For these features maximum depths were estimated from shadow measurements.

value of the constant C must be approximately correct; conversely, if C is not accurate, the two halves will not be symmetric. From this test, the accuracy of the derived depths are also calculated to be ± 25% of their true values to within a 90% confidence interval.

A total of 963 usable photoclinometric profiles were obtained of craters and basins on Ganymede and Callisto. For Ganymede, 810 profiles were derived, and in addition, maximum depths of 35 extremely flattened craters and basins were obtained by shadow measurements, resulting in a total of 845 measurements of depth. Of these, 363 measurements were obtained for craters on the heavily cratered terrain and 482 for craters on the grooved terrain. A total of 153 photoclinometric profiles were derived for craters on Callisto. A breakdown of the crater profiles by crater size and terrain type is given in Table I. Most of the profiles from Ganymede are from Voyager II images because these images have the highest surface resolution. The highest resolution images of Callisto were obtained by Voyager I but many of these images were smeared by spacecraft rotation; because of the difficulties in dealing with smeared images, most of the profiles of craters on Callisto were obtained from images with slightly less than maximum surface resolution. Table II lists the Voyager images that were used for this study and gives the number of profiles obtained from each image.

Ganymede - Heavily Cratered Terrain

Craters on Ganymede's heavily cratered terrain exhibit a large range of topographic relaxation. Examples of profiles of fresh and degraded craters 10 to 23 km in diameter on the heavily cratered terrain are shown in Figure 5. Craters as small as 10 km in diameter show significant flattening as compared to 10 km fresh craters. Commonly the crater floors are bowed-up.

TABLE II - Images used for photoclinometry*

FDS	# Craters	FDS	# Craters
	GANYMEDE		
Voyager 1		Voyager 2	
16404.56	35	20636.59	66
16405.02	11	20637.02	68 (74)
16405.04	28 (34)	20637.14	112 (114)
16405.10	19	20637.26	36
16405.12	19	20638.59	41 (60)
16405.18	16 (18)	20639.05	36
16405.22	15	20639.11	30
16405.28	10	20639.15	17
16405.30	13	20639.19	42
16405.32	6	20640.25	20
16405.42	9	20640.27	31
16405.48	22	20640.29	28
16405.50	4	20640.31	20
Subtotal	207 (215)	20640.33	24
		20640.37	11
		20640.41	21
		Subtotal	603 (630)

Total = 810 (845)

	CALLISTO		
Voyager 1		Voyager 2	
16421.27	24	20616.41	31
16421.59	21	20616.57	33
Subtotal	45	20617.25	29
		20617.41	15
		Subtotal	108

Total = 153

* The numbers in parentheses include several features for which useful photoclinometric profiles could not be obtained due to their extremely flattened topography and albedo contrasts with the surround plains. For these features maximum depths were estimated from shadow measurements.

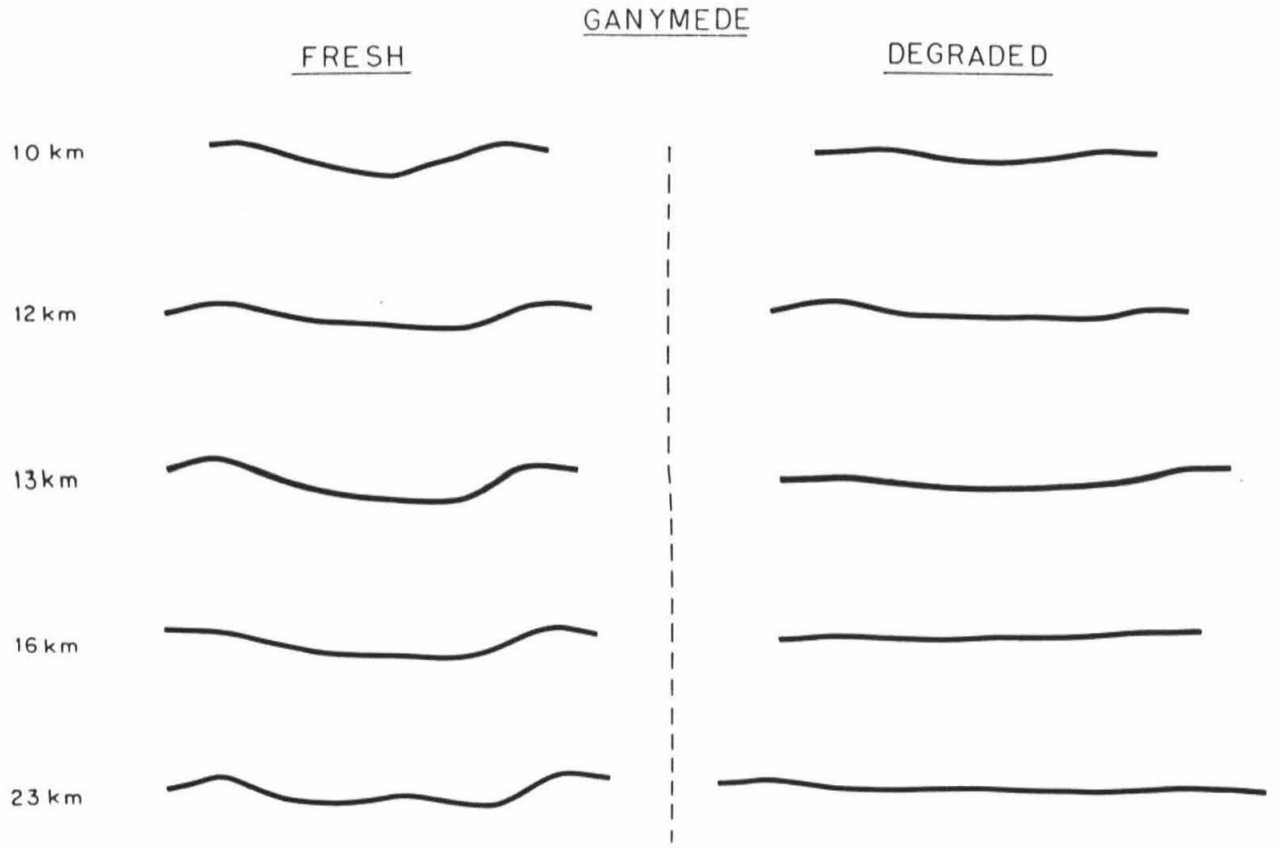

FIGURE 5 - Photoclinometric profiles of fresh and degraded craters 10-23 km in diameter on the heavily cratered terrain of Ganymede. The distances refer to the rim-to-rim diameter. The vertical scale is the same as the horizontal scale.

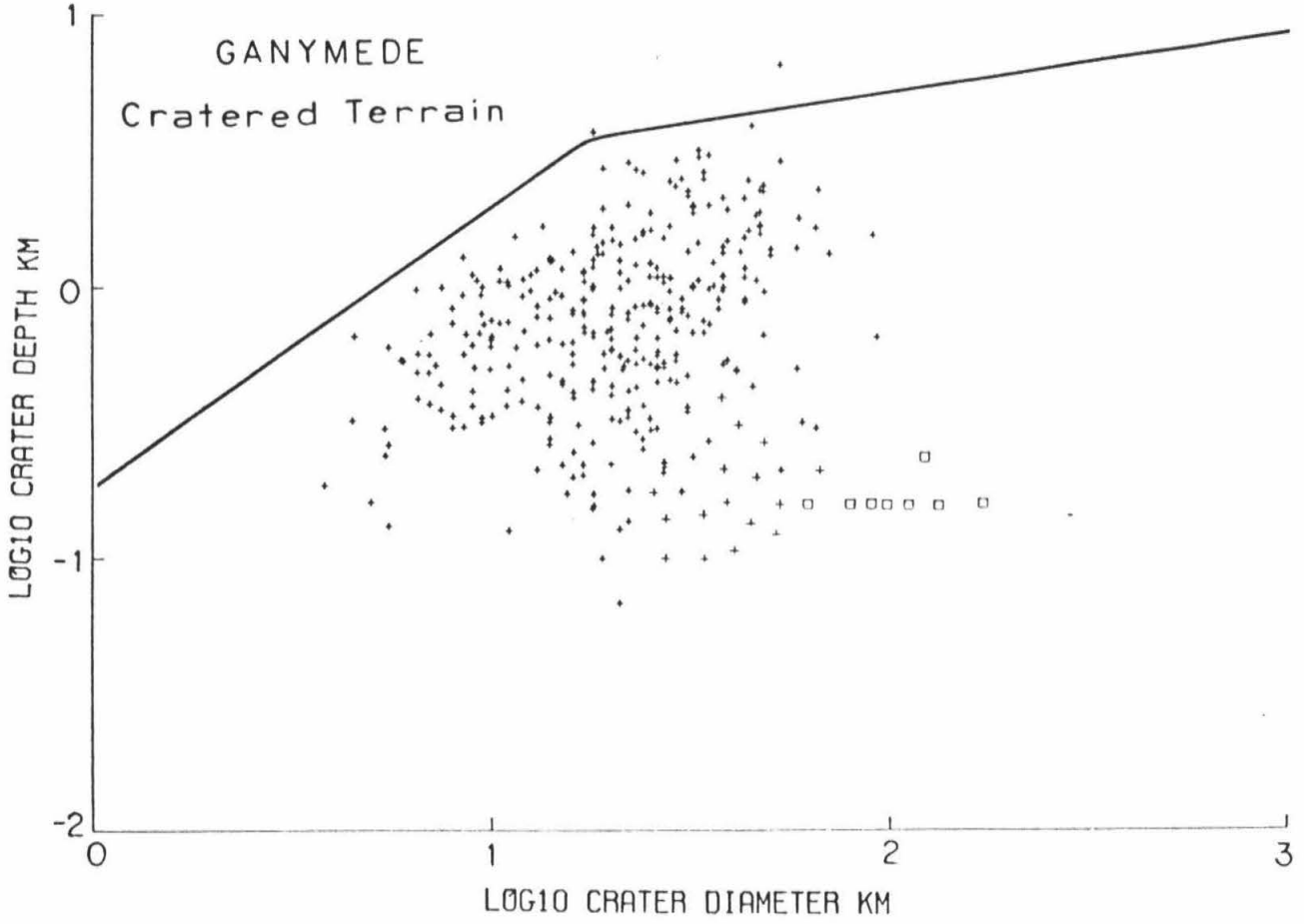

FIGURE 6 - Plot of maximum crater depth versus crater diameter for 379 craters on the heavily cratered terrain on Ganymede. The heavy solid line is the empirical fit for fresh lunar craters derived by Pike (1977). The open squares mark the maximum possible relief several palimpsests and penepalimpsests.

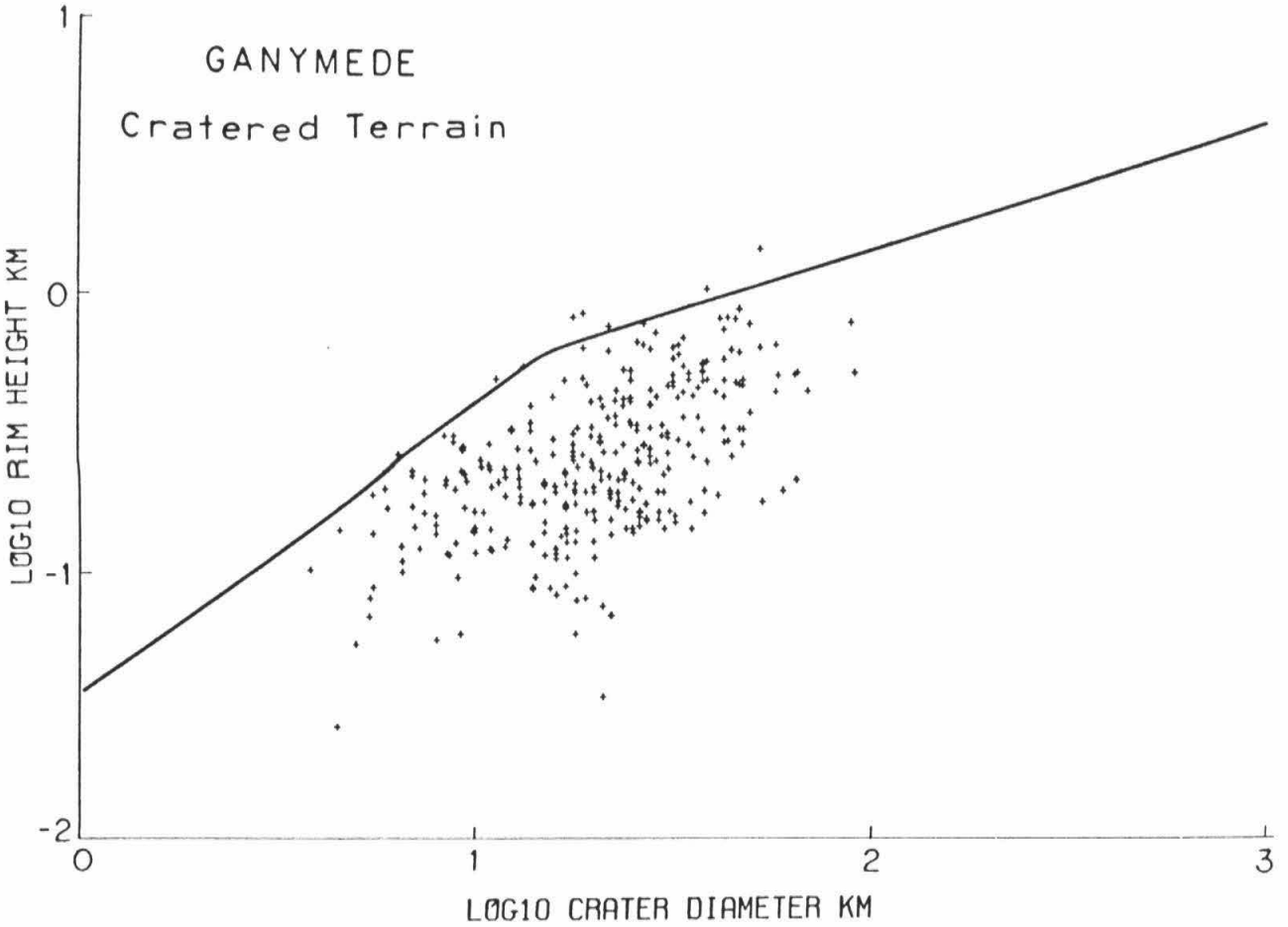

FIGURE 7 - Plot of Log_{10} crater rim height versus Log_{10} crater diameter for 379 craters on the heavily cratered terrain on Ganymede. The heavy solid line is the empirical fit for fresh lunar craters (Pike, 1977).

From the photoclinometric crater profiles, it is generally possible to accurately measure (within ± 25% of the true values) the maximum depth of a crater; depths of 363 craters and palimpsests on the heavily cratered terrain of Ganymede are shown plotted against diameter in Figure 6; also plotted is the empirical fit for fresh lunar craters, which is (Pike, 1977)

$$d = 0.196\, D^{1.010} \qquad D < 15\ km \tag{2a}$$

and

$$d = 1.044\, D^{0.301} \qquad D > 15\ km \tag{2b}$$

where d is the maximum crater depth below the crater rim and D is the crater diameter. It should be noted that because of the bowing up of the crater floors, the depths plotted in Figure 6 generally are not referenced to the center of the crater but rather to a region (a moat) just inside of the crater rim.

The depths of craters on the heavily cratered terrain on Ganymede are almost always less than for similar size craters on the Moon. Fresh craters, however, have depth-to-diameter ratios that are very similar to fresh lunar craters; this suggests that, for the craters studied, the maximum depths of fresh craters formed on Ganymede are controlled primarily by gravity rather than the physical properties of the material in the lithosphere at late stages in its evolution. (Lunar surface gravity is 162 cm sec^{-2} and for Ganymede the surface gravity is 142 cm sec^{-2}.)

Approximately 8% of the craters plotted in Figure 6 are within the probable error in the depth measurements of the curve for fresh lunar craters, and 26% are within two times the probable error of the lunar curve. The probable error is defined as ± 25% of the true value.

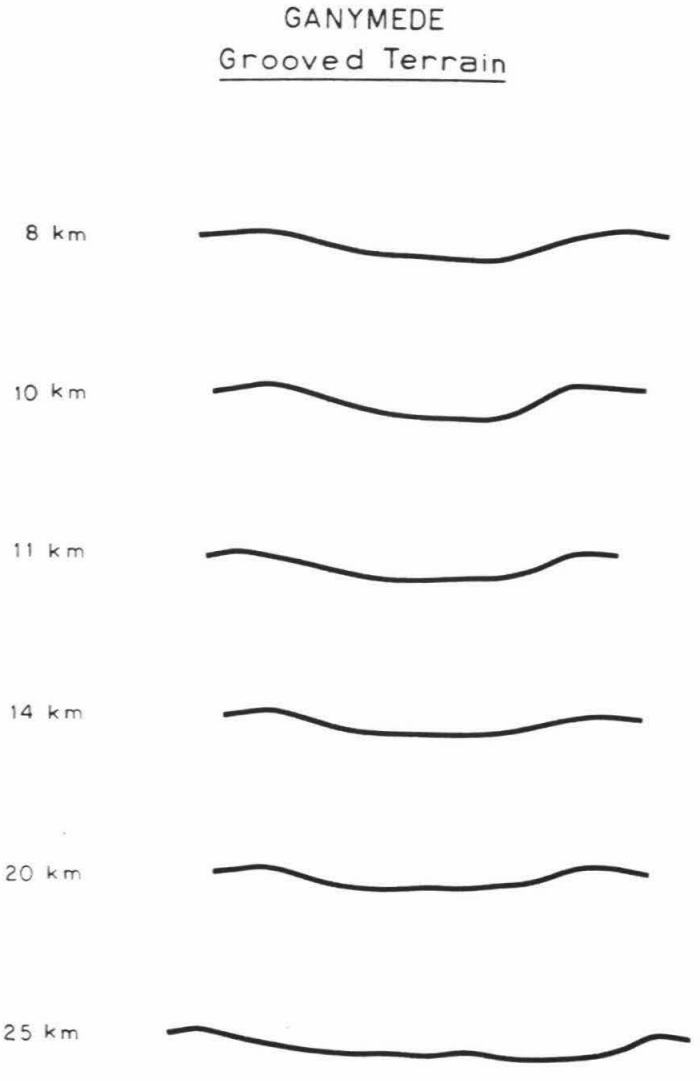

FIGURE 8 - Photoclinometric profiles of craters with rim diameters 8-25 km in diameter on the grooved terrain of Ganymede. (No vertical exaggeration.)

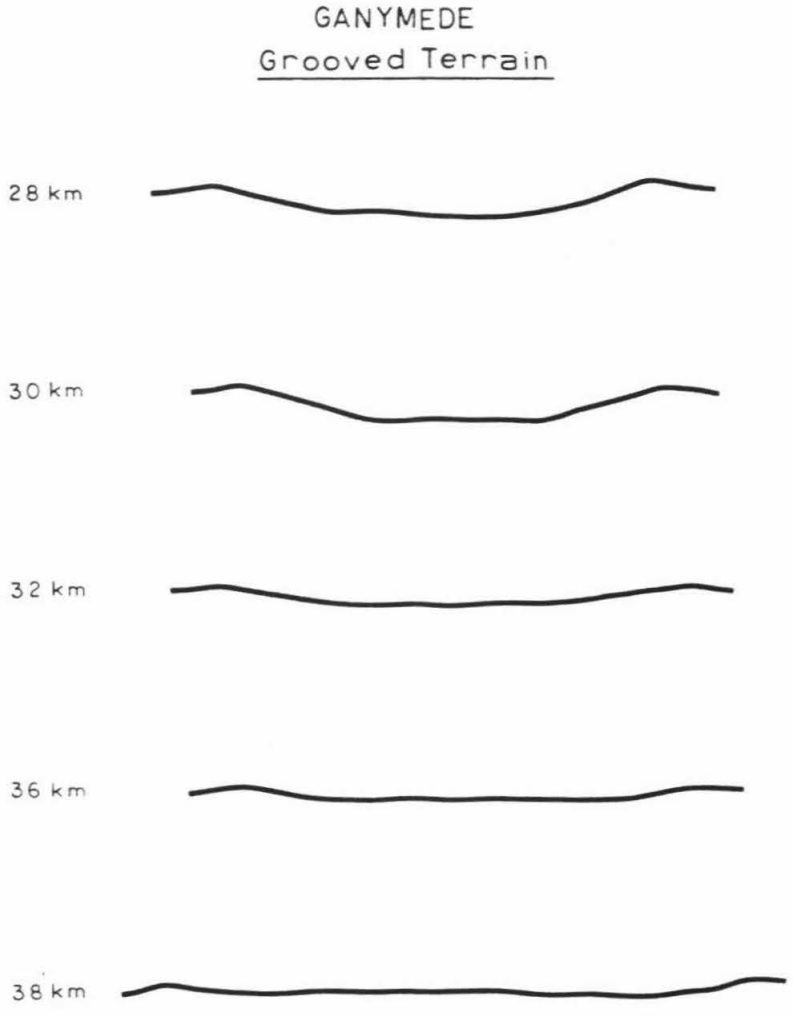

FIGURE 9 - Same as Figure 8 except this figure shows craters 28-38 km in diameter.

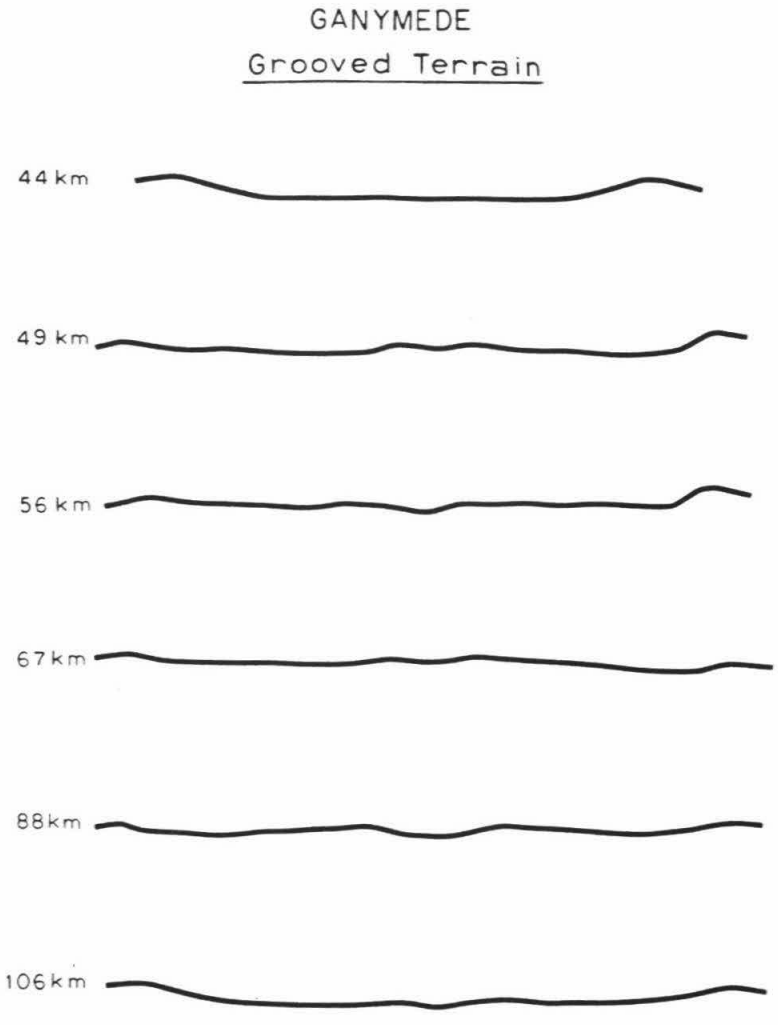

FIGURE 10 - Same as Figure 8 except this figure shows craters 44-106 km in diameter. Note the presence of a rimmed central pit and the broadly doming crater floors.

The crater rim height-to-diameter ratios for 330 craters on the heavily cratered terrain of Ganymede are plotted in Figure 7. Also shown is the empirical fit to fresh lunar craters, as determined by Pike (1977). For lunar craters the function is

$$h = 0.036\, D^{1.014} \qquad D < 15\ km \tag{3a}$$

and

$$h = 0.236\, D^{0.399} \qquad D > 15\ km \tag{3b}$$

where h is the rim height above the pre-crater level, as is indicated by the flat plain surrounding the crater.

The rim height for a given crater diameter is generally less than for lunar craters but the upper limit to the distribution is close to Pike's curve, which indicates that the rim heights for fresh Ganymedian craters are very similar to those of fresh lunar craters.

Examination of crater depth versus diameter for the heavily cratered terrain indicates no significant correlation with latitude. Also, no significant correlation of crater depth as a function of longitude is observed when profiles from the Voyager I images and those from the Voyager II images are compared.

Ganymede - Grooved Terrain

Examples of photoclinometric profiles of craters located on the grooved terrain of Ganymede are shown in Figures 8, 9, and 10. Figure 8 shows craters 8 to 25 km in diameter; no measured craters on the grooved terrain of Ganymede ≤ 15 km in diameter exhibit any substantial flattening of the topographic relief, in contrast to that observed for craters of this size on the heavily cratered terrain. Figure 9 shows craters 28 to 38 km in diameter; substantial flattening of craters ≥ 30 km in diameter is observed for some craters. Figure 10 shows craters in

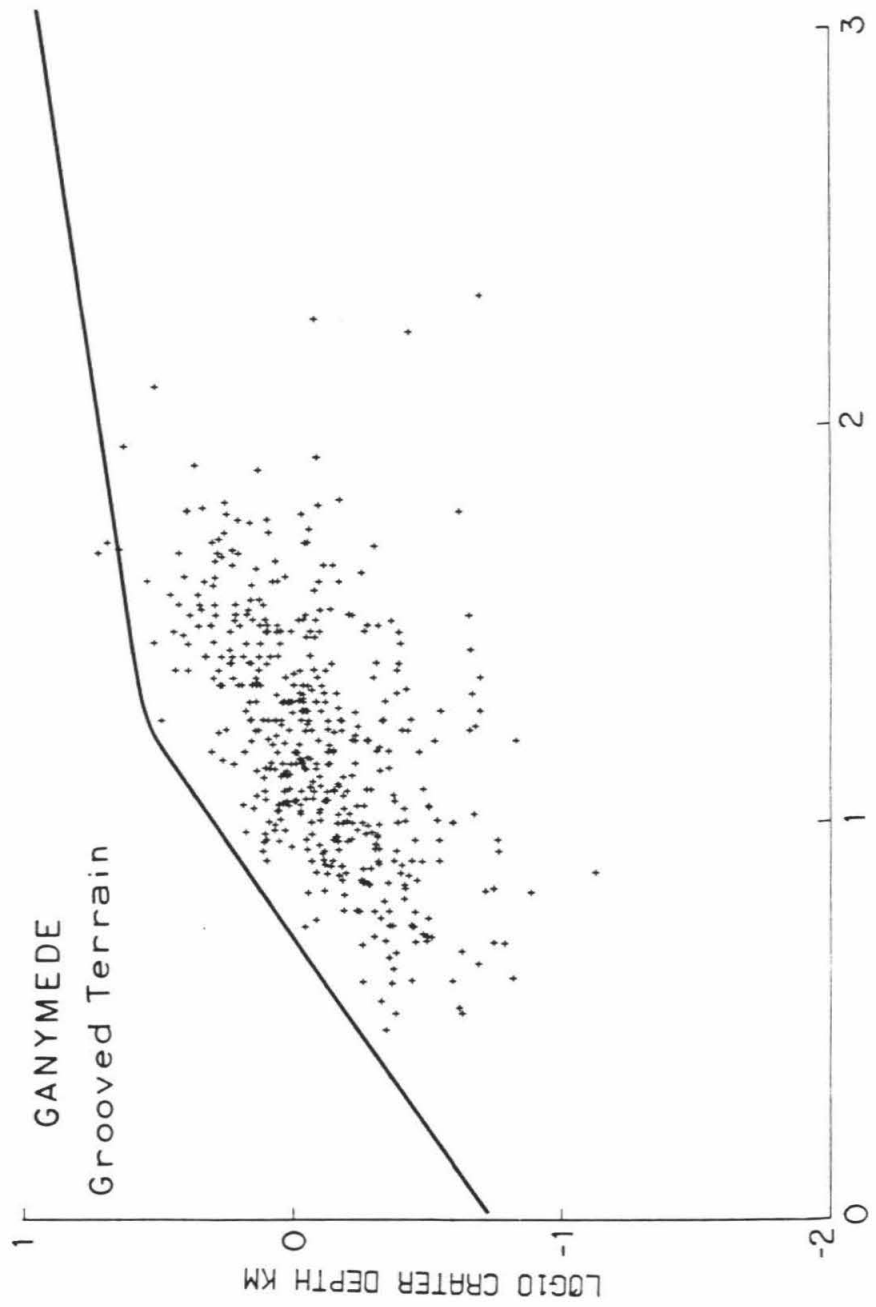

FIGURE 11 - Same as for Figure 6 except that this graph is for 482 craters on the grooved or smooth terrains on Ganymede.

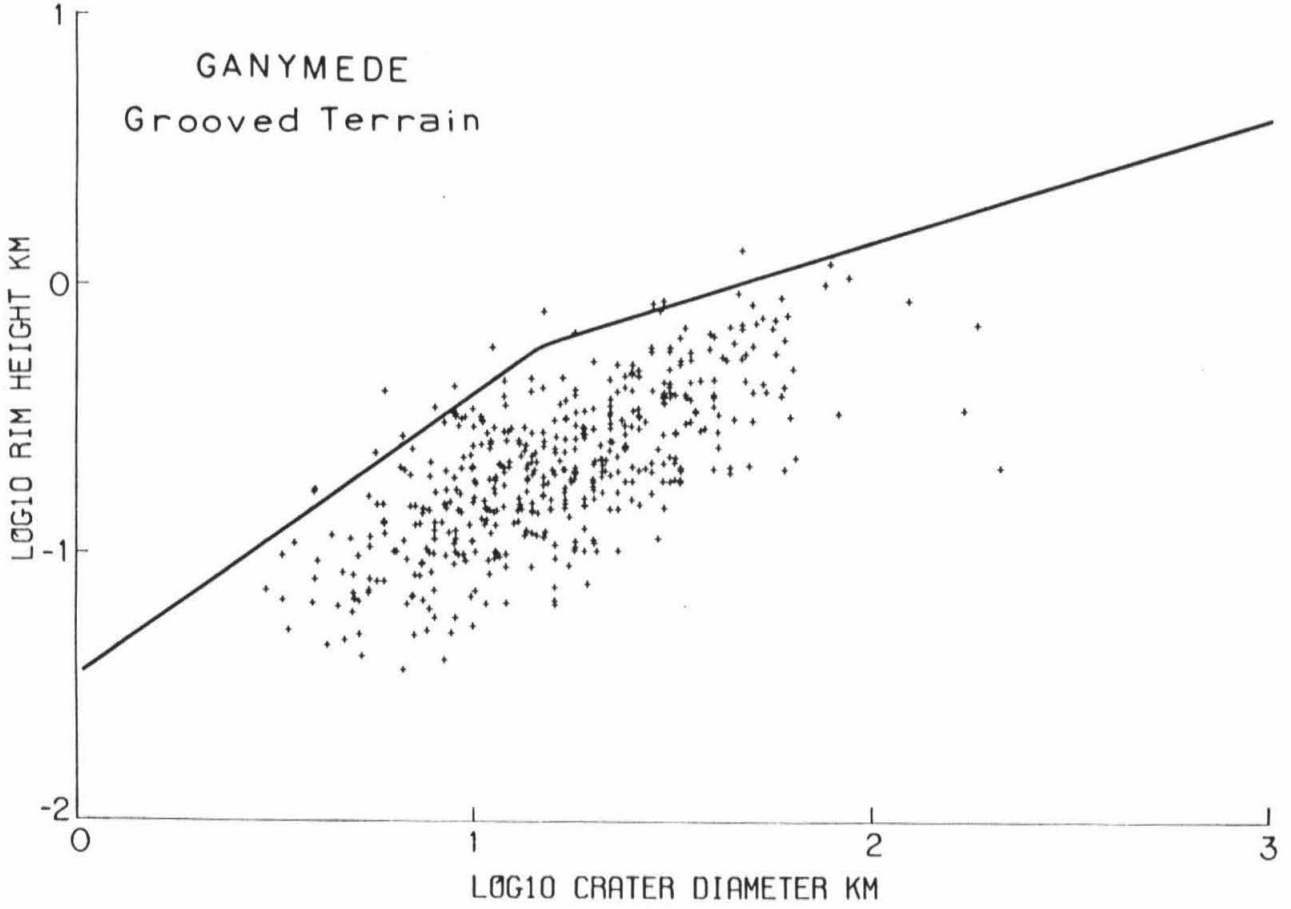

FIGURE 12 - Same as for Figure 7 except that this graph is for 482 craters on the grooved or smooth terrains on Ganymede.

the diameter range 44 to 106 km; most craters ≥ 50 km in diameter display broadly bowed-up floors. Note the presence of a rimmed central pit in craters ≥ 25 km in diameter.

Maximum depth-to-diameter ratios for 482 craters on grooved terrain are shown in Figure 11. The depths are generally shallower than for similar size lunar craters but are more densely clustered near the lunar curve than is observed for the craters on the heavily cratered terrain of Ganymede. Approximately 13% of the craters are within the probable error from the lunar curve, and 43% are within two times the probable error from the lunar curve, where the probable error is taken as ± 25% of the actual crater depth.

The rim height versus crater diameter for craters on grooved terrain are plotted in Figure 12; again the rim heights are generally less than for fresh lunar craters.

A wide range in crater density is observed for the grooved terrain, indicating a wide range in surface ages. The region of grooved terrain with the highest crater density is located near the south pole. Examination of crater depth versus diameter, for the grooved terrain, indicates that craters near the south polar region generally exhibit shallower depths than craters of similar size elsewhere. No significant correlation, however, of crater depth as a function of longitude is observed when profiles from the Voyager I images and those from the Voyager II images are compared.

Of great interest are the moderately well preserved basins on Ganymede. The Gilgamesh Basin is approximately 550 km in diameter with a central depression about 170 km in diameter; the central depression is shown in Figure 13. The degree of preservation of this structure will allow us to place limits on the present viscosity structure within the lithosphere of Ganymede, as will be

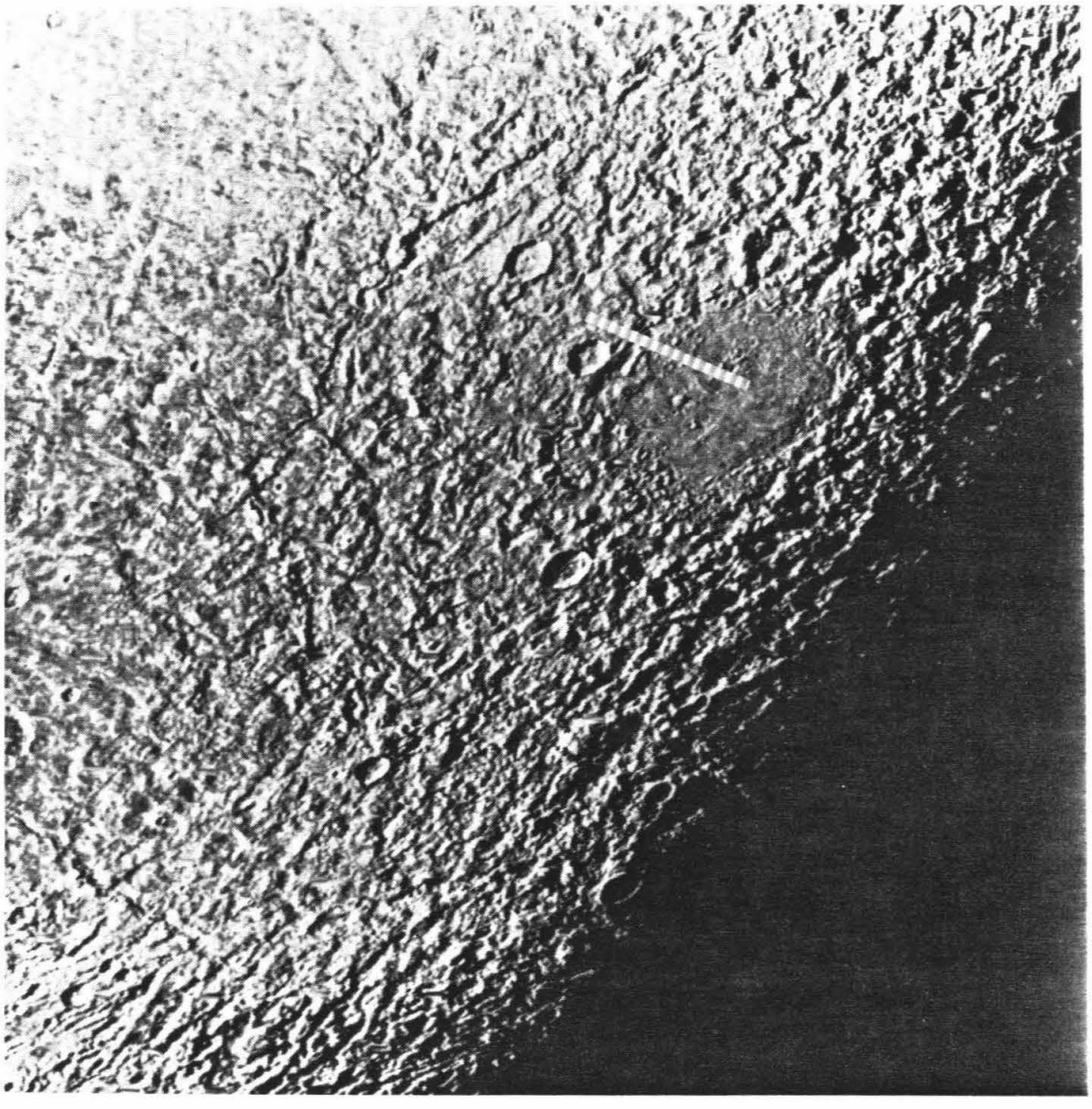

FIGURE 13 - Voyager II image of the relatively well-preserved Gilgamesh Basin. The broken line shows the location of the photoclinometric profile shown in Figure 14. (FDS 20638.14)

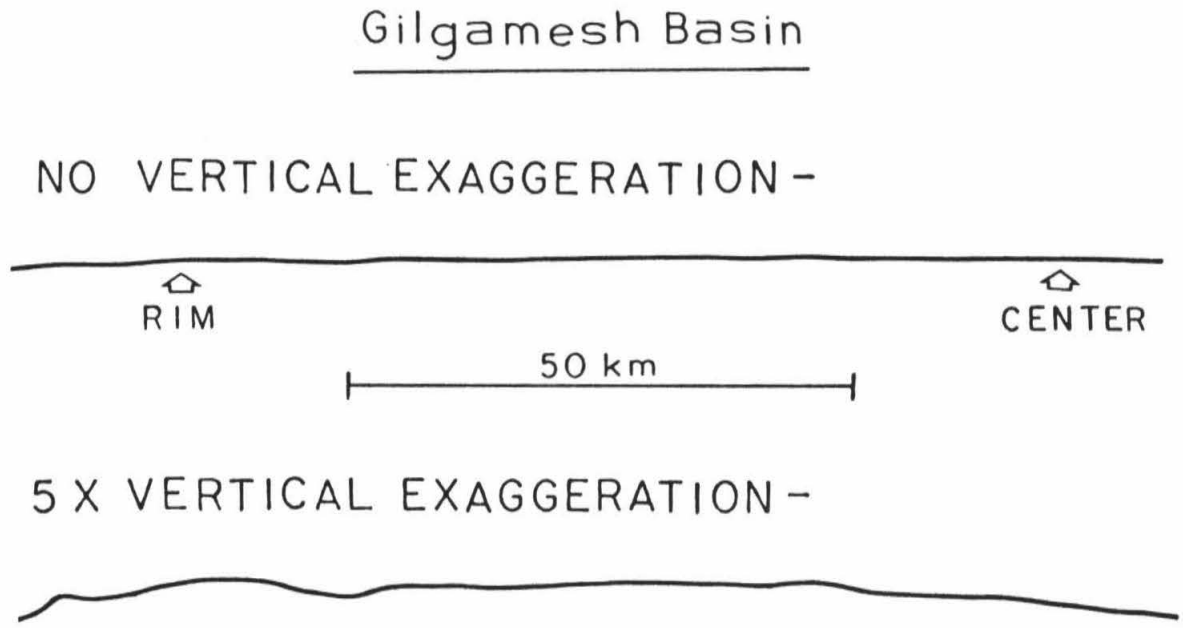

FIGURE 14 - Photoclinometric profile from the rim of the central depression to the center of the Gilgamesh Basin (illustrated in Figure 13). Note that the floor is extremely smooth.

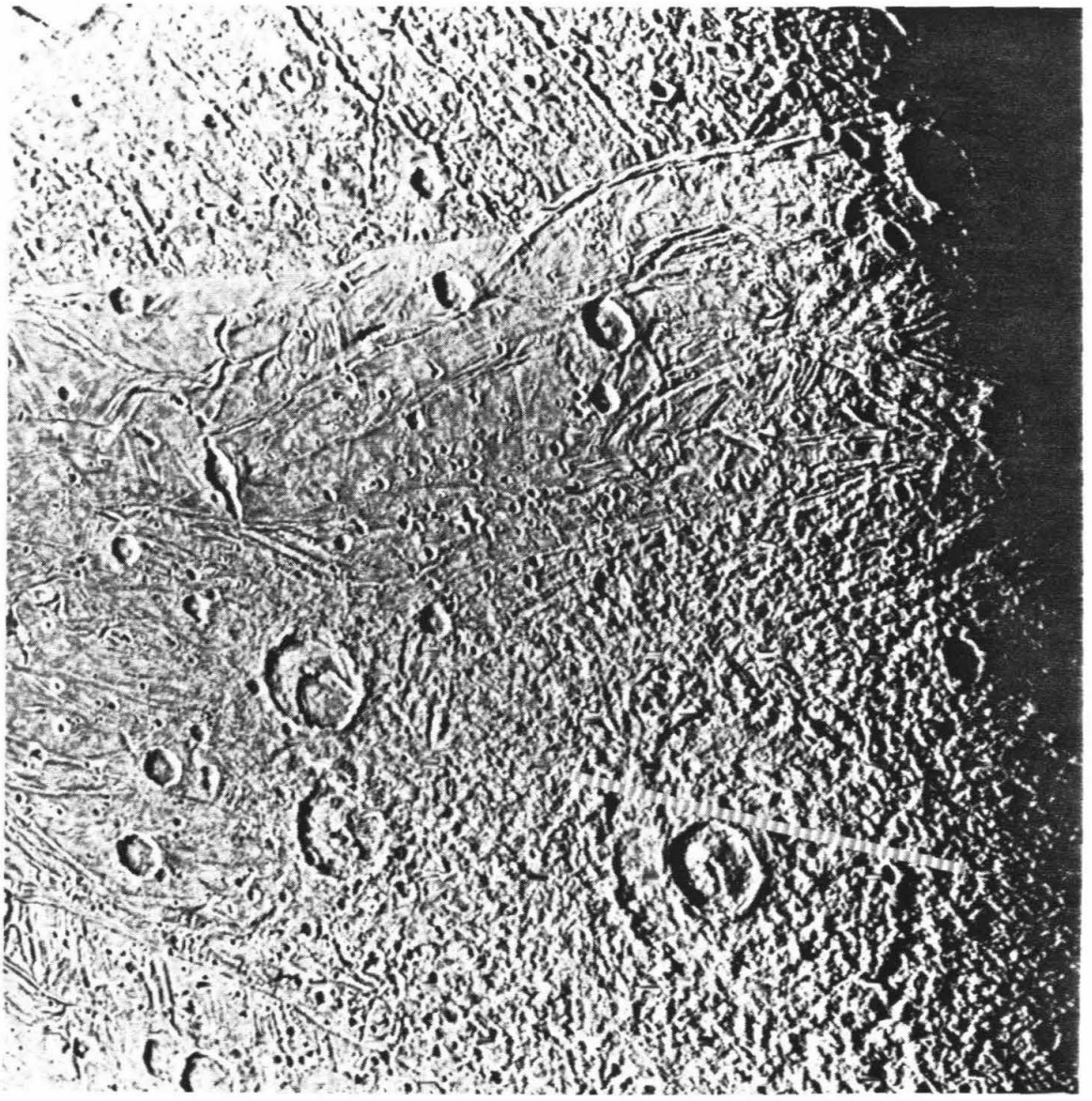

FIGURE 15 - Voyager II image of the extremely flattened Western Equatorial Basin on Ganymede. The broken line shows the location of the photoclinometric profile shown in Figure 16. (FDS 20638.39)

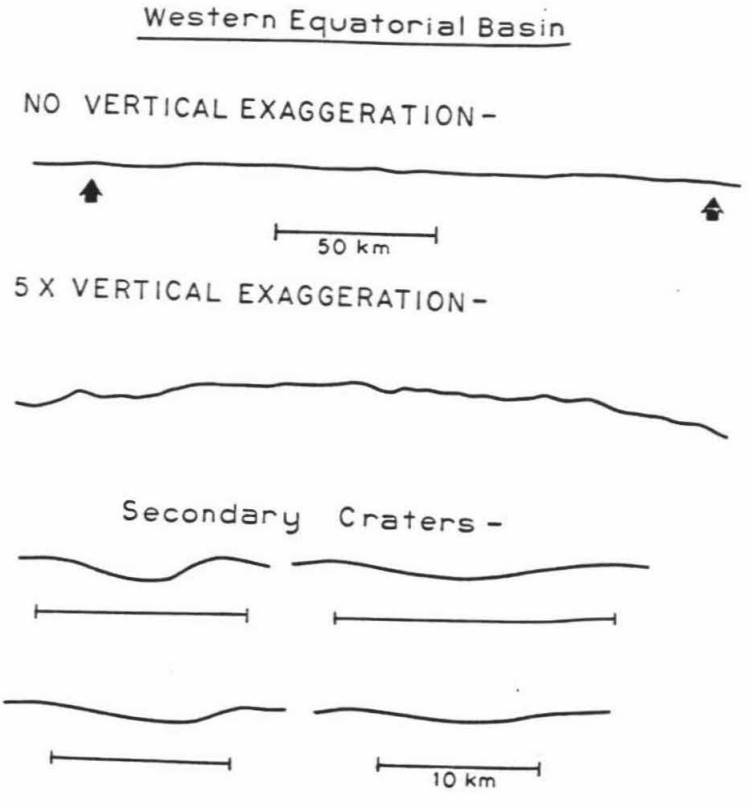

FIGURE 16 - Photoclinometric profile of the Western Equatorial Basin shown in Figure 15. The curvature of Ganymede is evident in the 5X vertical exaggeration. It appears that there is a slight depression just inside the basin rim (shown by the arrows). Also illustrated are photoclinometric profiles of four craters that that are interpreted to be secondary craters of this basin. These craters show little flattening as compared to fresh craters of the same diameter. The length bars for each of the secondary craters is 10 km.

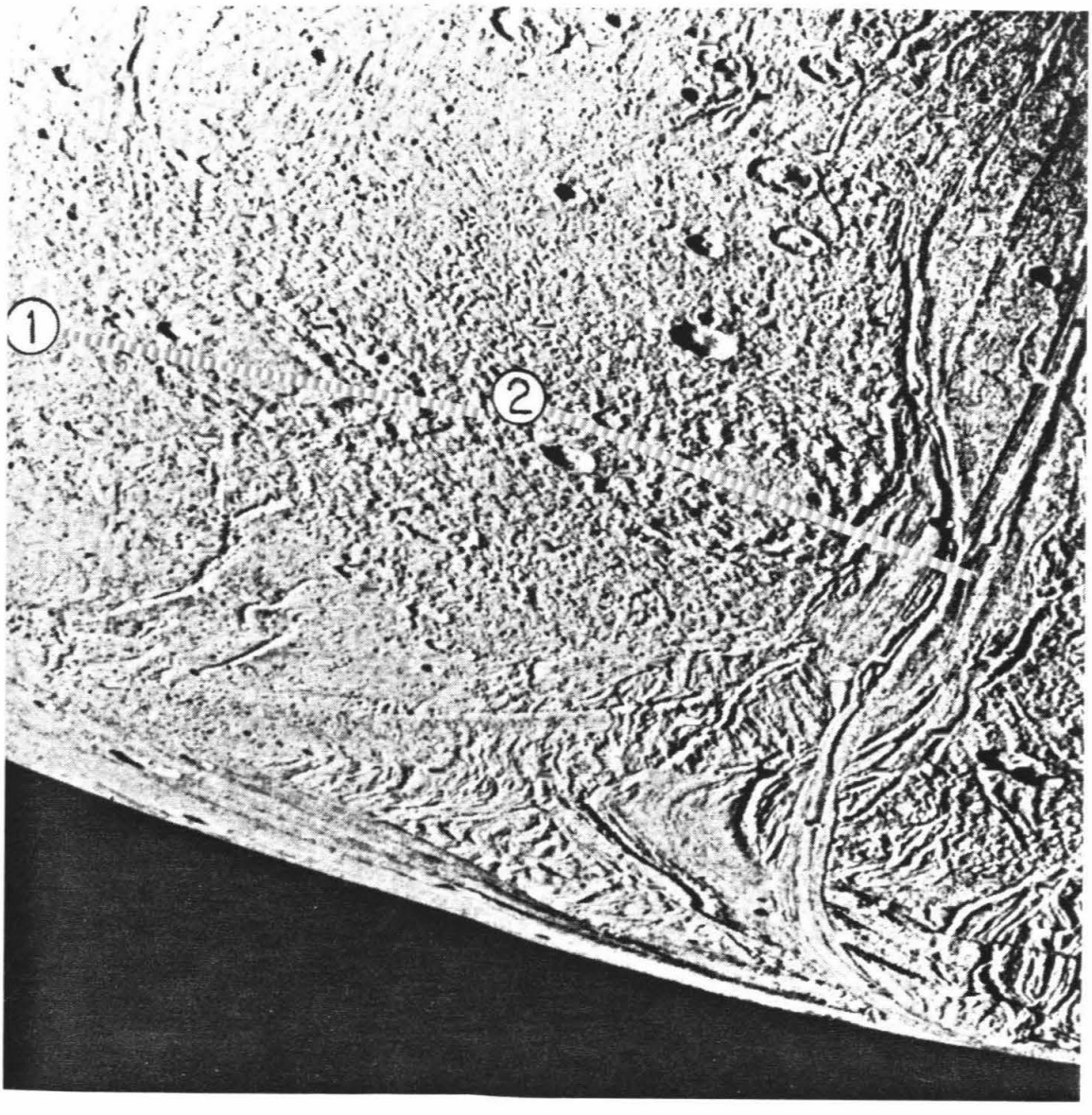

FIGURE 17 - Voyager II image of two penepalimpsests that are located near the south pole of Ganymede. The relatively smooth region, located near the center of this structure, is bounded by a raised rim interpreted to be the original crater rim. The diameter of the central structure in (1) is 60 km and for (2) the diameter is 64 km. Penepalimpsest (2) is cut on the right (east) by younger units of grooved terrain. The broken lines show the location of the photoclinometric profiles illustrated in Figure 18. (FDS 20640.31)

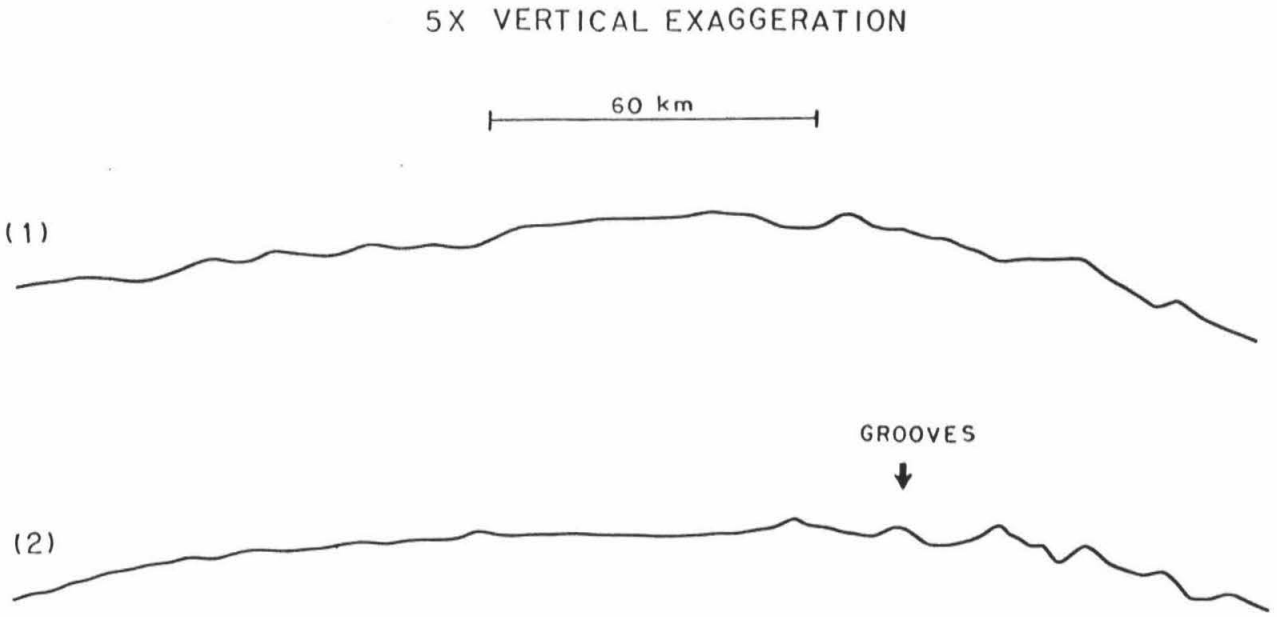

FIGURE 18 - Photoclinometric profiles of the two penepalimpsests shown in Figure 18. Note that the topographic relief of the grooves is greater than the relief in either the original crater or in the continuous ejecta blanket (the region just beyond he central crater). These profiles have a 5X vertical exaggeration.

discussed in greater detail later in this paper. A photoclinometric profile of the central portion of the Gilgamesh Basin (Figure 14) reveals that the floor of the central depression is relatively smooth and that the height of the rim is approximately 1 to 1-1/2 km above the floor of the depression.

The Western Equatorial Basin is approximately 185 km in diameter and is shown in Figure 15. A profile of the Western Equatorial Basin (Figure 16) shows that its floor is essentially at the pre-crater level and that the relief of the rim is about 1 km above this level. Immediately inside the rim there is a slight depression. Profiles of secondary craters of the Western Equatorial Basin show that little flattening of the topography of these craters has occurred (Figure 16). Both of these basins are discussed in detail in Passey and Shoemaker (1982).

Several features on Ganymede's grooved terrain that are more or less transitional in form between craters and palimpsests have been termed penepalimpsests (Passey and Shoemaker, 1982). A topographic profile of one of these features by Squyres (1980a) suggests that this feature is, at present, a domical upwarp with a diameter of ~250 km and a summit elevation 2 to 2-1/2 km above the surrounding terrain. Two other penepalimpsests, the original craters of which are approximately 60 km in diameter, are located near the south pole of Ganymede and are illustrated in Figure 17. Figure 18 shows photoclinometric profiles of these two features; the curvature of the satellite is evident in the vertically exaggerated profiles. The ejecta blanket of one of these penepalimpsests (Figure 18, profile 2) is cut by younger grooved terrain units (the beginning of the grooves is indicated by the arrow); the central crater of this feature does not exhibit a bowed up floor but the topographic relief is much less than for similar size fresh craters. The other penepalimpsest (Figure 18, profile 1) is slightly larger and exhibits a floor that is slightly bowed up with a

slight depression located just inside of the rim.

The majority of craters on the grooved terrain on Ganymede have retained much more of their original relief than have craters on the heavily cratered terrain. This is partially due to the difference in age between these terrain types (Shoemaker et al., 1982; Shoemaker and Wolfe, 1982), but must also reflect significant differences in the rheology of the lithosphere at different times, as will be discussed later.

Callisto

Examples of relatively fresh craters on Callisto are shown in Figure 19. Craters exhibiting subdued relief and bowed-up floors are also present on Callisto but these craters (at least those in the sample) do not appear to be as flattened as craters located on the heavily cratered terrain of Ganymede (Figure 20). One possible explanation of this is that because Callisto's surface is so much more heavily cratered than the heavily cratered terrain of Ganymede (as much as 5 times the local crater density in places), the oldest and most flattened craters on Callisto have been either obliterated by later impacts or are extremely difficult to recognize, owing to the high abundance of superposed craters, and, thus, were not included in the sample.

Maximum depth-to-diameter ratios for 153 craters on Callisto are plotted in Figure 21. Most of the craters are shallower than similar size lunar craters but a smaller range in depths is observed when comparing craters of a given size on Callisto with those on Ganymede (Figures 6 & 11). Approximately 17% of the craters in Figure 21 deviate no more than one probable error in depth measurement from the curve for fresh lunar craters, and 35% are within 2 times the probable error, where the probable error is ± 25% of the true depth.

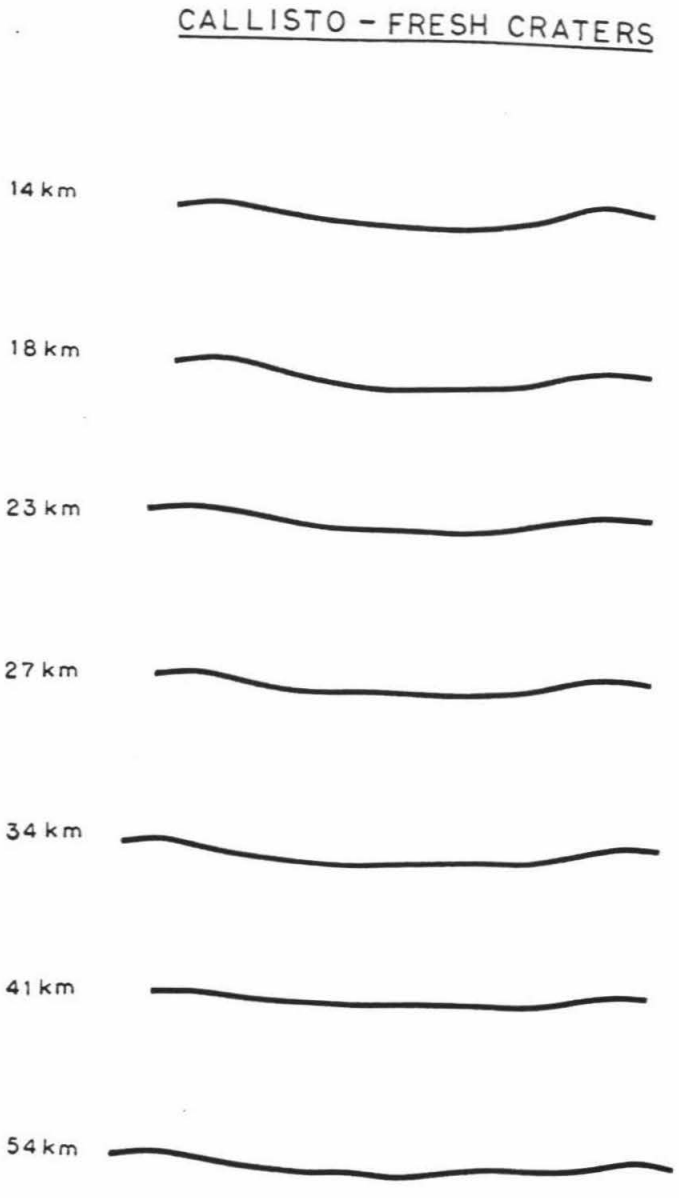

FIGURE 19 - Photoclinometric profiles of craters 14-54 km in diameter on Callisto that are relatively fresh appearing; these craters have depth-to-diameter ratios similar to fresh lunar craters.

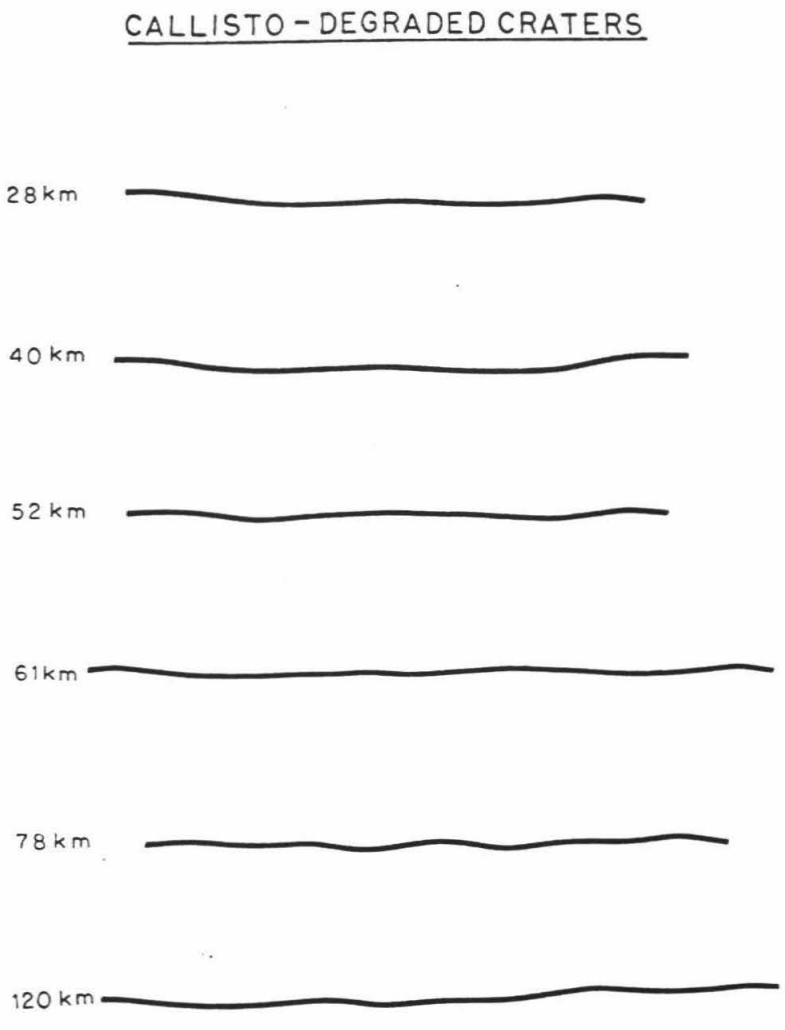

FIGURE 20 - Photoclinometric profiles of degraded craters 28-120 km in diameter on Callisto; the depth-to-diameter ratios for these craters are generally much less than for fresh lunar craters of similar size.

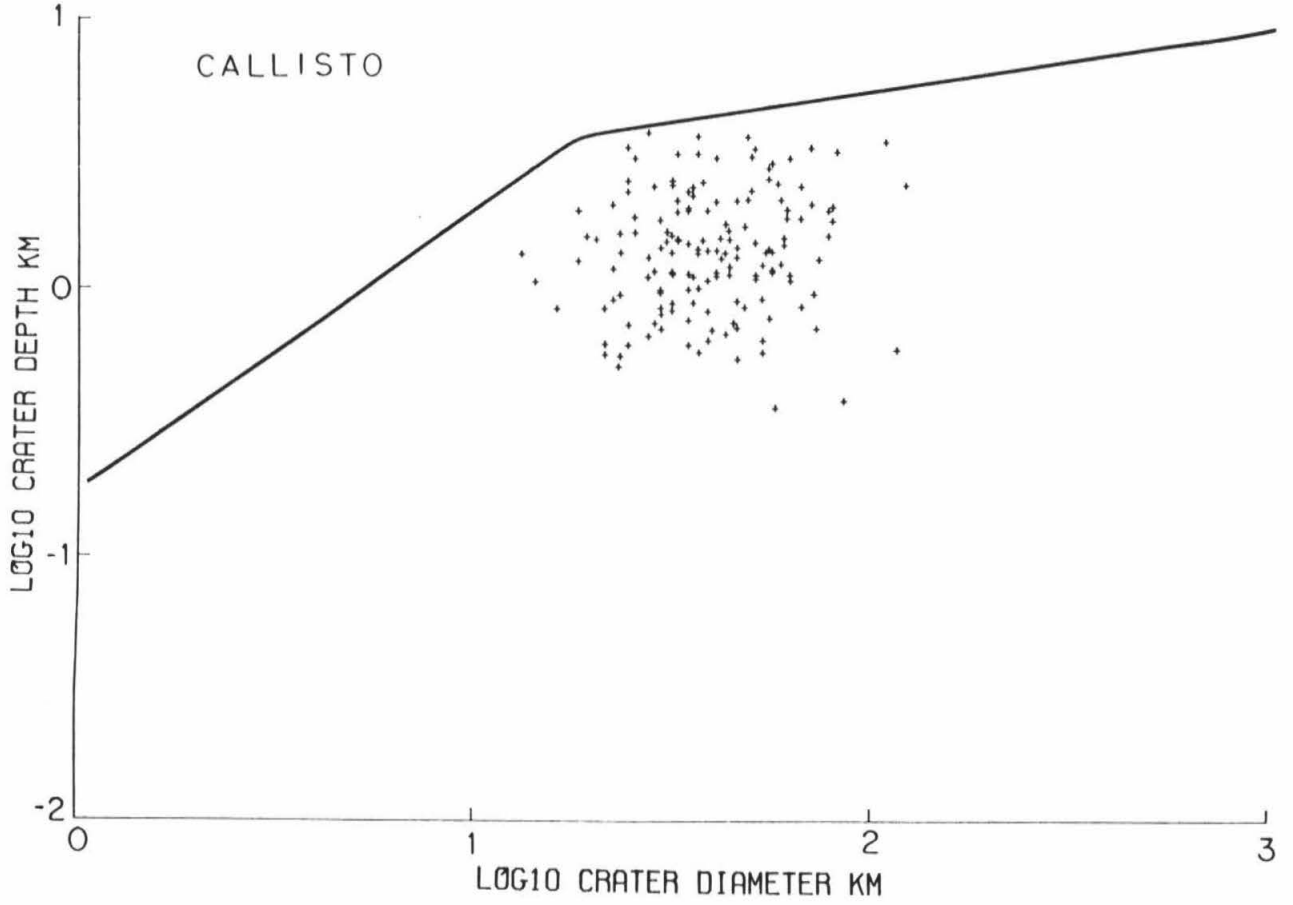

FIGURE 21 - Same as Figure 6 except that this graph is for 153 craters on Callisto.

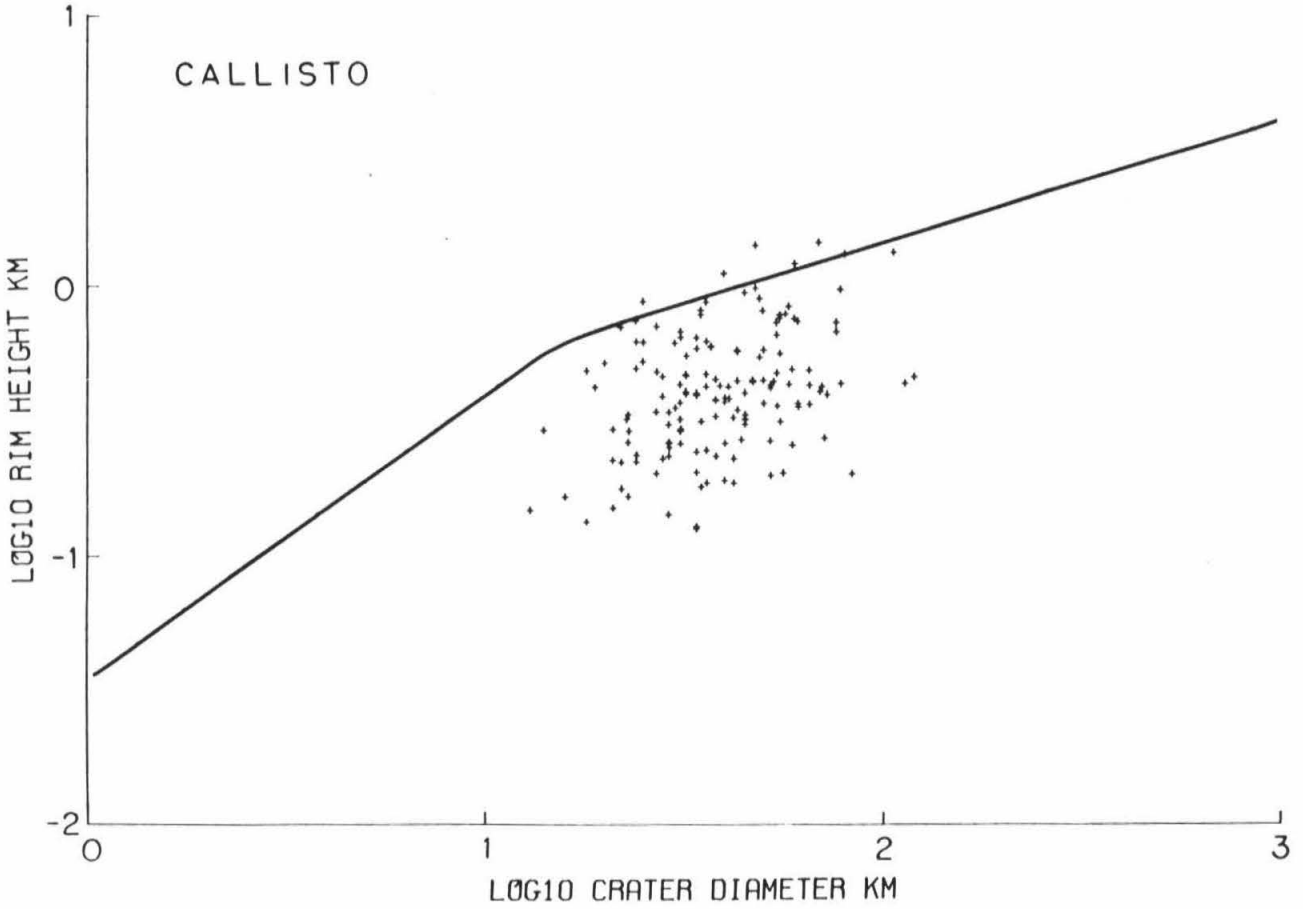

FIGURE 22 - Same as Figure 7 except that this graph is for 153 craters on Callisto.

Figure 22 shows a plot of rim height versus crater diameter for 153 craters on Callisto. The rim heights are generally less than for fresh lunar craters.

THEORY OF VISCOUS RELAXATION OF CRATERS

Viscosity of ice

It is well known that the strain rate $\dot{\varepsilon}$ of crystalline ice is not proportional to the stress γ but rather a power law relationship exists where

$$\dot{\varepsilon} = K\gamma^n \tag{4}$$

where n is a constant and is equal to about 4, and K is a constant (Glen, 1952). The flow law for glacial ice has been expanded in a polynomial power law form containing linear, cubic, and fifth-order terms (Colbeck and Evans, 1973)

$$\dot{\varepsilon} = B_1\gamma + B_2\gamma^3 + B_3\gamma^5 \ . \tag{5}$$

The presence of the linear term is suggested from analysis at low stresses and the fifth-order term was included to take into account the decrease in viscosity with increasing stress. Deformation mechanism maps for ice (Shoji and Higashi, 1978; Goodman et al., 1981) indicate that at the temperatures of interest in the lithospheres of Ganymede and Callisto (i.e. 120K - 180K) and at the effective deviatoric stress levels resulting from the perturbation of the surface by the crater relief (deviatoric stresses generally less than about 1.3×10^6 N m^{-2}), the dominant deformation mechanism is creep by boundary diffusion. For this deformation mechanism, Bromer and Kingery (1968) observed a strain rate which varied linearly with stress; thus, although the strain rate of ice is non-linear with stress at high stresses and/or high temperatures, for the lithospheres of Ganymede and Callisto, the approximation of a Newtonian viscous fluid appears to be adequate, at least to first order.

Viscosity gradient in icy lithospheres

Early in their histories, Ganymede and Callisto must have had relatively thin rigid icy lithospheres overlying convecting asthenospheres. The observed craters are supported by these structurally stable lithospheres. The base of the lithosphere would be determined by an effective viscosity that permits free convection in the underlying asthenosphere; nominally the effective viscosity of the convecting region is taken to be approximately 10^{18} poise. The boundary between the lithosphere and asthenosphere is not sharply defined but is actually a transition layer.

Except for transients produced by large impacts, heat flow through the predominantly icy lithosphere is governed almost entirely by the temperature difference between the top and base of the lithosphere, with the mode of heat transport through the lithosphere being conduction. The temperature at the top of the lithosphere is controlled by radiation, in the case of the absence of an insulating regolith layer, and the temperature at the base of the lithosphere is that temperature that would correspond to a viscosity of 10^{18} poise. For steady heat flow, the thermal gradient will be $\delta T/\delta Z = H/K$, where H is the heat flow and K is the conductivity of the lithosphere; actually the conductivity of ice K is a function of temperature T (Hobbs, 1974) and so the thermal gradient $\delta T/\delta Z$ will not be linear with depth. Over the temperature range of interest for the lithospheres of Ganymede and Callisto (i.e. 120 to 180 K), the range in the value of K is from ~4 W/m^2 to ~3 W/m^2; thus, for a constant heat flow, the thermal gradient will differ only slightly from a linear gradient with depth, Z. This will be discussed in greater detail later in this paper. Because the viscosity of ice is a strong function of temperature, with viscosity decreasing exponentially with increasing temperature (Hobbs, 1974), then a constant heat flow through an icy

lithosphere will approximately correspond to an exponentially decreasing viscosity gradient with depth.

Model for crater relaxation

The relaxation of craters in a medium of uniform Newtonian viscosity has been studied by Danes (1962, 1965) and Scott (1967). Viscous relaxation of topography in a medium where viscosity is a function of depth has been analyzed by Danes (1968), Brennen (1974), and more recently by Parmentier and Head (1981).

In this paper, the viscosity will be taken to be an exponential function of depth, at any given time. The axial symmetry of craters allows their topographic relief to be represented by a series of cylindrical harmonics. The relief $h(r)$, where r is the radial distance from the center, is given by

$$h(r) = \sum_{m=0}^{M} A_m \, J_o(k_m \, r) \tag{6}$$

where A_m is the amplitude of the m^{th} harmonic, J_o is the zero-order Bessel function, k_m is the wavenumber of harmonic m; the values of k_m are chosen such that $k_1, k_2, \cdots$ are the roots of $J_o(r) = 0$, and M is the upper limit to the number of harmonics used in the model (M = 30 for this study). The radial resolution used is $1/30^{th}$ of the crater rim radius and the limit to the radial distance used in the profile is twice the rim radius. The values of the constant A_m for the various harmonics can be calculated from

$$A_m = \frac{2}{J_1(k_m)} \int_0^1 r \, h(r) \, J_o(k_m r) \, dr \tag{7}$$

where J_1 is the first-order Bessel function, and r=1 corresponds to the maximum radial distance of the profile.

For the viscous flow in a medium whose state is constant with time, the time dependence of the topographic relief is given by

$$h(r,t) = \sum_{m=1}^{M} A_m J_o(k_m r) e^{\frac{-t}{\tau_m}} \tag{8}$$

where t is time, and τ_m is the relaxation time for a given harmonic wavenumber.

For this study, it is assumed that the viscosity is a function of depth with the form

$$\eta(z) = \eta_o e^{-\lambda z} \tag{9}$$

where $\eta(z)$ is the viscosity at depth z, η_o is the surface viscosity, and λ is the reciprocal e-folding depth for viscosity (i.e. $\lambda = L^{-1}$, where L is negative with depth). For this case, the relaxation time τ_m can be expressed (Brennen, 1974) as

$$\tau_m = \frac{\eta_o k_m \kappa}{\rho g} \tag{10}$$

where k_m is the wavenumber of the harmonic m, ρ is the density of the medium (for ice ρ=0.93 g cm^{-3}), g is the surface gravity (g =142 cm sec^{-2} for Ganymede and g =121 cm sec^{-2} for Callisto) and κ is defined as

$$\kappa = \frac{\lambda}{k}\left[1+\frac{1}{2}\left[\frac{\lambda}{\beta}+\frac{\beta}{\lambda}\left(\frac{\lambda}{k}\right)^2\left(1+\frac{2\beta}{\lambda}\right)^2\right]\right] \tag{11}$$

where

$$\beta = \left[\frac{1}{2}\left[k^2+\left(\frac{\lambda}{2}\right)^2+\left(k^2\lambda^2+\left(k^2+\left(\frac{\lambda}{2}\right)^2\right)^2\right)^{\frac{1}{2}}\right]\right]^{\frac{1}{2}} . \tag{12}$$

When λ/k is very small, τ_m (10) becomes

$$\tau_m = \frac{2\eta_o k_m}{\rho g} \tag{13}$$

which corresponds to the solution of Danes (1962, 1965) for a medium of

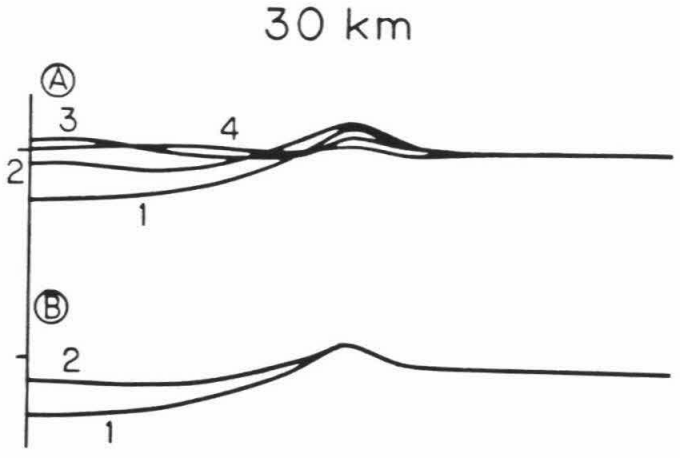

FIGURE 23 - Theoretical relaxation of a 30 km diameter crater in a viscous medium where viscosity decreases exponentially with depth from a surface viscosity of 10^{26} poise; for case (A) L = 1.0 km, and for case (B) L = 8.0 km. L is the e-folding depth of viscosity ($L = \lambda^{-1}$). The most flattened profile for each case corresponds to 4 Gy.

uniform viscosity.

Examples of theoretical crater relaxation

The theoretical relaxation of a 30 km crater on Ganymede is illustrated in Figure 23. The initial crater shape, at t=0, is modelled after fresh lunar craters (Pike, 1977). For the first example, the viscosity at the top of the lithosphere was chosen to be 10^{26} poise (the reason for choosing this value will become apparent later); the viscosity gradient was assumed to have an e-folding depth of 1.0 km, for an exponentially decreasing viscosity. Four distinct stages of relaxation can be identified from this first example (Figure 23a); these are (1) when the crater shape is similar to that of fresh lunar craters and the floor is not detectably bowed up, (2) when the crater floor is noticeably bowed up but when the elevation of the floor is below the pre-crater level (defined by the elevation of the surrounding plain beyond the ejecta deposit), (3) when the elevation of the bowed up floor exceeds the pre-crater level, and (4) when the crater relief is flattened to the point where only a small fraction of the initial rim relief remains and the crater floor is essentially at the pre-crater level.

The second example (Figure 23b) shows the theoretical relaxation of a 30 km diameter crater in a viscous medium where the viscosity at the top of the lithosphere is 10^{26} poise and the viscosity e-folding depth is 8 km. In this case the final form of the crater after 4 Gy is preserved with only slight bowing-up of the crater floor (Stage 2).

HISTORY OF CRATER PRODUCTION AND RELAXATION

Classification of craters by degree of relaxation

In order to determine the time history of a changing rheology based on crater statistics, it will be necessary to develop a scheme for differentiating

craters that have flattened to different stages of relaxation. Although depth versus diameter relationships may be useful in this regard (as illustrated in Figures 6, 11, and 21), the bowing up of the crater floor poses a problem in defining the point to which the depth measurement is assigned; also any absolute or systematic errors in the depth measurements from the photoclinometric profiles will be propagated. The method used in this paper is to assign the craters in the sample into four categories; these categories correspond to the four stages of relaxation that were observed in the theoretical relaxation studies. The four stages correspond to: (1) craters which do not display bowed up floors (i.e. those craters where the maximum depth is located at the center of the crater), (2) craters in which the bowing up of the floor can be discerned but where the elevation of the floor center does not exceed the pre-crater level, (3) craters in which the elevation of the bowed-up floor exceeds the pre-crater level, and (4) craters that are extremely flattened and the maximum relief is $\leq$ 200 meters. This classification scheme, illustrated by the photoclinometric profiles in Figure 24, covers the observed forms of craters on Ganymede and Callisto.

Table III-A lists the degree of flattening versus crater diameter for 363 craters and palimpsests on the heavily cratered terrain on Ganymede. It may be seen from the data in Table III that the fraction of small craters which exhibit bowed-up floors is not as large as the fraction of larger craters. This is in agreement with viscous relaxation theory which predicts that the rate of relaxation is proportional to the size of the topographic feature. Table III-B is for craters on the grooved terrain on Ganymede and Table III-C is for craters on Callisto.

Time scale for crater flattening

By combining the data presented in Table III with the cratering time scale for Ganymede and Callisto proposed by Shoemaker and Wolfe (1982), it is possible

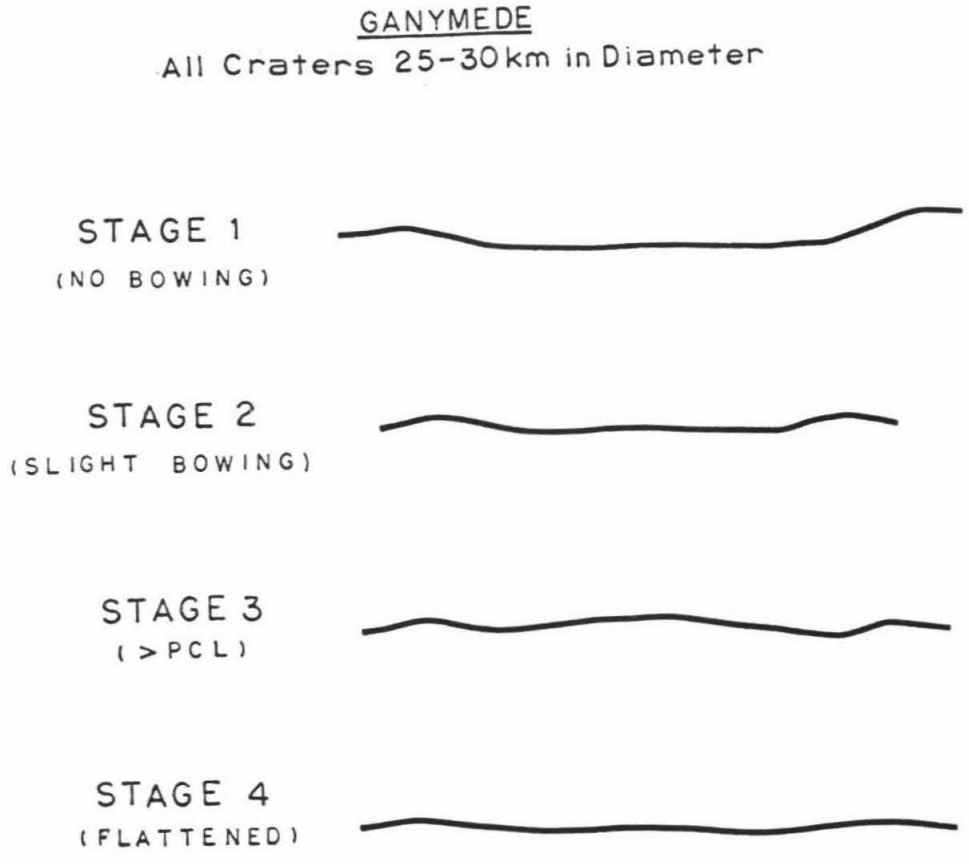

FIGURE 24 - Photoclinometric profiles of four craters 25-30 km in diameter that are located in the heavily cratered terrain of Ganymede. Each of these craters is presently preserved at a different stage of crater relaxation ranging from fresh (1) through bowed up floors (2-3), and finally to a very flattened stage (4). The vertical scale is the same as the horizontal scale.

TABLE III - Degree of bowing up versus diameter

Diameter (km)	No Bowing No.	%	Slight Bowing No.	%	Above PCL[1] No.	%	Flat[2] No.	%	Total No.
			(A) Ganymede - Heavily Cratered Terrain						
0-10	45	94	3	6	--	--	--	--	48
10-20	53	51	34	33	7	7	10	10	104
20-30	38	38	26	26	24	24	13	13	101
30-40	11	22	24	48	9	18	6	12	50
40-50	4	13	15	50	6	20	5	17	30
> 50	1	3	8	27	4	13	17	57	30
Total									363
			(B) Ganymede - Grooved Terrain						
0-10	119	92	10	8	--	--	--	--	129
10-20	129	74	41	23	3	2	2	1	175
20-30	43	52	31	38	7	9	1	1	82
30-40	17	35	30	61	2	4	--	--	49
40-50	6	32	12	63	1	5	--	--	19
> 50	1	4	21	75	3	11	3	11	28
Total									482
			(C) Callisto						
10-20	5	83	1	17	--	--	--	--	6
20-30	27	79	6	18	1	3	--	--	34
30-40	24	55	20	45	--	--	--	--	44
40-50	6	23	14	54	6	23	--	--	26
> 50	1	2	30	70	12	28	--	--	43
Total									153

[1] Above PCL -- Where crater floor has bowed-up above the pre-crater level.

[2] Where the maximum relief is less than 200 meters.

to determine the times for the onset of the various stages of crater flattening. It has been shown that model age differences between the leading and trailing hemispheres of Ganymede and of Callisto range up to about 200-300 MY (Passey and Shoemaker, 1982; Shoemaker et al., 1982; Passey, in press); by comparing the statistics on the degree of flattening of craters in the leading hemisphere with those in the trailing hemisphere, however, it was found that no significant difference exists in the degree of flattening; for the analysis presented here, the mean model age for the surface terrains (i.e. the age of the surface 90° from the apex of orbital motion) will be used. The effect of location on the satellite will be discussed later.

The model ages of the heavily cratered terrains of Ganymede and Callisto depend somewhat on the crater size used in determining age; surface model ages determined from craters ≥ 50 km in diameter are up to about 200 MY younger than ages determined from craters ≥ 10 km in diameter. These differences have been attributed to the loss of many of the large craters by viscous relaxation. The effect of this on the age determination can also be corrected for, but will be discussed later as a correction; this is done to avoid confusing the data with assumptions for loss statistics.

The mean model age that will be used for the heavily cratered terrain on Ganymede is 3.87 Gy, based on 250 craters ≥ 10 km/10^6 km^2 (Passey and Shoemaker, 1982); the mean model age for the grooved terrain used here is 3.65 Gy, based on 90 craters ≥ 10 km/10^6 km^2. The mean model age for the surface of Callisto is 4.10 Gy, based on 49 craters ≥ 30 km/10^6 km^2 (Passey, in press).

Figure 25 shows age versus the degree of flattening for various size craters on Ganymede; Figure 25a is for the heavily cratered terrain and Figure 25b is for the grooved terrain. As an example, 10 km craters on the heavily cratered

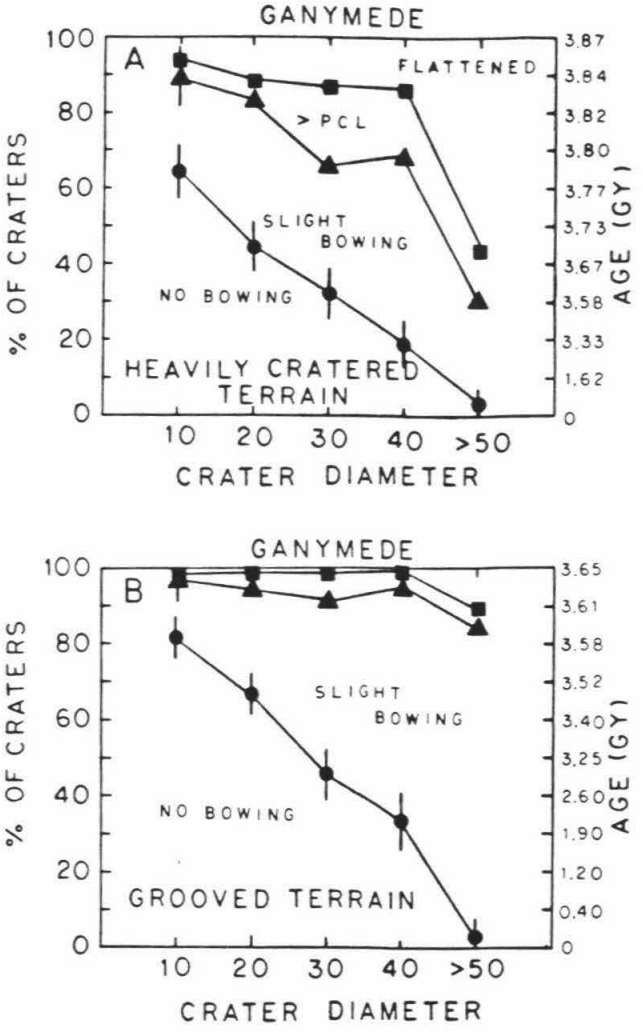

FIGURE 25 - This is a graphical representation of the data in Table III for Ganymede. Figure (A) is for the heavily cratered terrain and (B) is for the grooved terrain. The solid circles refer to crater floors that are slightly bowed-up, the solid triangles refer to craters for which the floors are bowed-up above the pre-crater level, and the solid squares are for craters which have a maximum topographic relief of less than about 200 meters (i.e. "flattened" craters). The ages on the right hand axis are derived from the cratering time scale of Shoemaker and Wolfe (1982). As an example, ~35% of the craters on the heavily cratered terrain that are 30 km in diameter, do not exhibit bowed-up floors; therefore, if a 30 km crater does not exhibit a bowed-up floor, its age is less than 3.58 GY; conversely if a 30 km crater displays a bowed-up floor but if the bowing up does not exceed the pre-crater level, that crater is older than 3.58 GY but less than ~3.80 GY.

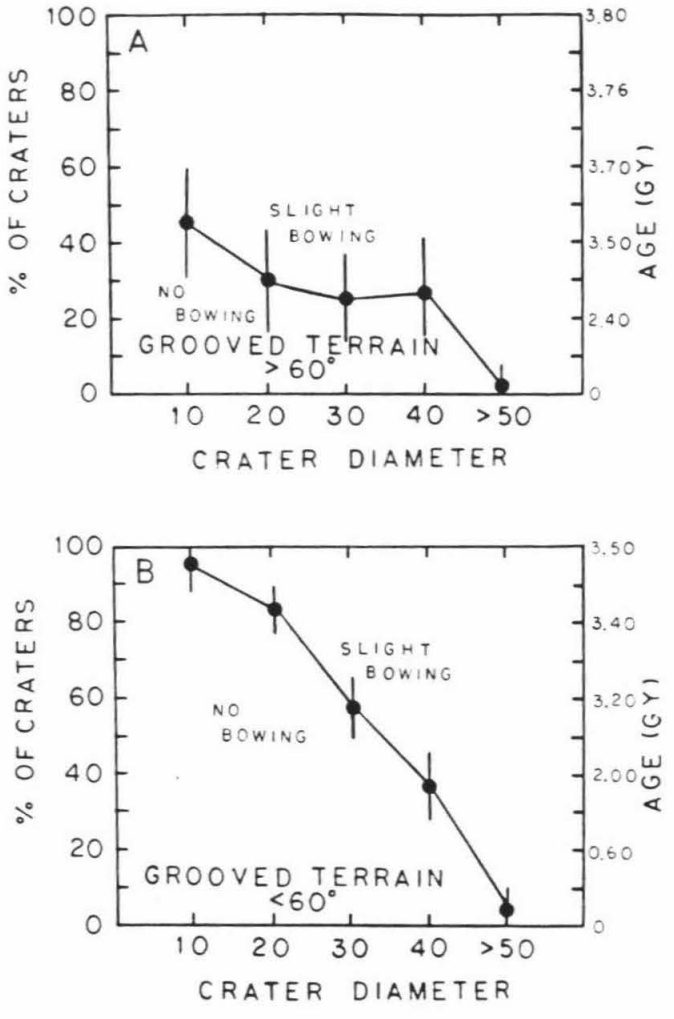

FIGURE 26 - Same as for Figure 25 except that this figure is exclusively for the grooved terrain of Ganymede. (A) is for the oldest grooved terrain which is located at latitudes > 60°; (B) is for younger grooved terrain which is located at latitudes < 60°.

terrain will display bowed-up floors (≥ Stage 2) if they formed prior to 3.78 Gy whereas 40 km craters will display bowed-up floors (circles, Figure 25a) if they formed prior to 3.33 Gy. Similarly, 10 km craters will display floors that are bowed-up above the pre-crater level (triangles, Figure 25a) if they formed prior to 3.84 Gy and 40 km craters will display this if they formed prior to 3.79 Gy.

In Figure 25b a similar distribution for craters on grooved terrain can be seen. Because the oldest grooved terrain is located near the south pole (age ~ 3.80 Gy) and because the craters in this region are the most flattened, the statistics from this region were subtracted from those of the rest of the grooved terrain; the resulting distributions for the onset of bowing-up of the crater floor versus crater diameter for two different age grooved terrain units are shown in Figure 26. From Figure 26 it is apparent that bowed-up floors will be present in 10 km diameter craters older than ~3.50 Gy, and in 30 km diameter craters older than ~3.20 Gy.

Comparison of these results with those obtained for the heavily cratered terrain on Ganymede suggests that at a given time, craters of a given size on grooved terrain were relaxing slightly faster than craters on the heavily cratered terrain. This difference can be seen by comparing the age versus degree of flattening in Figure 25a with that in Figure 25b for various size craters. This implies that at a given time, either the viscosity of the lithospheric material in the grooved terrain was slightly less than the viscosity of the material in the heavily cratered terrain, or that the viscosity gradient in the grooved terrain was steeper than in the adjacent heavily cratered terrain.

A similar plot of mean age versus the degree of flattening for various size craters on Callisto is shown in Figure 27. As an example, a 15 km crater will have a bowed-up floor if it formed before 4.07 Gy whereas a 45 km crater will

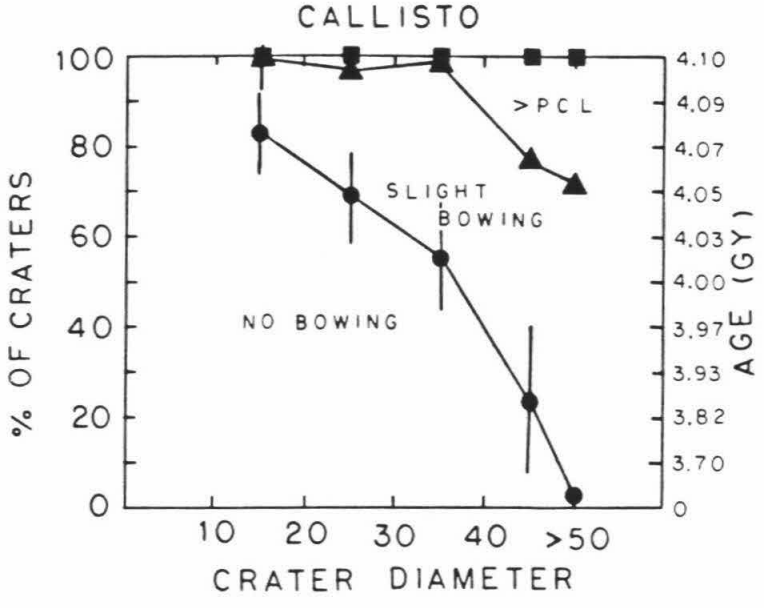

FIGURE 27 - Same as for Figure 25 except that this figure is for Callisto.

display a bowed-up floor if it formed before 3.85 Gy.

Time variable viscosity gradient

Based on the cratering time scale of Shoemaker and Wolfe (1982), most of the highly relaxed craters formed within 500 million years, or so, of the age of the surface on which they lie (age at 100% of craters, Figures 25, 26, and 27). During the remaining 3.0 to 3.5 Gy, little significant relaxation of craters ≤ 30 km in diameter has occurred. In order to have a large amount of relaxation within a relatively short time interval, and to have little subsequent relaxation during a much longer time interval requires that the overall effective viscosity of the lithosphere was significantly less during early periods than it was during later times. It is reasonable to expect that the overall lower effective viscosity of the upper lithosphere at an early period simply reflects a steeper viscosity gradient and, thus, a higher heat flow. It would also be expected that the heat flow decayed with time, regardless of the source, and that the viscosity gradient would also decay with time. Assuming that the viscosity gradient decays exponentially with time, the viscosity gradient can be expressed as

$$L(t) = L_F + (L_I - L_F)\exp(\frac{-t}{\tau_v}) \qquad (14)$$

where L_I is the initial e-folding depth of viscosity ($L_I = \lambda_I^{-1}$), L_F is the final e-folding depth of viscosity, t is time, and τ_v is the time constant for the rate of change of the viscosity gradient. Each of these variables, with the exception of time, are be treated as an independent variable in this study; the determination of the values of these quantities will depend on comparison of the statistics of observed crater relaxation with results from the theoretical model. For the case of a time variable viscosity gradient with depth, the constants for the various harmonics of the crater topography (7) and the corresponding relaxation times

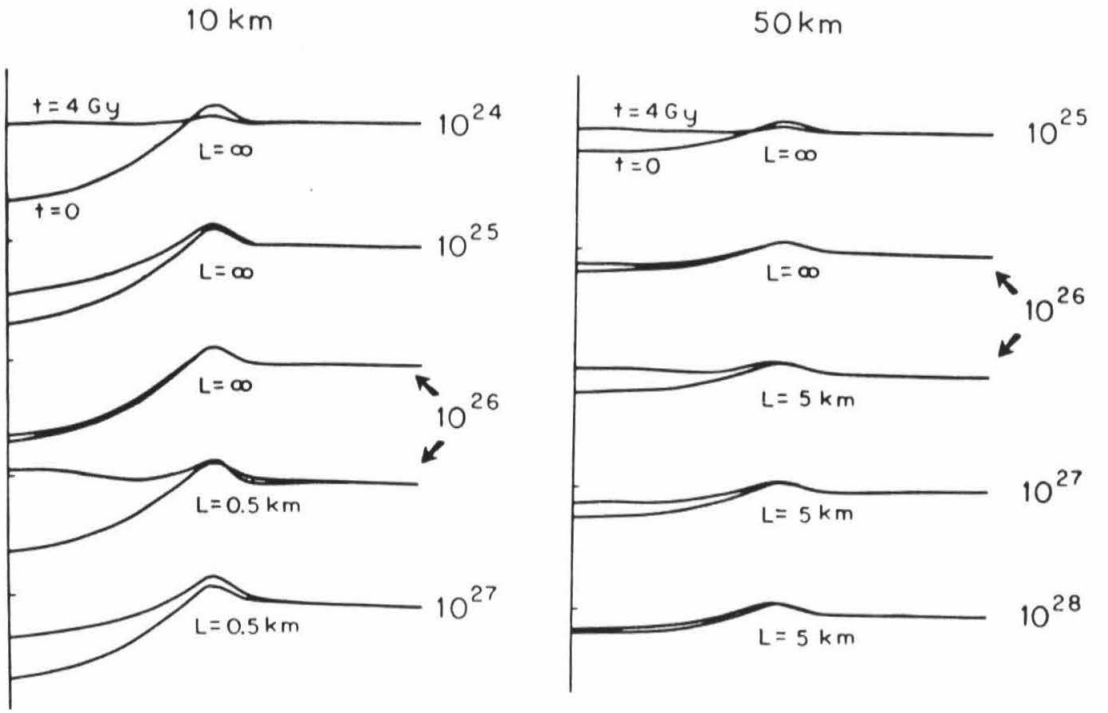

FIGURE 28 - The value for the viscosity at the top of the lithosphere is determined from this figure. Shown are examples of the results for crater relaxation as a function of time from the numerical model for various choices of surface viscosity. Shown are the theoretical relaxations of 10 km and 50 km diameter craters. The required criterion is that for a single surface viscosity, 10 km craters will be able to flatten under conditions of a steep viscosity gradient, whereas 50 km craters can be relatively well preserved under conditions of a relatively flat viscosity gradient. The only value for the surface viscosity that satisfies this is 10^{26} poise.

for the various harmonics τ_m (10) are recalculated after each time step.

Comparison of model with crater statistics

It is now necessary to determine the value of the surface viscosity (η_o). In that the surface viscosity to be used in the model for 10 km craters must be approximately the same as for 50 km craters in the same terrain, it is possible to assign limits to the surface viscosity η_o by determining what values of η_o will result in highly flattened 10 km craters (using a steep viscosity gradient with depth) at an early period in time, and yet allow for 50 km craters to be well preserved from a slightly later period in time (when the viscosity gradient was not as steep). It can be seen that if a 10 km diameter crater were formed in a half space of viscosity 10^{24} poise, and allowed to flatten for 4 Gy, extremely little of the initial topography would remain (Figure 28). Similarly, a 50 km diameter crater in a 10^{25} poise half space (i.e. L = infinity; no thermal or viscosity gradient) would also flatten beyond recognition if it were allowed to relax over a time period of 4 Gy; but this viscosity would allow a 10 km diameter crater to be preserved in a slightly relaxed state after 4 Gy. A 10 km diameter crater in a 10^{26} poise half space will not significantly flatten in 4 Gy, but if it is assumed that the viscosity of this medium decreases exponentially with depth, the 10 km diameter crater will flatten substantially in 4 Gy (assuming L = 0.5 km). A 50 km diameter crater can be preserved in various stages of relaxation by varying the viscosity gradient, in a medium with a surface viscosity of 10^{26}, 10^{27}, and 10^{28} poise. A surface viscosity of 10^{27} poise, or higher, will not allow for sufficient flattening of 10 km craters, even if a very steep viscosity gradient with depth exists; thus, surface viscosities $> 10^{27}$ poise are unacceptable to explain the observed flattened 10 km craters. Surface viscosities $\geq 10^{28}$ poise are too great to allow craters ≤ 50 km to flatten sufficiently over geologic time regard-

less of the viscosity gradient. The derived surface viscosity for the ice-rock mixture in the lithosphere of Ganymede is 10^{26} poise, with a possible range from 5 x 10^{25} to 5 x 10^{26} poise; this range is based on the fact that 10^{25} poise is too low for large craters, and 10^{27} poise is too high for small craters. For Callisto the value is probably the same, but because of the few number of flattened small craters ($\leq$ 20 km) in the sample, a surface viscosity of 10^{27} poise cannot be excluded. Surface viscosities in excess of 10^{28} poise are much too great. As the surface temperatures of both Ganymede and Callisto are very nearly the same (Squyres, 1980b), it will be assumed that the better constrained value of 10^{26} poise for the surface viscosity derived for Ganymede will be equally applicable to Callisto. Using this value for the surface viscosity, the e-folding depth, L_I, of viscosity at an early period in its history is found to be $\leq$ 1.0 km for Ganymede, and between 1.0 and 3.0 for Callisto, in order to produce the observed flattening of 10 km craters. In order to preserve the observed relief in 50 km craters, the e-folding viscosity depth, L_F, must have increased to between 10 and 30 km at a later period.

As a changing viscosity gradient is required to explain the variety of relaxed craters of different size observed on Ganymede and Callisto, our problem is to determine the approximate rate of change of this gradient with time. The data presented in Figures 25, 26, and 27 allow for this determination. It will be assumed that the viscosity gradient was decreasing exponentially with time, given in eq.(14). Figure 29 shows various model fits to the data from the heavily cratered terrain on Ganymede using various values of τ_v, L_I and L_F. The points marking the boundary between the 'Flattened" and "> PCL" craters are excluded from the comparison because the category 'Flattened" involves an absolute measurement of topographic relief and would be extremely biased by the

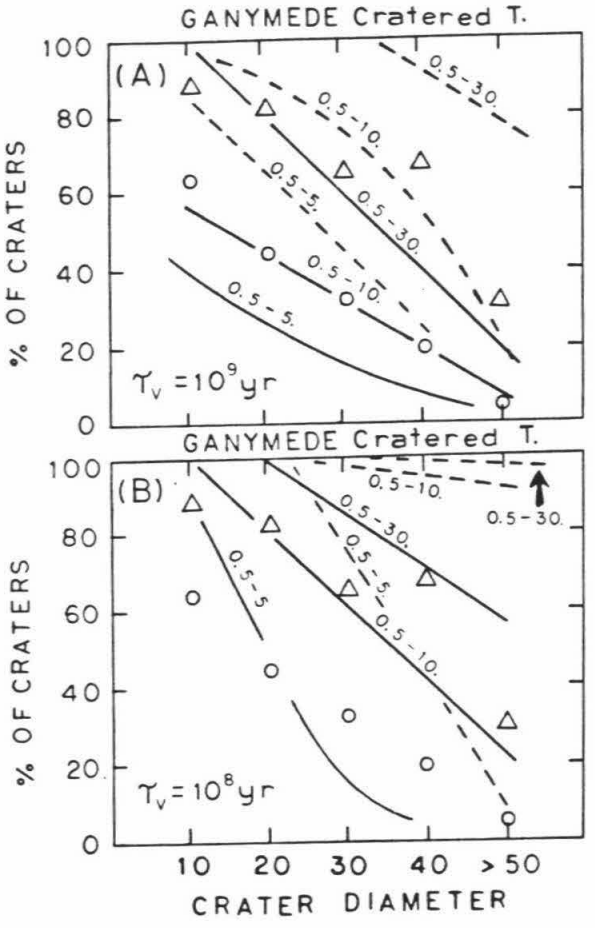

FIGURE 29 - Comparison of model calculations with part of the data illustrated in Figure 25. The open circles are frequencies at the onset of bowing up of the crater floor; the open triangles are the frequencies at which the bowing up of the crater floor exceeds the pre-crater level. The solid lines are to be compared to the circles and the broken lines are to be compared to the triangles. A reasonably good fit to both the circles and the triangles is found when τ_v, the e-folding time constant for the changing viscosity gradient, is 10^9 years, and the initial e-folding depth for viscosity L_I is -0.5 km and the final e-folding depth for viscosity L_F is -10. km as shown in (A). No reasonable fit to the data was achieved using τ_v of 10^8 years (B) within the constraints on L.

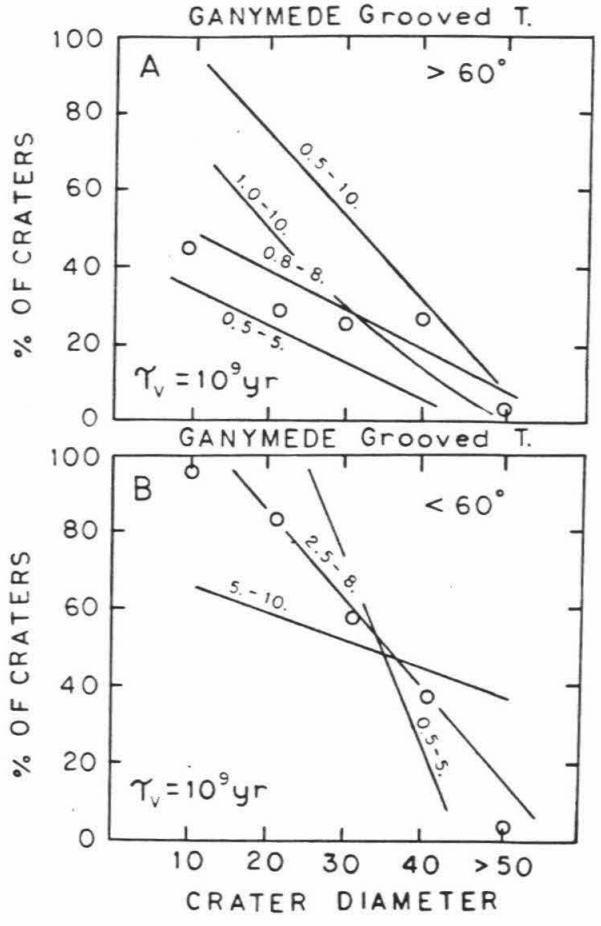

FIGURE 30 - Same as for Figure 29 except that this figure shows comparisons of results from the model with the data from the grooved terrain of Ganymede.

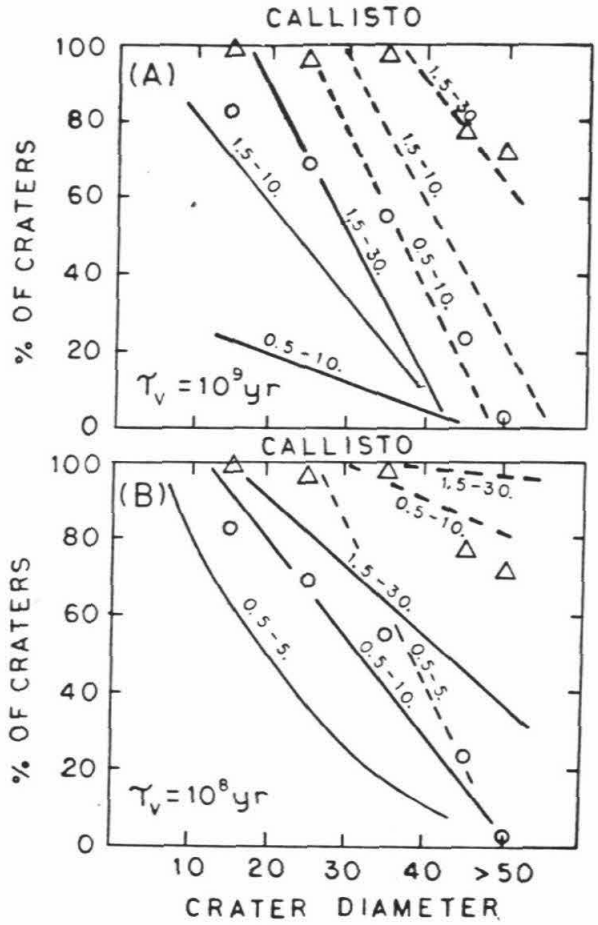

FIGURE 31 - Same as for Figure 29 except that this figure shows comparisons of results from the model with the data for Callisto. Reasonable fits to the data are found for both a τ_v of 10^8 and 10^9 years; these are discussed in the text.

assumption of the initial relief for the theoretical crater. The best fit to the data from the heavily cratered terrain assumes $\tau_v = 10^9$ years, $L_I = 0.5$ km, and $L_F = 10$ km. The possible range in L_I and L_F as a function of τ_v is shown in Figure 32.

Figure 30 shows various model fits to the data from the grooved terrain. Here, the best fit assumes $\tau_v = 10^9$ years, $L_I = 1$ km, and $L_F = 3$ to 5 km. The possible range in these values is shown in Figure 32.

Figure 31 shows a similar comparison for Callisto. The best fit is for $\tau_v = 10^8$ to 10^9 years, $L_I = 0.5$ to 1.5 km, and $L_F = 10$ to 30 km. the possible range in these values is shown in Figure 32.

THERMAL HISTORY

Temperature-Viscosity relationship for ice

Assuming that within the temperature-stress regime of interest ice behaves like an ideal Newtonian viscous fluid, the viscosity can be expressed in the form (Weertman, 1970)

$$\eta(T) = \eta_m \exp[A^*(\frac{T_m}{T} - 1)] \qquad (15)$$

where $\eta(T)$ is the viscosity at temperature T, η_m is the viscosity at the melting point, T_m is the temperature at the melting point, and A^* is a constant depending on the creep activation energy. For polycrystalline ice, $T_m = 273$ K, η_m is 10^{14} poise, and the published range in creep activation energies is from 42 to 67.5 kJ/mol (listed in Homer and Glen, 1978); these activation energies correspond to a range in A^* of from 18 to about 29.

From the determination of the viscosity at the top of the lithospheres of Ganymede and Callisto, of $\eta_o = 1.0 \pm 0.5 \times 10^{26}$ poise, it is now possible to empir-

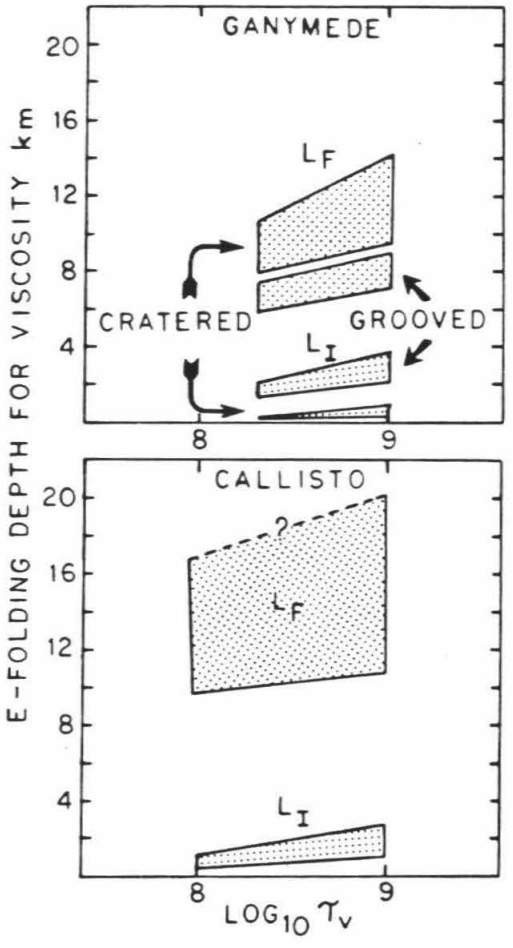

FIGURE 32 - Range in the acceptable values of L_I and L_F for variable choices of τ_v.

ically determine the value of the constant A^* for the ice-rock mixture in the lithospheres of Ganymede and Callisto. The mean equatorial surface temperature is ~120K for the heavily cratered terrain of Ganymede and ~125K for Callisto (Squyres, 1980b). These temperatures cannot be directly applied to the viscosity at the top of the lithosphere because an insulating regolith later must be present (Shoemaker et al., 1982). A regolith with a conductivity much less than the conductivity of a solid lithosphere must be present because there is no strong latitudinal dependence of flattening of craters on the heavily cratered terrain; near the polar regions, the surface temperature should be < 80K (Squyres, 1980b) and without an insulating regolith, craters near the poles should show much less relaxation than craters near the equator of equal age and size. Shoemaker et al. (1982) have calculated that on Ganymede, the thickness of the regolith near the south pole is of order ~40 meters thick; they also postulate that the thickness of the effective insulating regolith is controlled by thermal annealing at some depth within the regolith. They suggest that the temperature threshold above which the annealing process is efficient is approximately 130K, corresponding to the minimum surface temperature for which the ablation of H_2O frost on the surface of Ganymede is observed (Squyres, 1980b; Purves and Pilcher, 1980). Using T=130 ± 5 K and η= 1.0 ± 0.5 x 10^{26} poise in (15), yields a value for A^* of 25 ± 3.

Viscosity gradient versus thermal gradient

Using (15), it is possible to calculate a thermal gradient for a given e-folding depth of viscosity (L) for Ganymede and Callisto. Parmentier and Head (1981) have shown that for an exponentially decreasing viscosity with depth

$$\Delta_o = \frac{\delta T}{\delta Z}_{Z=0} = \frac{\lambda T_o^2}{A^* (T_m - T_o)} \qquad (16)$$

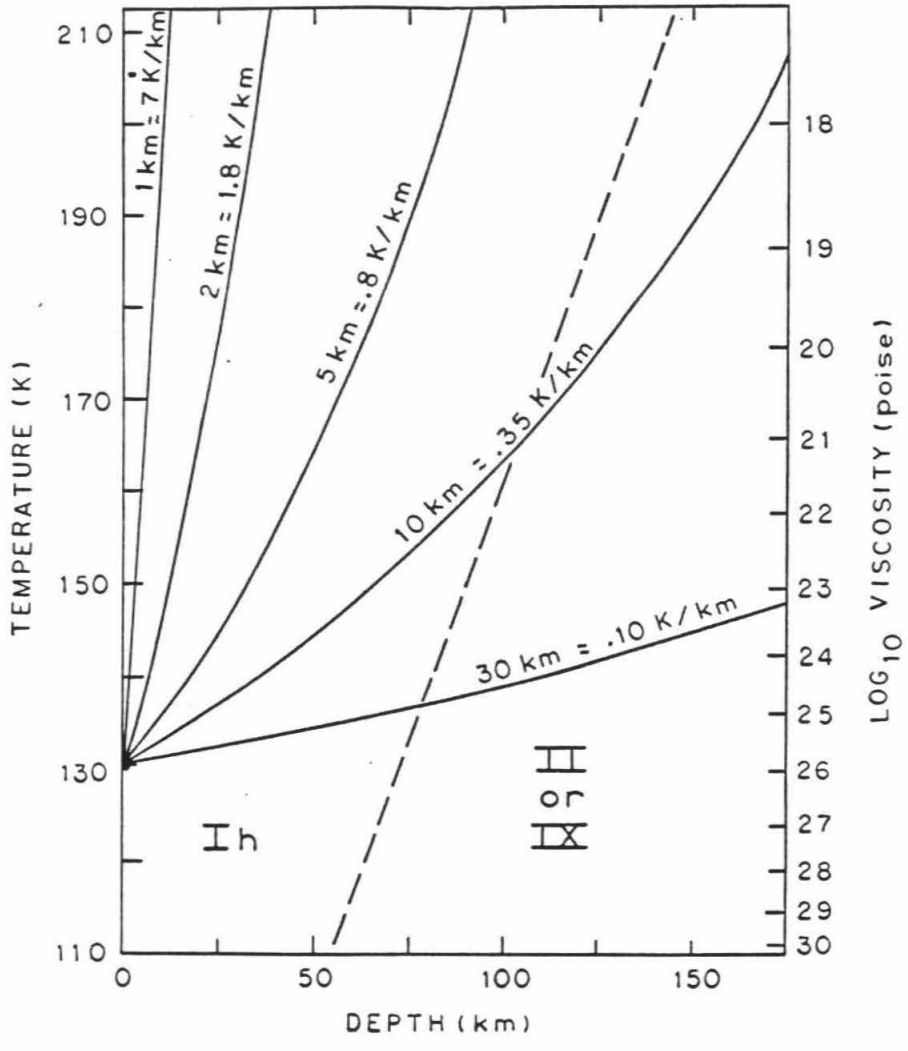

FIGURE 33 - Plot of Temperature and Log_{10} Viscosity (normalized at 130K = 10^{26} poise) as functions of depth. An exponential gradient of viscosity with depth (indicated by 1 km, 2 km, 5 km, etc.) can be approximated by a linear thermal gradient (7 K/km, 1.8 K/km, 0.8 K/km, etc.). The broken line marks the approximate phase boundary between ice Ih and ice II (or IX) (Hobbs, 1974).

where Δ_o is the thermal gradient immediately below the surface, T_o is the surface (top of lithosphere) temperature, and λ is the reciprocal e-folding viscosity depth ($\lambda = 1/L$). Relation (16) is valid only for the thermal gradient very near the surface and it should be noted that a linear thermal gradient with depth only approximates an exponential viscosity gradient, as is shown in Figure 33. From Figure 33 an e-folding viscosity depth of L=1 km is roughly the same as a linear near surface (< 25 km) thermal gradient of 7 K/km, L=2 km corresponds to ~1.8 K/km, L=5 km corresponds to ~0.8 K/km, L=10 km corresponds to ~0.3 K/km, and L=30 km corresponds to ~0.1 K/km. It should be pointed out that because of the strong exponential dependence of viscosity on temperature (15), the calculated thermal gradients are relatively insensitive to the choice of η_o (i.e. within the uncertainty of A^*).

Assuming a linear thermal gradient to model an exponential viscosity gradient is adequate but care must be taken in interpreting the thermal gradients derived from craters of different diameters. Because of the slight curvilinear trend illustrated in Figure 33, the derived thermal gradient averaged over shallow depths (< 25 km) will be slightly less than the derived thermal gradient averaged over greater depths (> 50 km). Figure 34 quantifies this effect; for example, an e-folding depth L of 2 km derived from craters 10-20 km in diameter (i.e. affected most by the thermal gradient in upper 25 km) yields a thermal gradient of ~2 K/km; for craters 50 km in diameter, the viscous flow occurs over much deeper regions and a gradient of ~3 K/km is indicated. Although the actual thermal gradient at any given time is only approximately linear with depth in the upper lithosphere, the corrections mentioned above allow for more meaningful interpretation of the results derived from the model, which contains

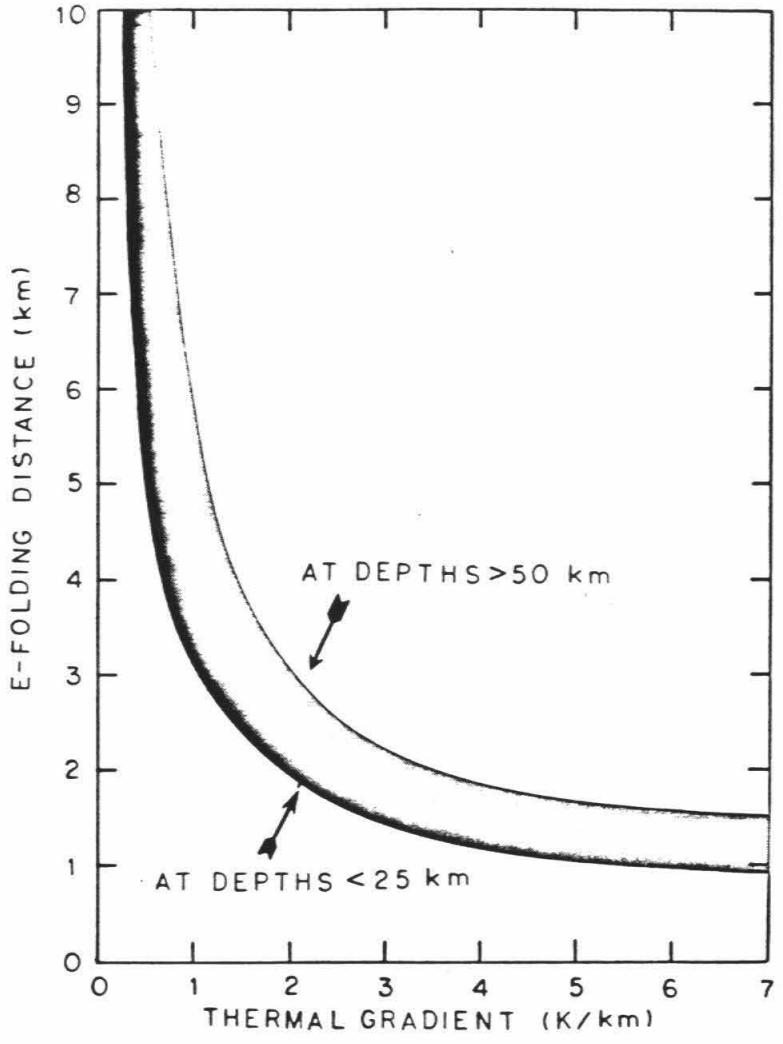

FIGURE 34 - The e-folding depth of viscosity (L or λ^{-1}) is plotted versus thermal gradient in this figure. Because of the slight curvilinear trend shown in Figure 33 of depth versus viscosity, the thermal gradient averaged over shallow depths (< 25 km) is slightly less than the thermal gradient for the same e-folding viscosity depth averaged over deeper regions (> 50 km).

slight errors inherent to the assumption that the viscosity varies exponentially with depth.

Derived thermal history

For Ganymede, the best fit for a surface viscosity of 10^{26} poise requires a thermal gradient in excess of ~14 K/km at a period of time ~3.87 GYA, and must have decreased to about 0.3 K/km by the present time (using the thermal gradient averaged over the top 25 km). Using the thermal gradients averaged over 50 km depth, the present thermal gradient for Ganymede is approximately 1.2 K/km (upper range of stippled region). For Callisto, it appears that the early thermal gradient was between 3 and 7 K/km and at the present day, the thermal gradient is between 0.3 and 0.1 K/km; using the thermal gradients averaged over 50 km depth, the present thermal gradient is between 0.8 and 1.2 K/km. Because of the nonlinear relation between the thermal gradient and the viscosity gradient, the e-folding time for the changing viscosity gradient (τ_v) is not the same as for a changing thermal gradient. Figure 35 shows the derived histories for the thermal gradients of Ganymede and Callisto; the approximate e-folding time for the changing thermal gradient is between 5 x 10^7 years (for the steep part of the curves) and 2 x 10^8 years, after the thermal gradient drops below about 3 K/km (solid lines).

Heat flow versus thermal gradient

Of primary interest is how the heat flow has changed with time. The heat flow at the top of the lithosphere for Ganymede at 3.87 Gy would be $\geq$ 3.2 x 10^{-2} W m^{-2} (Figure 36) based on a conductivity of 4 W m^{-1} deg^{-1} and a thermal gradient of $\geq$ 8 K/km. By 3.5 Gy the heat flow had declined to ~4.0 x 10^{-3} W m^{-2}, based on the same conductivity and a thermal gradient of ~1 K/km. If we use the thermal gradient averaged over 50 km depth (because of the inexactness of the

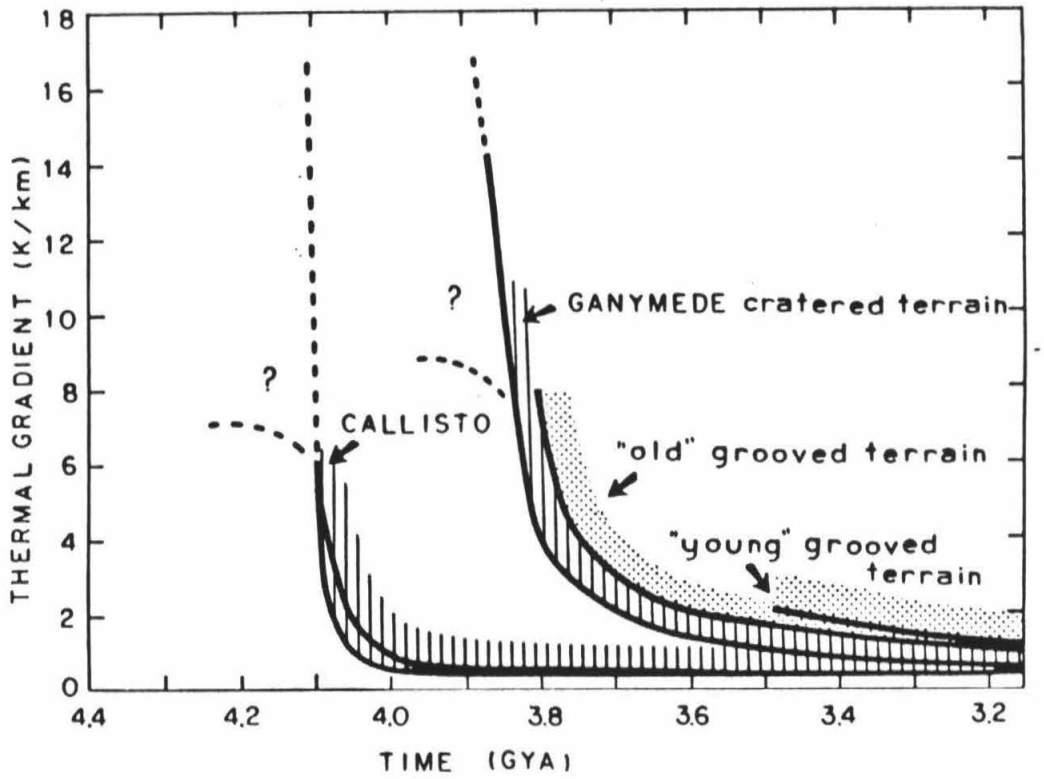

FIGURE 35 - The derived histories of the thermal gradient for Ganymede and Callisto are shown here. The broken line indicates the acceptable region that would take into account the loss of large craters by viscous relaxation during a period when the thermal gradient was relatively steep (> 8 K/km). The stippled regions show the derived thermal gradients averaged over 50 km depth; the heavy solid lines show the thermal gradients averaged over depths < 25 km. At any given time the thermal gradient in the grooved terrain is slightly steeper than the gradient derived for the heavily cratered terrain of Ganymede.

inversion of an exponential viscosity gradient to a linear thermal gradient) the upper bound to the heat flow at ~3.5 Gy is ~6.0 x 10^{-3} W m^{-2}, based on a conductivity of 3 W m^{-1} deg^{-1} (because of the warmer ice in the interior) and an upper limit to the thermal gradient would be ~2 K/km (refer to stippled region in Figure 35). Assuming that the viscosity at the top of the lithosphere has been maintained at 10^{26} poise, the present day heat flow would be 3.0 ± 1.4 x 10^{-3} W m^{-2}.

Corrections for crater loss

Because of the relatively steep thermal gradient on Ganymede around 3.87 Gya (and probably for Callisto around 4.10 Gya) required to flatten 10 km craters to the observed degree, craters much larger than 10 km, that formed during this period, must have flattened beyond the limit of recognition. Because of this, the ages shown in Figure 35 (based on number of crater ≥ 10 km in diameter) are probably slightly in error in the regions of the very steep thermal gradients. Also, a thermal gradient that continually increases with increasing age, at the derived rate, is not a physically reasonable assumption, thus, the possibility that the thermal gradient was maintained more or less constant prior to 3.9 Gya will now be investigated.

If the thermal gradient was indeed maintained constant at a reasonably high thermal gradient (> 8 K/km, but less than the 14 K/km calculated earlier), then the amount of relaxation occurring during a relatively short interval of time can be greater than the subsequent relaxation over the rest of geologic time when the thermal gradient is much less. Studies of crater relaxation indicate that a thermal gradient of about 8 K/km (L=0.8 km) maintained constant over a period of time of about 100 My prior to 3.9 Gya, will allow sufficient relaxation of 10 km craters so that with the subsequent relaxation after 3.9 Gya, the

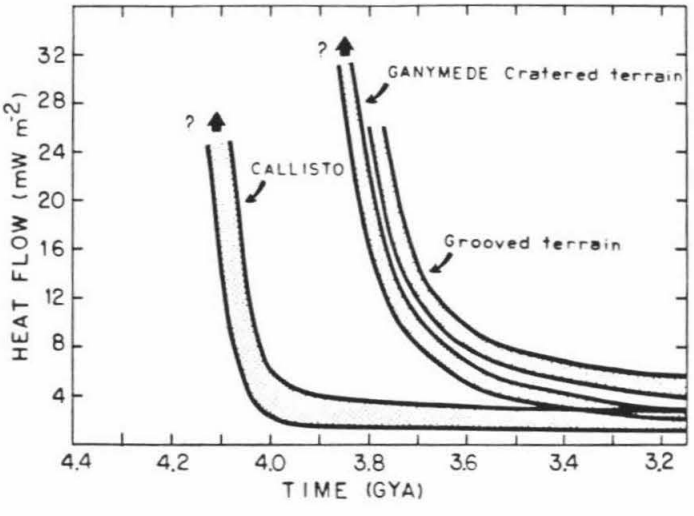

FIGURE 36 - Same as Figure 35 but this shows the history of the heat flow.

resultant crater form will be very much similar to the most flattened 10 km craters observed on Ganymede (Figure 37). At the end of this 100 My period of steady high heat flow, 30 km craters will be extremely flattened and essentially none of the original relief will be preserved for the remaining ~4 Gy; the 30 km craters that formed at times closer to the beginning of the exponential dropoff stage (i.e. near the end of the steady state high heat flow) will be preserved in varying degrees depending on exactly when they formed. A 50 km diameter crater will flatten beyond the threshold of recognition if they are allowed to flatten for 100 My with a steep viscosity gradient (L = 0.8 km) as is illustrated in Figure 37; the threshold of recognition occurs approximately where the maximum relief in a relaxed crater is less than ~100 meters. With a maximum topographic relief of ~100 meters, it would not be difficult to erase a crater by burial beneath the ejecta deposits of nearby craters, or by gardening of the surface by small primary and secondary projectiles. Almost all of the 50 km diameter craters will be preserved if they formed during the exponential dropoff period after the thermal gradient drops below about 6K/km (Figure 35). The preservation of small craters, thus, dates back to a period much earlier than does the preservation of large craters; this is what is observed on Ganymede and Callisto where crater ages from craters $\geq$ 10 km in diameter are generally older than crater ages from craters $\geq$ 50 km in diameter, based on the assumption of a population index of -2.2 for the size distribution of the craters produced by impact (Passey and Shoemaker, 1982; Passey, in press). The modified thermal history of Ganymede that satisfies taking into account of the loss of large craters at an early period, is shown by the regions marked by the question marks (?) in Figure 35. A possible early thermal history is shown by the broken line corresponding to a constant thermal gradient of about 8 K/km with the preservation of 10 km craters dating back to about 4.0 Gya. From the data on

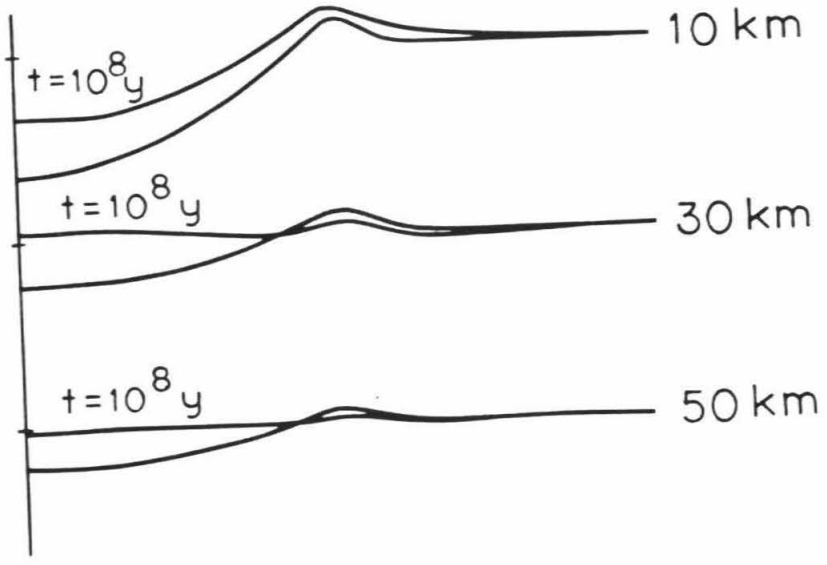

FIGURE 37 - Three different diameter craters, 10, 30, and 50 km, are shown here in their initial and final stages, assuming that the viscosity at the top of the lithosphere is 10^{26} poise, the e-folding depth for viscosity L is a constant 0.8 km, and that the flattening occurred over a time period of 10^8 years.

the degree of relaxation of craters on Ganymede, it is neither currently possible to uniquely determine the value of the hypothetical plateau region of thermal gradient nor is it possible to resolve the time dependence of the transition from a plateau region to the beginning of the exponential decline in the thermal gradient with time. From the analysis of crater relaxation, it is suggested that the thermal gradient on Ganymede at about 3.85 Gya was at, or exceeded, 8K/km; for Callisto the thermal gradient at about 4.10 Gya was at or exceeded about 3 K/km. From about 3.85 Gya on Ganymede, and 4.10 Gya on Callisto, the thermal gradients can be modelled to have dropped off exponentially with characteristic times of about 10^8 years.

Observed distribution of crater densities and model ages

It has been shown previously that crater retention ages vary over the surfaces of Ganymede and Callisto (Passey and Shoemaker, 1982; Passey, in press; Plescia and Boyce, in preparation). Generally, near the apex of orbital motion of these bodies (in the leading hemisphere), crater retention ages are calculated to be between 50 and 300 My younger than regions near the antapex (in the trailing hemisphere). These local age differences have been attributed to preferential loss of craters by viscous relaxation in the leading hemispheres resulting from the thermal effects arising from the presence of a regolith of variable properties (Passey, in press; Shoemaker et al., 1982). Also, the crater retention ages calculated from spatial crater densities at different diameter craters vary; generally the age calculated from densities at large crater diameters is less than the age calculated from the densities at smaller crater diameters. This is interpreted to indicate that large craters are not retained from as early a period in time as were small craters (Passey, in press; Passey and Shoemaker, 1982).

Comparison of profiles of craters in the leading hemispheres of Ganymede and Callisto with profiles of craters in the trailing hemisphere showed no significant difference in degree of relaxation. The heavily cratered terrain near the antapex of Ganymede (0° N, 270° W), has been estimated to be roughly 200 My older than the heavily cratered terrain near the apex (Shoemaker et al., 1982); if this age difference is real, some mechanism must lead to more rapid flattening of craters in the leading hemisphere than in the trailing hemisphere.

A probable mechanism leading to differences in viscous relaxation of craters between the leading and trailing hemispheres arises from the differential development of an insulating regolith. Shoemaker and others (1982) have shown that such a regolith must be present on Ganymede to explain the observed flattening of craters in the polar regions. The thickness of the insulating layer is controlled by the rate of regolith production versus the rate of regolith annealing. They point out that the base of the insulating regolith probably follows a threshold isotherm at which significant vapor transport of water occurs. Below this base, the icy regolith tends to be thermally annealed, and its conductivity would approach the conductivity of the solid icy bedrock. Above this base, the regolith remains a thermal insulator with a conductivity much less that of the icy lithosphere. The term insulating regolith will be used in discussion of this upper unannealed portion of the regolith.

Because of the greater cratering rate in the leading hemisphere, the rate of regolith production there will be higher than in the trailing hemisphere. As long as the heat flow from the interior is sufficiently high, the temperature at the top of the lithosphere (i.e. at the base of the insulating regolith) will be maintained constant at the annealing temperature of the regolith. If both the heat flow and cratering rate decline with time at about the same rate, the temperature at the

top of the lithosphere will ultimately decline because the level at which the regolith was previously annealed (during a period of high heat flow) is now higher than would be dictated by the lower heat flow, and no significant amount of new regolith would be formed because of the lower cratering rate. This decrease in temperature at the top of the lithosphere would result in an increase in the effective viscosity at that point, and because of the higher impact rate in the leading hemisphere, the cooling and stiffening at the top of the lithosphere would occur first in the trailing hemisphere and gradually progress toward the leading hemisphere as bombardment dropped off. This mechanism would operate under conditions of globally uniform heat flow.

We will now discuss the details of such a model. Because we will be concerned with temperature and viscosity changes near the surfaces of Ganymede and Callisto, it is important to look at the history of the surface temperature due to insolation. Theoretical solar models suggest that at ~4 Gy the luminosity of the sun was about 30% less than at present (Bahcall et al., 1982; Torres-Peimbert et al., 1969). This would translate into a temperature decrease at the surface of from the current 120K near the equator, to about 110K at ~4 Gy. The histories of the solar luminosity (Bahcall et al., 1982) and of the corresponding surface temperature of Ganymede, assuming that the albedo has been constant, are shown in Figure 38a.

If the impact rate is known, it is possible to calculate the global average rate of regolith production. From calculations presented in Shoemaker et al. (1982) the rate of regolith production (in meters/year) as a function of time is given by

$$\frac{\delta h}{\delta t} = 0.24[1.15 \times 10^{-8} yr^{-1} + 2.63 \times 10^{-8} yr^{-1} \times \qquad (17)$$

$$exp\,(6.93 \times 10^{-8} yr^{-1} \times [t - 3.3 \times 10^{9} yrs\,])]$$

where h is the regolith thickness in meters, and t is time in years. Integrating (17) for the total regolith thickness developed on Ganymede since time t_i yields

$$h = 0.24[1.15 \times 10^{-8} yr^{-1}(t_i - t) + 3.794 \times \qquad (18)$$

$$[exp\,(.693 \times 10^{-8} \times [t_i - 3.3\,x\ 10^{9}]) -$$

$$exp\,(.693 \times 10^{-8} \times [t - 3.3 \times 10^{9}])]]$$

where h is the total integrated regolith thickness (in meters) developed on a surface from time t_i to time t. The total thickness of the regolith h produced, until the present day, on a surface of a given age is shown in Figure 38b. A surface at 90° from the apex that is older than 4 Gy would have a regolith thickness in excess of 100 meters, whereas on a surface (or crater) that is $\sim 10^9$ years old, the total regolith produced to the present would only be about 4 meters thick.

If we assume that the regolith has a conductivity much lower than the conductivity of solid ice, then it is possible to determine the temperature offset across the regolith at any given time using the derived history of the thermal gradient (Figure 35). A simple two layer model for the regolith will be used here; the top layer is assumed to have a conductivity 10^{-4} that of solid crystalline ice, in agreement with thermal inertia measurements of Ganymede by Hansen (1973), and the lower layer is assumed to have a conductivity of 2×10^{-3} that of solid crystalline ice (higher because of compaction). The temperature offset ΔT across the regolith can be expressed as

$$\Delta T = \frac{\delta T}{\delta Z}[\,10^{4} h_u + 5 \times 10^{2}\,(h - h_u)] \qquad (19)$$

where h is the thickness calculated in (18), and h_u is the thickness of the upper

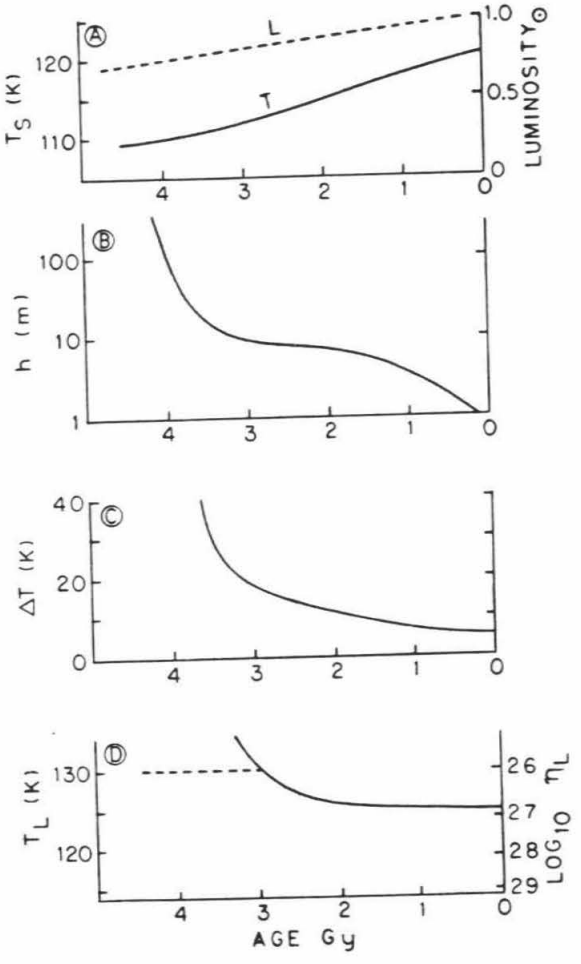

FIGURE 38 - (A) The normalized solar luminosity is shown by the broken line as a function of time in the past (from Bahcall, et al., 1982); also shown is the corresponding equatorial surface temperature. (B) The integrated thickness of the regolith as a function of time is shown in this figure. (C) The temperature offset ΔT across an insulating regolith is plotted as a function of age of a given surface. (D) Adding the temperature offset in (C) to the equatorial surface temperature shown in (A) results in the equatorial temperature at the top of the lithosphere T_L. The broken line at T_L = 130K is the probable highest temperature that the top of the lithosphere (base of the regolith) can attain because of thermal annealing of the regolith.

layer; h_u will be nominally taken as 0.5 m. The history of the temperature offset ΔT across a regolith on Ganymede is shown in Figure 38c. Equatorial temperature offsets ΔT in excess of ~20K are probably not realistic for Ganymede and Callisto because of thermal annealing within the regolith; this will be discussed below.

It is now possible to calculate the temperature at the top of the lithosphere (temperature at the base of the regolith) by convolving the temperature offset across the regolith ΔT (Figure 38c) with the surface surface temperature T_S (Figure 38a); this is shown in Figure 38d. Because of thermal annealing of the regolith at temperatures in excess of ~130K, the temperature at the top of the lithosphere T_L probably does not exceed this value; the thermal behavior of the annealed regolith is assumed to be similar to that of the icy lithosphere. Thus, prior to approximately 3 Gya, the value of T_L would be maintained approximately at ~130K, corresponding to a viscosity of 10^{26} poise, and by the present the value of T_L, at equatorial latitudes, would have dropped to ~ 125K, corresponding to a viscosity of approximately 10^{27} poise.

The degree of preservation of the Gilgamesh basin on Ganymede allows an upper limit to be placed on the viscosity at the top of the lithosphere during the period in which the collapse occurred. By modelling the collapse of the central depression of this structure (for which a photoclinometric profile was obtained, Figure 14) it was found that the maximum value that the surface viscosity could have and allow for the observed flattening is ~ 10^{27} poise; 10^{28} poise is too viscous to allow Gilgamesh to collapse to its current state. Because Gilgamesh is at 60° latitude, we cannot determine the present upper limit to the viscosity.

Assuming that the viscosity at the top of the lithosphere has increased with time from 10^{26} to 10^{27} poise, then the value of the calculated e-folding depth for

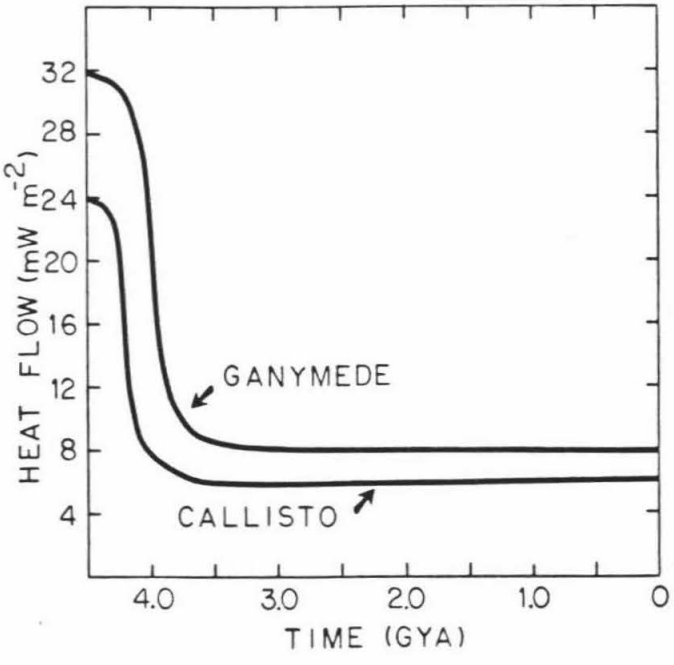

FIGURE 39 - Modified thermal history for Ganymede and Callisto assuming that the viscosity at the top of the lithosphere increased from 10^{26} poise, near 4 Gya, to 10^{27} poise, as shown in Figure 38d. The estimated error at any given time is ± 2 mW m^{-2}.

the viscosity gradient today (L_F should be decreased by approximately a factor of 2.0 to 2.5); the values derived for L_I and τ_v will not change significantly because these are constrained during the period in which the viscosity was maintained at 10^{26} poise. The corrected value of L_F for the heavily cratered terrain of Ganymede is from 4 to 5 km; for Callisto L_F would be 5 to 15 km. For the grooved terrain of Ganymede, the value for L_F would be 3 to 5 km.

The variations discussed above allow for corrections to be made to the derived thermal history (shown in Figures 35 and 36). The best estimate for the history of the heat flow, incorporating these changes is shown in Figure 39. Here, the heat flow was maintained more or less constant until ~4.1 Gy for Callisto, and ~3.9 Gy for Ganymede at a value of approximately 2.4 x 10^{-2} W m^{-2} and 3.2 x 10^{-2} W m^{-2}, respectively. After these times the heat flow dropped off exponentially, and the present values are 8 ± 2 x 10^{-3} W m^{-2} and 6 ± 2 x 10^{-3} W m^{-2}, respectively,for the heavily cratered terrains of Ganymede and Callisto. The heat flow through the grooved terrain of Ganymede, at any given time, would be approximately 5 ± 2 x 10^{-3} W m^{-2} higher than for the heavily cratered terrain on Ganymede.

Adaptation to other cratering time scales

The proposed cratering time scale of Shoemaker and Wolfe (1982) assumes that the cratering rate on Ganymede and Callisto has been more or less uniform during the last 3.3 Gy; prior to 3.3 Gya, it was assumed that in addition to the constant flux, there was an exponentially declining flux with time, referred to as the heavy bombardment; a high early flux is required because the observed density of craters is much too great to be explained by a constant impact flux over geologic time. By comparison with the lunar record, it was assumed that this high early impact flux decayed exponentially with time. The e-folding time of

this exponential bombardment τ_{HB}, was assumed to be 10^8 years, modelled after that observed for the Moon. In that most of the change in the thermal gradient in Ganymede and Callisto occurred prior to ~3.3 Gya, the flux of impacting objects on these satellites during the period of the rapid change in thermal gradient, was dominated by the exponentially declining "heavy bombardment", and this results in the high time resolution for crater relaxation between 4 and 3 Gya.

The time constant for the changing thermal gradient was determined, in the previous sections, to be between 7×10^7 and 2×10^8 years; coincidentally, these values are roughly similar to the assumed e-folding time constant τ_{HB} for the dropoff during heavy bombardment. If one assumes a different time constant τ_{HB} for the decline during a "heavy bombardment" period, then the corresponding change in the calculated e-folding time constant, for the changing thermal gradient and heat flow, will be approximately proportional, but the value for the initial thermal gradient will change; the value of the final thermal gradient, however, is quite insensitive to any but extreme changes in the proposed ages of the surfaces of Ganymede and Callisto.

If we assume that τ_{HB} was 2×10^8 years (instead of 10^8 years) then the approximate e-folding time constant for the changing thermal gradient and heat flow will be ~ 2×10^8 years, but the initial thermal gradient would be roughly 1 to 2 K/km less than the 8 K/km derived. This is required because of the longer time for significant crater relaxation to occur during a period of a relatively steep thermal gradient.

Generally, it can be stated that the derived rate of dropoff of thermal gradient and heat flow will mimic the assumed dropoff rate in the impact flux; rapid rates of dropoff in the impact flux requires that the derived early thermal gradients be higher than if the dropoff rate of impact flux is much lower.

REFERENCES CITED

Bahcall, J.N., Huebner, W.F., Lubow, S.H., Parker, P.D., and Ulrigh, R.K., (1982) Standard solar models and the uncertainties in predicted capture rates of solar neutrinos, Submitted to *Reviews of Modern Physics*,

Bonner, W.J.,and Schmall, R.A., (1973) A photometric technique for determining planetary slopes from orbital photographs, *U.S. Geol. Survey Prof. Paper 812-A*, 16 p.

Brennen, C., (1974) Isostatic recovery and the strain rate dependent viscosity of the Earth's mantle, *Jour. Geophys. Res.*, *79*, 3993-4001.

Bromer, A.M., and Kingery, W.D., (1968) Flow of polycrystalline ice at low stresses and small strains, *Jour. Appl. Phys.* ,*39*, p.1688.

Colbeck, S.C., and Evans, R.J. (1973) A flow law for temperate glacier ice, *Jour. Glaciology*, *12*, p. 71-86.

Danes, Z.F., (1962) Isostatic compensation of Lunar craters, Research Institute Univ. Puget Sound, Tacoma, Washington, RIR-GP-62-1, 11 p.

----------, (1965) Rebound processes in large craters, U.S. Geol. Survey Astrogeol. Stud. Annu. Prog. Rept. July 1, 1964 to July 1, 1965, Part A: Lunar and Planetary Investigations, Nov. 1965, p. 81-100.

----------, (1968) Isostatic processes in media of variable viscosity, 1. Cartesian geometry, *Icarus*, *9*, p. 1-7.

Glen, J.W., (1952) Experiments on the deformation of ice, *Jour. Glaciology*, *2*, p. 111-114.

Goodman, D.J., Frost, H.J., and Ashby, M.F., (1981) The plasticity of polycrystalline ice, *Philosophical Mag. A*, *43*, p. 665-695.

Hansen, O.L., (1973) Ten-micron eclipse observations of Io, Europa, and Ganymede, *Icarus*, *18*, p. 237-246.

Hobbs, P.V., 1974, **Ice Physics,** Clarendon Press: Oxford, 837 p.

Homer, D.R., and Glen, J.W., (1978) The creep activation energies of ice, *Jour. Glaciology*, *85*, p. 429-444.

Johnson, T.V., and McGetchin, T.R., (1973) Topography on satellite surfaces and the shape of asteroids, *Icarus*, *18*, p. 612-620.

Parmentier, E.M., and Head, J.W., (1979) Internal processes affecting surfaces of low-density satellites, *Jour. Geophys. Res.*, *84*, p. 6263-6276.

---------, (1981) Viscous relaxation of impact craters on icy planetary surfaces: Determination of viscosity variation with depth, *Icarus*, *47*, p. 100-111.

Passey, Q.R., (in press) Variations in crater density and model ages for Callisto's surface, submitted to *Icarus*.

Passey, Q.R., and Shoemaker, E.M., (1981a) Regional variation of crater density and model ages of Callisto's crust,(abstract) *Lunar and Planetary Science XII*, p. 816-818.

---------- (1982) Craters and basins on Ganymede and Callisto: Morphological indicators of crustal evolution, Chapter 12 *in* **The Satellites of Jupiter,** D. Morrison ed., University of Arizona Press, Tucson.

Pike, R.J., (1977) Size-dependence in the shape of fresh impact craters on the Moon, *in* **Impact and Explosion Cratering,** D.J. Roddy, R.O. Pepin, and R.B. Merrill (editors), Pergamon Press, New York, p. 489-509.

Plescia, J.B., and Boyce, J.M., (in preparation) Crater density on Ganymede.

Purves, N., and Pilcher, C.B., (1980) Thermal migration of water on the Galilean satellites, *Icarus*, *43*, p. 51-55

Scott, R.F., (1967) Viscous flow of Craters, *Icarus*, *7*, p. 139-148.

Shoemaker, E.M., Wilhelms, D., Lucchita, B., Plescia, J.B., and Squyres, S.W., (1982) The Geology of Ganymede, Chapter 13 *in* **The Satellites of Jupiter,** D. Morrison ed., University of Arizona Press, Tucson.

Shoemaker, E.M., and Passey, Q.R., (1979) Tectonic history of Ganymede, (Abstract) *EOS*, *60*, p. 869.

Shoemaker, E.M., and Wolfe, R.F. (1982) Cratering Time Scales for the Galilean Satellites, Chapter 10 *in* **The Satellites of Jupiter,** D. Morrison ed., University of Arizona Press, Tucson.

Shoji, H., and Higashi, A., (1978) A deformation mechanism map of ice, *Jour. Glaciology*, *21*, p. 419-427.

Smith, B.A., Soderblom, L.A., Johnson, T.V., Ingersoll, A.P., Collins, S.A., Shoemaker, E.M., Hunt, G.E., Masursky, H., Carr, M.H., Davies, M.E., Cook, A.F. II, Boyce, J., Danielson, G.E., Owen, T., Sagan, C., Beebe, R.F., Veverka, J., Strom, R.G., McCauley, J.F., Morrison, D., Briggs, G.A., and Suomi, V.E., (1979a) The Jupiter system through the eyes of Voyager 1, *Science*, *204*, p. 951-972.

Smith, B.A., Soderblom, L.A., Beebe, R., Boyce, J., Briggs, G., Carr, M., Collins, S.A., Cook, A.F. II, Danielson, G.E., Davies, M.E., Hunt, G.E., Ingersoll, A., Johnson, T.V., Masursky H., McCauley, J., Morrison, D., Owen, T., Sagan, C., Shoemaker, E.M., Strom, R., Suomi, V.E., and Veverka, J., (1979b) The Galilean satellites and Jupiter: Voyager 2 imaging science results, *Science*, *206*, p. 927-950.

Squyres, S.W. (1980a) Topographic domes on Ganymede: Ice vulcanism or isostatic upwarping, *Icarus*, *44*, p. 472-480.

---------- (1980b) Surface temperatures and retention of H_2O frost on Ganymede and Callisto, *Icarus*, *44*, p. 502-510.

---------- (1981) The topography of Ganymede's grooved terrain, *Icarus*, *46*, p. 156-168.

Squyres, S.W., and Veverka, J., (1981) Voyager photometry of surface features on Ganymede and Callisto, *Icarus*, *46*, p. 137-155.

Torres-Peimbert, S., Simpson, E., and Ulrich, R.K., (1969) Studies in stellar evolution. VII. Solar models, *Astrophys. Jour.*, *155*, p. 957-964.

Watson, K., (1968) Photoclinometry from spacecraft images, *U. S. Geol. Survey Prof. Paper 599-B*, 10 p.

Weertman, J., (1970) The creep strength of the Earth's mantle, *Reviews of Geophysics and Space Physics*, *8*, p. 145-148.

PAPER 4
RHEOLOGY OF ENCELADUS

by QUINN R. PASSEY

To be submitted to *ICARUS*

ABSTRACT

High resolution Voyager II images of Enceladus reveal that some regions on its surface are highly cratered; the most heavily cratered surfaces probably date back to a period of heavy bombardment. The forms of many of the craters, on Enceladus, are similar to those of fresh lunar craters, but many of the craters are much shallower in depth, and the floors of some craters are bowed up. The flattening of craters, and bowing up of the floors, are indicative of viscous relaxation of the topography. Analysis of the forms of the flattened craters suggests that the viscosity at the top of the lithosphere, in the most heavily cratered regions, is between 10^{24} and 10^{25} poise. The exact time scale for the collapse of the craters is not known, but probably was between 100 My and 4 Gy. The flattened craters are located in distinct zones that are adjacent to zones, of similar age, where craters have not flattened. The zones where flattened craters occur possibly are regions in which the heat flow was (or is) higher than in the adjacent terrains. Because the temperature at the top of the lithosphere of Enceladus would be less than, or equal to that of Ganymede and Callisto, if it is covered by a thick regolith, and because the required viscosity, on Enceladus, is one to two orders of magnitude less than for Ganymede and Callisto, it can be concluded that the lithospheric material, on Enceladus, is different from that of Ganymede and Callisto. Enceladus probably has a mixture of ammonia ice and water ice in the lithosphere, whereas the lithospheres of Ganymede and Callisto are composed primarily of water ice.

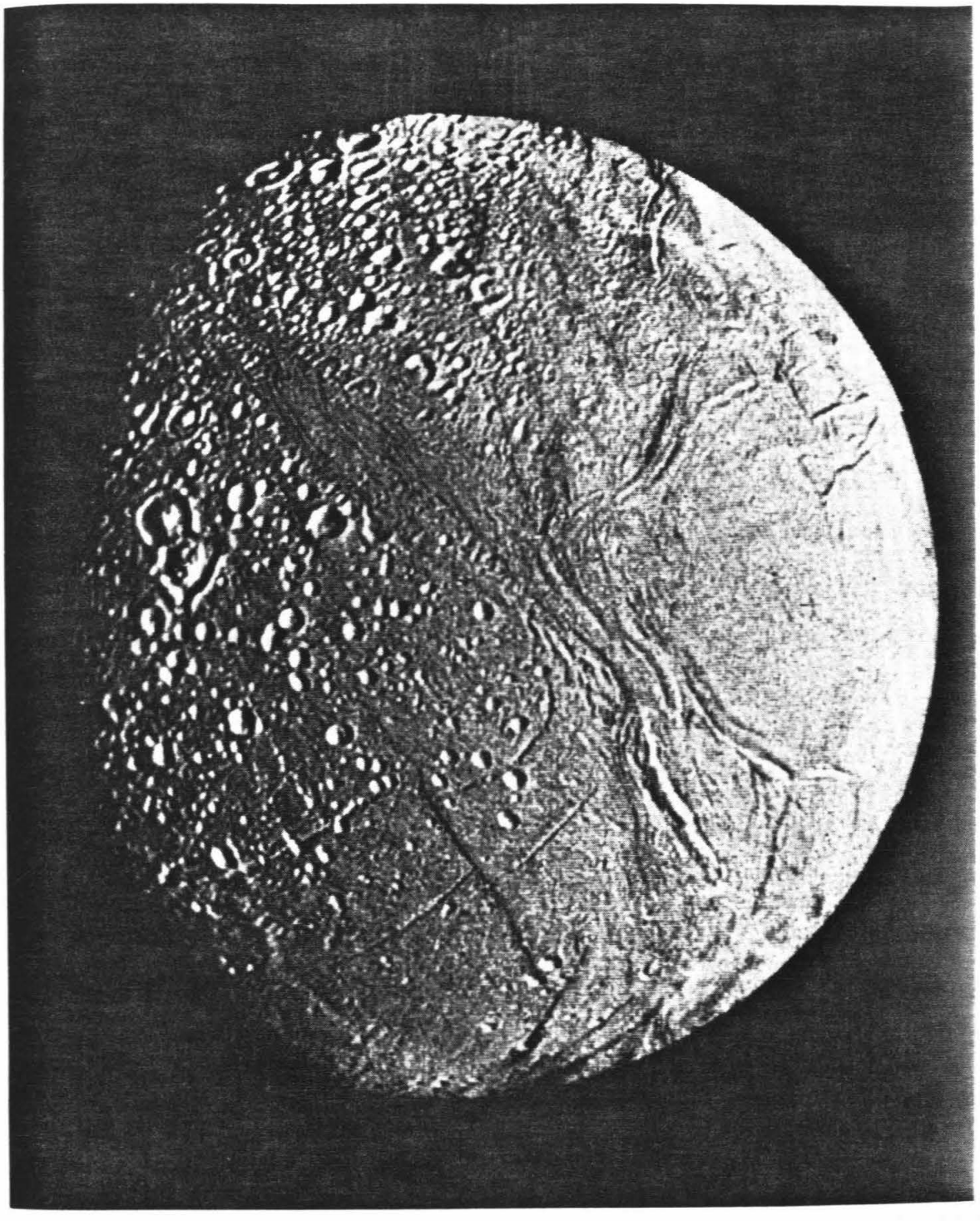

FIGURE 1.-- High resolution filtered image of Enceladus.

INTRODUCTION

Relatively low resolution Voyager I images of Enceladus (~11 km/lp) failed to reveal any craters; at similar resolution, many craters were observed on the other Saturnian satellites. It was concluded that if craters are present on Enceladus, they must be much smaller and/or more subdued than those on Mimas (Smith et al., 1981). The much higher resolution images acquired by Voyager II (Fig. 1) revealed that craters are present on Enceladus but that many display subdued relief; in addition, much of Enceladus has been resurfaced and there are large areas with very low crater density. Part of the resurfaced area is somewhat similar to the grooved terrain on Ganymede; also, the crater densities on some of these surfaces suggests that the youngest terrains are of order a few hundred million years old (Smith et al., 1982). The mechanism that has been proposed to produce the required heating needed for an internally active Enceladus is tidal heating (Yoder, 1979; Stevenson and Anderson 1981).

OBSERVATIONS

From the highest resolution images obtained of Enceladus (Fig. 1), it can be seen that there is a great range in spatial crater density on the various terrains of Enceladus. Some areas are heavily cratered with the density of approximately 1000 craters ≥ 10 km/10^6 km^2; other areas do not exhibit any visible craters at similar resolution. In the heavily cratered regions, many craters are extremely flattened while others display bowed up floors.

Photoclinometry

In order to study the topographic relief of the features on Enceladus in greater detail, the technique of photoclinometry was applied (Bonner and Schmall, 1973; Squyres, 1981; Passey and Shoemaker, in preparation). To

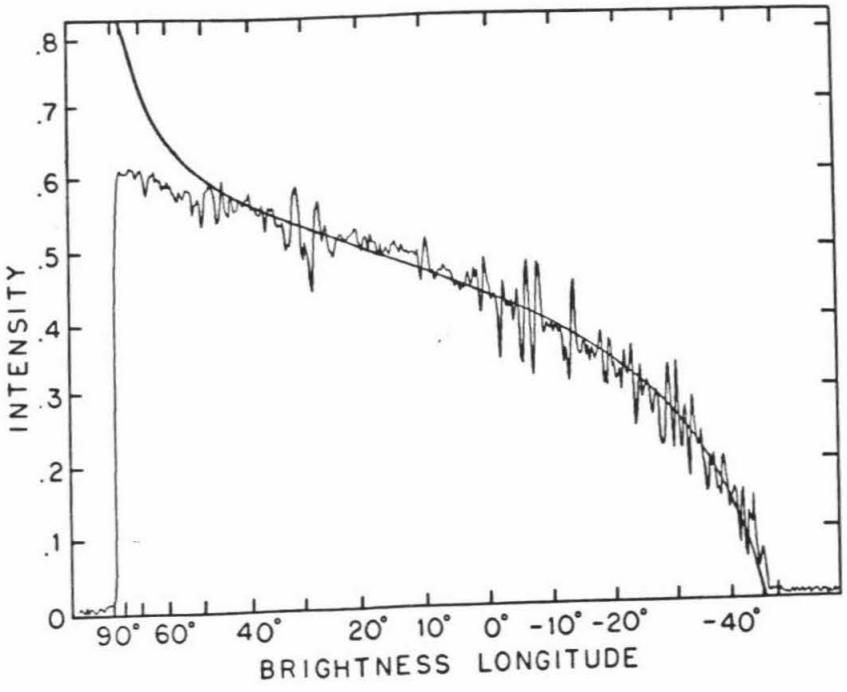

FIGURE 2.-- Normalized intensity scan across the disc of Enceladus. The limb corresponds to brightness longitude +90°, and the terminator to -47°. The smooth solid line shows a Lommel-Seeliger function fit to the data at brightness longitude 0°.

obtain accurate photoclinometric profiles, the photometric function of the surface material must be known. Figure 2 shows a comparison of a scan, from Voyager 2 image 44004.20, across the disc of Enceladus, with a theoretical Lommel-Seeliger function; this function was used successfully to model the observed photometric behavior of the surface of Ganymede (Squyres and Veverka, 1981). As can be seen, the theoretical function fits the data quite well for photometric longitudes less than 50°. The form of the theoretical function is

$$I = \frac{C\,\mu_o}{(\,\mu_o + \mu\,)} \qquad (1)$$

where I is intensity, C is a constant, $\mu_o = \cos(i)$, and $\mu = \cos(E)$, i is the incident angle and E is the emission angle. Knowing the values for i, E, and the phase angle for a given location, it is possible to calculate the value of the constant C using the observed image intensity I. Within an area of uniform albedo, the variation in the observed intensity of a given picture element (pixel) can be related to average absolute slope within the phase plane of the region covered by that pixel; then, from a string of adjacent pixels, it is possible to construct two-dimensional topographic profiles of the crater or feature of interest by integration of adjacent slopes, as is discussed by Squyres (1981).

Geological Terrains

As is discussed in Smith et al. (1982), the surface of Enceladus is made up of several distinct terrain units; these terrains differ in both the spatial density of superposed craters as well as in surface morphology. The terrain units used in this paper (shown in Figure 3) are similar to those discussed by Smith et al. (1982), but differ in both classification and boundary locations.

Cratered Terrain 1 (CT1).-- One type of terrain (CT1) displays craters that are extremely flattened or subdued (Smith et al., 1982), with depths much less

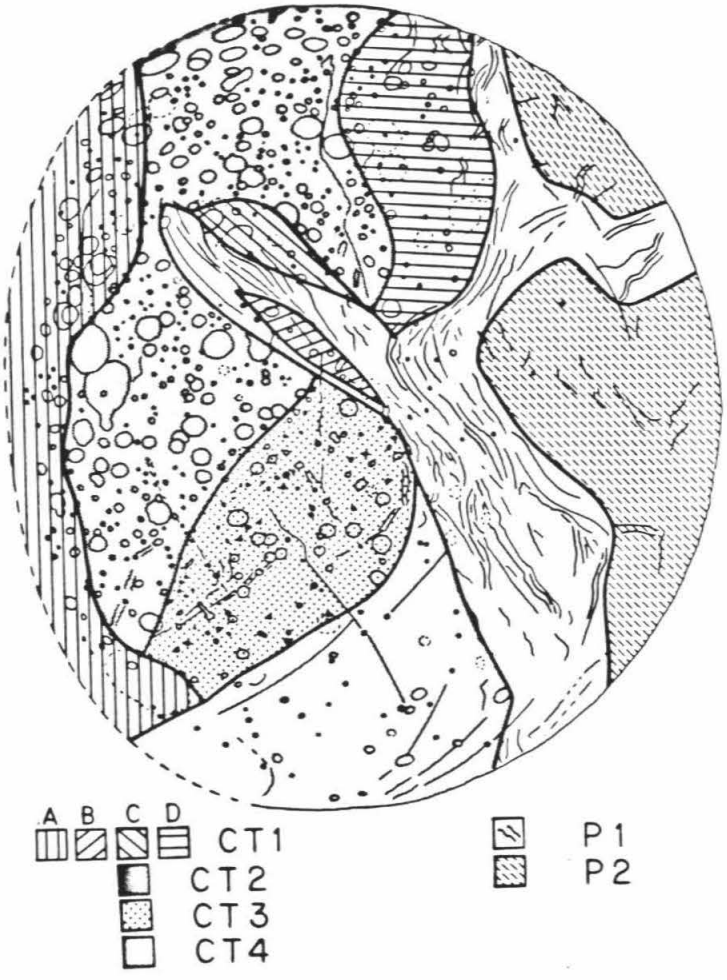

FIGURE 3.-- Generalized geologic map of Enceladus; the divisions are those discussed in this paper. Cratered terrains CT1-A through CT1-D are regions in which the majority of the superposed craters display very subdued topographic relief. Terrains CT2 through CT4 are regions discriminated by the density of superposed craters. Plains terrain P1 is similar to the grooved terrain on Ganymede, and terrain P2 is a smooth plains unit.

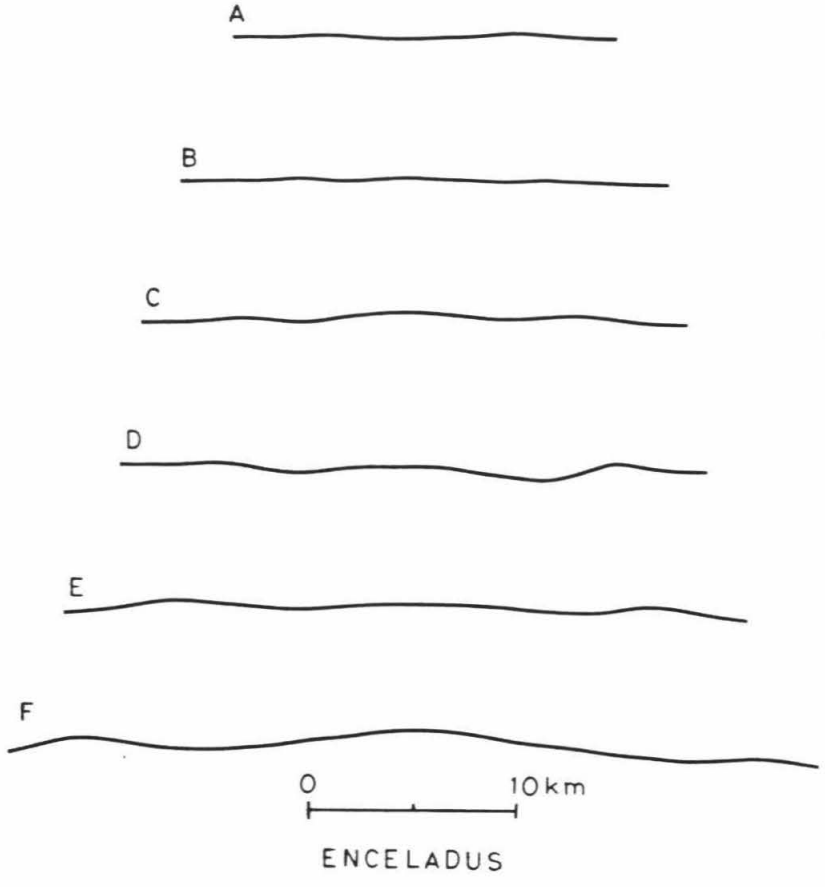

FIGURE 4.-- Photoclinometric profiles of six craters showing subdued relief and/or bowed up crater floors, indicative of viscous relaxation of relief. Profiles A through D are from craters within terrain CT1-A; profiles E and F are from craters within terrain CT2. No vertical exaggeration or removal of the planetary curvature is used in the construction of these profiles.

than the depths of similar size fresh lunar craters. Four separate regions of this terrain type have been identified on Enceladus for this study (Figure 3). Photoclinometric profiles of craters, located in CT1, that are extremely flattened, or display bowed-up floors, are shown in Figure 4 (profiles A-D). The maximum depths (below the crater rim) for a given size crater located in CT1 is generally much less than for a similar size fresh lunar crater; this is shown in Figure 5.

As was noted by Smith et al. (1982), the density of craters in the region that displays the relaxed craters (CT1-A) is about the same as the region in which craters 10 to 20 km in diameter have well preserved topography (CT2). They conclude from this that the two regions have experienced different thermal histories. The boundary between these two terrains is not well defined and appears diffuse. A gradational boundary between CT1 and CT2 suggests that, at one time, there was a gradient in the heat flow between these two regions.

Examination of the morphology of craters within CT1-A reveals that, for craters larger than 8 km in diameter, approximately 75% are substantially flattened, and 25% appear relatively fresh and unrelaxed. In contrast with what is observed on Ganymede, where craters are observed in all stages of relaxation, the craters in CT1-A are either highly flattened or fresh. This suggests that the crater flattening occurred as a discrete event sometime after the formation of 75% of the craters, but before the final 25% of the craters formed.

Terrains CT1-B and CT1-C (Fig. 3) have quite sharp boundary contacts with the adjacent plains. Figure 6 shows an enlargement of these regions with an accompanying sketch map. The contacts of terrain CT1-B with the surrounding rippled plains unit appear to be fault controlled. Faults also appear to form the western boundary of CT1-C with the rippled plains unit. Along this boundary two

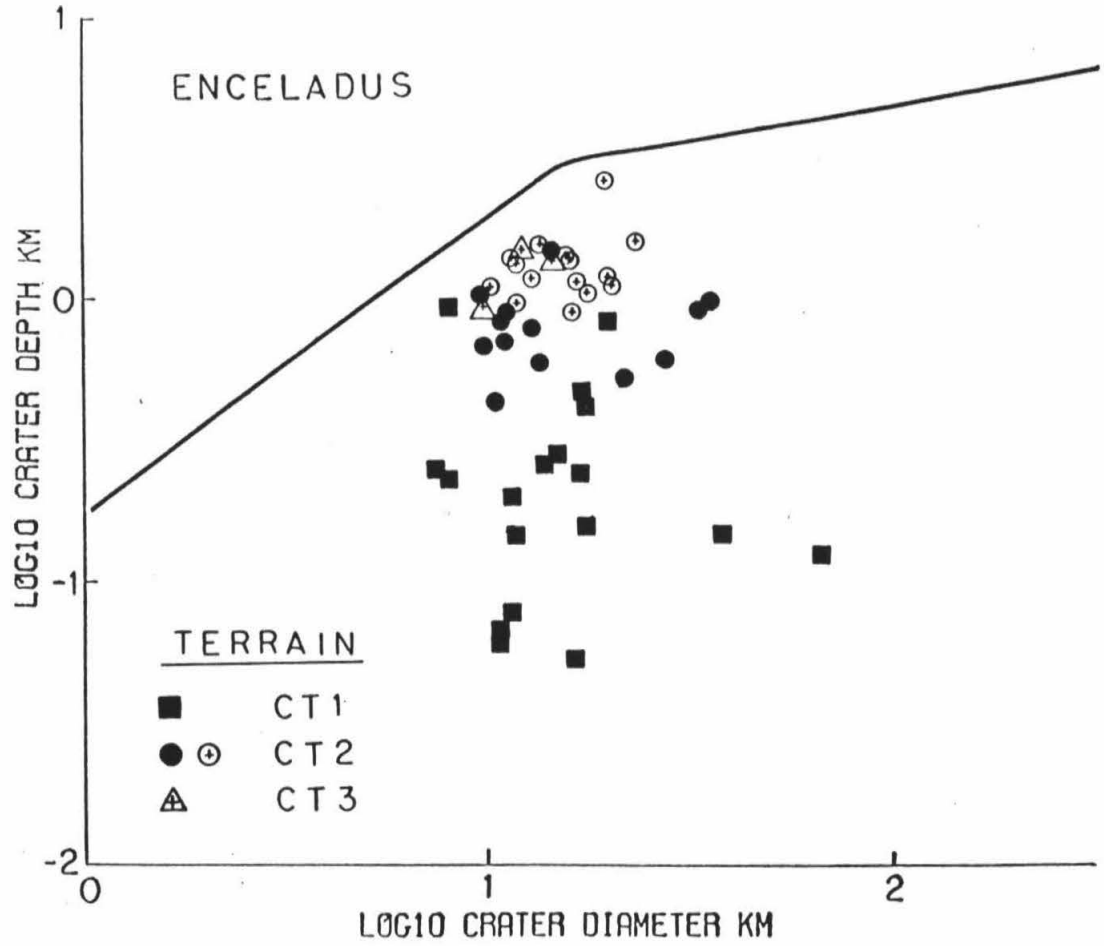

FIGURE 5.-- Maximum crater depth, below the crater rim, is plotted here versus the rim-to-rim crater diameter for 49 craters on Enceladus. The craters are classified according to terrain on which they occur. Solid circles indicate craters that are located in terrain CT2 within ~20 km of the boundary with terrain CT1 (as is shown in Figure 3). Open circles with the crosses indicate craters in CT2 that are farther than ~20 km from the boundary with terrain CT1. The heavy line is for fresh lunar craters (Pike, 1977), for comparison.

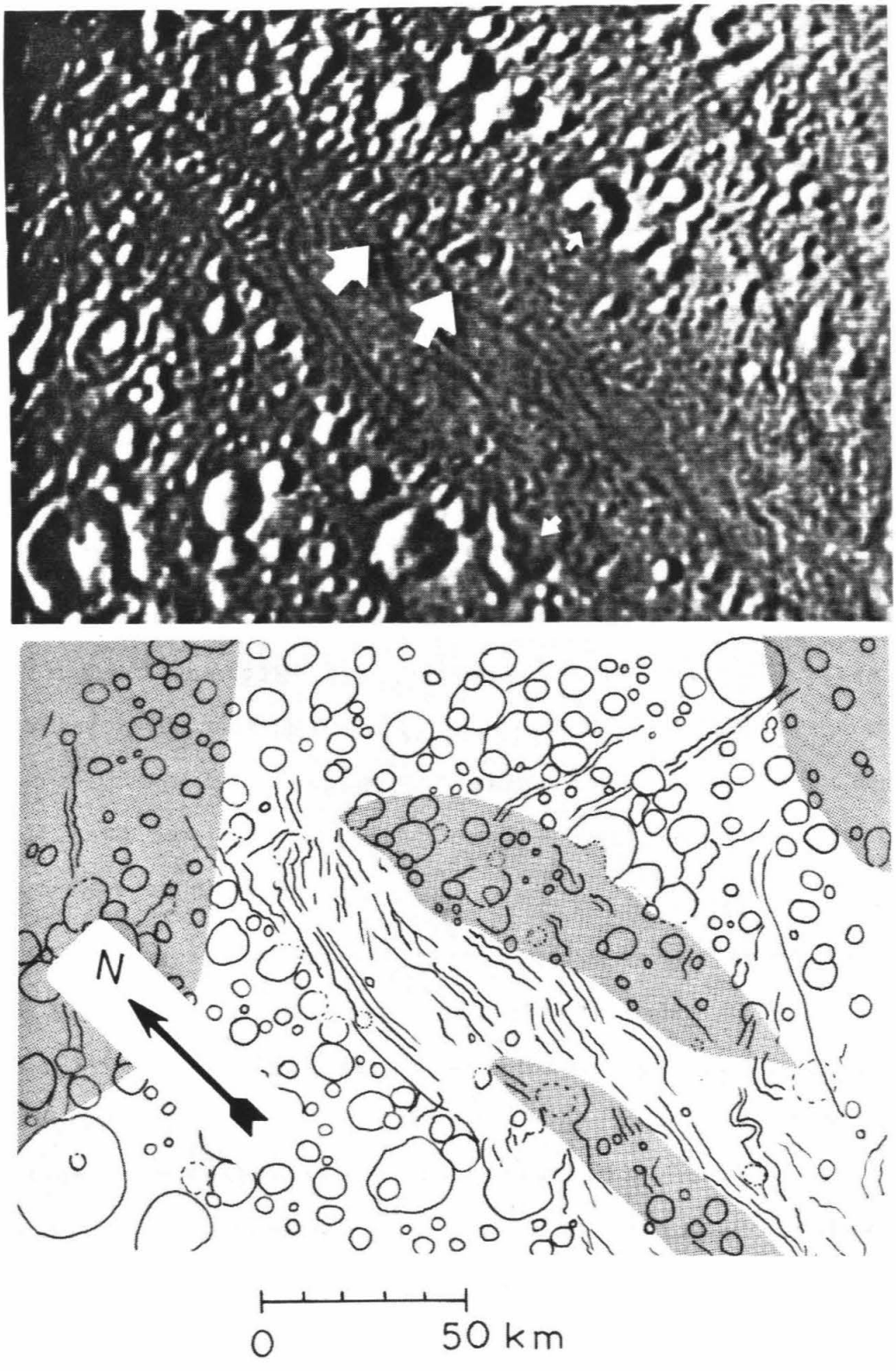

FIGURE 6.-- Enlargement of an area showing the boundaries between terrains CT1-B, and CT1-C with their surrounding terrains The shaded regions, on the accompanying sketch map, correspond to terrain CT1. The arrows mark the locations of craters that appear truncated (see text for discussion).

craters (large arrows, Figure 6) apparently have been truncated; careful examination of the shape and circularity of the two "truncated" craters, however, reveals that if they have been truncated, they have also been deformed by horizontal strain. The magnitude of the strain is between 10% and 30%, after correction for foreshortening. These two "truncated" craters are not necessarily cut and strained, however, but may be composites of superposed craters. The sketch map (Fig. 6) shows one possible interpretation of crater superposition that may have resulted in the illusion that these two craters are "truncated and strained"; it should be noted that at least two unambiguous cases of truncated craters are also shown in Figure 6 (small arrows).

The eastern boundary of terrain CT1-C and CT2 is gradational but is fairly well defined. One crater along this boundary, on terrain CT2, appears to be embayed by the material in CT1-C. The entire patch of CT1-C terrain may have been resurfaced by flooding; any preexisting craters that were not completely filled, would now appear much shallower than fresh craters, as do nearly all of the craters found within CT1-C.

A fourth terrain that displays craters with extremely shallow depths is CT1-D (Fig. 3). In this region, the vestigial rims of several relatively large craters (~20 km diameter) can be identified. The expected density of craters smaller than 10 km in diameter that would accompany the larger craters, is not found, however. If craters have disappeared by viscous relaxation of the topography, the large craters would flatten at rates much faster than the smaller craters, and so there should be a relative deficiency of large craters; this is not what is observed. If, on the other hand, the region was flooded, the largest craters would be the last features to disappear. The observed distribution of craters suggests that this region has experienced incomplete resurfacing by flooding.

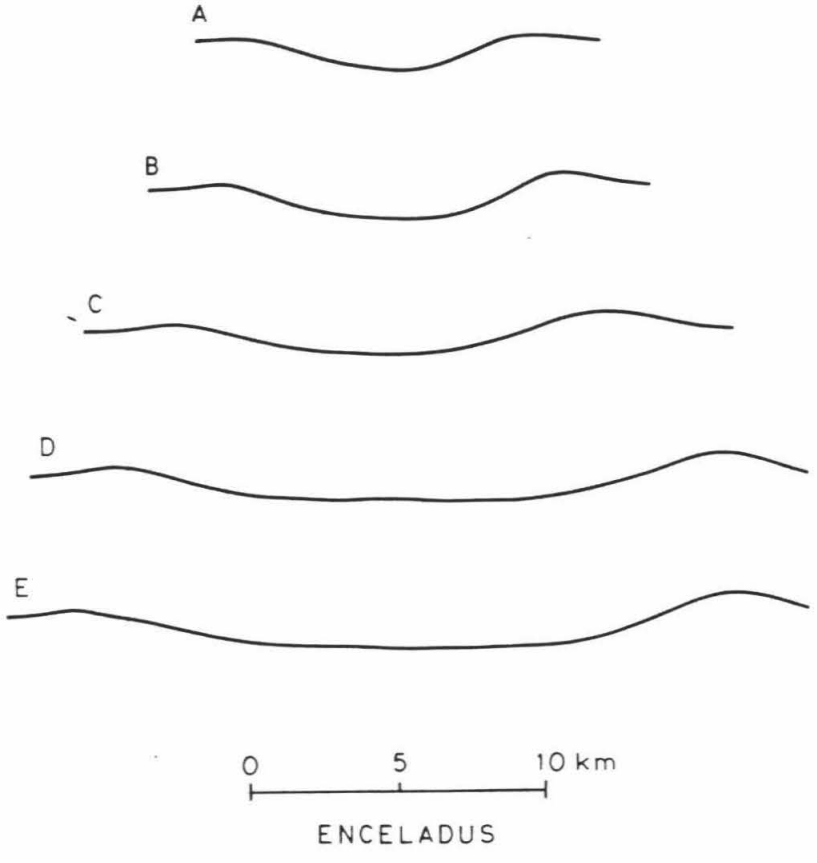

FIGURE 7.--Photoclinometric profiles of five fresh craters on terrains CT2 and CT3.

Cratered Terrain 2 (CT2).-- This terrain is characterized by a relatively high spatial density of craters; the density of craters on CT2 is essentially the same as for CT1-A (J.B. Plescia, personal communication). Topographic relief of most craters in CT2 is well preserved, in contrast to the flattened craters found in the adjacent terrain CT1-A. Although most of the craters display well preserved topographic relief, several of the largest craters (diameters > 20 km) exhibit bowed up floors; photoclinometric profiles of two of these craters are shown in Figure 4 (profiles E & F). Craters in CT2 that are within ~20 km of terrain boundary with CT1 (Fig. 3) generally have shallower depths than similar size craters located well away from the boundary with CT1 (see Figure 5). Representative examples of profiles of relatively fresh appearing craters in CT2 are shown in Figure 7.

Cratered Terrains 3 and 4 (CT3 & CT4).-- These terrains are distinguished from CT2 by a low density of superposed craters. The density of craters in CT3 is slightly higher than that in CT4 (Smith et al., 1982). All craters within these terrains appear relatively fresh and exhibit nearly lunar-like depth-to-diameter ratios. Several linear grooves or scarps, intersecting at angles close to 90°, cut these two terrains (Plescia and Boyce, 1981).

Plains Terrains (P1 & P2).-- At least two types of plains units are present on Enceladus. The first type (P1) is marked by long ridges and furrows somewhat similar to those found on the grooved terrain on Ganymede. The second type of plains terrain (P2) is essentially a smooth plain that is cut by rare grooves. Neither terrain exhibits any definite craters, and the ages of these surfaces have been estimated to be, at most, a billion years (Smith et al., 1982). Three photoclinometric profiles across ridges and furrows in P1 are shown in Figure 8; the locations of these profiles is shown in Figure 9. The spacing

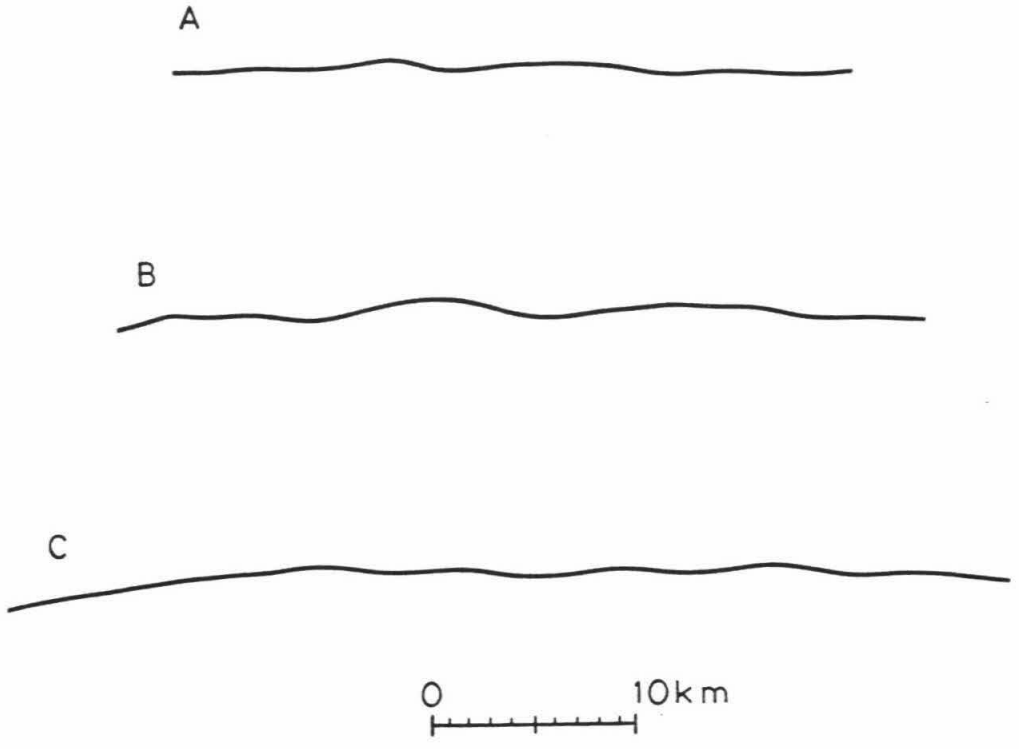

FIGURE 8.-- Three photoclinometric profiles across the rippled plains indicate that the heights of the ridges range from a few hundred meters to approximately 1 1/2 km.

between ridges ranges from about 7 to 15 km; the heights of the ridges range from a few hundred meters to approximately 1.5 km. The boundaries of these terrains with the cratered terrains are generally sharply defined. In some places the boundary is linear and craters are truncated at the boundary.

DISCUSSION

Source region for crater forming bodies

In order to obtain any information about the age of the flattened craters, and, thus, about any time limits as to how long it has taken to flatten them, it is necessary to discuss the possible source regions for the impacting bodies responsible for the formation of the observed craters. It has been suggested that Enceladus has been disrupted and reaccreted about four times since the last global resurfacing of Iapetus (Smith et al., 1982); the disruptions are probably a result of collisions with large objects that were in orbit around in the sun (i.e. possibly dynamically evolved Uranus and Neptune planetesimals). Objects that are at the same distance from Saturn as Enceladus (possibly objects in Lagrangian, or in horseshoe orbits) have also been subjected to this bombardment by extra-Saturnian objects, but these smaller objects will be smashed up at much faster rates; the fragments resulting from these collisions will not be gravitationally bound to each other (as would the large fragments of Enceladus), and they will be dispersed into orbits that are different than before the collision; but these fragments will remain to cross the orbit of Enceladus and will have a high probability of impacting Enceladus.

The majority of craters on Enceladus can be classified with the Population II craters observed on the other Saturnian satellites; this classification is based on the observed size-distribution of craters. As is discussed by Smith et al. (1981, 1982), the Population I craters probably resulted from the impacts of objects

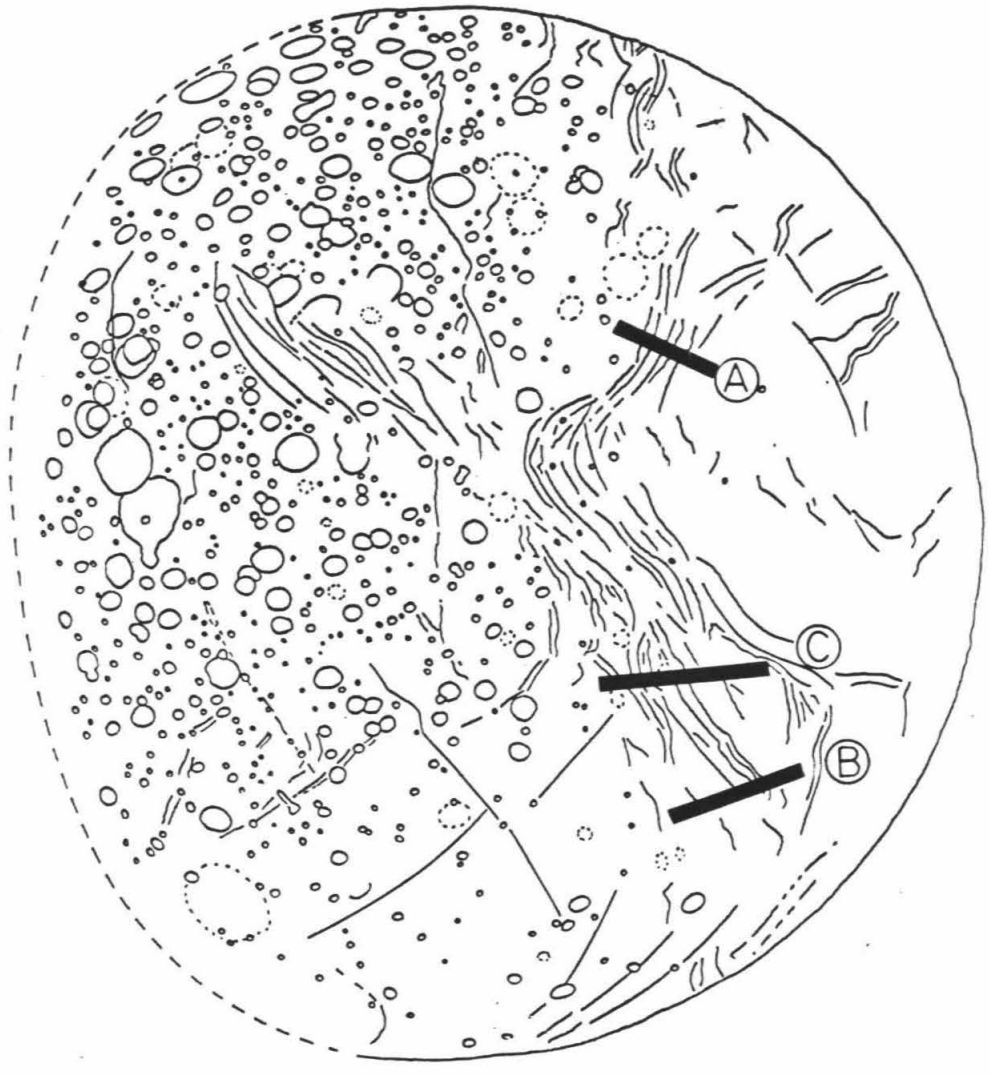

FIGURE 9.-- Sketch map showing the locations of the three photoclinometric profiles in Figure 8.

that originated in regions external to the Saturnian system; it is presumed that the Population I objects were also responsible for most of the craters observed on Ganymede and Callisto. The population II craters probably are formed by impact by orbiting debris from collisions between Population I projectiles and small Saturnian satellites. It is probable, therefore, that most of the craters observed on Enceladus were formed by objects that originated within the Saturnian system; furthermore, it is probable that these objects were fragments produced by the disruption of small bodies at Enceladus' orbit.

Because of the stochastic nature of the collision of objects external to the Saturnian system, with small bodies at Enceladus' orbit, it is not possible to determine the age of the surface units on Enceladus by counting the Population II craters. The probability of a collision of an extra-Saturnian object with a possible Lagrange satellite of Enceladus, however, would be much greater during the period of heavy bombardment, when the Population I objects were much more numerous. Thus, even though the craters on Enceladus might have been formed after the heavy bombardment period, chances are that they formed during this period (i.e. > 3.3 Gy). For the remainder of this paper, it will be assumed that the oldest surfaces on Enceladus are older than ~3.3 Gy.

Theoretical model for crater relaxation

Highly relaxed craters were observed on Ganymede and Callisto, and, from modelling the relaxation process, constraints were placed on the rheological and thermal histories of these bodies (Passey and Shoemaker, in preparation). For the analysis of the flattened craters on Ganymede and Callisto, it was assumed that the flattening was due to viscous relaxation of topography in the icy lithospheres, with gravity producing the driving force (i.e. isostatic relaxation). The discovery of flattened craters on Enceladus was somewhat surprising in that the

relaxation of topography requires that the effective viscosity at the top of Enceladus' lithosphere at one time must have been ~20 times less than the effectie viscosity at the top of the lithospheres of Ganymede and Callisto. This lower viscosity is required because of the much lower surface gravity on Enceladus. Nevertheless, the existence of bowed up floors is diagnostic of viscous relaxation of topography, and much of the flattening and bowing up of craters observed on Enceladus is almost certainly the result of viscous relaxation.

Because of the low bulk density of Enceladus of 1.1 g cm^{-3} (Smith et al., 1981), it is assumed that the satellite is composed of ices; presumably water ice is the predominant type. The viscosity of water ice is a strong function of the temperature, and, for any temperature gradient in the lithosphere increasing with depth, will be expressed as a decreasing viscosity gradient with depth. For water ice, a linear thermal gradient roughly translates into an exponential viscosity gradient.

The model used to study the theoretical relaxation of a crater on Enceladus is essentially the same model as is presented in Passey and Shoemaker (in preparation), and follows the methods of Danes (1965, 1968) and Brennen (1974); a similar model is presented by Parmentier and Head (1981). The model used here allows for the viscosity to be an exponential function of depth, but, in contrast with the analysis for Ganymede and Callisto, the viscosity gradient is assumed to be constant with time. The details of the theoretical model can be found in Passey and Shoemaker (in preparation). Of interest for this paper is the values for the viscosity at the top of the lithosphere, and the viscosity gradient with depth; the e-folding depth for decreasing viscosity is here designated as L.

COMPARISON OF MODEL WITH DATA

Time scale for crater collapse

Because the oldest surfaces on Enceladus are the same as the regions in which the flattened craters are observed (CT1-A), and because these surfaces are probably older than ~3.3 Gy, it is possible, although not likely, that the collapse of craters has occurred over a time period of 3 Gy or longer. Cratered terrain CT2 is approximately the same age as terrain CT1-A, but most of the craters on CT2 show only slight relaxation of topography; these craters (on CT2) have, therefore, lasted for at least ~3.3 Gy without significant relaxation.

Approximately 25% of the craters on terrain CT1-A show little flattening of their topography, and, thus, it is possible that the observed flattening of the craters on terrain CT1-A, occurred during a relatively short time interval, possibly during a pulse of 100 My or less. For analysis in this paper, it will be assumed that the relevant time scales for the observed crater flattening is between 100 My and 4 Gy; these two values will be studied as limiting cases.

Constraints on lithospheric viscosity

The highly flattened craters of interest are all found within terrain CT1, or within ~20 km of CT1 terrain boundary. If we assume that these craters have been relaxing for ~4 Gy in a medium of constant viscosity state, then it is possible to define a range in which the viscosity must lie. For this analysis, relaxation of craters of two diameters, 8 km and 30 km, will be modelled. These two crater sizes were chosen because some 8 km craters are significantly flattened on Enceladus (Figure 4, profile A), whereas, some 30 km diameter craters are only moderately flattened (Figure 4, profile F).

As is shown in Figure 10, 8 km diameter craters will not be preserved for 4 Gy

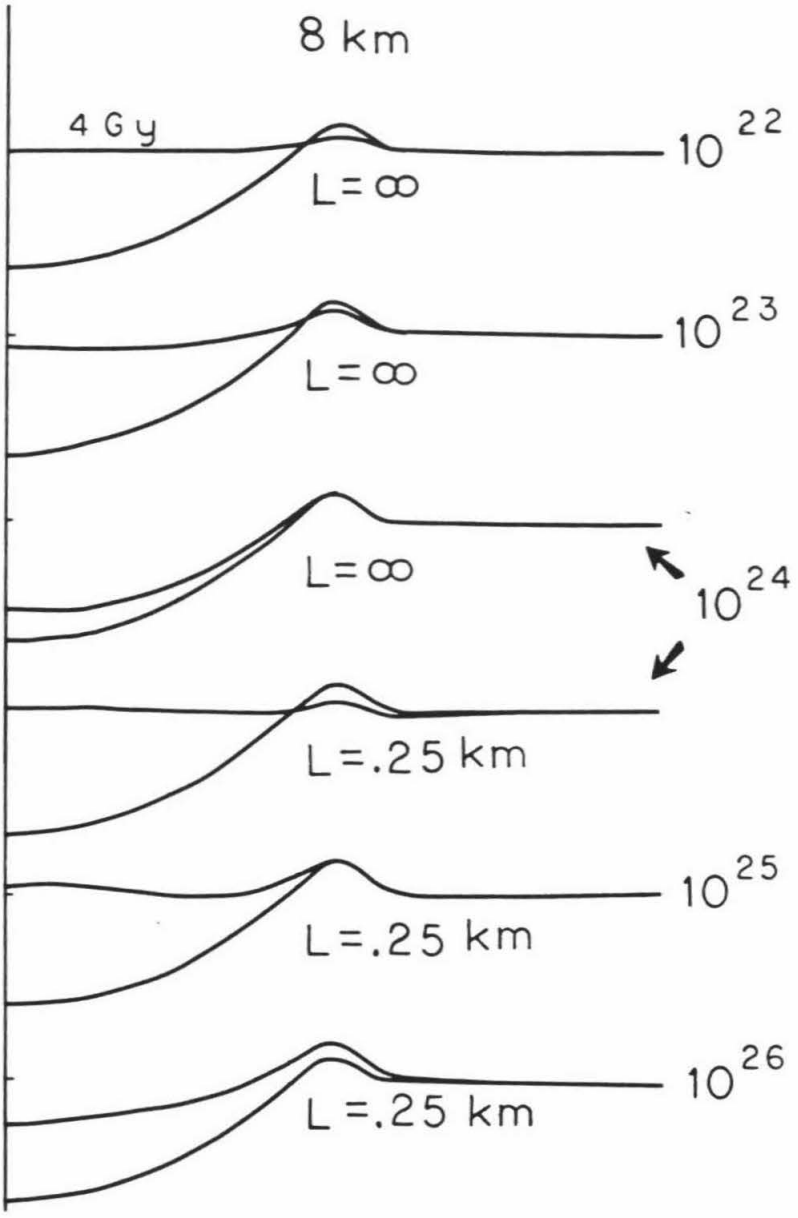

FIGURE 10.-- The theoretical viscous flattening of an 8 km diameter on Enceladus crater is shown here. The initial and final crater profiles (after 4 Gy) are illustrated for various choices for the surface viscosity (e.g. 10^{22} etc.) and various e-folding depths for viscosity (L).

TABLE I - Range of possible viscosities at the top of Enceladus' lithosphere based on 8 km relaxed craters; two different time scales for collapse are studied, 4 Gy, and 100 My.

Surface Viscosity[1] η_o (poise)	E-folding depth of viscosity 4 Gy	E-folding depth of viscosity 100 My
10^{26}	Too viscous	Too viscous
10^{25}	0.25 - 0.5 km	Too viscous
10^{24}	0.5 - 2.0 km	0.25 - 2.0 km
10^{23}	2.0 - Infinity	3.0 - Infinity
10^{22}	Viscosity too low	Infinity

[1] At the top of the lithosphere.

if the viscosity of the medium (here assumed to be a viscous half space, L = infinity) is less than 10^{23} poise; also, even if a very steep viscosity gradient is assumed (L = 0.25 km), a viscosity at the top of Enceladus' lithosphere of 10^{26} is too high to result in sufficient relaxation of an 8 km diameter crater in 4 Gy. Thus, in order to explain the observed flattening of 8 km craters on Enceladus in 4 Gy, the viscosity at the top of the lithosphere must have been between 10^{23} and 10^{25} poise; the range in e-folding depths for the various viscosities are given in Table I.

If it is assumed that the flattening of the 8 km craters occurred over a 100 My time period, limits to the viscosity can be determined from analogous arguments. From Figure 11, it can be seen that flattening of an 8 km diameter crater in 100 My requires that the viscosity of a uniform half space would have to be between 10^{21} and 10^{22} poise. If we assume a steep viscosity gradient during this period (L = 0.25 km), the required viscosity at the top of the lithosphere is less than $\sim 10^{25}$ poise; the determination of the viscosity depends on the choice for the e-folding depth of viscosity L, and the appropriate values are shown in Table I. Thus, the viscosity at the top of the lithosphere of Enceladus that will allow the observed flattening of 8 km diameter craters is between 10^{22} and 10^{25} poise.

Next we examine the values for the viscosity at the top of the lithosphere that will allow the preservation of 20 and 30 km diameter craters over time periods of ~3.3 Gy; these are the craters preserved on terrain CT2. Figure 12 shows the theoretical relaxation of a 30 km crater in a media of various viscosities. Assuming that medium is a uniform viscous half space, the required viscosity is between 10^{23} and 10^{24} poise. If we assume that a moderately steep viscosity gradient has existed, then if the observed collapse of the 30 km diameter crater

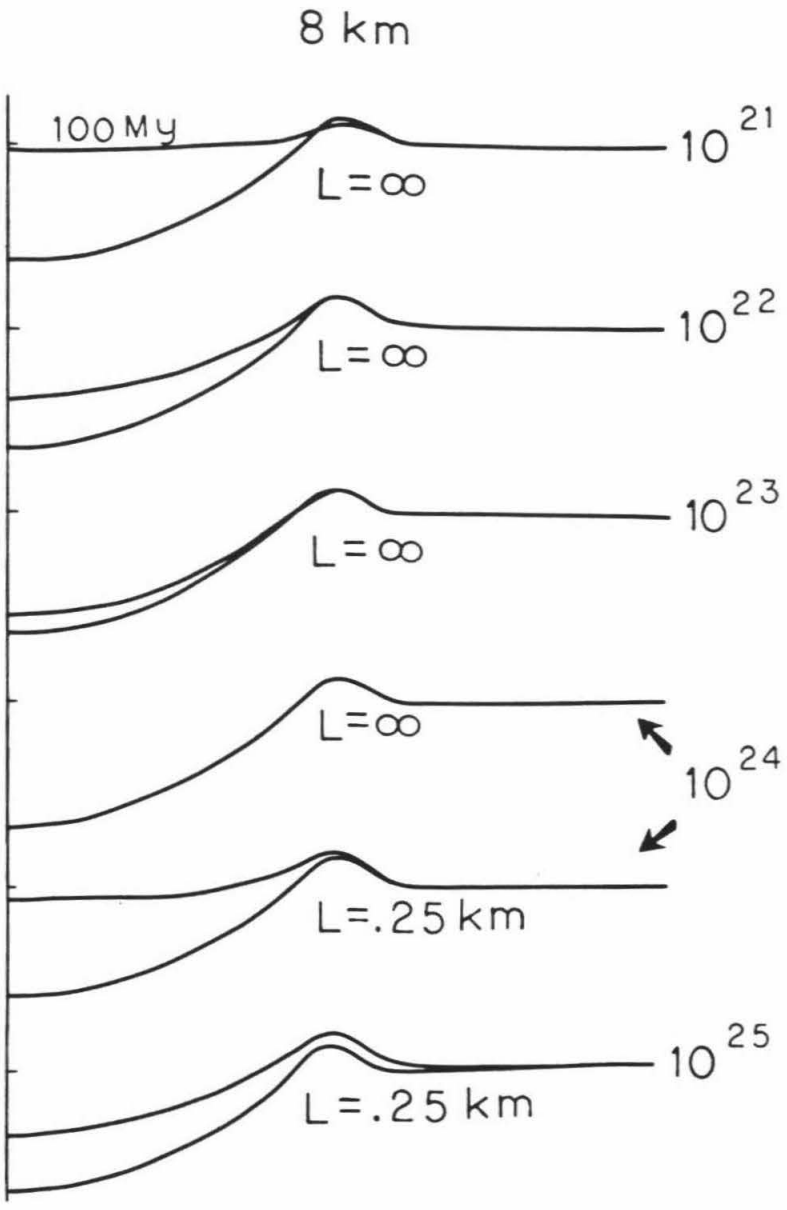

FIGURE 11.-- Same as for Figure 10 except that the final profiles assume that the flattening took place over a 100 My period.

shown in Figure 4 (profile F) occurred over a period of ~4 Gy, the required viscosity at the top of the lithosphere would range from 10^{25} to 10^{26}; if the observed collapse of this crater has taken only 100 My, then the required viscosity is approximately 10^{24} poise (using L = 1 km). In order to preserve craters 20 to 30 km in diameter in their current states of flattening, requires a viscosity at the top of the lithosphere of between 10^{23} to 10^{25} poise; for 20 km diameter craters that have not flattened significantly, the required viscosity at the top of the lithosphere is $> 10^{24}$ poise, assuming that these craters are older than 3.3 Gy. The possible viscosity gradients associated with the choices for surface viscosity are given in Table II.

It was found that the viscosity at the top of the lithosphere near the top of Ganymede's lithosphere was 10^{26} poise (Passey and Shoemaker, in preparation). This value of viscosity is much too high to allow for the relaxation of any 8 km craters on Enceladus, regardless of the viscosity gradient assumed. The range in possible viscosities at the top of Enceladus' lithosphere is 10^{23} to 10^{25} poise, with corresponding e-folding depths of viscosity ranging from infinity (half-space model) to less than 0.25 km. The implications of this will be discussed later.

Assuming that the viscosity at the top of the lithosphere beneath cratered terrain CT1-A is the same as that beneath terrain CT2, then a comparison of the results presented in Tables I and II further constrains the value for the viscosity at the top of the lithosphere. It can be seen that 10^{26} poise is too viscous to explain the observed collapse of 10 km craters in CT1-A and that 10^{23} poise is not viscous enough to retain 30 km craters over a period of billions of years; hence, these values are excluded and the viscosity at the top of the lithosphere in CT1-A and CT2 on Enceladus must be between 10^{24} and 10^{25} poise.

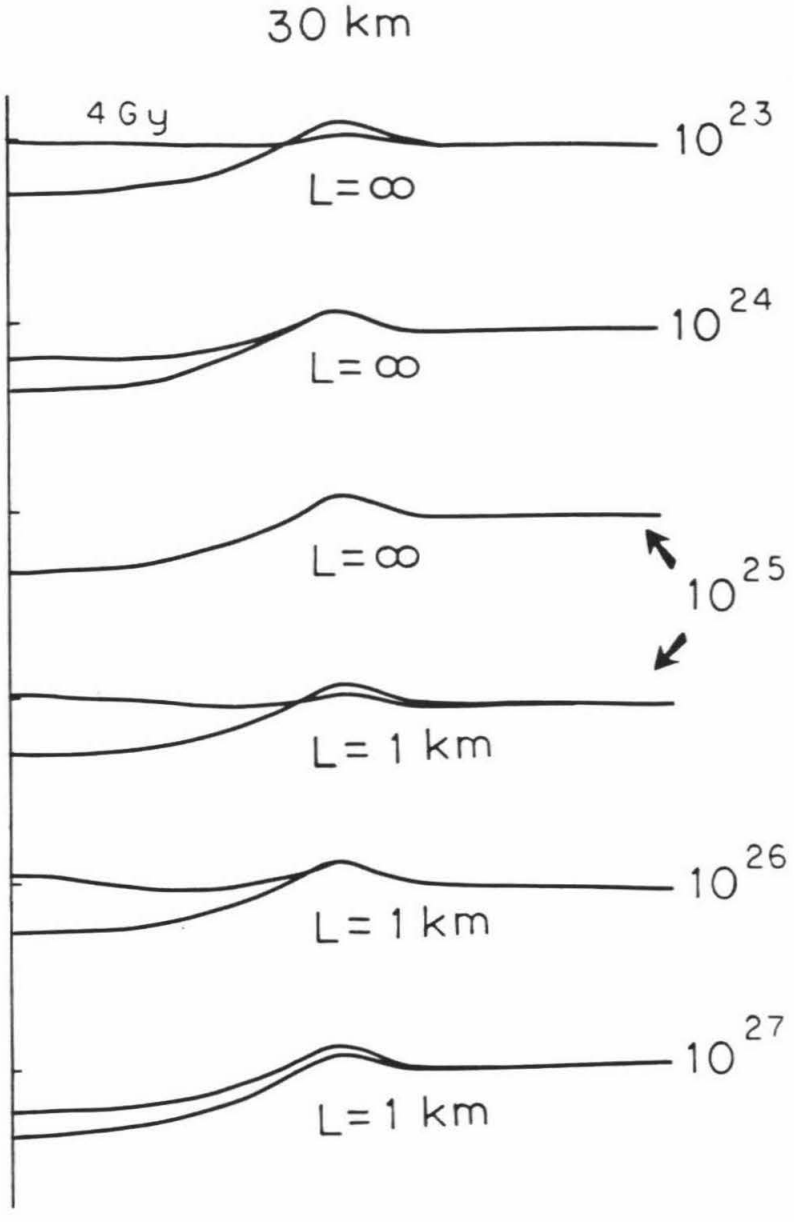

FIGURE 12.-- Same as for Figure 10 except that these profiles are for 30 km diameter craters.

TABLE II - Range of possible viscosities at the top of Enceladus' lithosphere based on slightly relaxed 30 km craters and unrelaxed 8 km craters in CT2.

Surface Viscosity η_o	E-folding depth of viscosity
10^{27}	Too viscous
10^{26}	0.5 - 1.0 km
10^{25}	1.0 - 5.0 km
10^{24}	3.0 - 10.0 km
10^{23}	Viscosity too low

[1] At the top of the lithosphere.

The relief observed within the plains terrain (P1) can be retained for at least several hundred million years on Enceladus with a viscosity at the top of the lithosphere of 10^{24} to 10^{25} poise provided that the e-folding depth of viscosity is greater than ~1 km. These values are only lower limits for the viscosity because no flattened craters are present on these terrains.

Formation of a regolith

The presence of a regolith on icy satellites has been discussed, in detail, elsewhere (Shoemaker et al., 1982; Passey, in press; Passey and Shoemaker, in preparation). The presence of an insulating regolith can greatly increase the rate at which craters (and other topographic features) will flatten by viscous relaxation in an icy lithosphere. This must also be true for Enceladus. The predicted thickness for the regolith on the most heavily cratered terrains on Enceladus (CT1-A and CT2) is a few hundred meters to approximately 1 km (based on calculations presented in Shoemaker et al., 1982). If the thermal conductivity of a thick regolith on Enceladus is much less than for the solid lithosphere, as it must be, then a thermal gradient of a few tenths of a degree per km, in the lithosphere, could translate into a temperature offset across the regolith of many tens of degrees K. The maximum thickness of this regolith would probably be limited by thermal annealing at the ~ 130K isotherm (Shoemaker et al., 1982); but, even for this case, the minimum temperature offset would be approximately 60K (based on an equatorial surface temperature of ~70K). This could substantially lower the effective viscosity at the top of the solid lithosphere in the regions of highest crater densities.

It should be noted that the same thickness regolith (and, thus, the same temperature at the top of the lithosphere) is predicted for both the CT1-A and CT2 terrains, but that craters are highly flattened in CT1-A, but not in CT2; thus, the

variations in crater flattening between these regions probably reflect variations in the ancient viscosity gradient rather than differences in the viscosities at the top of the lithosphere.

Terrains CT3, CT4, P1, and P2 (Figure 3) have been resurfaced within the relatively recent past, whether by flooding or other mechanisms; because the thickness of the regolith depends on the cratering history, and because these regions have low crater densities, it is reasonable to assume that the regoliths on these terrains are relatively thin, as compared to the regolith on the heavily cratered terrains. Accordingly, the temperature at the top of the lithosphere in these regions will be much colder (approaching the insolation controlled surface temperature for terrains with no regolith) than within terrains CT1-A and CT2. Thus, the viscosities at the top of the lithosphere in the sparsely cratered regions will be much higher; the previously determined upper limit of 10^{25} poise for the viscosity at the top of the lithosphere in CT1-A and CT2, is only a lower limit for the other terrains of lower crater density.

Thermal structure assuming water ice

From the determination that the viscosity at the top of the lithosphere was between 10^{24} and 10^{25} poise, in the regions of flattened craters, it can be concluded that the lithospheric material in Enceladus is not exactly the same as for the lithospheric material of Ganymede and Callisto. This is because a temperature of ~ 130 K is probably the highest temperature that an icy regolith can attain without annealing; assuming that the regoliths on Ganymede, Callisto, and Enceladus are thermally annealed, then the maximum temperature at the top of the lithospheres (i.e. at the base of the insulating regoliths) is ~130K. For Ganymede and Callisto, this temperature corresponds to a viscosity of 10^{26} poise, and for Enceladus, this same temperature would correspond to a viscosity

between 10^{24} and 10^{25} poise.

If, on the other hand, we assume that the regoliths on Ganymede and Callisto are thermally annealed at ~130K, but that the regolith on Enceladus is not quite thick enough to be thermally annealed, which is probable, then the temperature at the top of the lithosphere on Enceladus could be lower than ~130K. Even so, the derived viscosities are still one to two orders of magnitude less than for Ganymede and Callisto. This case definitely requires that the lithospheric material on Enceladus differs significantly from that of Ganymede and Callisto. One possible difference could be a mixture of ammonia ice with water ice (Stevenson and Anderson, 1981). The presence of a component with a low melting temperature probably would lower the effective viscosity of the mixture below that of pure water ice at temperatures a few tens of degrees below the eutectic temperature of the mixture.

Assuming that the regolith on Enceladus is annealed at ~130K, and assuming that the viscosity structure of the lithosphere is controlled predominantly by the water ice (not necessarily true, but a limiting case) then, the viscosity temperature relation would follow that for water ice, and is given by

$$\eta(T) = \eta_m \exp[A^*(\frac{T_m}{T} - 1)] \qquad (2)$$

where $\eta(T)$ is the viscosity at temperature T, η_m is the viscosity at the melting point, T_m is the temperature at the melting point, and A^* is a constant dependent on the creep activation energy. From the analysis of relaxed craters on Ganymede (Passey and Shoemaker, in preparation) the value for A^* was found to be 25. Using $\eta_m = 10^{14}$ poise at $T_m = 273$ K, it is possible to invert the derived viscosity gradients to thermal gradients. An e-folding depth of 0.25 km would correspond to a thermal gradient of > 20 K/km, and an e-folding depth of 0.5

km would correspond to a thermal gradient of ~10 K/km; similarly, L = 1.0 km corresponds to ~3 K/km, L = 3.0 corresponds to ~1 K/km, and L = 10 km corresponds to 0.5 K/km. It must be emphasized that these thermal gradients are for a pure water ice lithosphere and may not have any direct comparison if the lithosphere of Enceladus is a mixture of water ice and ammonia ice.

CONCLUSIONS

Enceladus has a complex geologic and rheologic history. The localized distribution of relaxed craters suggests that discrete regions exist (or existed) in which the effective viscosity of the lithosphere is lower than in adjacent regions; because the viscosity at the top of the lithospheres in these regions is probably the same, it implies that steeper viscosity gradients exist (or have existed) beneath some regions as compared to adjacent regions. These regions of steeper viscosity gradients probably were zones of higher heat flow.

The effective viscosity at the top of the lithosphere of Enceladus, in the regions of the flattened craters, must be between 10^{24} and 10^{25} poise in order to explain the wide diversity in relaxed and unrelaxed craters of various diameters. These values for viscosity are one to two orders of magnitude lower than was calculated for Ganymede and Callisto (Passey and Shoemaker, in preparation); because the temperature at the top of the lithosphere of Enceladus must be less than or equal to that on Ganymede and Callisto, (because of the presence of an insulating regolith), the composition of the lithosphere of Enceladus must be significantly different than of the lithospheres of Ganymede and Callisto. The lithosphere of Enceladus may be composed of a mixture of water ice and ammonia ice.

REFERENCES CITED

Bonner, W.J.,and Schmall, R.A., (1973) A photometric technique for determining planetary slopes from orbital photographs, *U.S. Geol. Survey Prof. Paper 812-A*, 16 p.

Brennen, C., (1974) Isostatic recovery and the strain rate dependent viscosity of the Earth's mantle *Jour. Geophys. Res.*, *79*, 3993-4001.

Danes, Z.F., (1962) Isostatic compensation of Lunar craters, Research Institute Univ. Puget Sound, Tacoma, Washington, RIR-GP-62-1, 11 p.

----------, (1965) Rebound processes in large craters, U.S. Geol. Survey Astrogeol. Stud. Annu. Prog. Rept. July 1, 1964 to July 1, 1965, Part A: Lunar and Planetary Investigations, Nov. 1965, p. 81-100.

----------, (1968) Isostatic processes in media of variable viscosity, 1. Cartesian geometry, *Icarus*, *9*, p. 1-7. Parmentier, E.M., and Head, J.W., (1981) Viscous relaxation of impact craters on icy planetary surfaces: Determination of viscosity variation with depth, *Icarus*, *47*, p. 100-111.

Passey, Q.R., and Shoemaker, E.M., (1982) Craters and basins on Ganymede and Callisto: Morphological indicators of crustal evolution, Chapter 12 *in* **The Satellites of Jupiter,** D. Morrison ed., University of Arizona Press, Tucson.

---------- (in preparation) Thermal evolution of the lithospheres of Ganymede and Callisto.

Pike, R.J., (1977) Size-dependence in the shape of fresh impact craters on the Moon, *in* **Impact and Explosion Cratering,** D.J. Roddy, R.O. Pepin, and R.B. Merrill (editors), Pergamon Press, New York, p. 489-509.

Plescia, J.B., and Boyce, J.M., (1981) Crater densities of the Saturnian satellites:

Enceladus, Iapetus, and Tethys, NASA TM-84211, p. 7-9.

Shoemaker, E.M., Lucchita, B., Wilhelms, D., Plescia, J.B., and Squyres, S.W., (1982) The Geology of Ganymede, *in* **The Satellites of Jupiter,** D. Morrison ed., University of Arizona Press, Tucson.

Smith, B.A., and the Voyager Imaging Team, (1981) Encounter with Saturn: Voyager 1 imaging science results, *Science, 212*, p. 163-191.

----------, (1982) A new look at the Saturn system: The Voyager 2 images, *Science, 215*, p. 504-537.

Squyres, S.W., (1981) The topography of Ganymede's grooved terrain, *Icarus, 46*, p. 156-168.

Squyres, S.W., and Veverka, J., (1981) Voyager photometry of surface features on Ganymede and Callisto, *Icarus, 46*, p. 137-155.

Stevenson, D.J., and Anderson, A., (1981) Volcanism and igneous processes in small icy satellites, EOS, 62, p. 1081.

Yoder, C.F., (1979) How tidal heating in Io drives the galilean orbital resonance locks, *Nature, 279*, p. 767-770.

PAPER 5

UPPER MANTLE VISCOSITY DERIVED FROM THE DIFFERENCE IN REBOUND OF THE PROVO AND BONNEVILLE SHORELINES: LAKE BONNEVILLE BASIN, UTAH

by QUINN R. PASSEY

Published in *JOURNAL OF GEOPHYSICAL RESEARCH*
Volume 86, pages 11701-11708

ABSTRACT

Twenty-four new field measurements of elevation of Provo-level and Bonneville-level shoreline terraces provide data for reanalysis of isostatic rebound in the Lake Bonneville basin. Analysis of the differential rebound between the Provo shoreline (maximum rebound of 43 m) and the Bonneville shoreline (maximum rebound of 69 m) requires that the latter be an equilibrium shoreline. Within the possible measurement errors, the Provo shoreline formed after the elastic lithosphere had attained at least 91 percent equilibration to the removal of the water load between the Bonneville and Provo shorelines; within the errors the Provo may also represent an equilibrium shoreline.

From the new data presented in this paper, the best estimate of the upper limit of effective viscosity of the uppermost mantle, assuming a half-space model and a 2000 year time interval between the Bonneville and Provo shorelines, is 2×10^{19} N sec m^{-2} (2×10^{20} poise). In addition, comparison of shoreline rebound profiles, for both shorelines, with theoretical plate flexure models indicates that the mean flexural rigidity of the Basin and Range lithosphere in this region is 1×10^{23} N m, or slightly less.

INTRODUCTION

Lake Bonneville was the largest of the late Pleistocene lakes which occupied portions of the Great Basin of the Western United States. At the time of its maximum filling, the lake covered an area greater than 49,000 km^2 (Fig. 1) and, in the central part of the lake, the maximum depth was approximately 340 meters.

Gilbert (1890) made an extensive study of the shoreline features of Lake Bonneville and in so doing he identified several different shoreline levels. Later workers (Morrison, 1965; Bissell, 1963; Hunt, Varnes, and Thomas, 1953; Williams, 1962) have also contributed to an understanding of the history of Lake Bonneville. Gilbert also noted that the highest shoreline, the Bonneville, is at a higher elevation on what were former islands in the middle of Lake Bonneville than at the edges of the basin. He correctly concluded that the central uplift was in response to the removal of the water load from the earth's surface. It has been shown by both Gilbert (1890) and Crittenden (1963a) that elastic deformation of the crust cannot explain the magnitude of the deformation observed. The deformation must have resulted as an isostatic response to the load by viscous flow within the uppermost mantle. Crittenden's work set an upper limit of between 0.9×10^{21} and 2×10^{21} poise to the uppermost mantle from the analysis of the rebound of the Bonneville shoreline.

Purpose of this study

The objective of this study is to set a new and more restrictive upper limit to the effective viscosity of the uppermost mantle from new measurements of the rebound of both the Bonneville and Provo shorelines in addition to an analysis of the differential rebound between these two shorelines. A reanalysis of the flexural rigidity of the lithosphere based on new rebound profiles of the shorelines within the Lake Bonneville basin is also included.

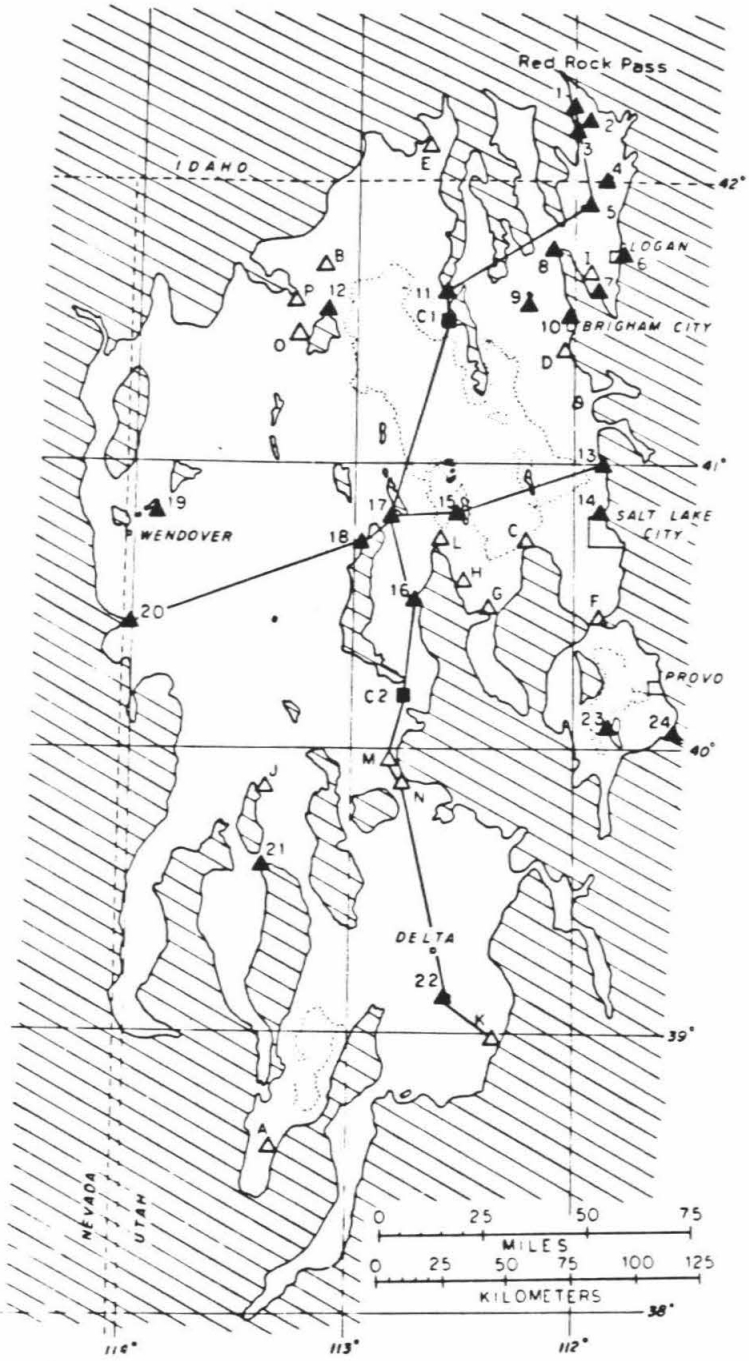

FIGURE 1 - When at its highest level (the Bonneville level), Lake Bonneville occupied the unpatterned area. The numbered solid triangles mark the locations of new elevation measurements of the Bonneville and Provo shorelines. The solid squares are measurements of Crittenden (1963). The open triangles mark the locations of similar measurements by Gilbert (1890), and are listed in Table II. The heavy solid lines show where the profiles in Figures 4 and 5 were constructed. Outlines of the present day Great Salt Lake, Utah Lake and Sevier Lake are dashed.

The field work for this project was carried out during the summer of 1979. The measurement method involved a hand level and 1.5 meter rod (Jacob's staff). Accurate topographic control was supplied from U.S. Geological Survey 7-1/2 or 15 minute topographic quandragle maps. Most of the elevations measured are linked to bench-mark elevations and are accurate to within ± 1 meter. Several measurements which could not be linked to bench-marks were referenced to hill-top elevations or spot elevations and are probably accurate to within ± 2 meters. The elevations of the shoreline terraces are referenced to the point of inflection of the terrace with the hill slope above the terrace. The precision of measurement of this point is generally within ± 1 meter.

History of Lake Bonneville since 25,000 years B.P.

The most recent studies (Scott, 1980; Currey, 1980) indicate that the latest filling of Lake Bonneville began about 25,000 years ago. This transgression may have been aided by the diversion of the Bear River into the Bonneville basin, which occurred sometime between 20,000 and 30,000 years B.P. (Bright, 1963).

Recent radiocarbon dates, provided by Meyer Rubin, on wood and charcoal from transgressive shoreline deposits indicate that the lake had not filled to the Bonneville level (the highest recorded level) until sometime after 17,500 ^{14}C years B.P.; at 17,500 ^{14}C years B.P. the lake was about 65 meters below the Bonneville level (Scott, 1980) (Fig. 2). Lake Bonneville probably occupied the Bonneville shoreline beginning sometime between 16,000 and 17,000 ^{14}C years B.P.

The amount of time the lake stood at the Bonneville level is not precisely known but radiocarbon dates suggest that the Provo shoreline, whose baseline is 100 ± 2 meters lower than the Bonneville shoreline, was occupied from about 14,000 to 12,500 ^{14}C years B.P. (Bright, 1963; Broecker and Orr, 1958; Broecker

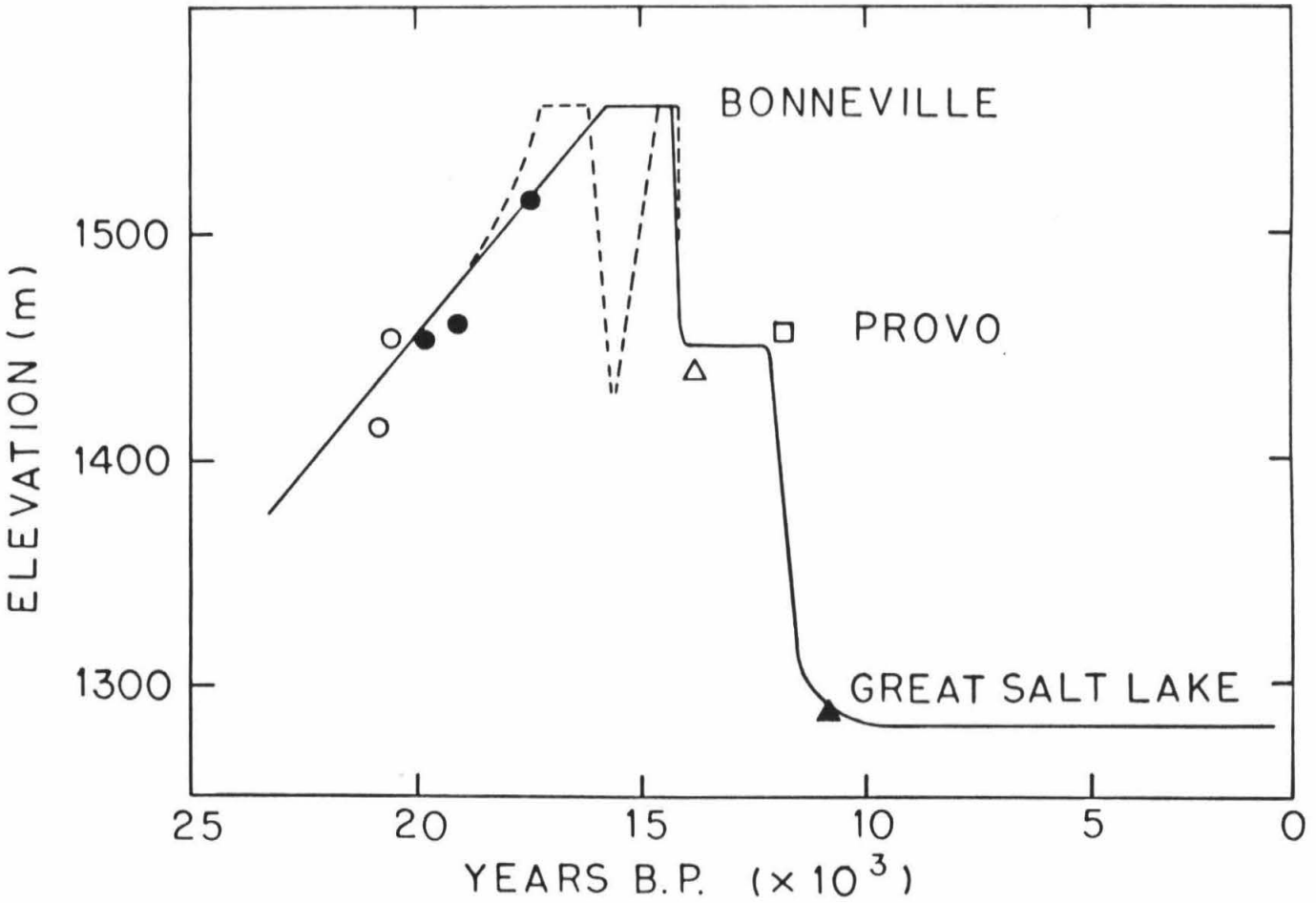

FIGURE 2 - Inferred history of Lake Bonneville levels since 25,000 years B.P. The solid line is the history suggested by Scott (1980) and the broken line is that defended by Currey (1980). The solid circles are radiocarbon dates from wood and charcoal by Meyer Rubin (reported in Scott, 1980), the open circlesare from wood (Broecker and Kaufman, 1965), the open triangle is from a freshwater shell (Bright, 1963), the solid triangle is from a freshwater shell (Miller et al., 1980), and the open square is from a land-snail shell (Broecker and Kaufman, 1965).

and Kaufman, 1965). The fall from the Bonneville to Provo level is generally believed to have resulted from the overflow of Lake Bonneville at Red Rock Pass in southeastern Idaho; this produced rapid downcutting of the outlet and the associated catastrophic flood in the Snake River Plain (Gilbert, 1890; Malde, 1968). The elevation of the bedrock channel in Red Rock Pass is 1450 meters (Williams and Milligan, 1968). This is very near the lowest measured elevation of the Provo level shoreline and suggests that the Provo level was maintained by overflow across the bedrock sill at Red Rock Pass. The baseline elevation for the Bonneville shoreline is 1550 ± 1 m (Crittenden, 1963a), and for the Provo shoreline, the baseline elevation is 1450 ± 1 m, corresponding to the elevation of the bedrock outlet.

A radiocarbon date from a gastropod shell indicates that by about 11,000 ^{14}C years B.P., the elevation of Lake Bonneville was within 10 meters of the Great Salt Lake (elevation 1280 meters) (Miller et al., 1980). The regression from the Provo level, therefore, occurred sometime prior to 11,000 ^{14}C years B.P.

Currey (1980) has proposed that Lake Bonneville occupied the Bonneville level twice between 19,000 and 13,000 ^{14}C years B.P.; the first transgression to the Bonneville level, culminating at about 16,500 ^{14}C years B.P., resulted in the formation of the prominent Bonneville shoreline terrace as well as a much less distinct single beach ridge about 6 meters above this terrace. The later transgression reached the Bonneville level around 15,000 ^{14}C years B.P. and accomplished little geomorphic reworking of the earlier Bonneville level deposits before the lake level dropped to the Provo level by 14,000 ^{14}C years B.P.

The Provo level is generally represented by the most conspicuous shoreline terraces within the Bonneville basin and must have been stably maintained for considerable time. Deltas and spits associated with this level extend up to

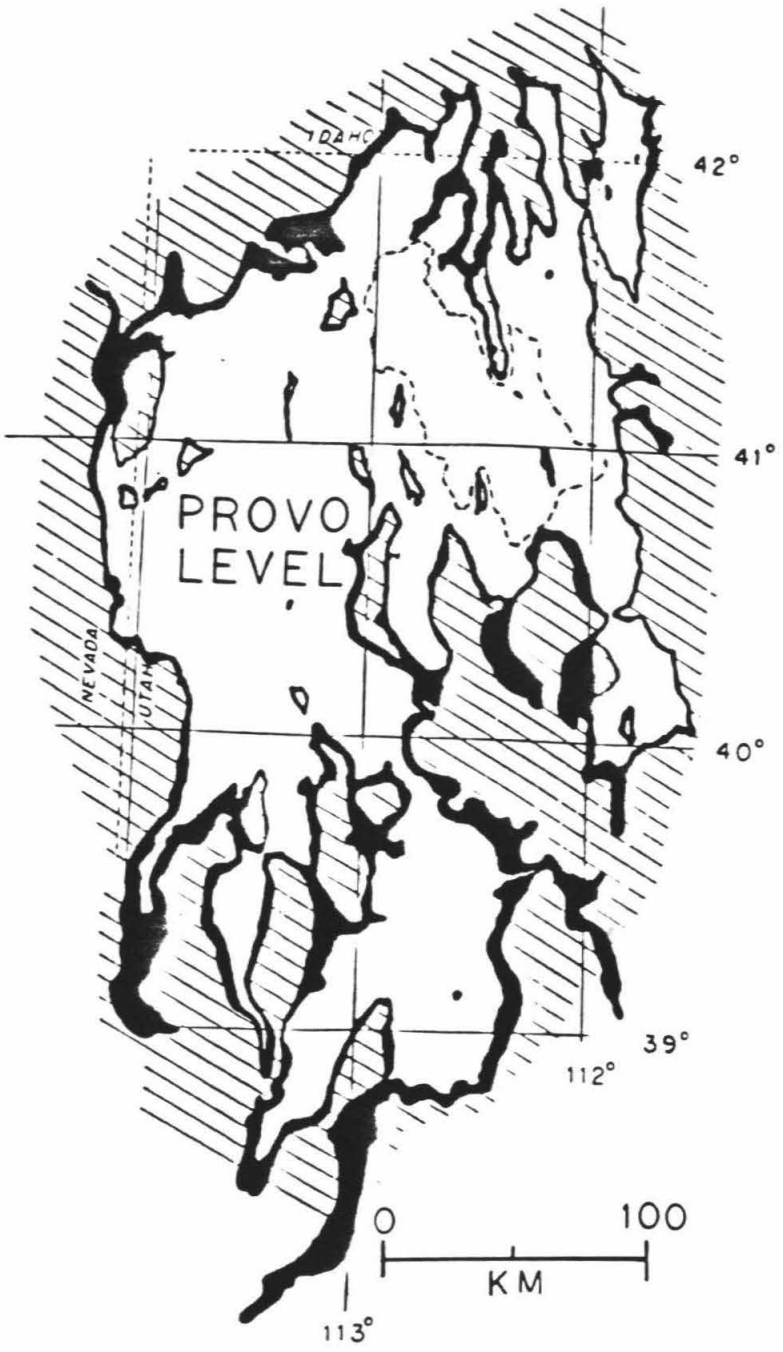

FIGURE 3 - Lake Bonneville occupied the unpatterned area when its surface was at the Provo level. The blackened areas mark zones that are above the Provo but below the Bonneville shorelines.

several kilometers into the basin. Radiocarbon dates suggest that the Provo level was maintained for about 2000 years (Broecker and Kaufman, 1965). Assuming that the major Bonneville shoreline (which was the one that was measured for this paper) represents a stable shoreline at approximately 16,000 ^{14}C years B.P., and that the Provo shoreline was stable at 13,000 ^{14}C years B.P., the best estimate of the time interval between the Bonneville and Provo shorelines is 2,000 ^{14}C years (refer to Fig. 2). This time interval is presently not well constrained; the range in the possible time between the Bonneville and Provo shorelines is from 500 years, or less, to a maximum of about 3500 years. Additional radiocarbon dates of shells and wood associated with the Bonneville level is needed and would greatly aid in constraining the time interval between the Bonneville and Provo shorelines.

NEW DATA

Table I displays twenty-four new measurements of elevation of the Bonneville and Provo shorelines. Figure 1 shows their corresponding locations. Sixteen additional elevations measured by Gilbert (1890) are listed in Table II; these complement the present work and aid in the construction of the rebound profiles.

The maximum rebound of the Bonneville shoreline is 69 ± 2 meters above the 1550 m elevation baseline; this corresponds to a maximum water depth of 339 ± 2 meters in the central region of the lake. Similarly, the maximum rebound of the Provo shoreline is 43 ± 2 meters above the 1450 m elevation baseline; this corresponds to a maximum water depth of 213 ± 2 meters (Figs. 4 & 5). Although the maximum water depth is recorded from only one measurement location (Table I, point 17), it is important to note that the depth of Lake Bonneville was within a few meters of the maximum depth to a radial distance of

TABLE I - NEW ELEVATION MEASUREMENTS OF THE PROVO AND BONNEVILLE SHORELINES

Point[1]	Location	U.S.G.S. Quadrangle	Provo[2] Elevation (m)	Bonneville[2] Elevation (m)
1	NW 1/4, Sec 5, T13S, R38E	Oxford, Idaho	1460[3]	1568
2	NE 1/4, Sec 25, T14S, R38E	Banida, Idaho	----	1548 ?
3	S 1/2, Sec 27, T14S, R38E	Clifton, Idaho	----	1551 ?
4	Sec 19, T16S, R40E	Franklin, Idaho	1466	1565
5	SW 1/4, Sec 4, T13N, R38E	Trenton, Utah	1463	1585
6	NW 1/4, Sec 36, T12N, R1E	Logan, Utah	1464	1564
7	E 1/2, Sec 13, T10N, R1W	Mount Pisgah, Utah	1466	1580
8	E 1/2, Sec 20, T12N, R2W	Cutler Dam, Utah	1468	1577
9	Sec 19, T10N, R3W	Bear River City, Utah	1472	1590
10	SE 1/4, Sec 7, T9N, R1W	Brigham City, Utah	1469	1588
11	T10N, R7W	Promontory Point, Utah	1484	1597
12	Sec 7 & 18, T10N, R11W	Hogup Bar, Utah	1481	1603
13	N 1/2, Sec 18, T3N, R1E	Farmington, Utah	1463	1579
14	NE 1/4, Sec 25, T1N, R1W	Salt Lake City N., Utah	1477	1590[5]
15	Sec 15, T1N, R6W	Corral Canyon, Utah	1490	1612
16	Sec 22 & 23, T3S, R8W	Timpie, Utah	1484	1615
17	Sec 14 & 15, T1N, R9W	Delle, Utah	1493	1619
18	Sec 25, T1N, R10W	Low, Utah	1492	1617
19	Sec 16 & 21, T1N, R18W	Tetzlaff Peak, Utah	1484	(1589)[4]
20	T5S, R19W	Ferguson Flat, Nev.-Utah	1463	1585
21	Sec 10,14 & 15, T14S, R14W	Sand Pass, Utah	1463	1571
22	Sec 29 & 30, T19S, R6W	Pavant Butte North, Utah	1477	1585
23	N 1/2, Sec 21, T8S, R1E	West Mountain, Utah	1458	1571
24	Sec 33 & 34, T8S, R3E	Spanish Fork Peak, Utah	1466	1568

[1] Refer to Figure 1.

[2] Generally ± 2 meters.

[3] ± 10 meters.

[4] From Crittenden (1963a)

[5] May be above a post-Lake Bonneville fault

TABLE II - PROVO AND BONNEVILLE SHORELINE ELEVATIONS, FROM GILBERT (1890)

Point[1]	Location	Provo Elevation[2] (m)	Bonneville Elevation[2] (m)
A	Wah Wah Valley	(1454)	(1557)
B	Kelton Butte	1484	1592
C	Black Rock	1477	1586
D	Willard	1472	1582
E	Snowsville	(1468)	(1579)
F	Point of Mountain	1458	1571
G	Stockton	1477	1591
H	Grantsville	1477	1593
I	Wellsville	(1463)	(1579)
J	Fish Springs	(1472)	(1588)
K	Fillmore	1461	1568
L	N. Stansbury Range	1489	1607
M	Cup Butte	1472	(1591)
N	Snowplow	1470	(1591)
O	West Hogup Mountains	1478	1603
P	Dove Creek	1465	1591

[1] Refer to Figure 1.

[2] Values in parentheses are not direct elevation measurements by Gilbert but were obtained from his terrace profiles.

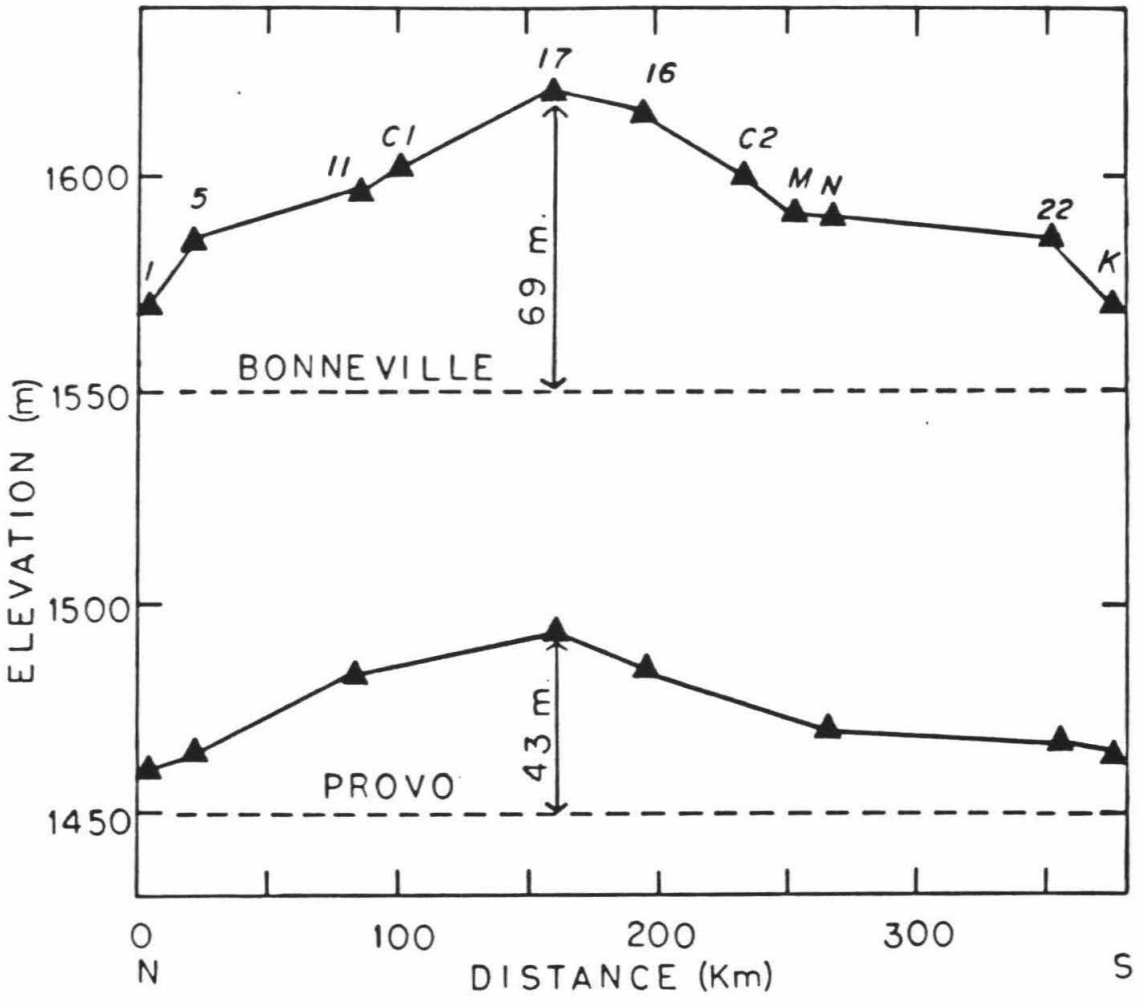

FIGURE 4 - A north-to-south profile across the Lake Bonneville basin showing the elevations of the Bonneville and Provo shorelines at several locations. Refer to Figure 1 and Tables I & II for the precise locations of the points. The broken lines are the baseline levels for the shorelines. For the Bonneville shoreline, the baseline elevation is 1550 ± 1 m (Crittenden, 1963a), and for the Provo shoreline, the baseline elevation is 1450 ± 1 m (Williams & Milligan, 1968). The difference in the amount of rebound of the Bonneville and Provo shorelines provides the basis for calculating the viscosity of the uppermost mantle.

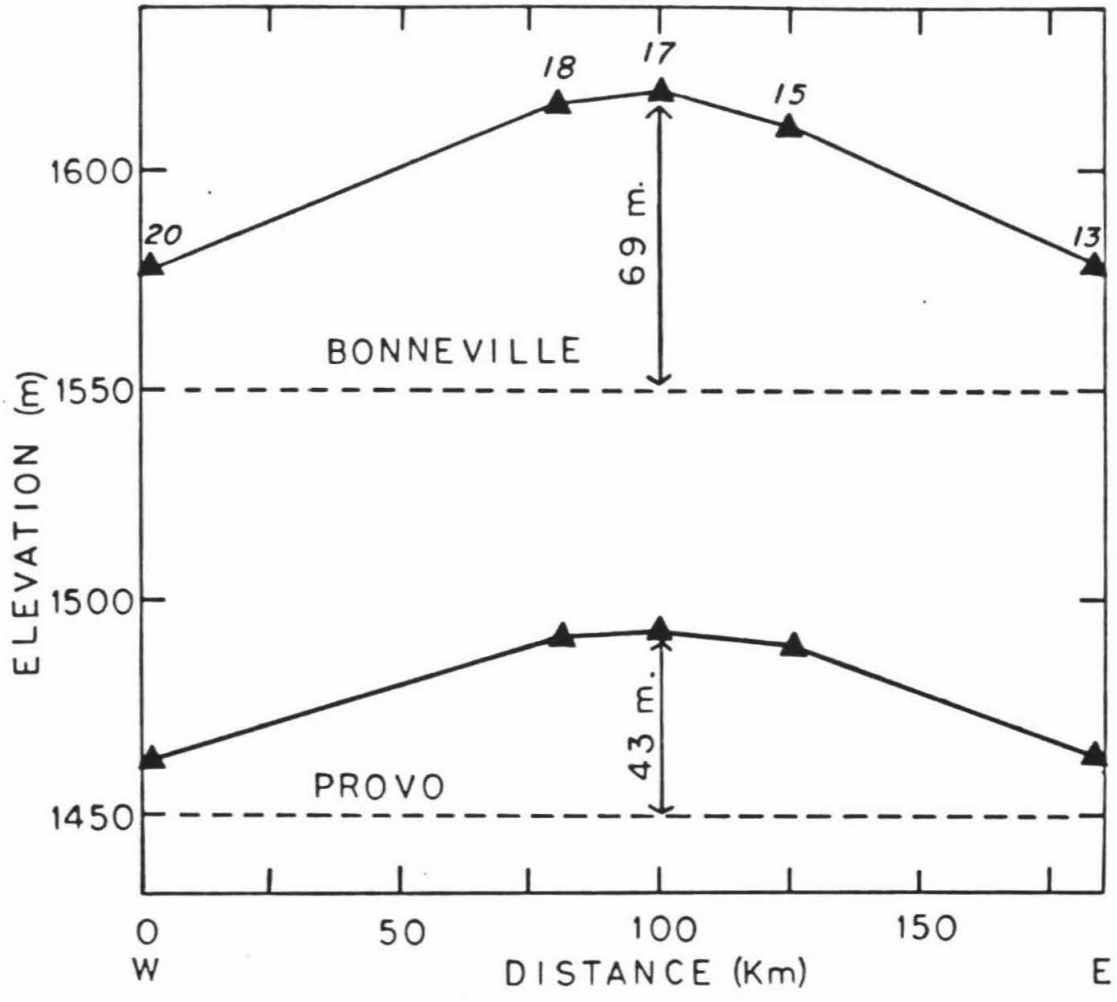

FIGURE 5 - Same as for figure 4 except this graph is a west-to-east profile across the Lake Bonneville basin showing the elevations of the Bonneville and Provo shorelines in several locations. (Note that the horizontal scale used in this profile is different than the one used in Figure 4).

about 50 km from that location.

DISCUSSION

Flexural Rigidity

Crittenden (1963 a,b) noted that the observed rebound of the Bonneville shoreline is only approximately 75 percent of the total possible isostatic deformation; he attributed this to a non-equilibrium Bonneville shoreline. Walcott (1970), in calculating the flexural rigidity of the lithosphere in this region, *assumed* that the Bonneville shoreline was in equilibrium but that the failure to attain 100 percent isostatic equilibrium was simply a result of the deformation being limited by the flexural rigidity of the lithosphere.

The new data on the rebound of the Provo shoreline allow for the testing of Walcott's assumption. The fraction of the total possible isostatic response (F_I) can be calculated by the following expression:

$$F_I = \left(\frac{\omega_{MAX}}{h_{MAX}}\right)\left(\frac{\rho_m}{\rho_w}\right) \qquad (1)$$

where ω_{MAX} is the maximum observed shoreline deformation (i.e. rebound), h_{MAX} is the maximum water depth, ρ_m is the density of the uppermost mantle (= 3.4 g cm^{-3}), and ρ_w is the density of water (= 1.0 g cm^{-3}).

For the Bonneville shoreline

$$F_I\,(Bonneville) = \left(\frac{69 \pm 2}{339 \pm 2}\right)\left(\frac{3.4}{1.0}\right) = 0.69 \qquad (1a)$$

and for the Provo shoreline

$$F_I\,(Provo) = \left(\frac{43 \pm 2}{213 \pm 2}\right)\left(\frac{3.4}{1.0}\right) = 0.69 \quad . \qquad (1b)$$

Similarly, for the differential rebound and water load between the Bonneville and Provo shorelines

$$F_I\,(B-P) = \left(\frac{26}{126}\right)\left(\frac{3.4}{1.0}\right) = 0.70 \quad . \tag{1c}$$

It would be impossible for the rebound of both the Bonneville and Provo shorelines (and similarly the differential rebound) to be the same fraction (i.e. 0.69-0.70) of the total possible isostatic value unless the lithospheric flexures, in adjustment to the loading, were stopped by the flexural rigidity of the lithosphere. Moreover, this requires that both shorelines had time to obtain a high degree of isostatic equilibrium. Therefore, the assumption of Walcott (1970) that the Bonneville shoreline was in equilibrium must be correct but, in addition, the Provo shoreline also must have been at (or very near) equilibrium.

Cathles (1975) has shown that if the flexural rigidity of the crust is of order 6 x 10^{23} N m, a simple cylindrical load with the areal extent of Lake Bonneville (radius 100 km) would be approximately 70% supported by isostatic adjustment; the remainder would be supported by the resistance of the crust to flexure.

One can estimate the flexural rigidity of the elastic layer (lithosphere) by modeling the crustal flexure due to the load of Lake Bonneville at different shoreline levels and by comparing the calculated lithospheric displacements with the observed shoreline displacements, as is shown in figures 4 and 5. Following the method of Brotchie and Silvester (1969) for calculating the deflection, ω, from a cylindrical load, the deflection within the loaded circle, ω_i, can be expressed as

$$\omega_i = \frac{\rho_w\, h}{\gamma}\left(\, a\; ker'a\;\; ber\; x - a\; kei'a\; bei\; x + 1\,\right) \tag{2}$$

and the deflection outside the loaded circle, ω_o , can be expressed as

$$\omega_o = \frac{\rho_w\, h}{\gamma}\left(a\; ber'a\;\; ker\; x - a\; bei'a\;\; kei\; x\,\right) \tag{3}$$

In these equations, ρ_w is the density of the load, h is the height (or depth) of the

load, $x = r / L$ where r is the radial distance from the center of the load and L is the "radius of relative stiffness" and is defined as

$$L^4 = \frac{D}{(E\ T / R_E^2 + \rho_m)} \tag{4}$$

where D is the flexural rigidity and is defined as

$$D = \frac{E\ T^3}{[\ 12\ (1 - \nu^2)]} \tag{5}$$

where E is the Young's modulus, T is the thickness of the crust, ν is Poisson's ratio ($\nu = 0.25$), R_E is the middle surface radius (radius of earth), and ρ_m is the density of the mantle; $\gamma = \rho_m + E\ T / R_E^2$, $a = A / L$ where A is the radius of the cylindrical load, ber, bei, ker and kei are the zero order Bessel-Kelvin function and the primed functions (e.g. *ber'*) are the first derivatives of those functions. For the calculations presented in this paper, the flexural rigidity, $D = 1 \times 10^{23}$ N m for $T = 24$ km and $D = 4 \times 10^{23}$ N m for $T = 37$ km, $E = 8.35 \times 10^{10}$ N m^{-2}, $R_E = 6350$ km, $\rho_m = 3400$ kg m^{-3}, and $\rho_w = 1000$ kg m^{-3}.

The simplest model of Lake Bonneville assumes two adjacent cylindrical loads, a main body, and a smaller body which will be referred to, in this paper, as the Delta load. The main body of the lake can be modeled as a cylindrical load, centered at 41° N and 113° W, with a radius of 100 km and a depth, h, of 310 meters; the Delta load can be modeled as a cylinder, centered at 39° 20' N and 112° 40' W, with a radius of 60 km and a depth of 120 meters. This model is similar to the model studied by Brotchie (1971) and a comparison of the predicted displacement of the Bonneville shoreline with the observed displacement (Fig. 6ab) shows that for this model the best fit to the Bonneville shoreline assumes a flexural rigidity of approximately 4×10^{23} N m. The fit of this model to the data is reasonably good except at the east and west lake boundaries, as is shown in figure 6b.

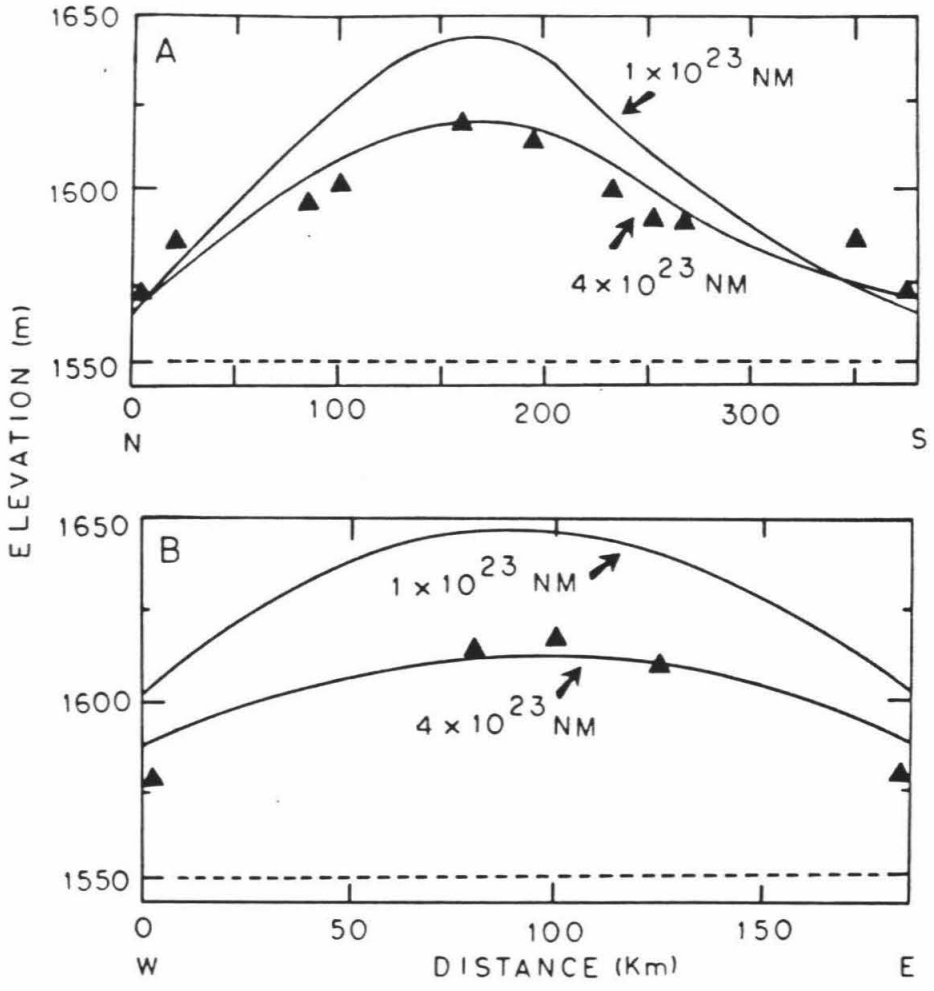

FIGURE 6 - Calculated deflections of the Bonneville shoreline, assuming two flexural rigidities for the lithosphere, using a model of the load of Lake Bonneville as two simple cylinders, the centers of which are 180 km apart; the main body of the lake is expressed as a cylinder 100 km in radius and 310 meters deep, and the Delta body of the lake is expressed as a cylinder 60 km in radius and 120 meters deep. Figure (a) is a north-south profile, and figure (b) is a west-east profile.'

Figures 7 and 8 show the predicted and observed displacements for both the Bonneville and Provo shorelines using a more realistic model for the distribution of the load where the lake bodies are deeper near their centers than at their boundaries. A better fit to the observed displacements is obtained with this more realistic model; a flexural rigidity of 1×10^{23} N m, or slightly less, is suggested from this model and this is comparable with the flexural rigidity of $5 \pm 2 \times 10^{22}$ N m calculated by Walcott (1970). With a flexural rigidity as low as 10^{23} N m, the acceleration of isostatic adjustment by flexural stresses in the crust is not significant. Variations between the predicted response and the observed rebound probably are due to errors in the modelling of the distribution of the water load, but may also be due, in part, to inaccuracies in assuming the lithosphere to be a simple elastic plate of uniform properties (c.f. Walcott, 1970).

Figures 7 and 8 (the more realistic model) show that the observed maximum displacements of the Bonneville and Provo shorelines, of 69 meters and 43 meters respectively, are at, or very near, their equilibrium values for a 1×10^{23} N m elastic layer; moreover, the general fit of this more realistic model to the data is much better (particularly in the east and west boundaries) than the fit of the simpler model shown in figure 6.

Isostatic Rebound

Relaxation time constant.-- The time dependence of the observed deformation is assumed to be controlled by the viscous response the uppermost mantle, which is overlain by a purely elastic plate. The uppermost mantle is assumed to be an incompressible Newtonian fluid of uniform viscosity where the inertial effects are negligible. For this case the deformation can be expressed as

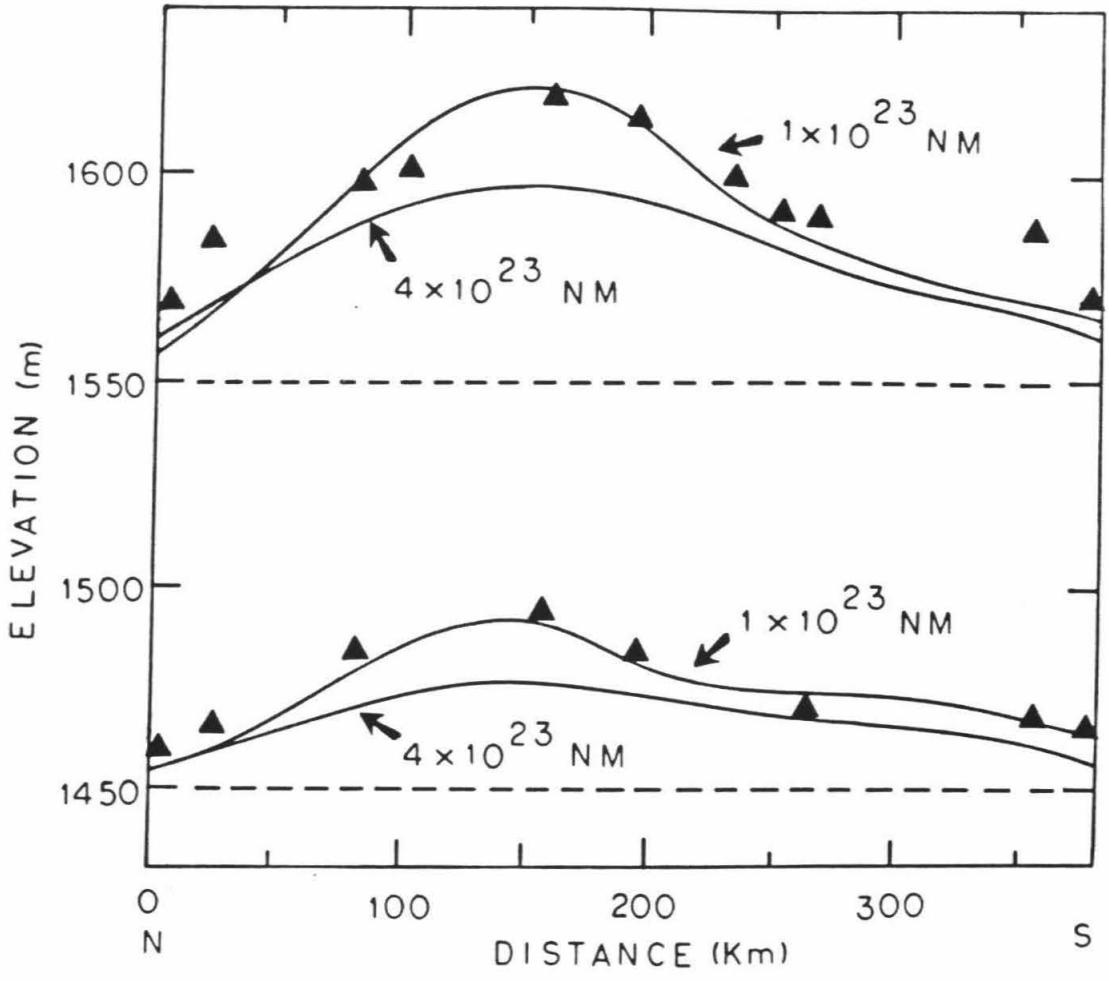

FIGURE 7 - Calculated deflection for the N-S profile of both the Bonneville and Provo shorelines using a more realistic model for the distribution of the water load. The broken lines are the baseline levels, the solid triangles mark the observed shoreline rebound measurements and the solid lines mark the calculated rebound assuming two different flexural rigidities for the lithosphere. For the Bonneville-level curves (upper set), the main body of the lake was modeled as a stack of three cylindrical positive loads centered at 41° N and 113° W; the top cylinder was assumed to have a radius, A, of 100 km and a depth, h, of 110 m, the middle cylinder has a radius of 80 km and a depth of 110 m, and the bottom cylinder has a radius of 60 km and a depth of 120 m. The Delta load was modeled as two stacked cylindrical positive loads centered at 39° 20' N and 112° 40' W. The top cylinder has a radius, A, of 60 km and a depth, h, of 100 m, and the bottom cylinder has a radius of 30 km and a depth of 80 m. A third cylindrical load with the opposite deflection (negative) of the two lake bodies was used to compensate for the lack of circular symmetry in the main body of Lake Bonneville. This negative load was centered at approximately 40° 30' N and 112° 35' W; it was assumed to have a radius of 30 km and a height of 200 meters. For the Provo curves, the top cylinder of both bodies of water (the main body and the Delta body) were removed but the negative load remained unchanged.

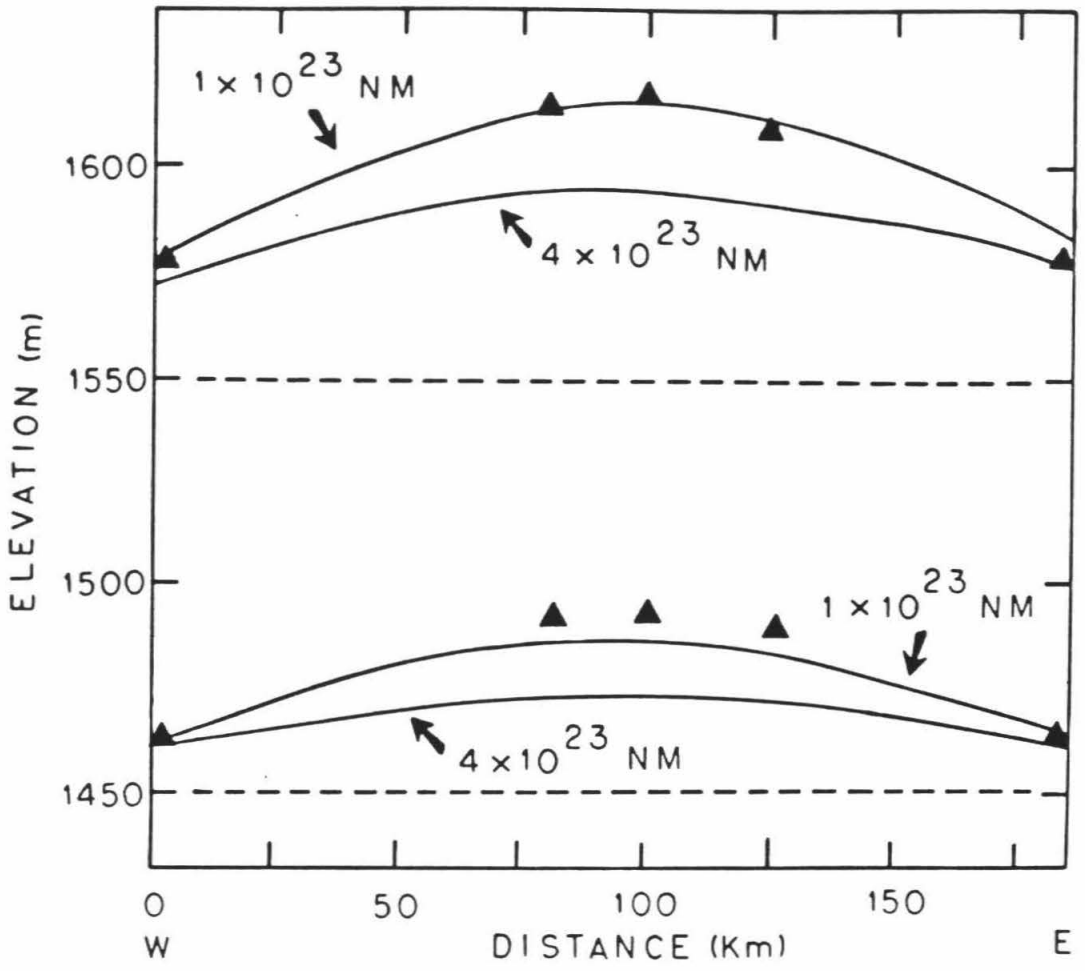

FIGURE 8 - Same as for Figure 7 except that these curves are for the W-E profile of the shoreline rebound.

$$d = 1 - exp(-t/\tau) \tag{6}$$

Solving eqn (6) for τ yields

$$\tau = \frac{-t}{ln(1-d)} \tag{7}$$

where d is the fraction of the ultimate response occurring at any instant t (in years after the application or removal of the load), and τ is the relaxation time constant.

The fraction of the ultimate response, d, can be expressed as

$$d = \frac{\omega_{MAX}}{\omega_E} \tag{8}$$

where ω_{MAX} is the maximum observed deformation and ω_E is the maximum expected deformation. In that the Bonneville shoreline represents an equilibrium shoreline, ω_E can be expressed as

$$\omega_E = \frac{[F_I\,(Bonneville)]\,(h_{MAX})\,(\rho_w)}{\rho_m} \tag{9}$$

where $F_I\,(Bonneville)$ is obtained from eqn (1a). From the Provo shoreline rebound data

$$\omega_E = \frac{(0.69)\,(213\ m)}{(3.4)} = 43\ meters.$$

Therefore, from these data, and from eqn (8)

$$d = \frac{43}{43} = 100\%$$

which suggests that, excluding possible errors in the measurements, the Provo shoreline was also in equilibrium; this was previously suggested in that $F_I\,(Provo) = F_I\,(Bonneville)$. This implies that relaxation time for the viscous response was very short as compared to the time interval between the

Bonneville and Provo shorelines.

From an analysis of the possible errors in the field measurements it is possible to calculate the lower limit of the total possible response (i.e. d_{MIN}). From equation (1a) the maximum value for F_I (*Bonneville*) is

$$F_I\,(Bonneville) = \left(\frac{69 + 2}{339 - 2}\right)\left(\frac{3.4}{1.0}\right) = 0.716\,.$$

Similarly, using this value in equation (9) yields

$$\omega_E = \frac{(.716)(213 + 2)}{3.4} = 45\ meters\,,$$

Substituting ω_E = 45 m into equation (8) and utilizing the lowest allowable value of the maximum rebound of the Provo shoreline yields

$$d_{MIN} = \left(\frac{43 - 2}{45}\right) = 91\ \%\,.$$

Thus, within the possible errors, the minimum value of the fraction of the ultimate response, d_{MIN}, to the unloading of the water load between the Bonneville and Provo shorelines was 91 percent, at the time the Provo shoreline formed.

As previously was mentioned, the time interval between the Bonneville and Provo shorelines is not well constrained but is between 500 years (and possibly less) to approximately 3500 years. The current best estimate is 2000 years; this allows for a ~1000 year period for lithospheric adjustment after the fall from the Bonneville level to the Provo level during which time the stable Provo shoreline had not yet formed (refer to the solid line, Figure 2).

Using d_{MIN} = 91 percent, the corresponding relaxation time, τ, can be calculated from equation (7), or

$$\tau = \frac{-t}{ln(\,1 - .91\,)} = \frac{t}{2.41} \quad .$$

Within the time constraints on t, the range in τ is from 208 years (t = 500 years) to 1450 years (t = 3500 years). The best estimate for τ is 830 years (t = 2000 years) (refer to Figure 9).

From these new data it can be seen that the maximum relaxation time of 1450 years is much less than either τ = 4000 years calculated by Crittenden (1963a) or τ = 2500 years calculated by Walcott (1970); the best estimate for τ of 830 years is even lower and suggests a substantial revision of the calculated effective viscosity of the uppermost mantle.

Effective viscosity of uppermost mantle.-- Crittenden (1963ab), using a relaxation time, τ, of 4,000 years, calculated an effective viscosity of the uppermost mantle to be 0.9 x 10^{21} poise (9 x 10^{19} N sec m^{-2}). Similarly, Walcott calculated an effective viscosity of approximately 6 x 10^{20} poise from a relaxation time of 2500 years.

The viscosity η of a half-space as a function of relaxation time τ is

$$\eta = \frac{\rho_m \, g \, \tau}{2 \, f} \qquad (10)$$

where ρ_m is 3.4 g cm^{-3}, g is 980 cm sec^{-2}, and

$$f = \frac{\pi \sqrt{L^2 + M^2}}{L \, M} \qquad (11)$$

with L and M the horizontal dimensions of the load (Heiskanen and Vening Meinesz, 1958). For Lake Bonneville, f = 2.2 x 10^{-7} cm^{-1} (Crittenden, 1963a). Substituting equation (11) into equation (10) yields

$$\eta = (\,2.4 \, x \, 10^{17}\,)\,\tau \qquad (12)$$

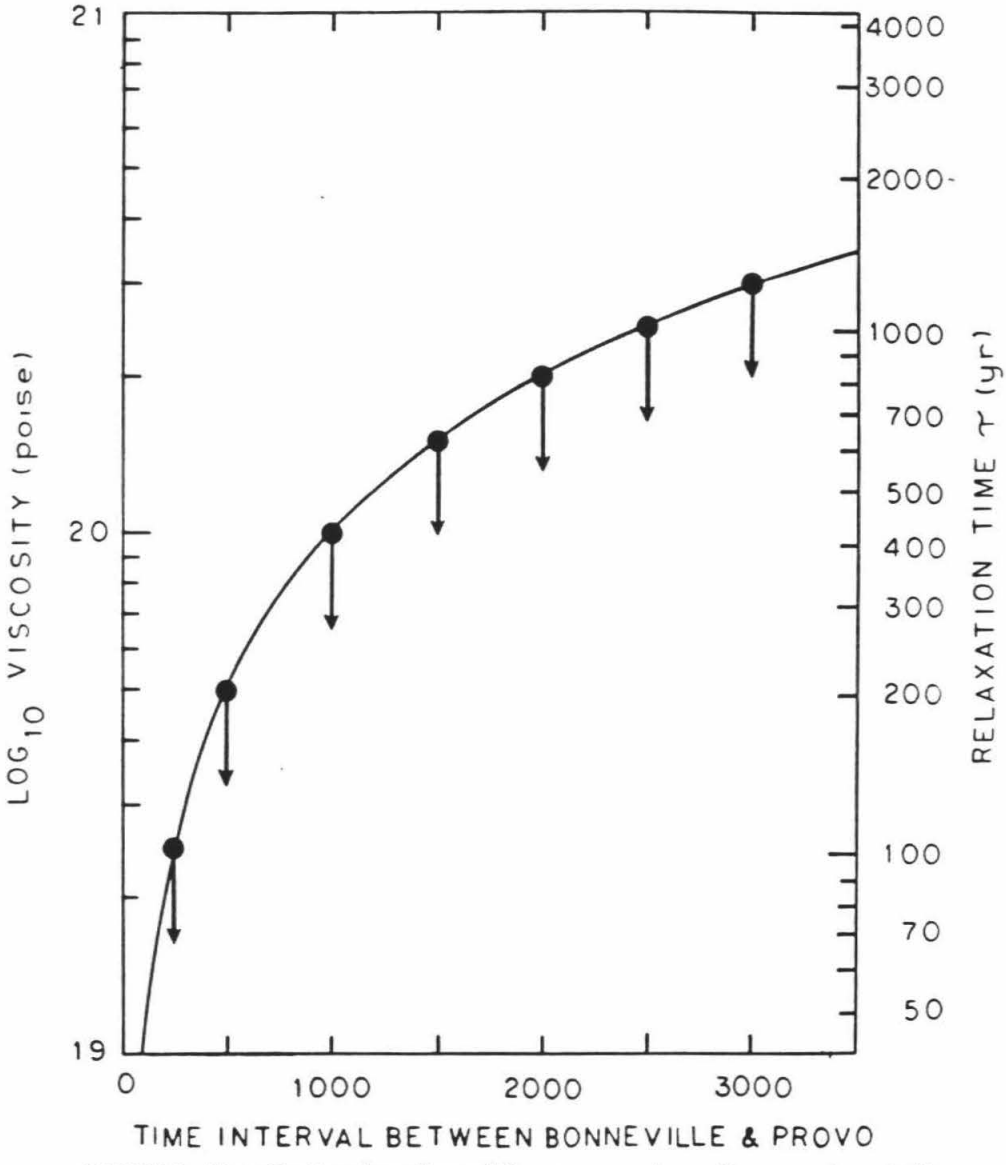

FIGURE 9 - The effective viscosity η of the uppermost mantle, assuming a half-space model, and the relaxation time τ are shown in this figure as functions of the time interval (in years) between the Bonneville and Provo shorelines. The solid circles mark the maximum values of effective viscosity assuming that the Provo shoreline was at least 91% equilibrated, as is discussed in the text.

where η is in poise and τ is in years. Within the constraints of the time interval between the Bonneville and Provo shorelines, the calculated effective viscosity of the uppermost mantle varies from 5 x 10^{19} to 3.5 x 10^{20} poise; the best value being 2 x 10^{20} poise (refer to Figure 9).

If one uses the criterion of Cathles (1975) for the calculation of f in equation (10), equation (11) becomes

$$f = \frac{2\pi}{\lambda} \tag{13}$$

where λ is 5.2 x R_0 , and R_0 for Lake Bonneville is 100 km. Substituting equation (13) for f in equation (10) results in calculated effective viscosities approximately 1.8 times higher than those shown in figure 9.

If it is assumed that most of the isostatic compensation occurs within a channel, such as in the case of an asthenosphere, the viscosity of that channel will be less than that calculated for a half-space. A harmonic load of wavelength λ = 520 km, as for Lake Bonneville, will adjust approximately 5.4 times more slowly if it is applied to a 75 km-thick channel than it would if it were applied to a half-space, and the corresponding channel viscosities would be 5.4 times less (Cathles, 1975).

CONCLUSIONS

From the new data presented in this paper, it can be shown that the Bonneville shoreline was an equilibrium shoreline and that the Provo shoreline may also have been an equilibrium shoreline. Error analysis of the rebound measurements place a lower limit of 91 percent equilibration to the Provo shoreline with an upper limit of 100 percent.

Analysis of the Bonneville shoreline rebound profiles, by numerical modelling of the response to the load (approximated by two simple adjacent cylindrical

loads, each of uniform depth), suggests a flexural rigidity of the lithosphere of about 4×10^{23} N m; this is comparable to the value calculated by Brotchie and Silvester (1969). Comparison of the rebound profiles with the results of more realistic modelling of the vertical and areal distribution of the load, however, suggests that 4×10^{23} N m is too great, and a flexural rigidity of 1×10^{23} N m, or slightly less, is suggested; this in agreement with studies by Walcott (1970).

The calculated effective viscosity of the uppermost mantle, below the Lake Bonneville basin, that was "originally anomalously low [and is] now even more so" (quoted from Walcott, 1970) has, once again, been shown to be even lower. Assuming a half-space model, the range in the upper limit to the effective viscosity of the uppermost mantle is from 5×10^{19} to 3.5×10^{20} poise. This range in viscosity is primarily due to the poor constraints on the time interval between the Bonneville and Provo shorelines; using 2000 years for this interval, the best estimate of the effective viscosity is 2×10^{20} poise. The relatively low effective viscosity may be associated with the high heat flow in the Great Basin and probably is related to the Quaternary volcanism in this region. The magnitude of the flexural rigidity suggests that the lithosphere in this region is approximately 25 km thick and this thickness may also be controlled by the relatively steep geothermal gradient found here.

ACKNOWLEDGMENTS

I would like to thank K. E. Sieh for the basic idea behind this project. I would also like to express an appreciation to B. H. Hager and B. G. Bills for helpful discussions concerning the analysis and interpretation of the flexural rigidity. I am indebted to M. D. Crittenden Jr. for comments and suggestions concerning the shoreline measurements. I also thank L. M. Cathles and S. T. Crough for

critical reviews that greatly improved the interpretation and presentation of the major results presented here. This work was supported, in part, by NASA Grant NSG-7316.

REFERENCES CITED

Bissell, H.J., 1963, Lake Bonneville: Geology of southern Utah Valley, Utah: *U.S. Geol. Survey Prof. Paper 257-B*, p.101-130.

Bright, R.C., 1963, Pleistocene Lakes Thatcher and Bonneville, Southeastern Idaho: PhD Thesis, University of Minnesota, Minneapolis, 292 p.

Broecker, W.S., and Kaufman, Aaron, 1965, Radiocarbon chronology of Lake Lahontan and Lake Bonneville II, Great Basin:. *Geol. Soc. America Bull.*, *76*, p. 537-566.

Broecker, W.S., and Orr, P.C., 1958, Radiocarbon chronology of Lake Lahontan and Lake Bonneville: *Geol. Soc. America Bull.*, *69*, p. 1009-1032.

Brotchie, J.F., and Silvester, R., 1969, On crustal flexure: *Jour. Geophys. Res. 74*, p. 5240-5252.

Brotchie, J.F., 1971, Flexure of a liquid-filled spherical shell in a radial gravity field: *Modern Geology*, *3*, p. 15-23.

Bullen, K.E., 1975, *The Earth's Density:* John Wiley & Sons, New York, 420 p.

Cathles, L.M. III, 1975, *The Viscosity of the Earth's Mantle:* Princeton Univ. Press, Princeton, N.J., 386 p.

Crittenden, M.D., 1963a, New data on the isostatic deformation of Lake Bonneville: *U.S. Geol. Survey Prof. Paper 454-E*, 31 p.

---------, 1963b, Effective Viscosity of the Earth derived from Isostatic Loading of Pleistocene Lake Bonneville: *Jour. Geophys. Res.*, *68*, p. 5517-5530.

Currey, D.R., 1980, Coastal Geomorphology of Great Salt Lake and Vicinity: *Utah Geol. and Mineral Survey Bull.*, *116*, p. 69-82.

Gilbert, G.K., 1890, Lake Bonneville: *U.S. Geol. Survey Monograph, 1*, 438 p.

Heiskanen, W.A, and Vening Meinesz, F.A., 1958, *The Earth and its Gravity Field:* McGraw-Hill Co., New York, 470 p.

Hunt, C.B., Varnes, H.D., and Thomas, H.E., 1953, Lake Bonneville: Geology of northern Utah Valley, Utah; *U.S. Geol. Survey Prof. Paper 257-A*, 99 p.

Malde, H.E., 1968, The catastrophic late Pleistocene Bonneville Flood in the Snake River Plain, Idaho: *U.S. Geol. Survey Prof. Paper 596*, 52 p.

Miller R.D., Van Horn, R., Scott, W.E., and Forester, R.M., 1980, Radiocarbon date supports concept of continuous low levels of Lake Bonneville since 11,000 years B.P.: *Geol. Soc. America, Abstracts with Programs, 12*, p. 297.

Morrison, R.B., 1965, New evidence on Lake Bonneville Stratigraphy and history from southern Promontory Point, Utah: *U.S. Geol. Survey Prof. Paper 525-C*, p. 110-119.

Scott, W.E., 1980, Quaternary Stratigraphy of the Wasatch Front: *U.S. Geol. Survey Open File Report 80-842, Summaries of Technical Reports, Volume X*, p. 121-124.

Walcott, R.I., 1970, Flexural rigidity, thickness, and viscosity of the lithosphere: *Jour. Geophys. Res., 75*, p. 3941-3954.

Williams, J.S., 1962, Lake Bonneville: Geology of southern Cache Valley, Utah: *U.S. Geol. Survey Prof. Paper 257-C*, p. 131-152.

Williams, J.S., and Milligan, J.H., 1968, Bedrock configuration and altitude, Red Rock Pass, Outlet of Lake Bonneville, Southeastern Idaho: Univ. Wyoming contributions to Geology, v. 7, no. 1, p. 67-72.

APPENDIX

Craters used for Photoclinometric Analysis
Lists and Index Maps

FDS Ganymede Mosaic

CRATER	LATITUDE	TERR	DIAM(KM)	MAXDEPTH	CENTER DEPTH	RIM HEIGHT	TYPE
4	-32.0	G1	18.2	-1.75	-1.75	0.30	BOWL
8	-22.0	G1	15.4	-1.70	-1.70	0.43	BOWL
10	-53.0	AC	53.0	-2.87	-2.85	0.64	PIT
11	-54.0	AC	32.0	-1.85	-1.85	0.46	PIT
12	-70.0	G2	27.9	-2.42	-2.42	0.57	PEAK
14	-55.0	G2	28.1	-3.22	-3.22	0.40	PIT
18	-43.0	G1	18.0	-3.03	-3.03	0.65	BOWL
19	-45.0	G1	18.0	-1.41	-0.98	0.20	SMTH
20	-17.0	G1	18.0	-1.15	-0.89	0.20	SMTH
21	-16.0	G1	35.0	-1.93	-1.93	0.55	PIT
23	-25.0	G1	14.0	-0.81	-0.81	0.28	BOWL
24	-26.0	G1	20.0	-1.02	-0.93	0.51	SMTH
27	-36.0	G1	17.0	-0.66	-0.57	0.24	PEAK
28	-33.0	G1	15.0	-1.50	-1.50	0.25	PEAK
30	-36.0	G1	15.0	-0.34	-0.34	0.18	BOWL
32	-38.0	G1	11.0	-1.03	-1.03	0.24	BOWL
33	-37.0	AC	18.0	-1.17	-1.17	0.28	PEAK
36	-37.0	AC	14.0	-0.47	-0.24	0.13	SMTH
38	-42.0	AC	18.0	-0.45	-0.40	0.31	PIT
39	-44.0	AC	15.0	-0.92	-0.92	0.14	BOWL
41	-43.0	AC	21.0	-1.12	-1.12	0.23	BOWL
46	-43.0	G1	23.9	-2.41	-2.32	0.45	SMTH
47	-45.0	AC	17.0	-0.80	-0.80	0.17	SMTH
48	-46.0	AC	17.0	-1.12	-1.07	0.18	SMTH
49	-45.0	AC	29.0	-0.44	0.02	0.17	SMTH
51	-46.0	G1	11.0	-0.54	-0.54	0.14	BOWL
52	-48.0	AC	23.9	-0.72	-0.29	0.17	PEAK
53	-57.0	AC	25.0	-0.30	-0.14	0.14	SMTH
54	-57.0	AC	14.0	-0.28	-0.19	0.09	SMTH
55	-57.0	AC	19.9	-0.64	-0.41	0.30	SMTH
56	-48.0	AC	14.0	-0.32	-0.28	0.18	SMTH
57	-48.0	G1	11.0	-0.58	-0.58	0.19	BOWL
58	-49.0	G1	14.0	-1.64	-1.36	0.44	BOWL
59	-50.0	G1	13.0	-0.79	-0.79	0.16	BOWL
60	-50.0	AC	45.1	-0.43	-0.24	0.26	PIT
62	-49.0	AC	15.0	-0.92	-0.92	0.12	SMTH
63	-56.0	AC	20.0	-0.79	-0.79	0.17	BOWL
65	-54.0	AC	21.9	-0.76	-0.76	0.20	PEAK
66	-54.0	AC	24.9	-0.33	0.04	0.15	SMTH
69	-58.0	G1	20.0	-1.44	-1.44	0.34	BOWL
70	-59.0	G1	17.0	-1.02	-1.02	0.31	BOWL
71	-61.0	G1	25.0	-1.69	-1.51	0.50	SMTH
74	-61.0	AC	10.0	-0.75	-0.75	0.17	BOWL
76	-64.0	G2	20.0	-1.00	-0.84	0.29	SMTH
77	-32.0	G1	13.0	-1.10	-1.10	0.26	BOWL
78	-31.0	G1	14.0	-1.08	-1.08	0.23	BOWL
79	-46.0	AC	14.0	-0.90	-0.90	0.32	BOWL
80	-46.0	AC	18.0	-0.68	-0.53	0.27	SMTH

Ganymede Mosaic

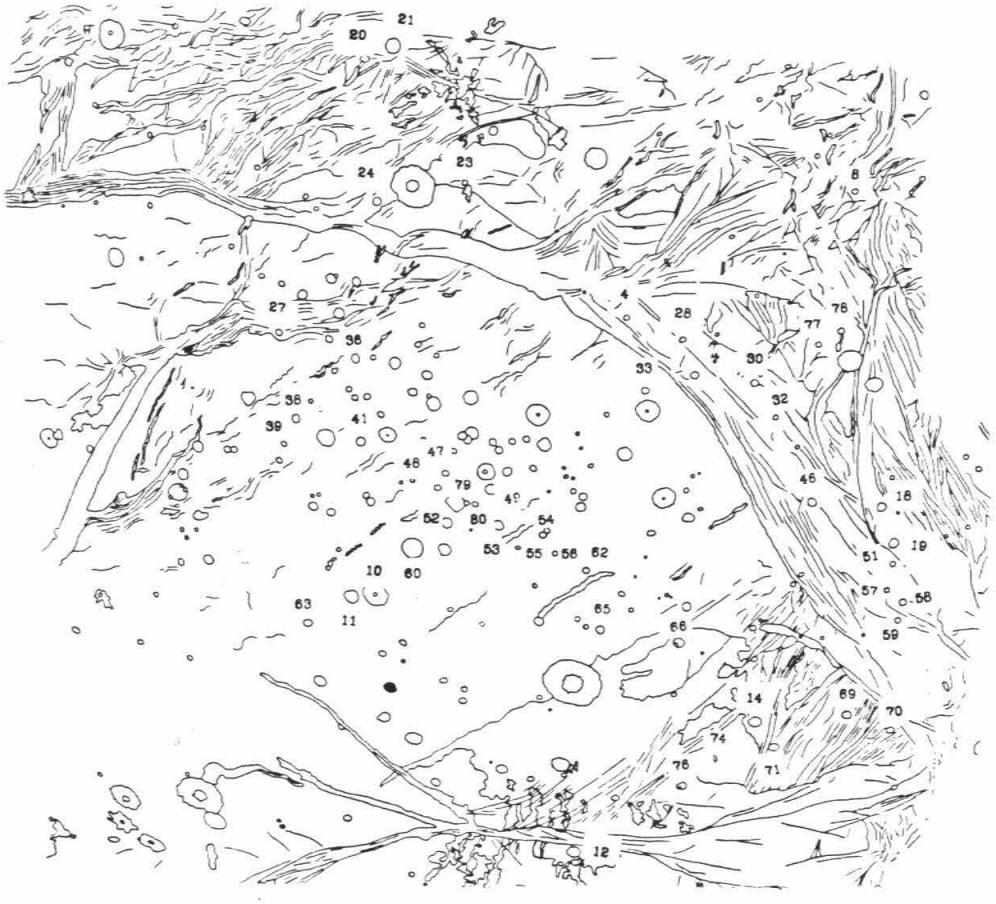

FDS 1E4C456 Ganymede

CRATER	LATITUDE	TERR	DIAM(KM)	MAXDEPTH	CENTER DEPTH	RIM HEIGHT	TYPE
1	-31.4	AC	27.0	-1.50	-1.50	0.28	SMTH
2	-32.7	AC	27.9	-0.75	-0.69	0.24	PIT
3	-30.5	AC	19.0	-1.44	-1.44	0.49	PEAK
4	-33.3	G1	40.0	-0.80	-0.48	0.35	SMTH
5	-34.7	G1	18.0	-1.28	-1.28	0.33	BOWL
6	-34.4	G1	27.0	-1.70	-1.70	0.30	SMTH
7	-36.4	G1	24.1	-0.83	-0.73	0.25	PIT
8	-40.6	AC	19.0	-2.69	-2.69	0.63	BOWL
9	-48.9	AC	15.0	-1.15	-1.15	0.21	BOWL
10	-55.4	AC	25.0	-1.85	-1.85	0.49	PIT
11	-52.7	AC	13.0	-1.14	-1.14	0.22	BOWL
12	-47.6	AC	29.1	-2.89	-2.89	0.42	SMTH
13	-45.8	AC	24.0	-2.61	-2.54	0.53	PEAK
14	-49.3	AC	31.1	-2.14	-1.82	0.46	SMTH
15	-53.4	AC	33.0	-3.15	-3.15	0.65	PIT
16	-57.7	AC	21.0	-0.55	-0.29	0.29	PEAK
17	-59.8	AC	24.9	-1.08	-1.03	0.34	SMTH
18	-61.6	G1	40.0	-0.67	-0.20	0.20	PIT
19	-66.7	G1	16.0	-1.41	-1.41	0.31	BOWL
20	-70.2	G1	40.1	-3.43	-3.43	0.63	PIT
21	-27.9	G1	123.0	-3.22	-1.32	0.85	PIT
22	-28.3	G1	24.0	-2.69	-2.69	0.27	BOWL
23	-29.6	G1	19.0	-0.89	-0.83	0.15	SMTH
24	-33.0	G1	17.0	-0.39	-0.31	0.19	SMTH
25	-34.8	G1	15.0	-1.98	-1.86	0.78	BOWL
26	-39.4	AC	33.1	-2.97	-2.39	0.60	PEAK
27	-43.4	AC	19.0	-1.31	-1.31	0.26	SMTH
28	-44.9	AC	23.1	-2.67	-2.59	0.45	BOWL
29	-53.9	AC	18.0	-3.67	-3.67	0.82	BOWL
30	-57.4	G1	18.1	-0.46	-0.28	0.30	SMTH
31	-58.9	G1	25.9	-2.08	-2.08	0.45	BOWL
32	-63.1	AC	24.9	-0.52	0.06	0.42	SMTH
33	-65.6	AC	52.9	-4.88	-4.88	1.46	PIT
34	-59.8	AC	22.9	-1.49	-1.32	0.36	PEAK
35	-75.0	G1	47.0	-2.62	-2.16	0.70	PIT

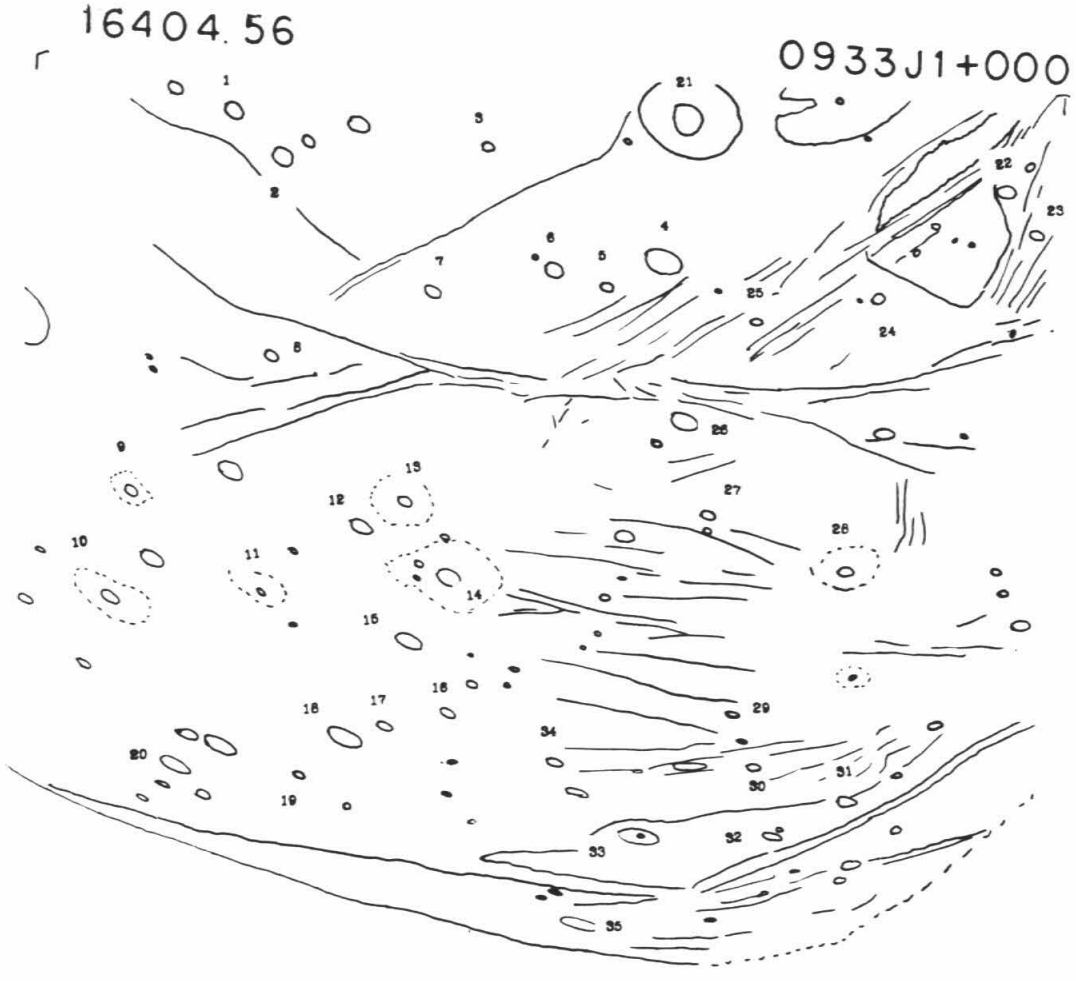
16404.56
0933J1+000

FDS 1640504 Ganymede

CRATER	LATITUDE	TERR	DIAM(KM)	MAXDEPTH	CENTER DEPTH	RIM HEIGHT	TYPE
1	-13.5	AC	30.0	-2.46	-2.46	0.31	BOWL
3	-12.0	AC	47.0	-2.24	-2.24	0.47	PIT
4	-14.4	AC	29.9	-0.18	-0.11	0.14	SMTH
5	-15.2	AC	16.0	-0.20	-0.14	0.11	SMTH
6	-17.1	AC	34.9	-0.27	-0.27	0.18	PIT
7	-16.3	AC	47.0	-1.55	-1.55	0.32	PIT
8	-14.1	AC	23.0	-0.29	-0.05	0.20	PIT
9	-18.3	AC	18.0	-0.65	-0.59	0.25	SMTH
10	-21.9	AC	24.0	-0.54	-0.01	0.15	SMTH
11	-22.1	AC	14.0	-0.26	-0.22	0.09	SMTH
12	-24.7	AC	20.0	-0.33	-0.14	0.11	SMTH
13	-21.8	AC	26.0	-0.30	0.21	0.17	SMTH

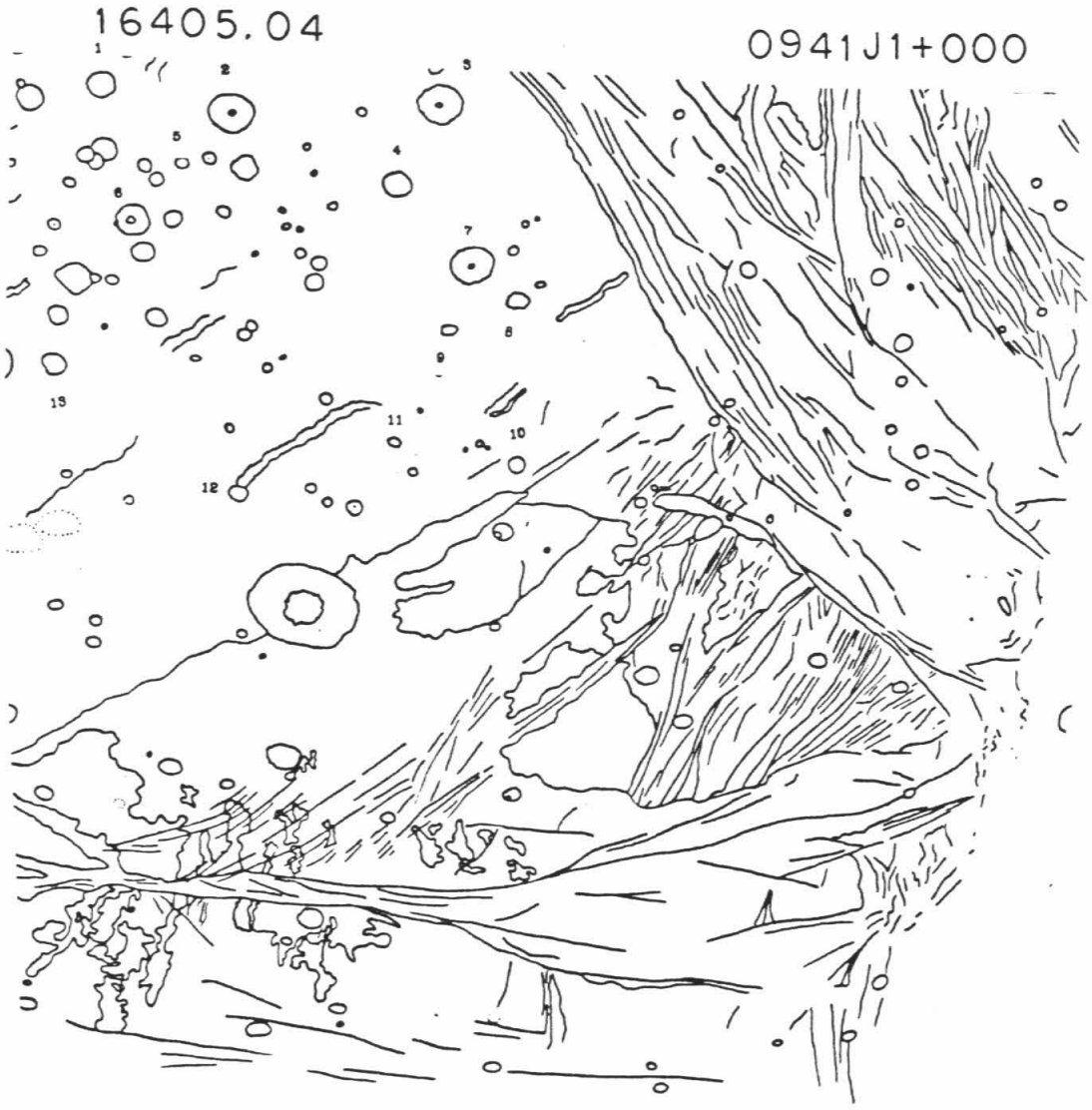
16405.04
0941J1+000

FDS 1640510 Ganymede

CRATER	LATITUDE	TERR	DIAM(KM)	MAXDEPTH	CENTER DEPTH	RIM HEIGHT	TYPE
1	-26.0	G1	66.5	-4.18	-4.07	1.04	PIT
2	-32.0	AC	22.1	-0.41	-0.06	0.14	PIT
3	-32.0	AC	17.1	-0.89	-0.79	0.14	SMTH
4	-34.0	AC	27.0	-0.21	0.04	0.18	SMTH
5	-34.0	AC	23.9	-1.55	-1.55	0.39	PIT
6	-36.0	AC	21.9	-0.33	-0.01	0.07	PIT
7	-38.0	AC	22.0	-1.05	-1.05	0.19	SMTH
8	-40.0	AC	30.9	-0.47	0.13	0.17	SMTH
9	-39.0	AC	58.1	-0.50	0.14	0.44	PIT
10	-41.5	AC	39.0	-0.53	0.04	0.25	PIT
11	-43.0	AC	38.0	-0.96	-0.62	0.32	PIT
12	-42.0	AC	36.0	-1.22	-0.96	0.43	PIT

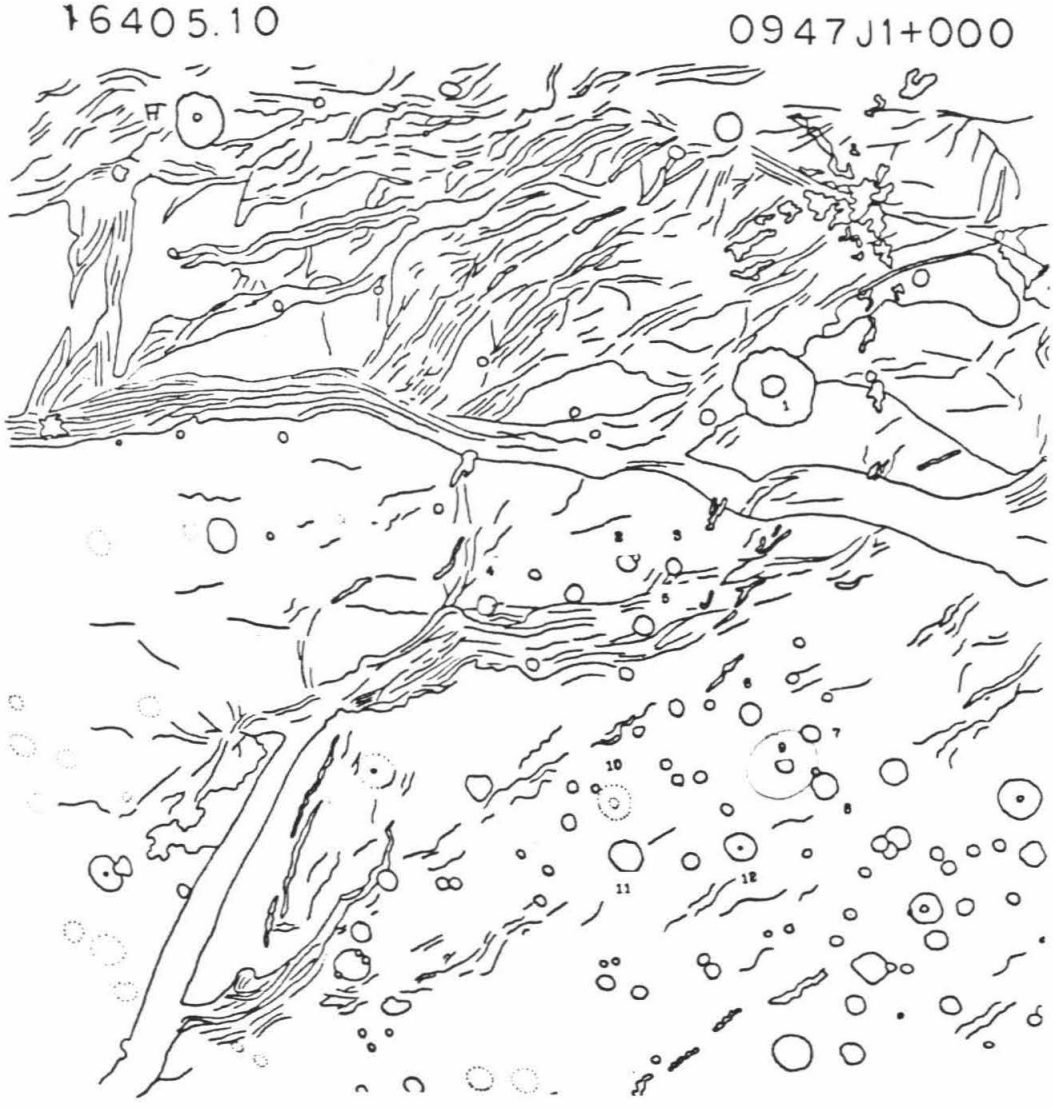
16405.10
0947J1+000

FDS 1640512 Ganymede

CRATER	LATITUDE	TERR	DIAM(KM)	MAXDEPTH	CENTER DEPTH	RIM HEIGHT	TYPE
1	-0.7	G1	44.9	-1.93	-1.88	0.31	PIT
2	-10.5	AC	64.9	-0.30	0.05	0.22	SMTH
3	-9.9	G1	18.0	-1.09	-1.09	0.21	PEAK
4	-7.9	G1	48.0	-3.66	-3.66	0.54	PIT
5	-8.9	G1	35.1	-2.62	-2.08	0.52	PEAK

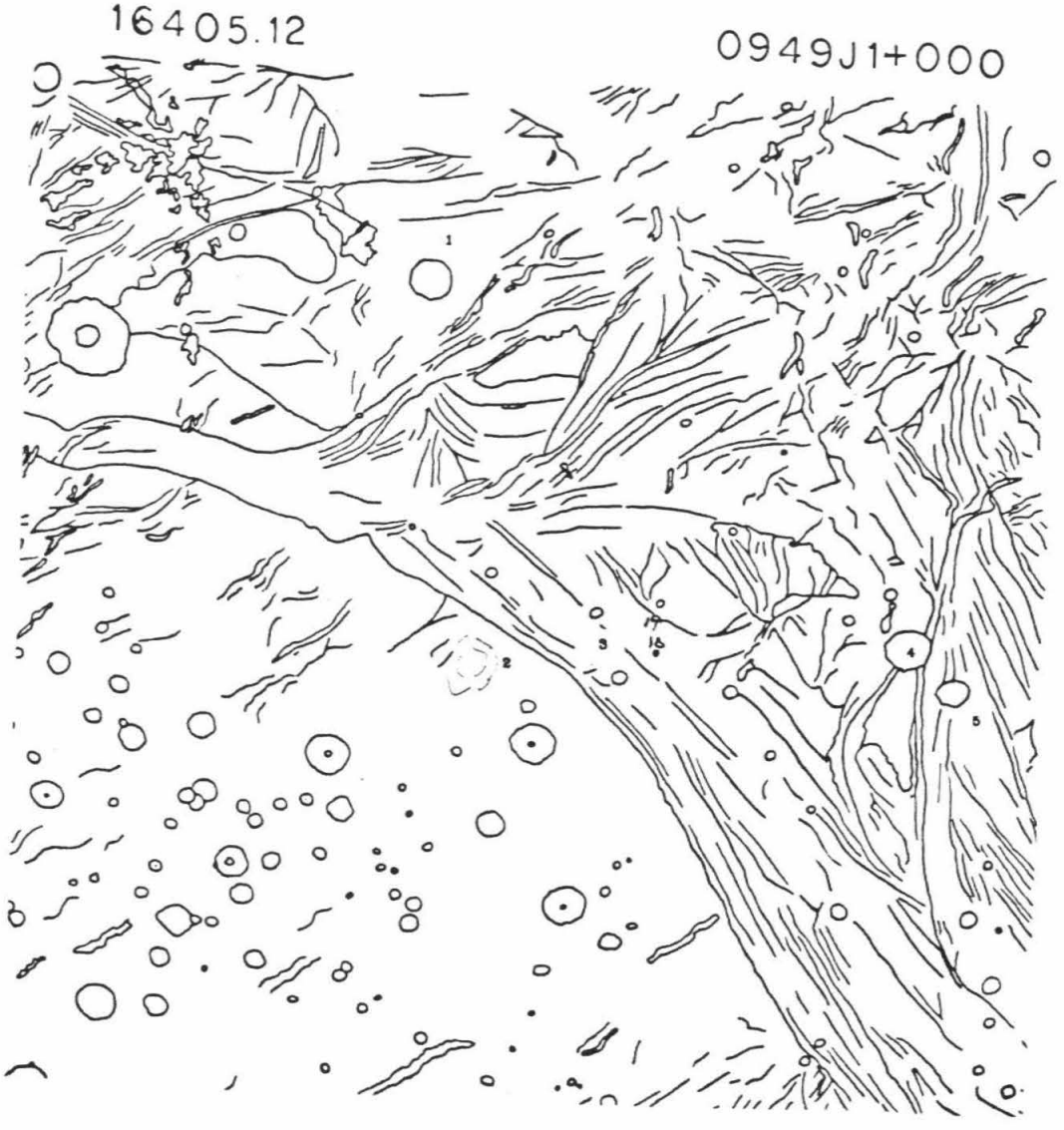
16405.12
0949J1+000

FDS 1640518 Ganymede

CRATER	LATITUDE	TERR	DIAM(KM)	MAXDEPTH	CENTER DEPTH	RIM HEIGHT	TYPE
1	14.3	G1	35.1	-1.62	-1.37	0.37	PIT
2	5.3	AC	43.0	-2.05	-2.07	0.33	PIT
3	8.2	AC	22.5	-0.58	-0.35	0.18	PIT
4	6.8	AC	22.0	-0.35	-0.19	0.19	SMTH
5	6.0	AC	35.0	-0.97	-0.69	0.28	SMTH
6	6.2	C1	9.8	-0.52	-0.40	0.13	PEAK
7	10.5	G1	20.1	-0.45	0.0	0.16	SMTH
8	12.0	C1	34.0	-2.16	-2.16	0.30	FCWL
9	1.3	C1	9.9	-0.60	-0.60	0.11	BOWL
10	-0.6	G1	8.0	-0.71	-0.71	0.13	FOWL
11	-2.3	C1	57.0	-1.24	-0.62	0.54	PIT
12	9.8	G1	33.9	-0.79	-0.59	0.38	SMTH
13	10.9	G1	23.0	-1.95	-1.95	0.39	FCWL
14	12.4	C1	24.0	-0.93	-0.81	0.30	SMTH
15	3.6	G1	37.0	-2.22	-1.97	0.28	SMTH
16	0.2	G1	31.0	-2.21	-2.21	0.41	FCWL

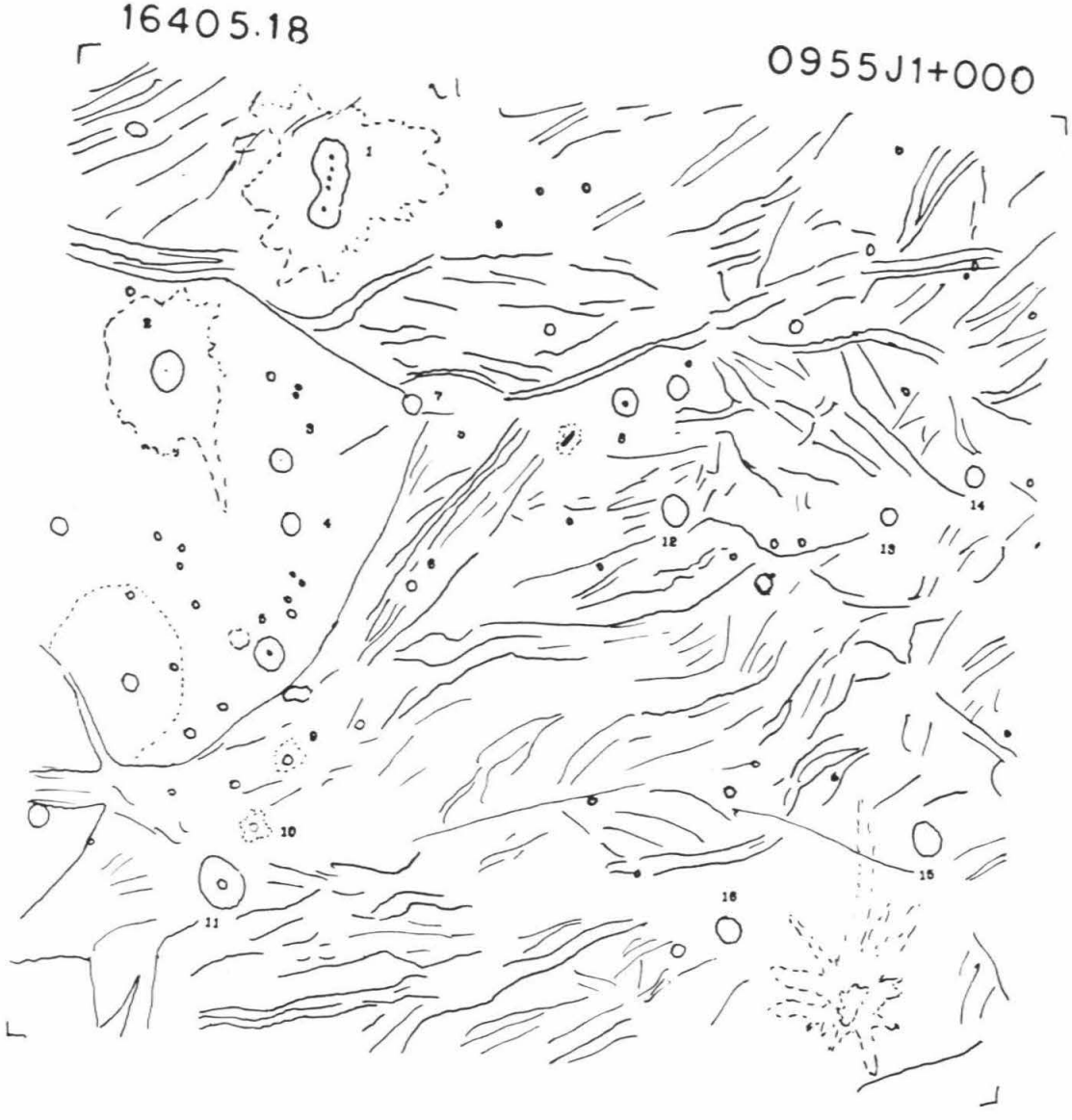
16405.18
0955J1+000
1
2
3
4
5
6
7
8
9
10
11
12
13
14
15
16

FDS 1640522 Ganymede

CRATER	LATITUDE	TERR	DIAM(KM)	MAXDEPTH	CENTER DEPTH	RIM HEIGHT	TYPE
1	21.5	AC	22.1	-0.14	-0.14	0.07	SMTH
2	20.5	AC	17.9	-0.15	-0.15	0.06	SMTH
3	19.9	AC	25.9	-0.50	-0.50	0.15	SMTH
4	17.4	AC	38.0	-0.52	-0.40	0.20	SMTH
5	15.7	AC	26.0	-0.51	-0.51	0.16	SMTH
6	14.2	G1	32.9	-0.60	-0.52	0.18	SMTH
7	6.4	AC	32.0	-0.24	-0.24	0.15	SMTH
8	5.7	AC	16.0	-0.52	-0.52	0.12	PEAK
9	22.5	AC	28.0	-2.42	-2.27	0.63	PEAK
10	20.4	AC	23.9	-0.25	-0.04	0.23	SMTH
11	19.2	AC	53.0	-0.21	0.15	0.18	PIT
12	19.0	AC	21.0	-0.07	0.0	0.03	SMTH
13	14.5	AC	17.0	-0.78	-0.78	0.23	BOWL
14	13.4	AC	21.0	-0.13	-0.01	0.07	SMTH
15	10.9	AC	48.0	-0.66	-0.31	0.29	PIT

16405.22

0959J1+000

FDS 1E4C528 Ganymede

CRATER	LATITUDE	TERR	DIAM(KM)	MAXDEPTH	CENTER DEPTH	RIM HEIGHT	TYPE
1	29.1	G1	31.9	-1.63	-1.42	0.19	PIT
2	24.0	AC	41.1	-0.49	-0.02	0.19	PIT
3	23.4	AC	11.9	-0.38	-0.38	0.12	PIT
4	22.8	G1	35.9	-1.42	-1.42	0.33	PIT
5	21.6	G1	10.1	-0.38	-0.38	0.18	BOWL
6	31.1	G1	54.0	-0.86	-0.29	0.39	PIT
7	28.3	G1	17.0	-1.36	-1.18	0.20	SMTH
8	29.8	AC	10.9	-0.36	-0.08	0.12	SMTH
9	27.9	G1	14.0	-0.97	-0.97	0.22	BOWL
10	21.4	G1	25.1	-1.44	-1.44	0.33	BOWL

16405.28 0965J1+000

FCS 1e40530 Ganymede

CRATER	LATITUDE	TERR	DIAM(KM)	MAXDEPTH	CENTER DEPTH	RIM HEIGHT	TYPE
1	40.0	G1	33.1	-0.62	-0.30	0.20	SMTH
2	36.0	G1	38.0	-0.83	-0.74	0.29	PIT
3	34.2	G1	32.1	-0.91	-0.63	0.28	PIT
4	34.0	G1	19.9	-1.04	-1.04	0.19	PEAK
5	30.2	G1	209.9	-0.20	2.50	0.20	PAL
6	28.3	G1	14.0	-0.73	-0.73	0.12	BOWL
7	28.5	G1	16.9	-0.89	-0.89	0.17	BOWL
8	29.6	G1	39.9	-1.18	-1.18	0.38	BOWL
9	26.5	G1	22.0	-0.78	-0.78	0.32	SMTH
10	25.2	G1	17.9	-0.74	-0.74	0.19	PEAK
11	24.9	G1	15.0	-0.70	-0.70	0.16	PEAK
12	24.1	G1	40.0	-1.13	-0.69	0.44	PIT
13	22.9	G1	19.0	-0.78	-0.78	0.15	BOWL

16405.30 0967J1+000

FDS 1640532 Ganymede

CRATER	LATITUDE	TERR	DIAM(KM)	MAXDEPTH	CENTER DEPTH	RIM HEIGHT	TYPE
1	36.1	G1	30.0	-1.01	-0.52	0.38	SMTH
2	36.8	G1	14.0	-0.58	-0.58	0.14	BOWL
3	33.1	C1	12.1	-0.53	-0.53	0.10	BOWL
4	25.1	G1	16.0	-0.15	-0.10	0.06	SMTH
5	29.1	AC	18.0	-0.17	0.09	0.14	SMTH
6	30.0	C1	21.9	-0.87	-0.87	0.24	BOWL


16405.32
0969J1+000

FDS 1640542 Ganymede

CRATER	LATITUDE	TERR	DIAM(KM)	MAXDEPTH	CENTER DEPTH	RIM HEIGHT	TYPE
1	54.9	G1	49.1	-0.50	0.18	0.21	PEAK
2	53.7	G1	19.0	-0.87	-0.87	0.29	BOWL
3	53.5	G1	32.0	-0.55	-0.05	0.38	PEAK
4	48.8	G1	16.0	-0.30	-0.22	0.07	SMTH
5	45.2	G1	16.1	-0.60	-0.60	0.09	PEAK
6	43.3	G1	32.9	-0.22	0.06	0.18	SMTH
7	36.4	G1	29.9	-1.14	-1.14	0.37	PIT
8	34.8	G1	18.0	-1.15	-1.15	0.24	PEAK
9	33.5	G1	12.0	-0.70	-0.70	0.18	BOWL

16405.42

0979J1+000

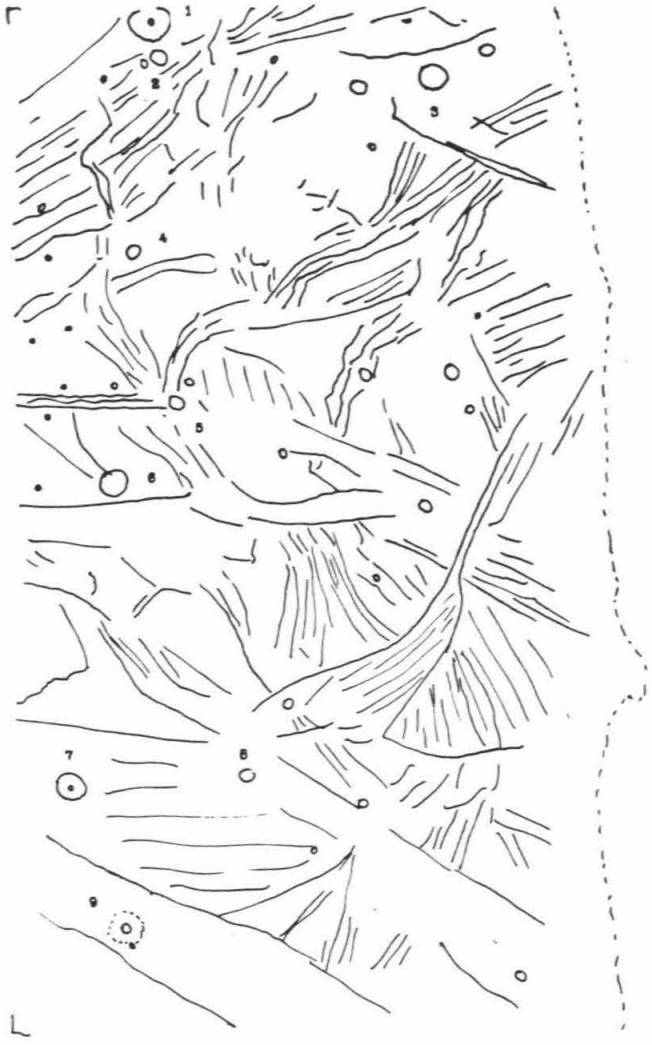

FDS 164C54E Ganymede

CRATER	LATITUDE	TERR	DIAM(KM)	MAXDEPTH	CENTER DEPTH	RIM HEIGHT	TYPE
1	68.3	G1	33.0	-2.38	-2.22	0.62	SMTH
2	68.0	G1	25.0	-1.41	-1.34	0.40	SMTH
3	64.5	G1	36.0	-1.32	-1.15	0.33	SMTH
4	61.1	G1	24.5	-1.24	-1.07	0.46	SMTH
5	63.2	G1	34.5	-1.28	-0.53	0.43	PEAK
6	66.5	G1	25.0	-1.69	-1.69	0.46	PEAK
7	63.5	G1	26.0	-2.09	-2.09	0.45	BOWL
8	60.3	G1	61.0	-2.14	-2.10	0.75	PIT
9	56.7	G1	22.0	-1.35	-1.20	0.33	SMTH
10	52.3	G1	23.1	-1.05	-1.05	0.20	BOWL
11	52.4	G1	22.0	-1.30	-1.30	0.26	BOWL
12	51.6	G1	22.5	-1.64	-1.64	0.50	SMTH
13	50.0	G1	32.1	-1.40	-1.26	0.22	SMTH
14	68.7	G1	50.5	-1.87	-0.98	0.70	SMTH
15	70.7	G1	78.0	-2.29	-2.25	1.16	PIT
16	63.8	G1	56.1	-1.43	-0.23	0.67	PIT
17	59.4	G1	22.0	-1.58	-1.58	0.37	PEAK
18	53.1	G1	25.0	-1.67	-1.67	0.21	BOWL
19	49.7	G1	30.0	-1.23	-0.84	0.43	PEAK
20	50.7	G1	16.0	-0.52	-0.52	0.19	BOWL
21	49.1	G1	19.0	-1.48	-1.43	0.33	SMTH
22	48.0	G1	17.0	-0.85	-0.85	0.26	BOWL

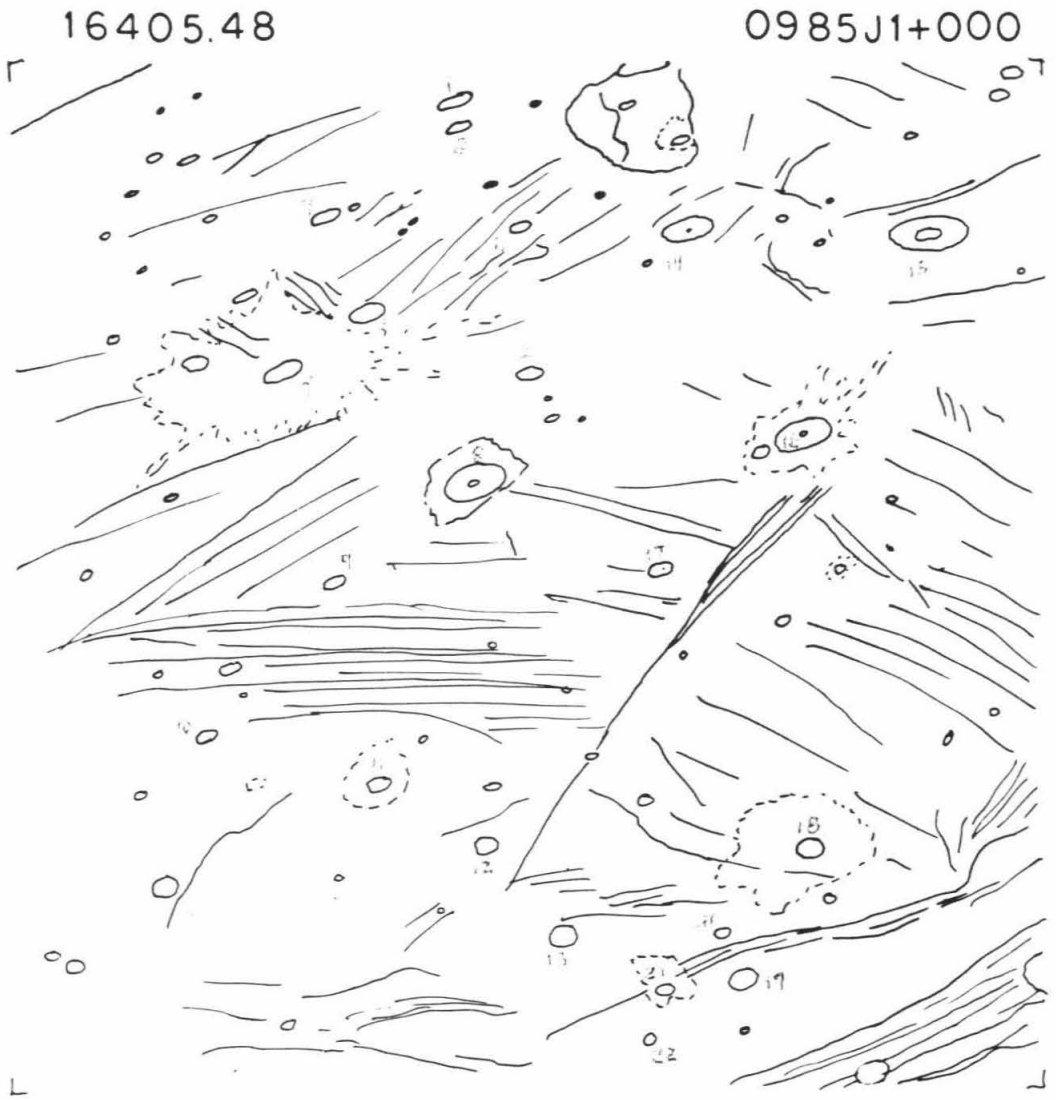
16405.48
0985J1+000

FDS 1640550 Ganymede

CRATER	LATITUDE	TERR	DIAM(KM)	MAXDEPTH	CENTER DEPTH	RIM HEIGHT	TYPE
1	72.9	G1	44.0	-1.67	-1.53	0.68	SMTH
2	66.6	G1	39.1	-1.55	-1.95	0.57	BOWL
3	65.4	G1	19.9	-1.08	-1.08	0.17	BOWL
4	61.1	G1	22.0	-1.54	-1.54	0.29	BOWL


16405.50
0987J1+000

FDS 2003659 Ganymede

CRATER	LATITUDE	TERR	DIAM(KM)	MAXDEPTH	CENTER DEPTH	RIM HEIGHT	TYPE
1	44.4	AC	37.0	-0.83	0.56	0.46	SMTH
2	40.1	AC	21.0	-0.98	-0.28	0.42	PEAK
3	39.0	AC	34.0	-2.61	-2.04	0.69	PIT
4	31.0	AC	48.0	-2.33	-0.77	0.49	PIT
6	32.9	AC	17.9	-0.97	-0.75	0.20	SMTH
8	38.9	AC	17.9	-1.00	-0.66	0.19	SMTH
9	40.5	AC	46.1	-1.05	-0.43	0.48	PIT
10	40.4	AC	44.9	-3.87	-2.72	0.63	SMTH
12	33.8	AC	37.1	-0.89	0.0	0.36	PIT
13	33.5	AC	29.0	-0.53	-0.02	0.20	SMTH
14	44.4	AC	31.9	-1.95	-1.63	0.64	SMTH
15	30.9	AC	29.0	-0.56	-0.17	0.16	PIT
16	30.9	AC	17.0	-0.90	-0.90	0.23	SMTH
17	30.7	AC	22.0	-0.53	0.0	0.22	SMTH
18	30.9	AC	35.0	-1.98	-1.89	0.49	SMTH
20	26.8	AC	35.1	-0.72	-0.71	0.14	PIT
21	27.0	AC	26.0	-0.83	0.17	0.32	PIT
22	24.5	AC	38.0	-1.32	-0.84	0.56	PIT
23	23.3	AC	32.0	-1.98	-1.73	0.58	PIT
24	22.9	AC	28.1	-1.07	0.17	0.45	SMTH
25	21.8	AC	20.0	-0.70	-0.50	0.41	SMTH
26	24.7	AC	35.1	-3.01	-2.74	0.52	PIT
27	22.1	AC	26.0	-1.66	-1.66	0.26	PIT
28	20.8	AC	22.1	-0.18	-0.16	0.16	SMTH
29	22.8	AC	26.1	-0.50	-0.25	0.25	SMTH
30	23.9	AC	16.0	-1.34	-1.34	0.30	BOWL
31	23.6	AC	44.1	-1.60	-1.55	0.29	PIT
32	20.8	AC	19.9	-0.22	0.18	0.13	SMTH
33	18.6	AC	37.9	-1.09	-1.05	0.17	PIT
34	18.7	AC	17.9	-0.42	-0.10	0.13	SMTH
35	41.2	AC	25.0	-0.87	-0.24	0.41	SMTH
36	39.7	AC	43.0	-0.87	-0.65	0.43	PIT
37	40.2	AC	31.9	-0.66	-0.46	0.16	PIT
38	43.7	AC	28.0	-0.82	-0.82	0.40	PIT
39	42.4	AC	20.0	-0.40	-0.23	0.24	SMTH
40	43.5	AC	30.0	-0.90	-0.24	0.22	SMTH
41	40.7	AC	21.5	-0.51	-0.51	0.27	SMTH
42	40.8	AC	46.0	-1.81	-1.77	0.81	PIT
43	37.2	AC	33.0	-1.05	-0.90	0.30	SMTH
44	35.9	AC	58.9	-1.76	-1.64	0.51	PIT
45	33.6	AC	21.3	-0.49	0.01	0.39	PIT
46	33.5	AC	27.0	-1.09	-0.36	0.65	SMTH
47	37.4	AC	29.0	-2.32	-2.32	0.72	PIT
48	36.7	AC	24.0	-0.85	-0.31	0.28	SMTH
49	32.4	AC	47.1	-1.86	-1.53	0.88	PIT
50	35.2	AC	16.0	-0.79	-0.79	0.21	BOWL
51	34.7	AC	28.1	-0.76	-0.19	0.40	SMTH
52	30.4	AC	23.9	-0.28	-0.26	0.22	SMTH
53	29.9	AC	19.2	-0.50	-0.40	0.17	SMTH
54	28.3	AC	33.0	-1.44	-0.76	0.42	PIT
55	27.4	AC	43.0	-1.50	-1.23	0.58	PIT
56	27.0	AC	48.1	-0.95	-0.95	0.32	PIT
57	26.6	AC	31.1	-1.34	-0.94	0.30	SMTH
58	25.0	AC	47.1	-1.67	-1.29	0.61	PIT
59	24.7	AC	24.0	-0.36	-0.03	0.23	SMTH
60	24.7	AC	17.0	-0.20	0.16	0.15	SMTH
61	23.8	AC	19.9	-0.58	-0.10	0.25	SMTH
62	20.3	AC	25.0	-1.21	-1.21	0.53	PIT
63	19.8	AC	26.0	-1.17	-0.87	0.33	SMTH
63	19.8	AC	9.4	-0.93	-0.93	0.27	BOWL
64	23.8	AC	19.4	-0.68	0.12	0.47	SMTH
65	23.2	AC	18.4	-1.39	-1.39	0.24	BOWL
66	23.0	AC	14.0	-0.76	-0.64	0.18	SMTH
67	23.9	AC	6.0	-0.53	-0.53	0.17	SMTH
68	18.4	AC	22.0	-1.98	-1.33	0.62	PIT
69	33.6	AC	7.3	-0.51	-0.51	0.12	BOWL

20636.59 0452J2-001

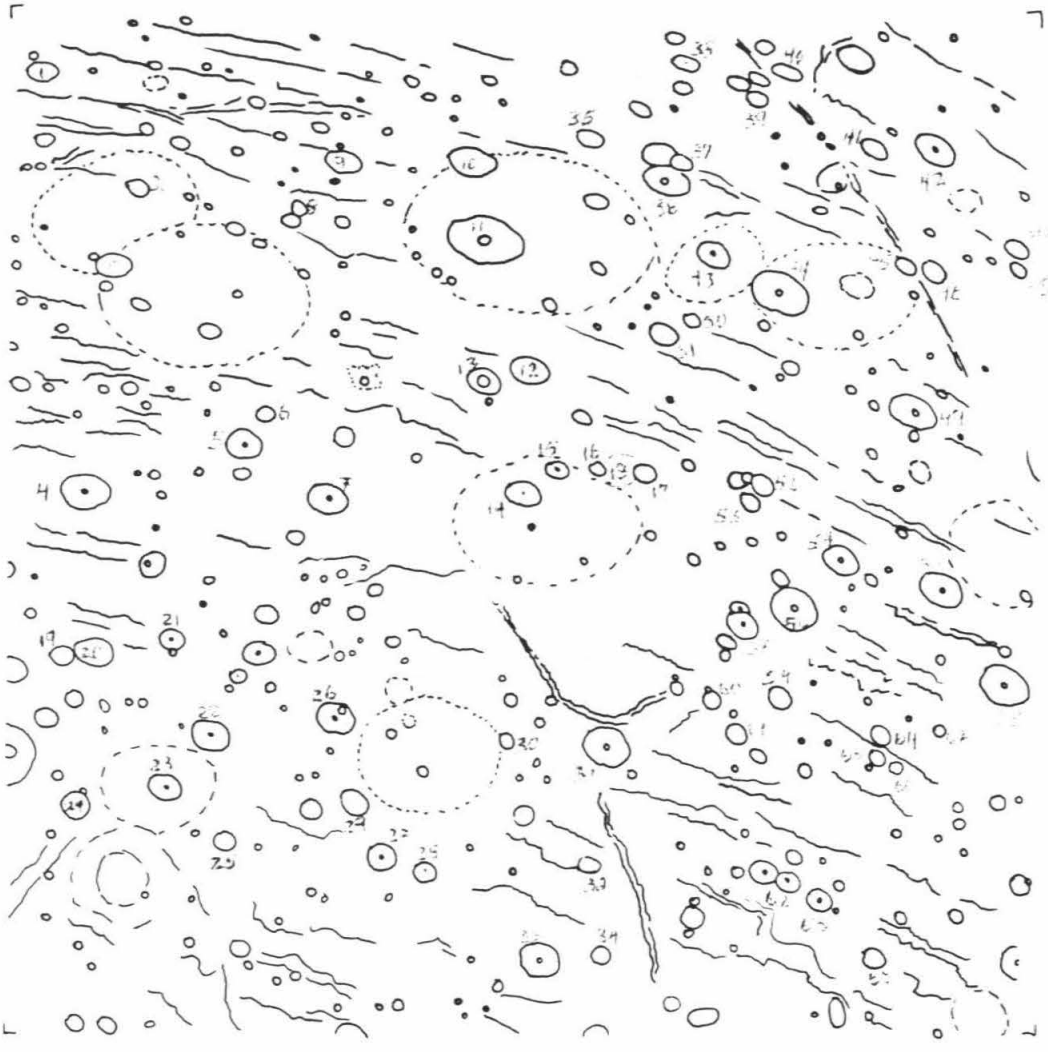

FDS 2063702 Ganymede

CRATER	LATITUDE	TERR	DIAM(KM)	MAXDEPTH	CENTER DEPTH	RIM HEIGHT	TYPE
1	37.8	AC	9.6	-0.73	-0.73	0.21	BOWL
2	35.6	AC	19.0	-1.92	-1.92	0.84	BOWL
3	34.7	AC	22.9	-0.84	0.08	0.41	PEAK
4	37.9	AC	58.1	-1.38	-1.31	0.65	PIT
5	36.0	AC	27.0	-1.03	-1.03	0.77	PIT
6	36.4	AC	39.0	-1.90	-1.57	0.49	PIT
7	35.8	AC	31.0	-0.78	-0.38	0.26	PIT
8	34.4	AC	50.0	-1.29	-1.17	0.78	PIT
9	35.3	AC	13.0	-0.85	-0.85	0.18	BOWL
10	35.3	AC	16.1	-0.39	0.09	0.20	PEAK
11	37.4	AC	51.9	-0.65	-0.59	0.52	PIT
12	33.0	AC	59.9	-0.32	-0.28	0.20	PIT
13	32.0	AC	27.1	-0.23	-0.05	0.18	SMTH
14	32.2	AC	13.0	-0.61	-0.61	0.24	BOWL
15	31.6	AC	12.0	-0.46	-0.36	0.19	SMTH
16	30.6	AC	25.1	-0.85	0.21	0.33	SMTH
17	32.1	AC	30.9	-0.36	-0.03	0.24	PIT
18	31.7	AC	25.1	-1.60	-1.60	0.21	PIT
19	31.9	AC	26.0	-1.08	-0.66	0.17	PIT
20	31.1	AC	27.0	-0.52	0.09	0.28	PIT
21	29.4	AC	31.1	-2.23	-2.23	0.46	PIT
22	28.4	AC	20.0	-0.43	-0.02	0.20	SMTH
23	28.4	AC	43.1	-0.90	0.49	0.49	PIT
24	28.9	AC	42.0	-1.33	0.06	0.81	SMTH
25	28.3	AC	28.0	-0.45	-0.45	0.28	PIT
26	27.3	AC	31.0	-0.35	-0.19	0.31	SMTH
27	27.6	AC	19.0	-0.10	0.0	0.08	SMTH
28	25.4	AC	16.0	-0.62	-0.60	0.26	SMTH
29	25.6	AC	38.0	-0.99	-0.99	0.48	PIT
30	25.0	AC	23.1	-0.65	-0.62	0.22	PIT
31	22.2	AC	17.0	-0.71	-0.71	0.13	SMTH
32	22.7	AC	20.0	-0.59	-0.59	0.20	SMTH
33	24.0	AC	21.0	-0.32	-0.03	0.30	SMTH
34	25.6	AC	48.0	-2.22	-2.08	0.47	PIT
35	26.6	AC	24.0	-1.59	-1.42	0.42	PIT
36	24.5	AC	21.0	-1.24	-1.18	0.29	PIT
37	24.5	AC	17.1	-1.14	-1.14	0.21	PIT
38	22.8	AC	21.0	-1.43	-1.43	0.29	SMTH
39	21.3	AC	20.1	-0.83	-0.83	0.16	PIT
40	21.9	AC	38.0	-1.09	-0.08	0.56	PIT
41	20.5	AC	65.0	-1.63	-1.60	0.51	PIT
42	17.1	AC	28.0	-1.08	-0.56	0.33	PEAK
43	16.0	AC	16.1	-0.25	-0.18	0.08	SMTH
44	16.9	AC	26.1	-0.45	-0.43	0.20	PIT
45	15.2	AC	20.9	-0.55	-0.23	0.22	SMTH
46	19.0	AC	9.9	-0.50	-0.50	0.14	BOWL
47	18.3	AC	26.1	-0.58	-0.29	0.25	PIT
48	19.8	AC	15.0	-0.45	-0.23	0.15	PEAK
49	18.2	AC	32.0	-1.00	-0.73	0.48	SMTH
50	17.1	AC	30.0	-0.83	-0.28	0.33	PIT
51	16.1	AC	26.1	-0.64	-0.64	0.27	SMTH
52	15.6	AC	27.0	-0.51	-0.21	0.16	PIT
53	15.8	AC	14.0	-1.27	-1.27	0.34	BOWL
54	15.6	AC	7.1	-0.67	-0.67	0.15	BOWL
55	14.4	AC	19.1	-0.57	-0.27	0.20	SMTH
56	15.0	AC	15.1	-0.61	-0.30	0.21	PEAK
57	13.3	AC	38.0	-1.39	-1.39	0.53	PIT
58	13.6	AC	34.0	-2.46	-2.46	0.55	PIT
59	14.3	AC	18.1	-0.16	-0.09	0.08	SMTH
60	14.0	AC	26.0	-0.56	-0.35	0.15	PIT
61	17.8	AC	44.0	-2.43	-2.20	0.82	PIT
62	15.8	AC	22.1	-2.83	-2.22	0.76	PEAK
63	15.0	AC	17.1	-1.04	-0.83	0.48	SMTH
64	15.3	AC	23.0	-1.20	-1.20	0.33	PIT
65	12.9	AC	32.0	-0.99	0.38	0.51	SMTH
66	14.1	AC	47.1	-1.65	-0.77	0.88	PIT
67	12.8	AC	13.0	-0.77	-0.55	0.27	SMTH
68	14.0	AC	34.0	-0.68	0.39	0.36	SMTH

20637.02 455J2-001

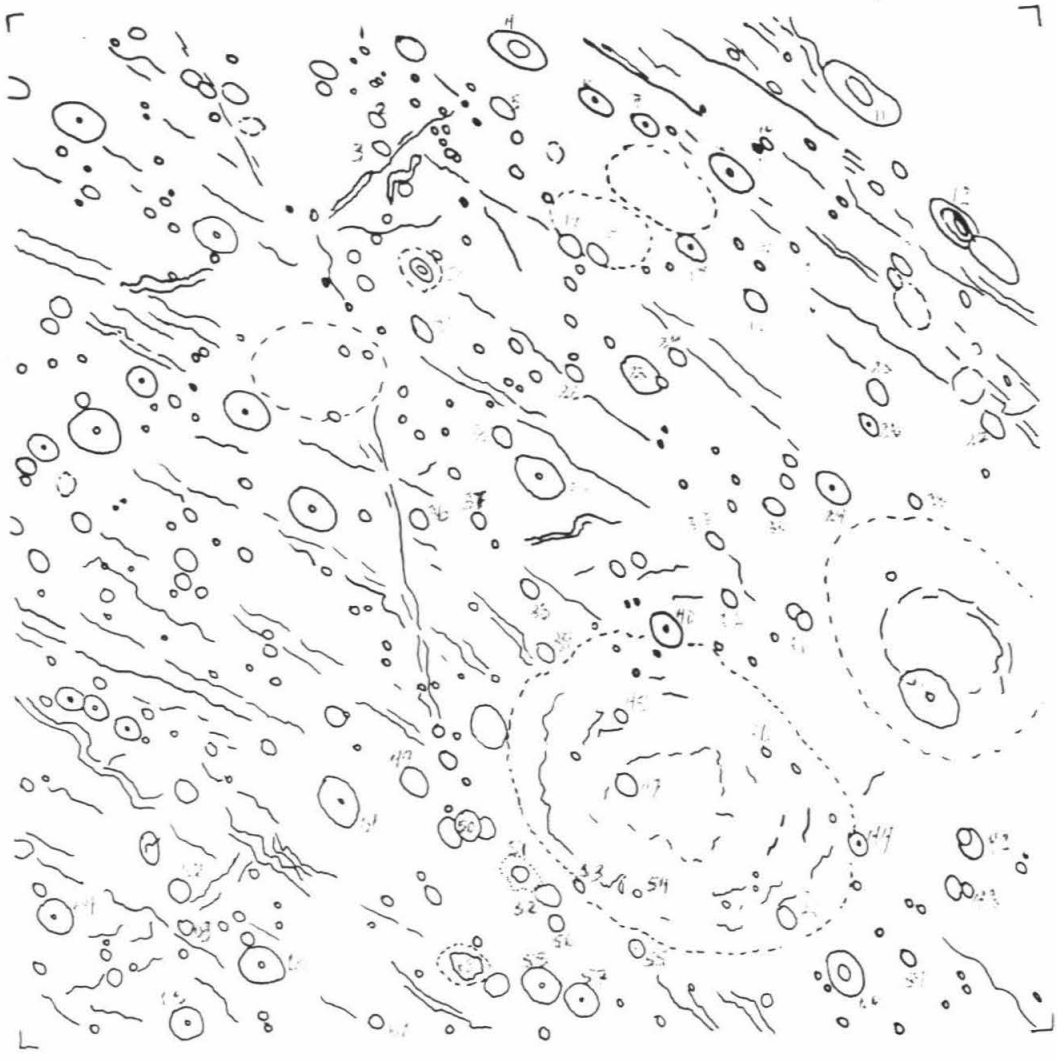

FDS 2063714 Ganymede

CRATER	LATITUDE	TERR	DIAM(KM)	MAXDEPTH	CENTER DEPTH	RIM HEIGHT	TYPE
1	13.0	AC	26.0	-0.81	0.24	0.67	PIT
2	13.0	AC	33.9	-0.74	-0.59	0.44	PIT
4	12.0	AC	38.0	-2.11	-2.11	0.52	BOWL
5	12.7	AC	5.4	-0.30	-0.30	0.07	BOWL
6	12.4	AC	6.5	-0.97	-0.97	0.26	BOWL
7	11.8	AC	6.0	-0.54	-0.54	0.20	BOWL
8	12.6	AC	12.1	-0.69	-0.69	0.13	SMTH
9	12.9	AC	10.9	-0.42	-0.42	0.14	SMTH
10	13.5	AC	43.0	-1.08	0.03	0.74	PIT
11	12.4	AC	12.0	-0.92	-0.92	0.23	BOWL
12	12.3	AC	14.0	-1.24	-0.88	0.39	PEAK
13	12.9	AC	16.5	-0.31	-0.18	0.14	SMTH
14	13.3	AC	5.0	-0.16	-0.16	0.05	BOWL
15	13.4	AC	11.0	-0.51	-0.51	0.20	BOWL
16	10.9	AC	9.5	-0.99	-0.99	0.28	BOWL
16	10.9	AC	14.5	-0.95	-0.83	0.25	SMTH
17	8.9	AC	23.1	-0.43	-0.17	0.18	PIT
18	8.7	AC	7.5	-0.44	-0.44	0.19	BOWL
19	9.4	AC	23.0	-0.52	0.08	0.27	SMTH
20	9.2	AC	20.1	-1.47	-1.47	0.24	SMTH
21	9.0	AC	10.5	-1.16	-0.95	0.17	PEAK
22	9.6	AC	11.5	-1.52	-1.52	0.49	BOWL
23	9.3	AC	8.5	-0.56	-0.56	0.22	SMTH
24	8.8	AC	8.5	-1.28	-1.28	0.30	BOWL
25	9.9	AC	18.0	-1.25	-1.25	0.31	BOWL
26	10.2	AC	15.0	-0.44	-0.08	0.21	SMTH
27	9.2	AC	17.9	-1.54	-1.54	0.26	BOWL
28	9.9	AC	9.0	-0.61	-0.51	0.13	SMTH
30	10.0	AC	7.0	-0.37	-0.37	0.23	BOWL
31	11.1	AC	10.0	-0.66	-0.66	0.15	SMTH
32	11.2	AC	5.5	-0.60	-0.60	0.14	BOWL
33	11.2	AC	4.6	-0.66	-0.66	0.14	BOWL
34	10.7	AC	13.4	-1.66	-1.27	0.54	PEAK
36	8.9	AC	9.5	-0.79	-0.79	0.27	BOWL
37	8.6	AC	7.5	-0.35	-0.35	0.17	BOWL
39	7.0	AC	10.0	-0.64	-0.64	0.14	BOWL
40	7.6	AC	18.4	-1.31	-1.31	0.33	SMTH
42	8.4	AC	38.9	-1.90	-1.38	1.04	PIT
43	8.1	AC	7.5	-0.99	-0.99	0.22	BOWL
44	7.3	AC	12.0	-1.06	-0.94	0.22	SMTH
45	6.7	AC	10.5	-1.04	-1.04	0.24	SMTH
46	7.4	AC	12.5	-1.10	-0.26	0.32	PEAK
47	8.2	AC	38.9	-1.46	-0.78	0.57	PIT
48	8.5	AC	12.6	-0.96	-0.96	0.32	BOWL
50	6.1	AC	15.9	-0.57	-0.42	0.42	SMTH
51	7.0	AC	65.9	-2.26	-2.22	0.52	PIT
52	7.1	AC	13.1	-0.36	-0.34	0.19	SMTH
53	6.2	AC	17.9	-0.27	-0.11	0.10	SMTH
54	4.5	AC	8.0	-0.34	-0.34	0.06	BOWL
55	5.2	AC	6.5	-0.57	-0.57	0.10	BOWL
56	5.1	AC	5.4	-0.24	-0.24	0.08	BOWL
57	4.6	AC	10.0	-0.33	-0.12	0.12	SMTH
58	4.4	AC	8.0	-0.73	-0.73	0.15	BOWL
59	4.5	AC	22.0	-0.80	-0.36	0.36	PEAK
60	5.8	AC	8.5	-0.93	-0.93	0.21	BOWL
61	4.0	AC	18.0	-1.64	-1.50	0.21	BOWL
62	6.1	AC	7.0	-0.48	-0.48	0.17	BOWL
63	4.6	AC	8.5	-0.31	-0.31	0.12	SMTH
65	6.1	AC	7.0	-0.56	-0.56	0.22	BOWL
66	5.4	AC	11.0	-0.74	-0.70	0.23	BOWL

20637.14 0467J2-001

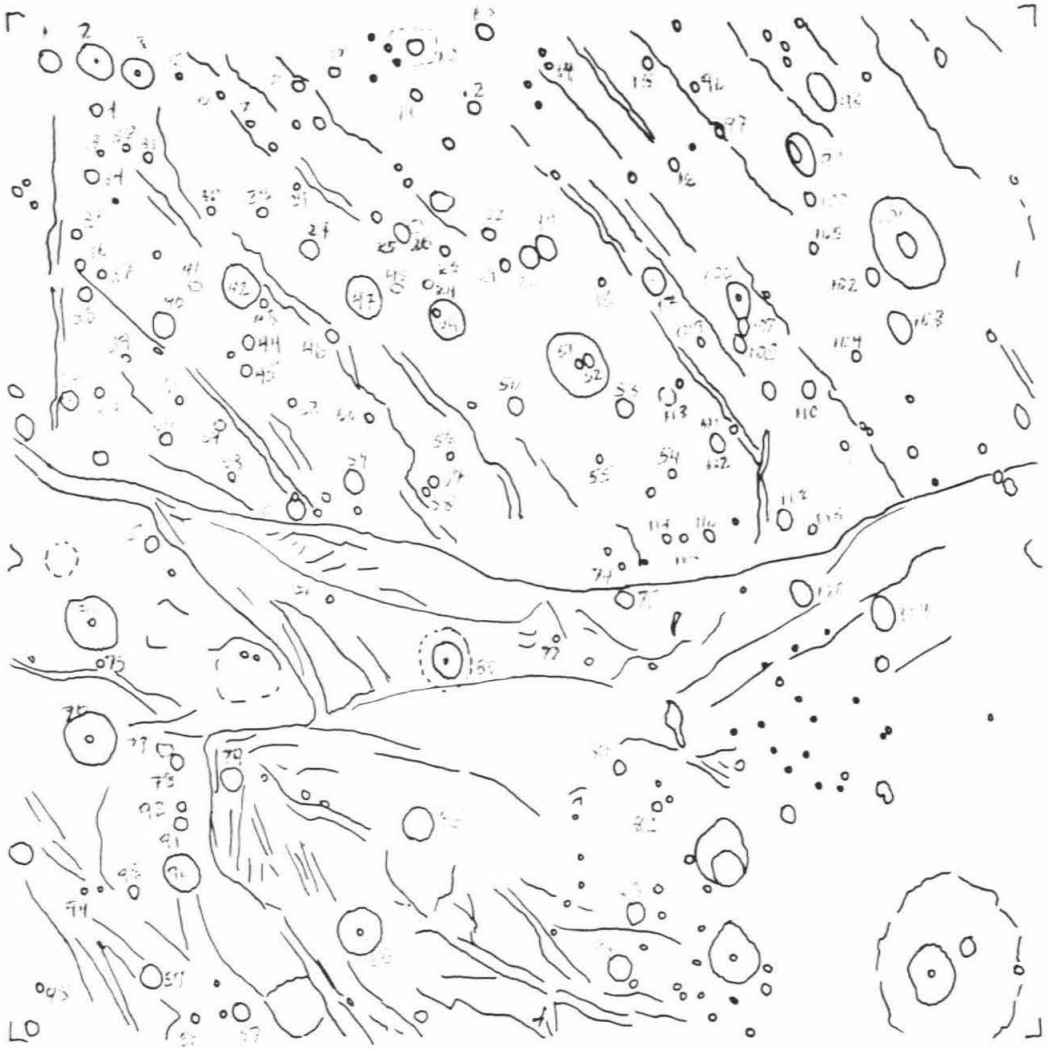

68	6.1	AC	16.9	-0.22	0.0	0.09	SMTH
69	11.4	AC	14.2	-1.25	-1.15	0.10	SMTH
70	12.8	AC	50.1	-1.36	-1.34	0.37	PIT
71	2.2	G1	4.0	-0.36	-0.36	0.17	BOWL
72	1.6	G1	5.0	-0.18	-0.18	0.07	PEAK
73	2.4	G1	17.1	-0.74	-0.67	0.31	SMTH
74	3.1	AC	5.5	-0.26	-0.26	0.19	SMTH
76	-0.5	G1	45.0	-1.15	-0.98	0.60	PIT
77	-0.7	G1	10.0	-0.55	-0.55	0.34	BOWL
78	-0.9	G1	14.0	-1.01	-0.92	0.09	SMTH
79	-1.2	G1	25.9	-1.82	-1.62	0.47	SMTH
80	1.1	G1	37.0	-2.81	-2.32	0.43	SMTH
81	-0.9	G1	12.1	-0.51	-0.51	0.09	PEAK
82	-1.5	G1	9.0	-0.28	-0.27	0.06	SMTH
83	-3.6	G1	20.0	-0.75	-0.55	0.11	SMTH
84	-4.7	G1	24.9	-0.71	-0.66	0.29	SMTH
85	-2.1	G1	33.9	-1.45	-1.45	0.68	PIT
86	-4.1	G1	43.0	-1.35	-0.95	0.52	PIT
87	-5.6	G1	16.0	-0.80	-0.70	0.24	SMTH
88	-5.7	G1	9.0	-0.68	-0.68	0.19	BOWL
89	-5.0	G1	22.9	-1.36	-1.11	0.23	SMTH
90	-3.0	G1	29.9	-2.74	-1.80	0.85	PEAK
91	-2.0	AC	9.9	-0.60	-0.53	0.14	SMTH
92	-1.8	AC	9.0	-1.10	-1.10	0.30	BOWL
93	-3.3	AC	11.0	-1.04	-1.02	0.24	PEAK
94	-3.3	G1	4.0	-0.43	-0.43	0.06	PEAK
95	-5.2	G1	7.0	-0.55	-0.55	0.07	BOWL
96	12.9	AC	9.0	-0.41	-0.34	0.20	SMTH
97	12.1	AC	11.0	-1.01	-1.01	0.28	BOWL
98	13.1	AC	41.0	-0.49	0.12	0.44	SMTH
99	11.7	AC	20.0	-1.64	-1.64	0.33	BOWL
100	10.8	AC	13.0	-0.21	0.03	0.20	PEAK
101	10.1	AC	50.1	-1.54	-1.50	0.75	PIT
102	9.3	AC	17.0	-0.89	-0.89	0.17	BOWL
103	8.4	AC	30.0	-0.80	-0.80	0.20	BOWL
104	7.6	AC	9.9	-0.33	-0.33	0.23	BOWL
105	9.7	AC	10.5	-0.73	-0.73	0.25	BOWL
106	8.6	AC	36.0	-1.00	-1.00	0.26	PIT
107	6.0	AC	15.5	-0.17	-0.15	0.09	SMTH
108	7.6	AC	15.0	-0.22	-0.16	0.18	SMTH
109	7.6	AC	9.5	-0.32	-0.32	0.17	SMTH
110	6.8	AC	16.0	-0.41	-0.34	0.12	SMTH
111	5.9	AC	8.0	-0.83	-0.83	0.16	BOWL
112	5.6	AC	17.1	-0.68	-0.47	0.11	SMTH
113	6.3	AC	27.1	-0.22	-0.14	0.15	SMTH
114	3.6	AC	8.0	-0.30	-0.30	0.14	BOWL
115	3.7	AC	6.6	-0.39	-0.39	0.11	BOWL
116	3.8	AC	11.5	-0.60	-0.49	0.21	PEAK
117	4.2	AC	18.0	-1.00	-0.89	0.18	SMTH
118	4.0	AC	9.0	-0.36	-0.36	0.29	BOWL
119	2.4	G1	30.0	-0.86	-0.67	0.15	SMTH
120	2.7	G1	24.0	-0.75	-0.75	0.24	BOWL

20637.14 0467J2-001

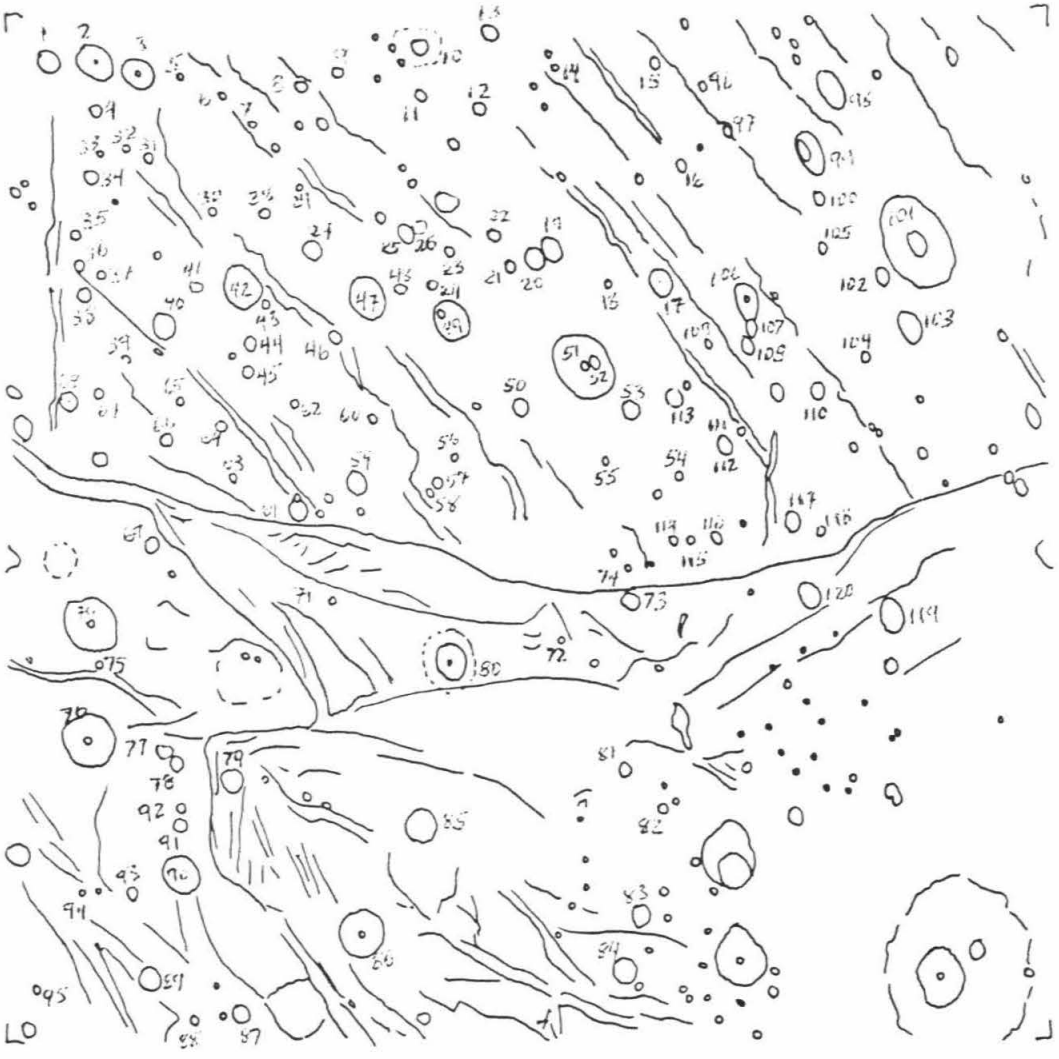

FDS 2063726 Ganymede

CRATER	LATITUDE	TERR	DIAM(KM)	MAXDEPTH	CENTER DEPTH	RIM HEIGHT	TYPE
1	-2.7	G1	50.0	-0.88	-0.24	0.39	SMTH
2	-3.0	G1	30.0	-0.79	-0.79	0.36	SMTH
3	-2.0	G1	13.7	-0.44	-0.44	0.18	PEAK
4	-4.7	G1	53.0	-1.22	-0.76	0.42	SMTH
7	-4.8	G1	56.9	-1.59	-1.53	0.72	PIT
8	-4.8	G1	183.1	-0.83	-0.69	0.69	SMTH
9	-4.3	G1	13.2	-1.07	-1.07	0.14	BOWL
10	-4.8	G1	10.0	-0.85	-0.85	0.15	PEAK
11	-5.0	G1	76.0	-1.34	-1.30	0.58	PIT
12	-8.7	G1	17.9	-0.46	-0.41	0.20	SMTH
13	-8.6	G1	15.0	-0.95	-0.80	0.41	SMTH
14	-7.6	G1	7.1	-0.34	-0.34	0.08	BOWL
15	-8.0	G1	4.7	-0.23	-0.23	0.05	BOWL
16	-7.8	G1	32.0	-0.82	-0.73	0.38	SMTH
17	-8.9	G1	8.0	-0.76	-0.76	0.17	BOWL
18	-8.7	G1	7.5	-0.63	-0.63	0.14	BOWL
19	-9.5	G1	7.0	-0.38	-0.38	0.15	BOWL
20	-11.0	G1	30.0	-1.11	-1.11	0.38	SMTH
21	-11.2	G1	22.0	-0.99	-0.90	0.30	PEAK
22	-10.8	G1	16.5	-0.58	-0.50	0.36	SMTH
23	-11.1	G1	9.4	-0.51	-0.51	0.10	BOWL
24	-11.7	G1	13.7	-0.90	-0.90	0.19	BOWL
25	-7.8	G1	11.3	-0.74	-0.74	0.16	BOWL
26	-11.7	G1	15.1	-0.70	-0.70	0.12	BOWL
27	-13.3	G1	16.8	-0.70	-0.70	0.20	BOWL
28	-14.9	G1	23.5	-0.99	-0.73	0.31	PEAK
29	-14.4	G1	9.9	-1.15	-1.15	0.23	PEAK
30	-14.1	G1	9.3	-0.53	-0.53	0.20	PEAK
31	-17.3	G1	63.1	-1.78	-1.74	0.48	PIT
32	-17.8	G1	8.5	-1.28	-1.28	0.30	BOWL
33	-18.1	G1	6.7	-0.13	-0.10	0.04	SMTH
34	-19.0	G1	12.3	-0.79	-0.65	0.22	PEAK
35	-16.0	G1	4.7	-0.41	-0.41	0.08	BOWL
36	-16.4	G1	8.5	-0.41	-0.41	0.15	PEAK
37	-16.0	G1	8.0	-0.28	-0.28	0.06	BOWL
38	-16.4	G1	26.0	-1.13	-1.13	0.32	PEAK

20637.26 0479J2-001

FDS 2063655 Ganymede

CRATER	LATITUDE	TERR	DIAM(KM)	MAXIDEPTH	CENTER DEPTH	RIM HEIGHT	TYPE
1	-30.3	G1	7.7	-0.72	-0.59	0.06	PEAK
2	-31.8	G1	5.7	-0.47	-0.47	0.15	PEAK
3	-32.0	G1	7.4	-0.74	-0.72	0.09	PEAK
4	-32.8	G1	16.7	-1.87	-1.84	0.44	SMTH
5	-33.1	G1	3.3	-0.23	-0.23	0.07	BOWL
6	-32.2	G1	10.7	-1.12	-0.96	0.15	PEAK
7	-31.7	G1	3.6	-0.47	-0.47	0.11	BOWL
8	-33.9	G1	3.0	-0.45	-0.45	0.07	BOWL
9	-34.0	G1	3.3	-0.41	-0.41	0.10	BOWL
10	-35.0	G1	26.0	-1.51	-1.38	0.20	PIT
11	-34.2	G1	13.4	-1.35	-1.08	0.29	PEAK
12	-34.0	G1	9.0	-0.88	-0.73	0.33	PEAK
13	-33.3	G1	6.3	-0.46	-0.46	0.10	PEAK
14	-36.2	G1	17.5	-1.09	-0.49	0.19	PEAK
15	-36.2	G1	9.5	-1.16	-1.10	0.09	PEAK
16	-36.6	G1	33.0	-0.89	-0.46	0.21	PIT
17	-35.7	G1	8.0	-0.84	-0.84	0.11	PEAK
18	-37.3	G1	12.5	-0.66	-0.42	0.29	PEAK
19	-38.1	G1	5.7	-0.82	-0.82	0.23	BOWL
20	-38.5	G1	8.7	-1.00	-1.00	0.12	SMTH
21	-38.8	G1	15.7	-1.06	-0.67	0.20	SMTH
22	-38.6	G1	17.0	-1.75	-1.34	0.37	PIT
23	-38.1	G1	10.5	-0.93	-0.63	0.31	PEAK
25	-40.2	G1	15.7	-0.94	-0.66	0.16	PEAK
26	-40.4	G1	15.0	-0.74	-0.74	0.11	SMTH
27	-41.2	G1	10.8	-0.79	-0.67	0.06	PEAK
28	-41.7	G1	9.2	-0.69	-0.63	0.10	PEAK
29	-30.1	G1	20.0	-1.36	-1.36	0.21	SMTH
30	-31.1	G1	8.5	-0.88	-0.88	0.20	BOWL
31	-32.4	G1	22.0	-1.85	-1.66	0.35	SMTH
32	-32.4	G1	11.3	-1.05	-1.05	0.29	SMTH
33	-33.2	G1	39.9	-2.11	-0.96	0.38	PEAK
34	-33.5	G1	9.4	-1.48	-1.48	0.22	BOWL
35	-34.1	G1	46.1	-1.82	-1.09	0.91	PIT
36	-35.9	G1	8.9	-1.27	-1.27	0.33	BOWL
37	-37.1	G1	11.9	-0.74	-0.74	0.15	PEAK
38	-37.6	G1	81.9	-0.81	-0.71	0.32	SMTH
39	-37.6	G1	12.1	-1.02	-0.88	0.26	PEAK
40	-36.2	G1	10.2	-1.10	-1.10	0.18	BOWL
41	-39.9	G1	28.2	-1.95	-1.53	0.83	PEAK
42	-40.6	G1	22.3	-1.34	-1.34	0.26	SMTH

20638.59 0572J2-001

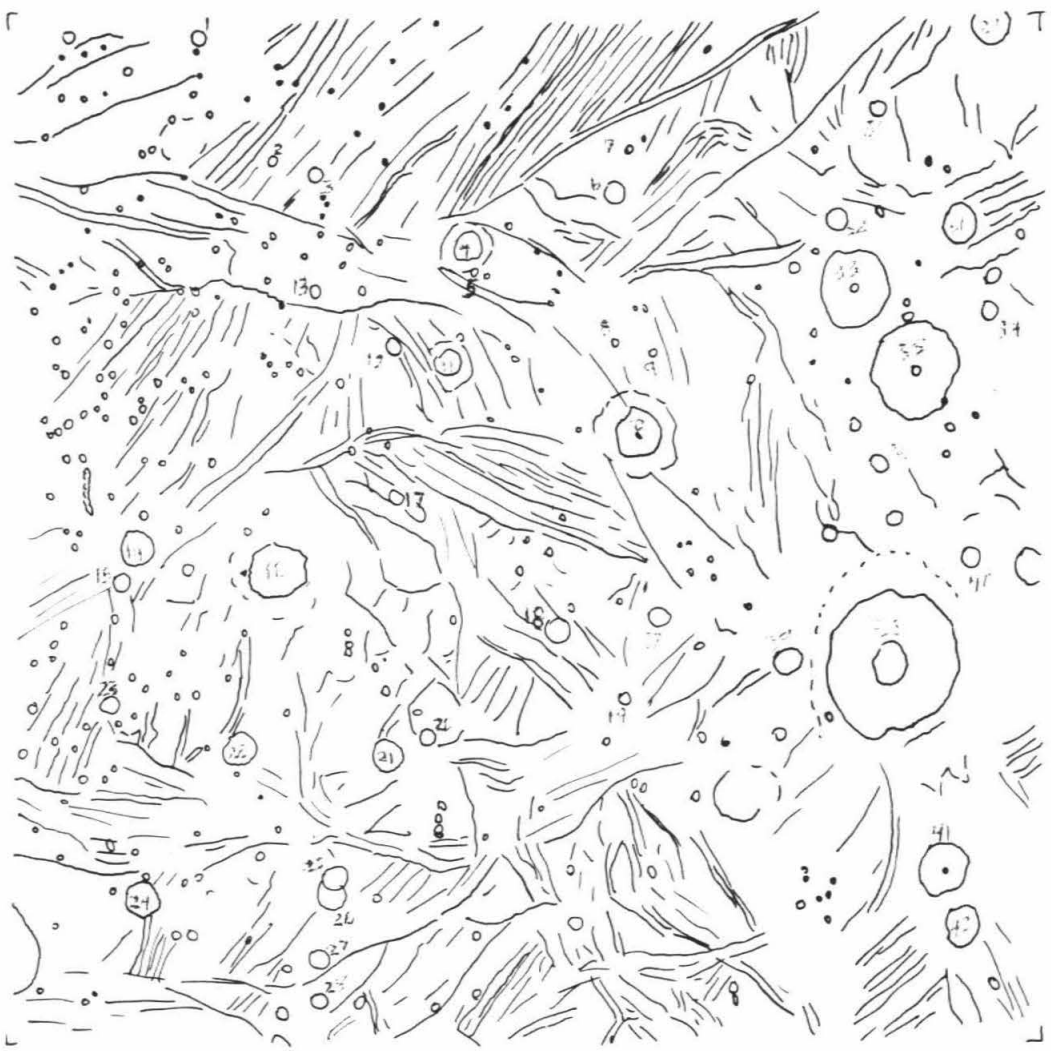

FDS 2063505 Ganymede

CRATER	LATITUDE	ERR	DIAM(KM)	MAXDEPTH	CENTER DEPTH	RIM HEIGHT	TYPE
1	-43.9	C1	6.0	-0.49	-0.49	0.13	BOWL
2	-43.5	G1	3.4	-0.24	-0.24	0.05	BOWL
3	-43.8	G1	29.0	-0.89	-0.89	0.24	PIT
4	-44.6	G1	5.0	-0.45	-0.45	0.07	BOWL
5	-45.1	G1	9.3	-0.84	-0.84	0.14	PEAK
6	-45.8	C1	6.0	-0.56	-0.56	0.13	PEAK
7	-46.0	C1	5.5	-0.36	-0.36	0.07	BOWL
8	-46.2	C1	6.0	-0.44	-0.44	0.08	BOWL
9	-46.7	C1	18.0	-0.93	-0.75	0.11	SMTH
10	-45.5	G1	4.6	-0.44	-0.44	0.06	PEAK
11	-45.9	C1	7.7	-0.65	-0.65	0.10	PEAK
12	-46.4	C1	8.0	-1.24	-1.24	0.34	PEAK
13	-47.0	G1	11.1	-1.52	-1.52	0.26	BOWL
14	-46.0	C1	22.0	-1.81	-1.81	0.44	BOWL
16	-48.3	G1	7.6	-0.55	-0.55	0.10	SMTH
17	-48.8	G1	9.9	-0.48	-0.48	0.07	SMTH
18	-47.7	G1	8.6	-0.48	-0.48	0.17	PEAK
19	-48.7	G1	41.1	-1.06	-0.57	0.24	PIT
21	-49.7	C1	46.9	-1.58	-1.00	0.52	PIT
22	-49.9	C1	12.9	-1.27	-1.27	0.14	PEAK
23	-49.7	G1	8.5	-0.67	-0.45	0.10	PEAK
24	-49.7	G1	10.1	-0.63	-0.46	0.16	SMTH
25	-50.4	C1	20.0	-0.82	-0.82	0.17	SMTH
26	-50.9	G1	11.7	-0.42	-0.24	0.21	SMTH
27	-50.7	G1	13.4	-1.05	-0.51	0.24	PEAK
28	-50.5	G1	12.3	-0.67	-0.41	0.21	PEAK
29	-50.3	C1	10.4	-0.67	-0.67	0.32	SMTH
30	-50.9	G1	6.7	-0.19	-0.10	0.11	PEAK
32	-46.2	G1	4.0	-0.55	-0.55	0.17	BOWL
33	-46.2	C1	4.0	-0.26	-0.26	0.08	BOWL
34	-45.4	C1	9.3	-1.26	-1.26	0.31	BOWL
35	-44.3	G1	29.4	-2.51	-1.76	0.78	PEAK
37	-49.2	C1	50.1	-1.98	-1.53	0.58	PIT
39	-40.9	G1	10.0	-0.25	-0.03	0.05	PEAK
44	-41.9	C1	8.0	-0.48	-0.38	0.07	PEAK
45	-42.2	C1	7.6	-0.51	-0.51	0.05	PEAK

20639.05 0578J2-001

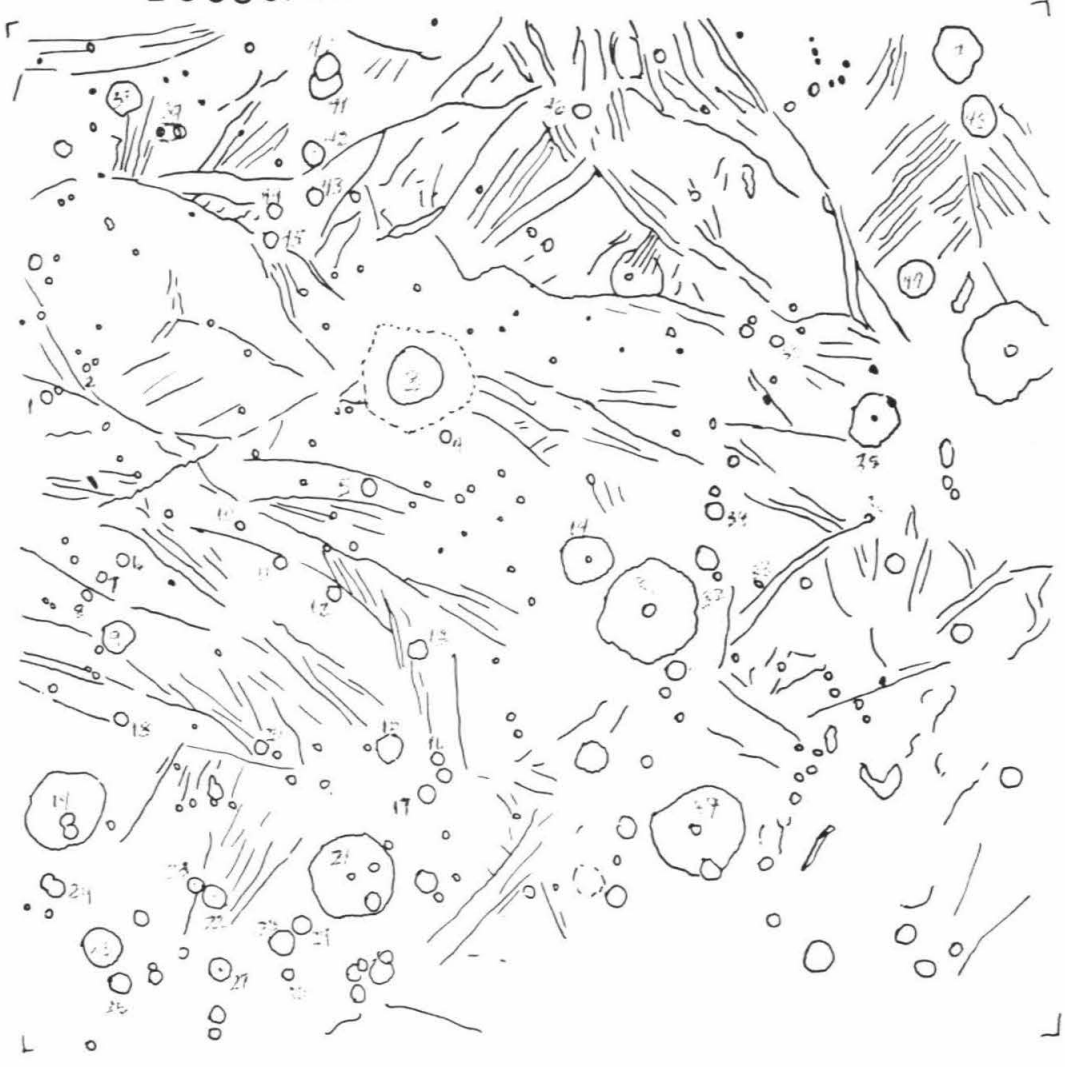

FDS 2063511 Ganymede

CRATER	LATITUDE	TERR	DIAM(KM)	MAXDEPTH	CENTER DEPTH	RIM HEIGHT	TYPE
1	-47.8	G1	7.0	-0.52	-0.45	0.19	PEAK
2	-48.1	G1	6.0	-0.64	-0.64	0.12	PEAK
3	-48.2	G1	14.5	-0.88	-0.88	0.14	PEAK
4	-48.3	G1	7.8	-0.48	-0.48	0.08	BOWL
5	-48.5	G1	9.0	-1.12	-1.12	0.41	BOWL
6	-49.8	G1	11.4	-0.89	-0.76	0.10	PEAK
7	-49.2	G1	6.6	-0.64	-0.64	0.21	PEAK
8	-49.8	G1	12.0	-1.26	-1.15	0.43	PEAK
9	-49.9	G1	10.0	-1.22	-1.22	0.29	BOWL
10	-49.7	G1	47.0	-1.89	-1.47	0.67	PIT
11	-50.3	G1	10.6	-0.79	-0.67	0.30	SMTH
12	-50.5	G1	13.9	-0.74	-0.49	0.40	PEAK
13	-50.9	G1	6.7	-0.87	-0.87	0.27	PEAK
14	-51.1	G1	7.5	-0.07	-0.07	0.07	SMTH
15	-49.9	G1	11.9	-0.83	-0.67	0.21	SMTH
16	-49.8	G1	8.9	-0.68	-0.39	0.09	PEAK
17	-50.7	G1	13.6	-1.15	-0.94	0.12	PEAK
18	-50.8	G1	9.0	-1.24	-1.24	0.32	BOWL
19	-50.9	G1	11.9	-1.07	-0.79	0.38	SMTH
20	-51.4	G1	7.8	-0.76	-0.70	0.22	SMTH
22	-54.0	G1	11.6	-1.35	-1.09	0.21	PEAK
23	-54.9	G1	5.5	-0.90	-0.90	0.16	SMTH
25	-48.3	G1	21.4	-0.84	-0.64	0.20	SMTH
26	-49.2	G1	10.9	-0.31	-0.19	0.09	PEAK
27	-50.0	G1	13.6	-1.21	-1.21	0.20	SMTH
28	-49.2	G1	50.0	-0.90	-0.67	0.31	PIT
29	-49.7	G1	11.2	-1.08	-0.86	0.58	SMTH
30	-48.8	G1	6.0	-0.58	-0.58	0.40	BOWL
31	-50.7	G1	20.0	-0.91	-0.91	0.18	SMTH
32	-52.3	G1	8.8	-0.79	-0.79	0.15	BOWL

20639.11 0584J2-001

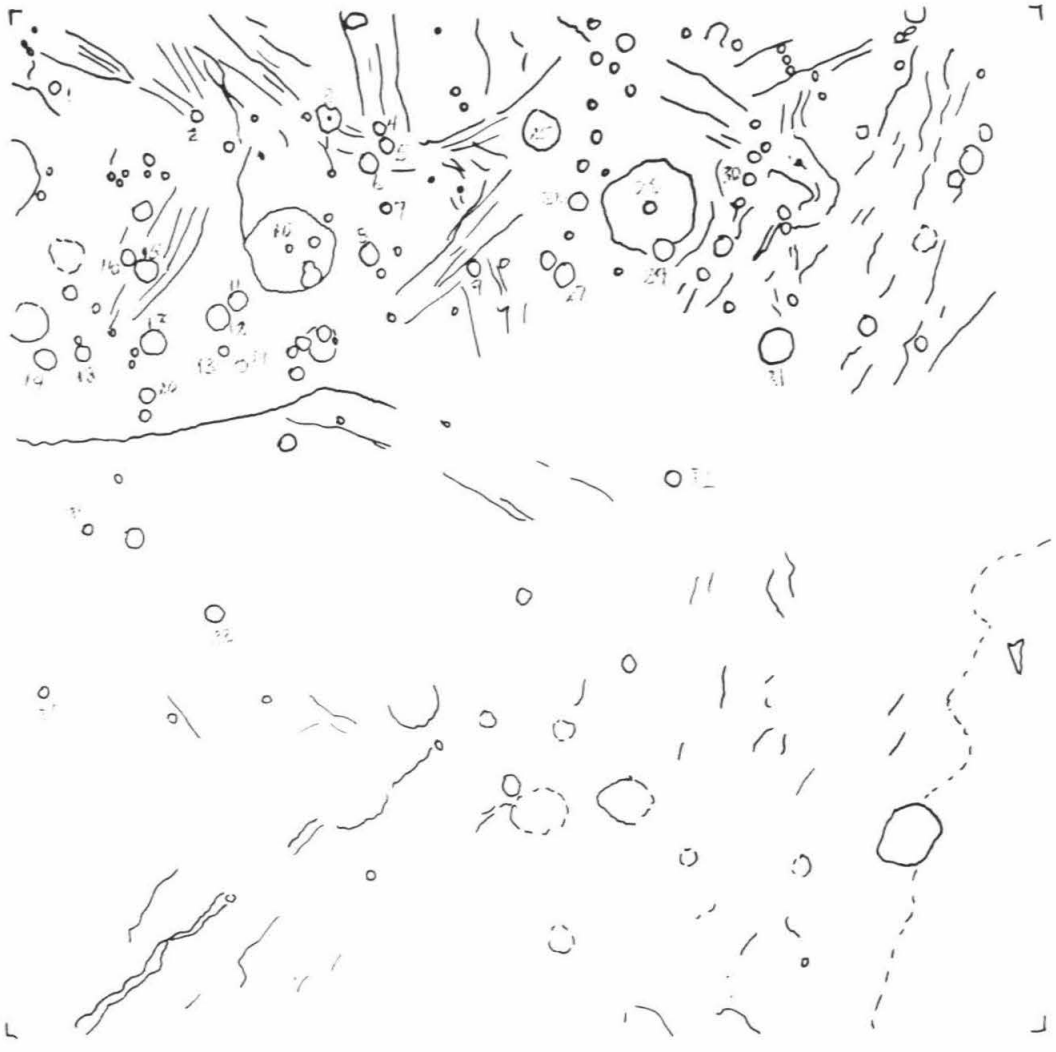

FDS 2063515 Ganymede

CRATER	LATITUDE	TERR	DIAM(KM)	MAXDEPTH	CENTER DEPTH	RIM HEIGHT	TYPE
1	-58.5	G1	8.5	-0.62	-0.54	0.11	SMTH
3	-58.5	G1	5.0	-0.35	-0.35	0.08	BOWL
4	-59.4	G1	30.1	-1.10	-1.10	0.36	SMTH
6	-61.1	G1	6.7	-0.76	-0.76	0.20	PEAK
7	-62.1	G1	4.9	-0.55	-0.55	0.11	BOWL
8	-63.2	G1	5.5	-0.42	-0.42	0.10	BOWL
9	-64.3	G1	21.0	-0.22	-0.19	0.19	SMTH
10	-64.6	G1	6.4	-0.38	-0.38	0.10	PEAK
11	-64.9	G1	18.0	-1.23	-1.23	0.38	PIT
12	-66.7	G1	10.7	-0.93	-0.77	0.15	PEAK
13	-67.5	G1	59.0	-1.75	-1.00	0.88	PIT
14	-68.8	G1	11.9	-0.92	-0.86	0.20	PEAK
15	-68.3	G1	21.1	-0.94	-0.94	0.21	SMTH
16	-61.0	G1	30.0	-1.69	-1.39	0.21	PEAK
17	-61.4	G1	170.2	-0.37	-0.33	0.33	SMTH
18	-64.0	G1	17.0	-0.22	-0.22	0.17	PIT
19	-64.5	G1	32.1	-1.26	-1.26	0.28	SMTH

20639.15 058J2-001

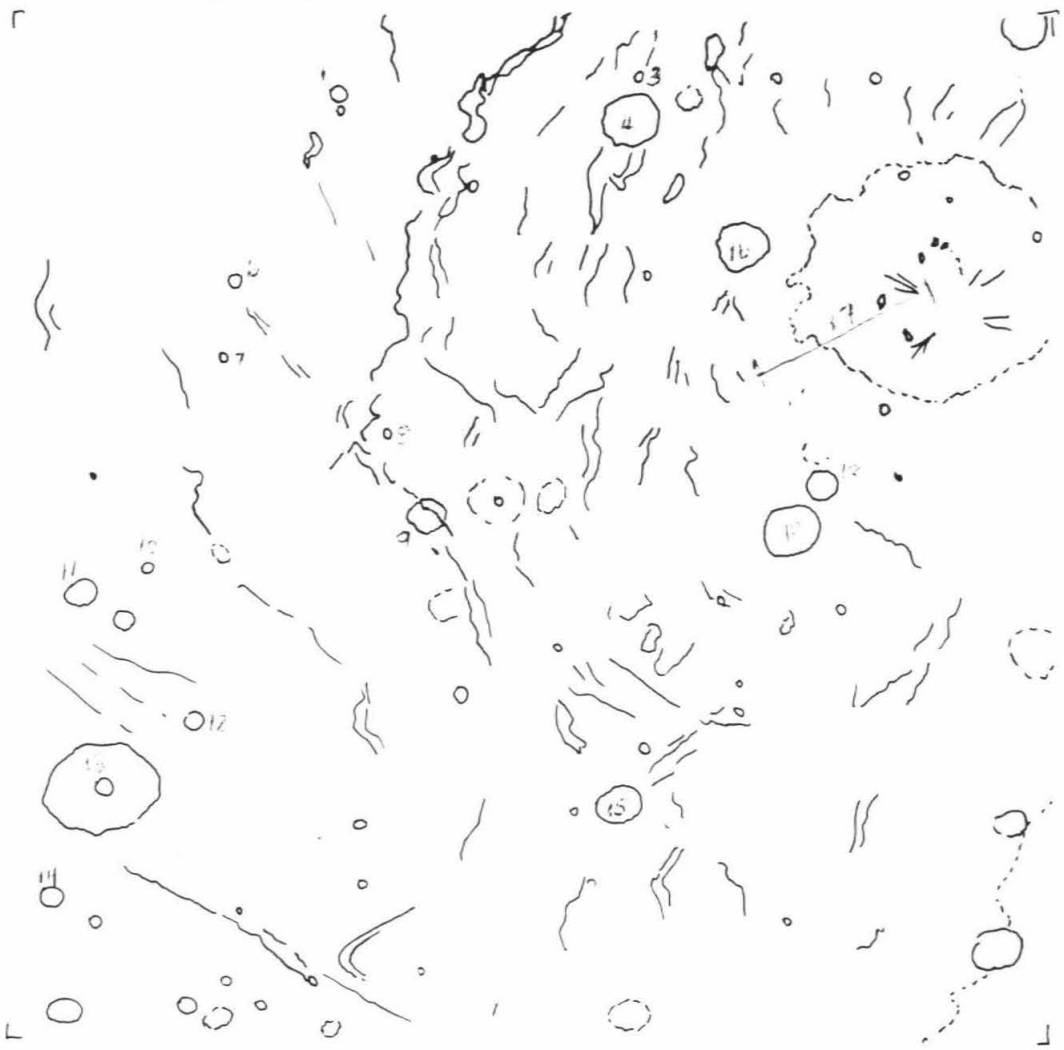

FDS 2063919 Ganymede

CRATER	LATITUDE	TERR	DIAM(KM)	MAXDEPTH	CENTER DEPTH	RIM HEIGHT	TYPE
1	-66.5	G1	8.8	-0.49	-0.44	0.05	SMTH
2	-67.4	G1	59.0	-0.92	-0.45	0.38	PIT
3	-66.7	G1	11.5	-0.84	-0.84	0.14	PEAK
4	-68.8	G1	11.3	-0.98	-0.98	0.14	PEAK
5	-68.7	G1	8.5	-0.76	-0.76	0.15	BOWL
6	-67.2	G1	7.1	-0.54	-0.54	0.05	PEAK
7	-66.8	G1	11.4	-1.25	-1.25	0.19	PEAK
8	-66.4	G1	4.3	-0.42	-0.42	0.04	PEAK
9	-68.0	G1	27.9	-1.31	-1.31	0.17	PIT
10	-69.7	G1	5.7	-0.31	-0.30	0.08	SMTH
11	-69.9	G1	7.2	-0.65	-0.65	0.15	BOWL
12	-70.5	G1	14.9	-0.98	-0.44	0.28	PEAK
13	-70.6	G1	9.9	-0.68	-0.68	0.20	SMTH
14	-70.9	G1	15.0	-0.44	-0.34	0.26	SMTH
15	-71.1	G1	10.8	-0.38	-0.38	0.14	BOWL
16	-72.0	G1	11.3	-0.74	-0.74	0.10	PEAK
17	-72.1	G1	8.4	-0.17	-0.17	0.04	SMTH
18	-72.5	G1	19.3	-0.67	-0.67	0.08	SMTH
19	-72.4	G1	13.6	-0.82	-0.82	0.17	PIT
20	-71.8	G1	15.6	-0.73	-0.73	0.14	SMTH
21	-71.6	G1	11.1	-1.12	-1.12	0.25	BOWL
23	-71.3	G1	15.0	-0.97	-0.82	0.19	PEAK
24	-72.2	G1	4.1	-0.15	-0.15	0.09	BOWL
25	-72.5	G1	7.5	-0.33	-0.19	0.10	PEAK
26	-73.1	G1	52.5	-1.78	-1.78	0.74	PIT
27	-73.4	G1	14.1	-1.19	-1.19	0.19	BOWL
28	-74.1	G1	22.0	-0.91	-0.91	0.14	SMTH
29	-73.8	G1	8.6	-0.49	-0.14	0.15	PEAK
30	-74.5	G1	9.1	-0.60	-0.60	0.17	PEAK
31	-74.4	G1	23.0	-0.20	0.10	0.14	PIT
32	-74.8	G1	13.6	-0.89	-0.62	0.25	PEAK
33	-74.6	G1	24.0	-1.87	-1.87	0.41	SMTH
35	-75.3	G1	10.8	-1.38	-1.38	0.28	PEAK
36	-75.5	G1	14.3	-0.92	-0.76	0.20	PEAK
37	-77.0	G1	18.8	-0.58	-0.47	0.28	PEAK
38	-78.6	G1	11.4	-0.97	-0.97	0.18	PEAK
39	-78.5	G1	31.1	-1.99	-1.79	0.42	SMTH
40	-68.2	G1	21.1	-0.76	-0.76	0.17	SMTH
41	-70.0	G1	6.8	-0.18	-0.08	0.06	SMTH
42	-73.6	G1	20.2	-0.95	-0.66	0.22	PEAK
43	-74.1	G1	15.4	-0.47	-0.37	0.16	PEAK
44	-76.6	G1	27.0	-0.22	-0.18	0.20	SMTH

20639.19 0592J2-001

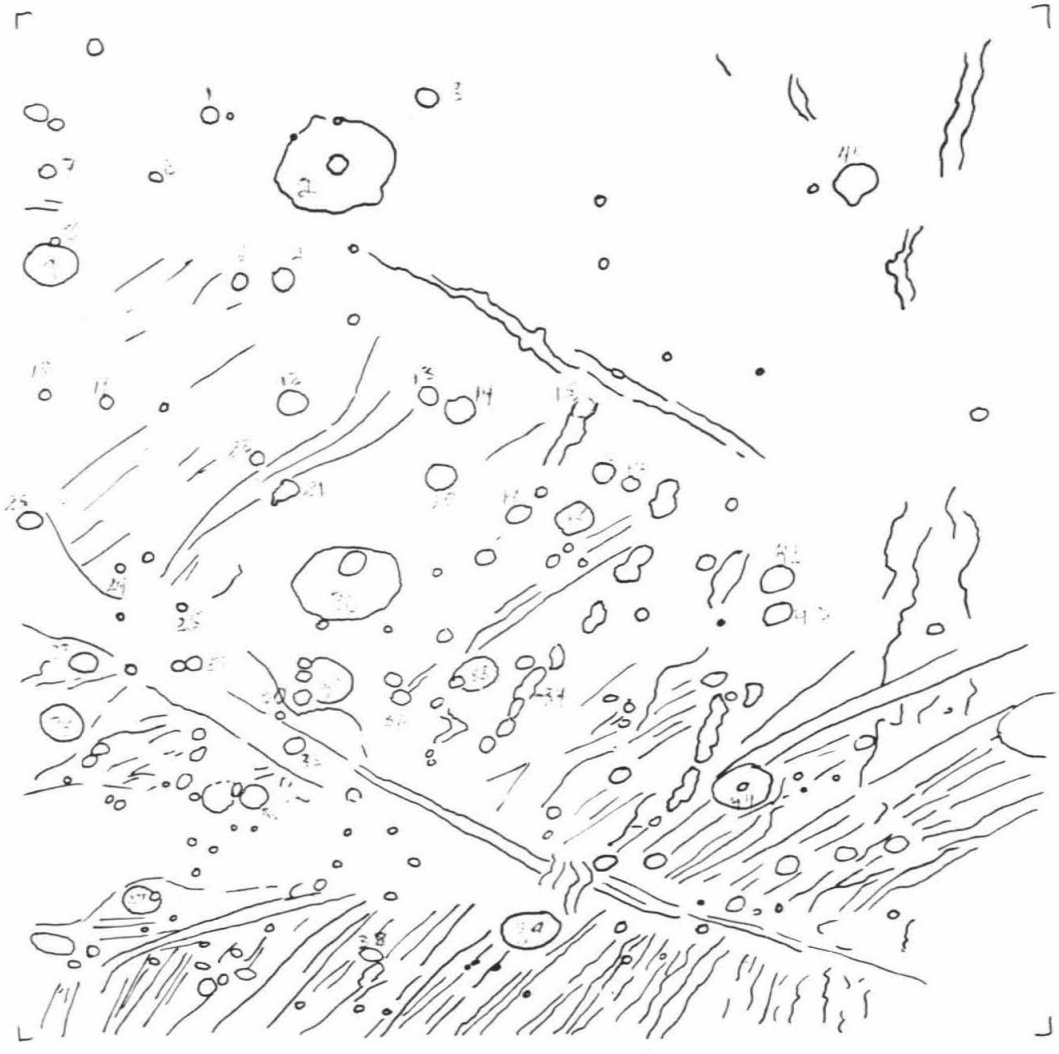

FDS 2064025 Ganymede

CRATER	LATITUDE	TERR	DIAM(KM)	MAXDEPTH	CENTER DEPTH	RIM HEIGHT	TYPE
1	-65.6	G1	4.4	-0.20	-0.20	0.12	BOWL
2	-65.5	G1	5.2	-0.32	-0.32	0.05	BOWL
3	-70.4	G1	7.2	-0.55	-0.51	0.13	PEAK
6	-71.2	G1	13.2	-1.02	-0.60	0.23	PEAK
14	-73.6	G1	7.4	-0.40	-0.40	0.09	BOWL
16	-71.5	G1	24.0	-0.41	0.06	0.25	PIT
17	-71.2	G1	5.2	-0.50	-0.50	0.07	BOWL
18	-71.8	G1	25.5	-1.66	-1.43	0.32	PIT
19	-73.3	G1	12.6	-0.84	-0.75	0.13	PEAK
20	-73.6	G1	21.0	-0.41	-0.15	0.20	PIT
22	-74.7	G1	8.3	-0.77	-0.77	0.13	BOWL
23	-75.5	G1	6.8	-0.38	-0.38	0.05	BOWL
24	-74.7	G1	9.0	-0.70	-0.70	0.11	BOWL
25	-75.1	G1	13.0	-0.65	-0.53	0.13	PEAK
26	-74.1	G1	5.5	-0.44	-0.44	0.08	BOWL
27	-76.1	G1	20.8	-1.14	-1.01	0.25	PIT
28	-76.1	G1	7.8	-0.35	-0.35	0.15	PEAK
29	-79.6	G1	20.0	-0.82	-0.82	0.25	SMTH
30	-78.7	G1	10.5	-0.61	-0.61	0.25	PEAK
31	-80.4	G1	43.5	-0.71	-0.67	0.20	PIT

20640.25 0658J2-001

FDS 2064027 Ganymede

CRATER	LATITUDE	TERR	DIAM(KM)	MAXDEPTH	CENTER DEPTH	RIM HEIGHT	TYPE
1	-71.5	AC	8.6	-0.67	-0.61	0.12	PEAK
2	-75.2	C2	13.7	-1.25	-1.04	0.21	PEAK
3	-76.6	G1	7.5	-0.81	-0.81	0.14	BOWL
4	-76.4	C1	11.2	-0.76	-0.76	0.17	PEAK
5	-75.8	C1	7.3	-0.67	-0.66	0.13	PEAK
6	-73.9	C2	5.5	-0.36	-0.36	0.11	PEAK
7	-73.2	AC	3.8	-0.19	-0.19	0.10	SMTH
8	-72.9	AC	5.5	-0.13	-0.13	0.09	BOWL
10	-72.3	AC	4.5	-0.32	-0.32	0.03	BOWL
11	-72.0	C2	5.0	-0.32	-0.32	0.07	BOWL
12	-71.8	AC	9.2	-1.05	-1.05	0.06	BOWL
13	-72.0	AC	6.5	-0.48	-0.48	0.12	BOWL
14	-71.9	C2	16.1	-1.23	-1.23	0.27	PEAK
15	-70.9	C2	41.1	-2.50	-2.50	0.32	PIT
16	-70.7	C2	17.9	-0.65	-0.15	0.10	SMTH
17	-73.9	C1	59.9	-2.45	-2.41	0.41	PIT
18	-74.4	C1	16.0	-0.58	-0.37	0.11	SMTH
19	-74.5	C1	31.1	-1.31	-1.25	0.38	PIT
20	-75.4	C1	12.2	-0.86	-0.75	0.28	PEAK
21	-76.4	C1	14.4	-0.94	-0.72	0.22	SMTH
22	-76.6	C1	20.4	-0.91	-0.91	0.10	SMTH
23	-77.9	G1	16.5	-1.15	-1.04	0.22	PEAK
24	-79.9	G1	9.3	-0.48	-0.39	0.16	PEAK
25	-80.1	G1	9.2	-0.68	-0.62	0.29	PEAK
26	-78.0	G1	7.8	-0.66	-0.60	0.14	SMTH
27	-78.6	C1	10.0	-0.25	-0.15	0.25	SMTH
28	-77.7	G1	23.0	-0.50	-0.06	0.17	SMTH
29	-79.4	C1	9.5	-1.06	-1.06	0.32	PEAK
30	-80.2	C1	32.9	-1.92	-1.48	0.50	SMTH
31	-78.8	C1	18.8	-1.00	-1.00	0.29	PEAK
32	-77.6	C1	31.0	-0.53	-0.36	0.39	PIT

20640.27 0660J2-001

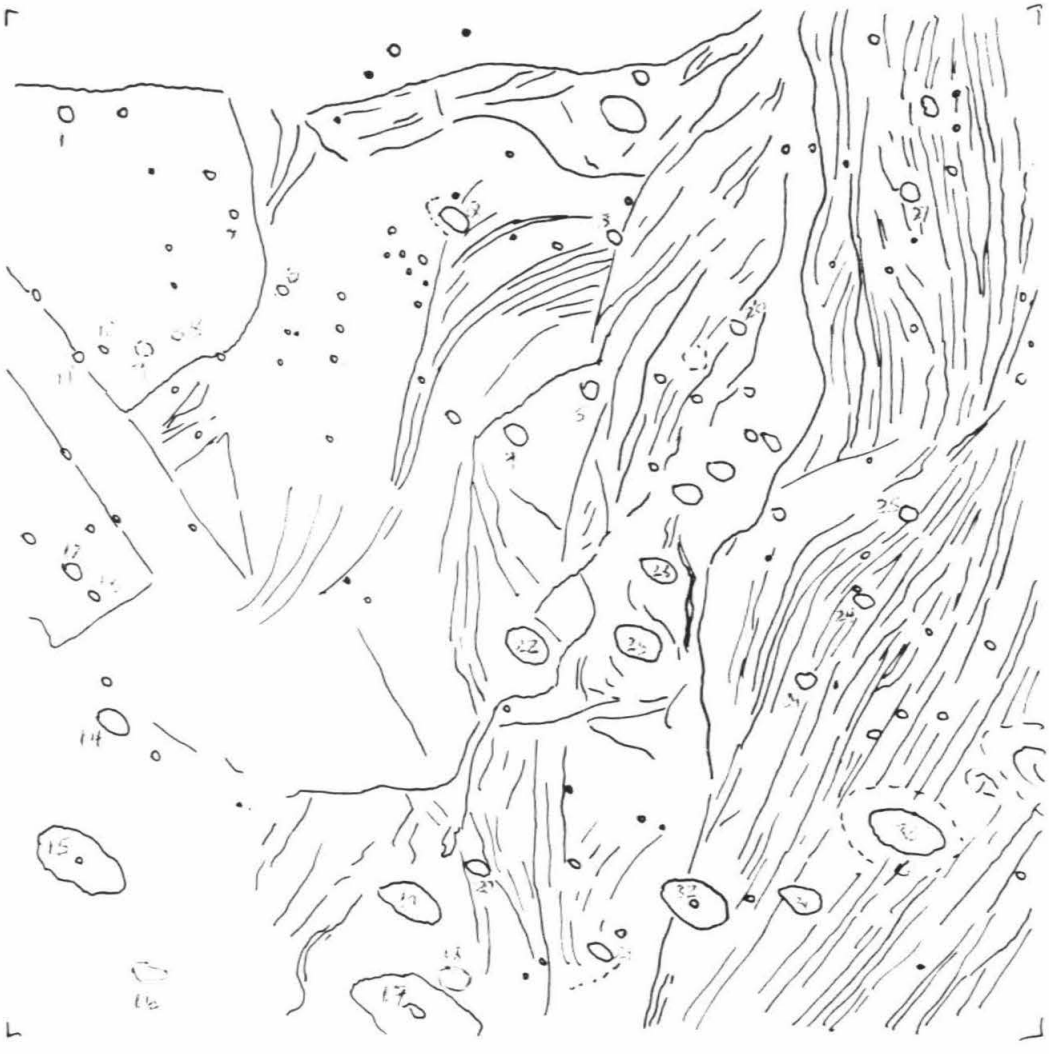

FDS 2064025 Ganymede

CRATER	LATITUDE	TERR	DIAM(KM)	MAXDEPTH	CENTER DEPTH	RIM HEIGHT	TYPE
1	-67.1	G2	17.6	-0.88	-0.77	0.18	SMTH
2	-67.3	G2	16.0	-0.53	-0.36	0.07	SMTH
3	-71.8	G2	18.0	-1.43	-1.43	0.40	PEAK
4	-70.8	G2	40.5	-1.93	-1.93	0.28	PIT
5	-68.6	G2	9.9	-0.65	-0.65	0.11	SMTH
6	-66.2	G2	5.5	-0.35	-0.35	0.15	BOWL
7	-68.0	G2	14.4	-0.86	-0.86	0.12	BOWL
8	-67.6	G2	34.5	-2.19	-2.09	0.30	PIT
9	-67.3	G2	20.1	-1.07	-0.92	0.11	SMTH
10	-65.8	G2	8.0	-0.42	-0.42	0.12	PEAK
11	-69.7	G2	20.9	-0.91	-0.77	0.22	PIT
12	-66.2	G2	18.0	-0.87	-0.87	0.20	SMTH
13	-60.9	G2	7.0	-0.52	-0.52	0.07	BOWL
14	-61.7	G2	16.5	-0.37	-0.33	0.15	SMTH
15	-64.8	G2	13.1	-0.60	-0.51	0.15	PIT
16	-76.5	G1	24.0	-1.33	-1.33	0.18	PIT
17	-77.5	G1	31.0	-0.48	-0.48	0.23	PIT
18	-75.4	G1	12.0	-0.70	-0.58	0.35	PEAK
19	-74.2	G1	31.0	-1.56	-1.46	0.48	PIT
20	-74.4	G1	12.1	-0.33	-0.33	0.06	PIT
21	-75.4	G1	60.0	-2.44	-2.39	0.61	PIT
22	-76.4	G1	14.1	-0.91	-0.65	0.15	PEAK
23	-72.4	G1	11.0	-0.93	-0.88	0.12	PEAK
24	-73.0	G1	18.0	-0.36	-0.02	0.26	PEAK
25	-73.1	G1	5.5	-0.35	-0.35	0.07	BOWL
26	-71.4	G2	8.0	-0.36	-0.30	0.11	PEAK
27	-70.5	G2	25.9	-1.32	-1.27	0.34	PIT
28	-68.9	G2	28.0	-1.48	-1.26	0.55	PIT

20640.29 0662 J2-001

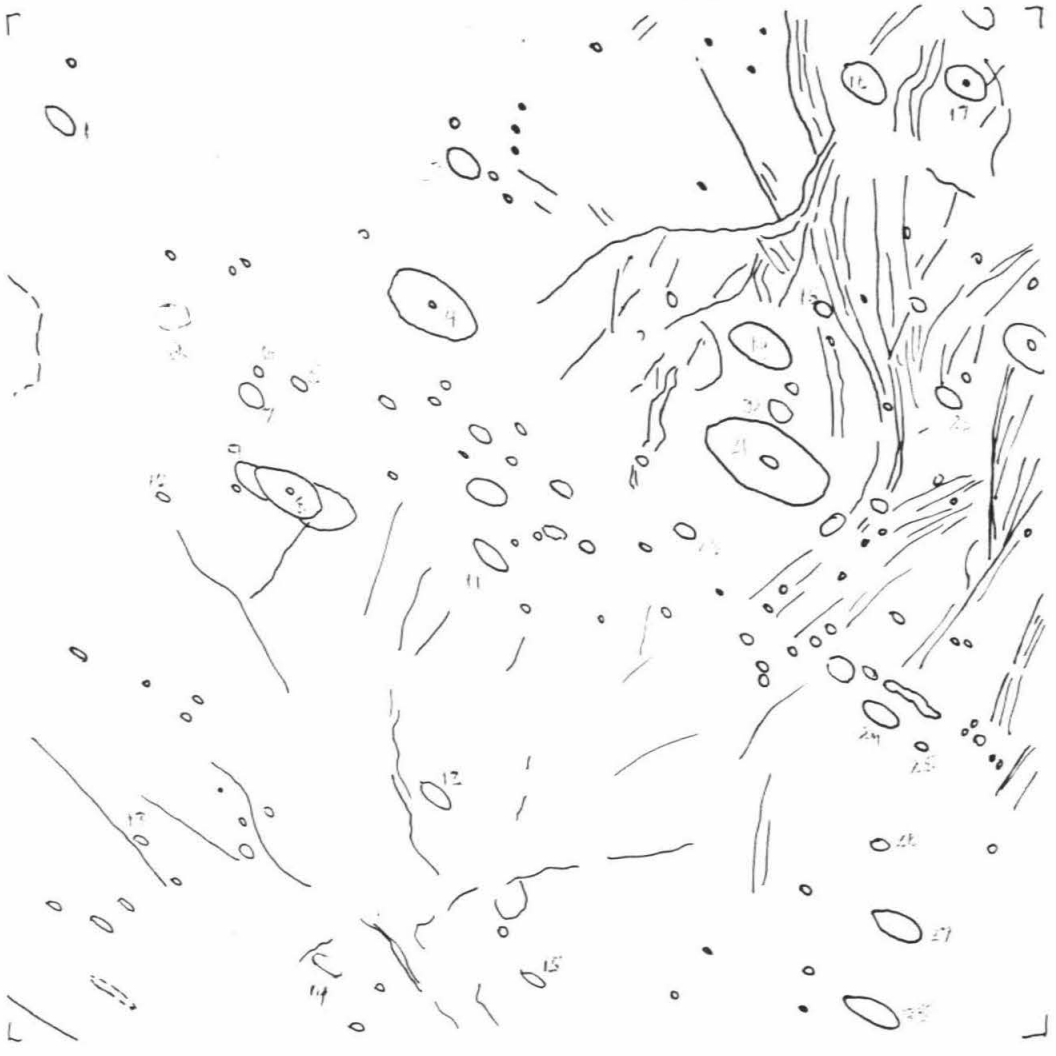

FDS 2064031 Ganymede

CRATER	LATITUDE	TERR	DIAM(KM)	MAXDEPTH	CENTER DEPTH	RIM HEIGHT	TYPE
1	-73.7	G2	24.9	-0.40	-0.08	0.16	SMTH
2	-73.2	G2	23.0	-0.81	-0.76	0.10	PIT
3	-73.8	G2	19.0	-0.20	0.16	0.10	SMTH
4	-73.2	G2	29.8	-0.40	-0.40	0.18	SMTH
5	-75.7	G2	10.8	-0.64	-0.64	0.13	BOWL
6	-77.7	G2	30.0	-0.54	-0.31	0.39	PIT
7	-75.7	G2	14.3	-1.80	-1.80	0.23	PEAK
8	-70.3	G2	17.4	-0.57	-0.52	0.09	SMTH
9	-70.5	G2	64.1	-0.67	-0.22	0.22	SMTH
11	-72.4	G2	12.0	-0.63	-0.63	0.28	BOWL
12	-71.5	G2	22.0	-1.40	-1.40	0.19	BOWL
13	-69.0	G2	34.0	-0.72	-0.37	0.37	PIT
14	-66.6	G2	10.5	-0.21	0.0	0.13	PIT
16	-62.3	G2	17.4	-0.21	0.04	0.13	SMTH
17	-79.2	G2	21.5	-0.38	0.04	0.22	SMTH
18	-79.9	G2	28.0	-0.40	0.18	0.20	SMTH
19	-76.5	G2	19.0	-0.28	-0.07	0.12	SMTH
20	-75.9	G2	15.7	-1.18	-1.00	0.14	PEAK
21	-74.4	G2	28.0	-1.11	-1.05	0.21	SMTH
22	-72.3	G2	60.0	-0.24	-0.20	0.20	SMTH

20640.31

0664J2-001

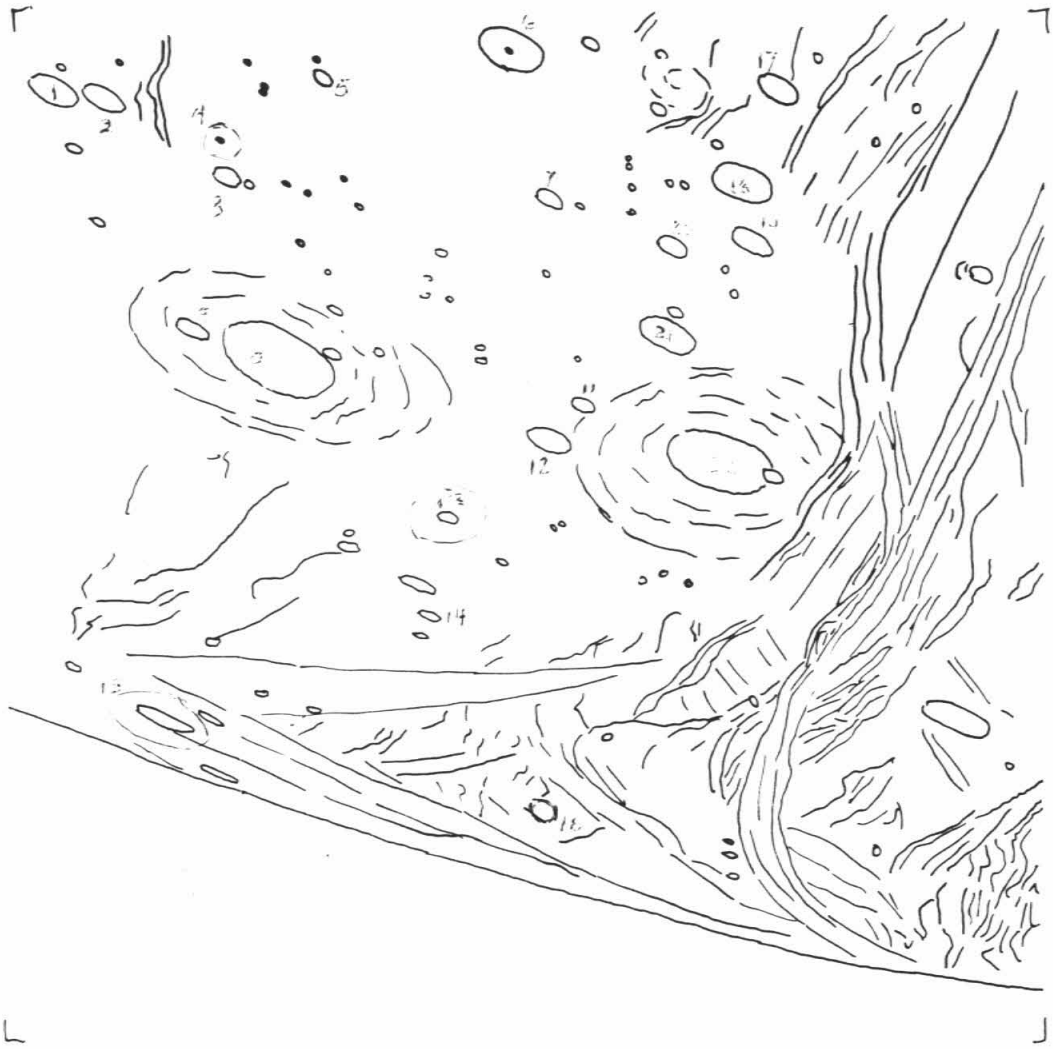

FDS 2064033 Ganymede

CRATER	LATITUDE	TERR	DIAM(KM)	MAXDEPTH	CENTER DEPTH	RIM HEIGHT	TYPE
1	-66.5	G2	17.0	-1.33	-1.25	0.16	SMTH
2	-67.8	AC	9.3	-0.67	-0.67	0.23	ECWL
3	-67.1	AC	16.0	-0.82	-0.82	0.20	SMTH
4	-67.1	AC	11.1	-0.13	-0.05	0.12	SMTH
5	-65.1	G2	21.0	-0.68	-0.57	0.22	SMTH
6	-67.6	AC	43.1	-1.16	-1.16	0.29	PIT
7	-68.5	AC	28.0	-0.96	-0.91	0.27	PIT
8	-68.5	AC	13.9	-0.64	-0.50	0.13	PEAK
9	-68.4	AC	29.0	-0.69	-0.59	0.25	PIT
10	-68.0	AC	70.0	-1.32	-0.17	0.45	PIT
11	-69.5	G2	9.6	-0.57	-0.52	0.09	PEAK
12	-70.0	G2	19.0	-0.91	-0.90	0.16	PEAK
13	-71.6	AC	9.1	-0.50	-0.42	0.10	PEAK
14	-70.5	G2	11.4	-0.75	-0.68	0.13	PEAK
15	-69.6	G1	5.2	-0.30	-0.30	0.10	PEAK
16	-70.0	G1	5.2	-0.33	-0.33	0.04	PEAK
17	-68.7	G2	7.3	-0.37	-0.37	0.08	PEAK
18	-70.3	G1	31.0	-1.99	-1.83	0.56	SMTH
19	-71.8	G1	26.1	-0.86	-0.67	0.15	SMTH
20	-71.0	AC	25.0	-1.22	-1.22	0.18	SMTH
21	-71.3	AC	14.0	-0.33	0.09	0.27	SMTH
22	-73.0	G2	10.6	-1.13	-0.98	0.13	PEAK
23	-73.0	G2	29.9	-1.25	-1.25	0.27	PIT
24	-66.1	G1	13.0	-1.04	-0.91	0.25	PEAK

20640.33 0666J2-001

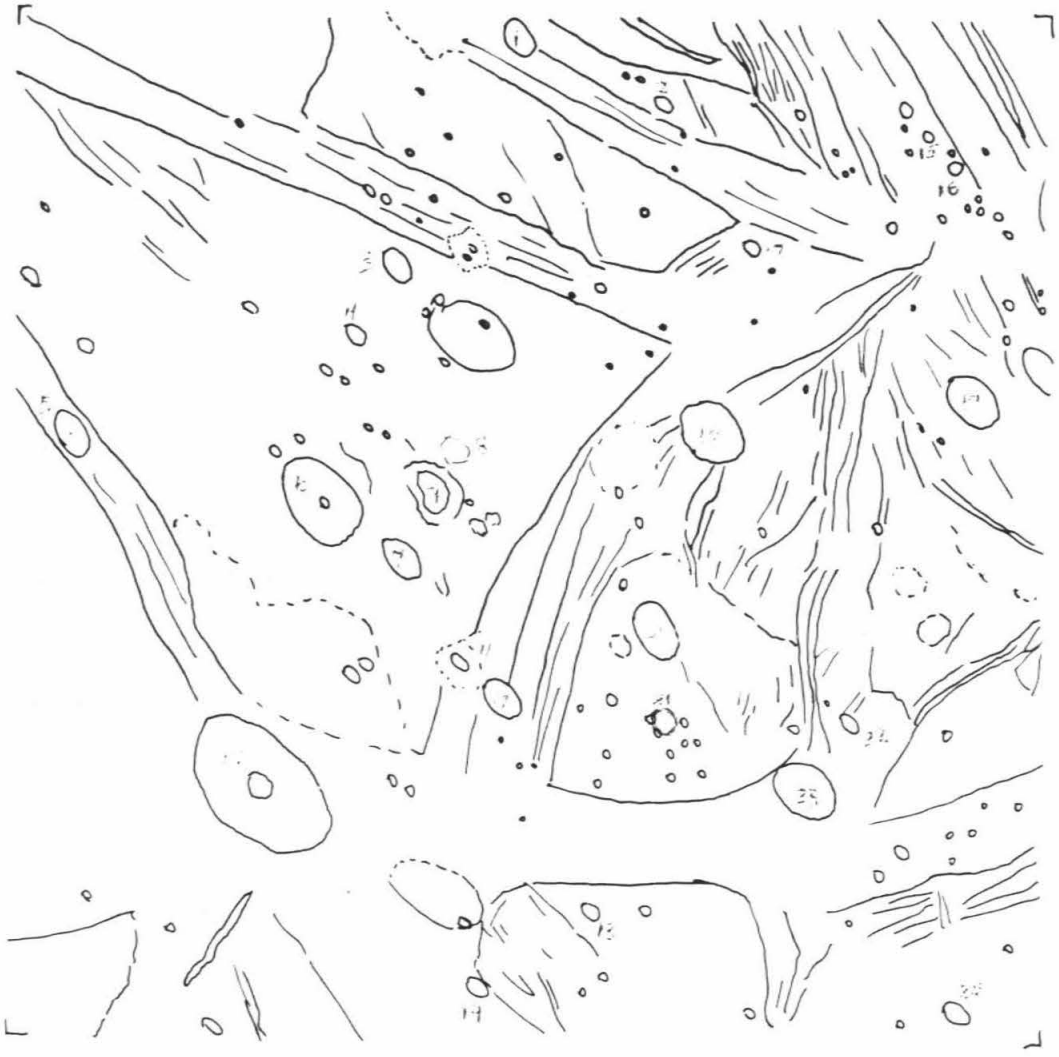

FDS 2C64C37 Ganymede

CRATER	LATITUDE	TERR	DIAM(KM)	MAXDEPTH	CENTER DEPTH	RIM HEIGHT	TYPE
1	-7E.E	G1	11.3	-C.42	-0.35	0.09	PEAK
2	-79.1	C1	11.E	-C.65	-C.4S	0.10	SMTH
3	-E1.3	G1	13.4	-C.47	-0.44	0.12	SMTH
4	-EC.5	C1	43.S	-C.77	-0.73	0.21	PIT
5	-80.0	G1	5.0	-C.1E	-0.1E	0.C6	BOWL
E	-7S.E	G1	18.0	-C.66	-0.62	0.10	PIT
7	-7E.7	C1	S.C	-C.17	-0.12	0.12	SMTH
8	-80.4	C1	1E.0	-C.53	-0.23	0.23	PEAK
S	-E1.1	G1	31.1	-1.23	-1.23	0.18	PIT
10	-E2.1	C1	S.C	-C.35	-0.3S	0.10	BOWL
10	-E2.1	C1	10.1	-C.29	-0.2S	0.10	PEAK

20640.37 0670J2-001

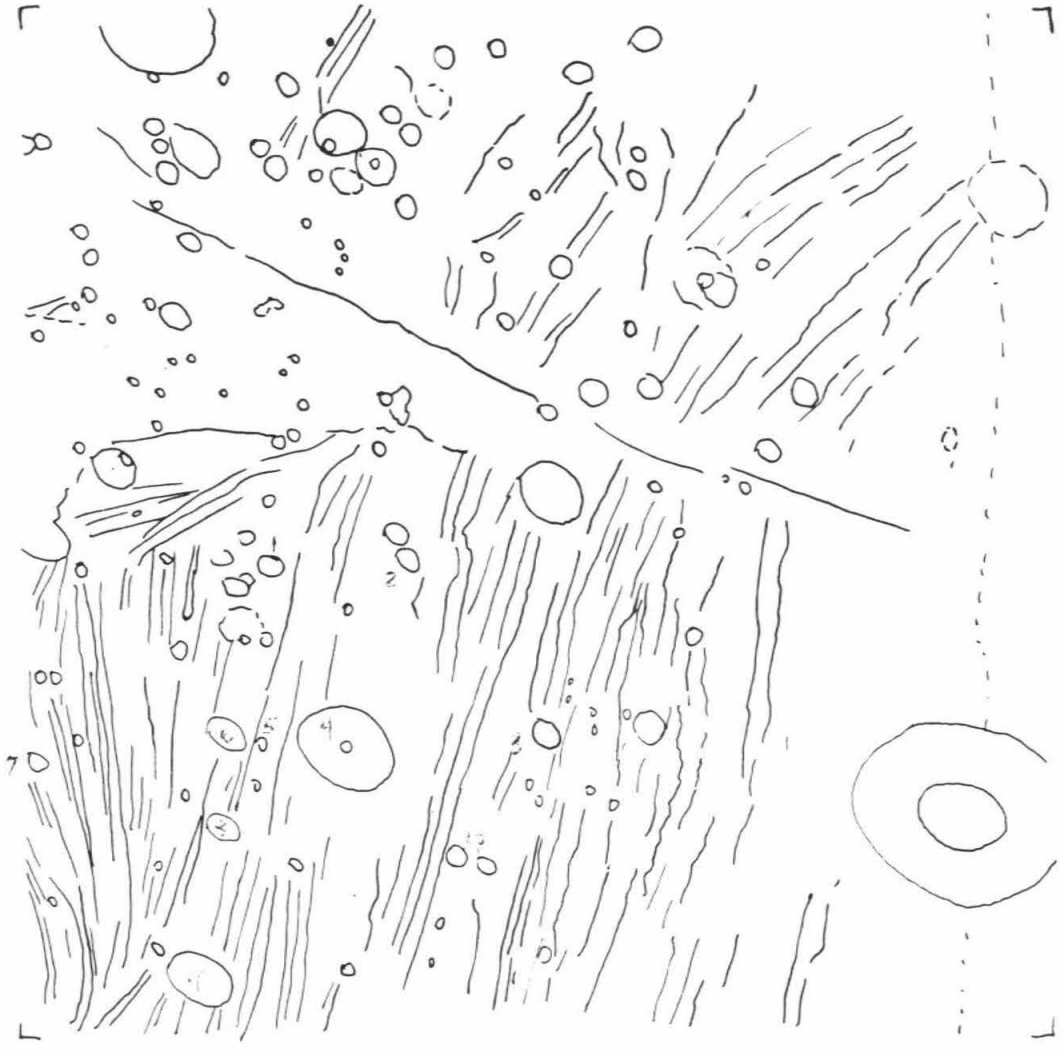

FDS 2064041 Ganymede

CRATER	LATITUDE	TERR	DIAM(KM)	MAXDEPTH	CENTER DEPTH	RIM HEIGHT	TYPE
5	-78.0	G1	10.0	-0.41	-0.41	0.21	PIT
6	-78.1	G1	7.0	-0.44	-0.40	0.24	PEAK
7	-78.0	G1	14.9	-1.13	-1.03	0.16	PEAK
8	-80.2	G1	9.2	-0.48	-0.40	0.14	PEAK
9	-82.2	G1	25.0	-0.49	0.05	0.18	PIT
10	-82.3	G1	10.1	-0.79	-0.71	0.07	PEAK
12	-80.2	G1	33.1	-1.62	-1.25	0.51	PIT
13	-78.9	G1	19.0	-0.92	-0.92	0.27	PEAK
14	-77.7	G1	31.1	-1.13	-1.13	0.57	PIT
15	-76.5	G1	14.0	-0.92	-0.57	0.14	PEAK
16	-77.4	G1	39.1	-1.41	-1.29	0.65	PIT
17	-80.9	G1	33.1	-1.47	-1.27	0.20	PIT
18	-81.6	G1	11.0	-0.31	-0.17	0.08	PEAK
19	-84.4	G1	62.0	-0.80	-0.68	0.32	PIT
20	-83.4	G1	48.0	-1.66	-0.43	0.43	PEAK
21	-83.0	G1	19.1	-0.49	-0.23	0.11	PEAK
22	-84.7	G1	26.0	-1.21	-0.98	0.29	SMTH
23	-87.2	G1	42.0	-0.55	0.0	0.53	PIT
24	-86.5	G1	29.0	-0.83	-0.74	0.11	SMTH
25	-85.6	G1	31.9	-0.43	0.0	0.21	SMTH
26	-83.8	G1	19.0	-0.91	-0.72	0.27	PIT

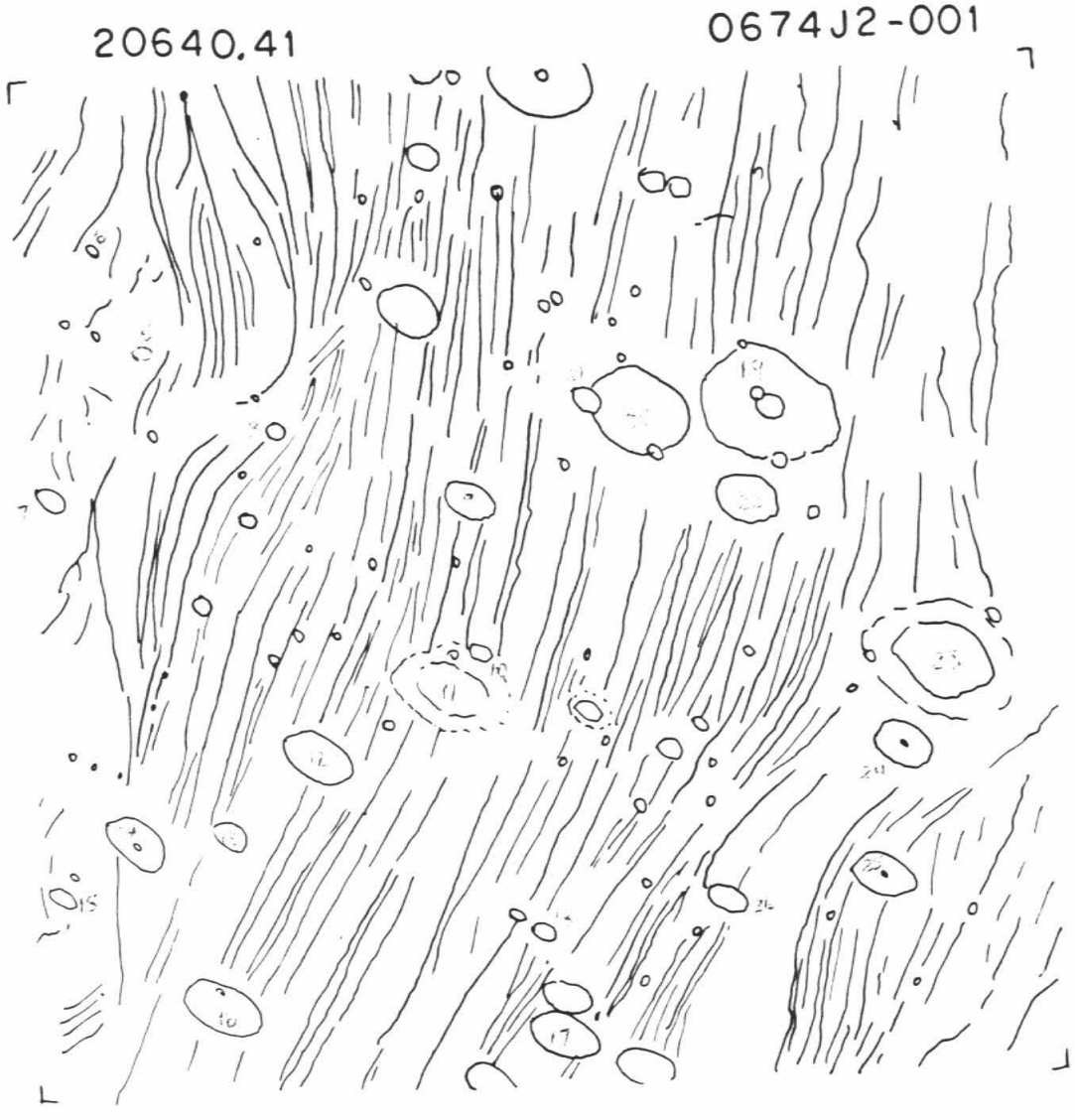
20640.41
0674J2-001

Callisto

FDS 1642127 0124J1+001

CRATER	LATITUDE	TERR	DIAM(KM)	MAXDEPTH	CENTER DEPTH	RIM HEIGHT	TYPE
1	18.1	AC	78.0	-1.72	-1.54	0.44	PIT
5	19.7	AC	46.9	-0.83	-0.70	0.45	PIT
6	20.9	AC	22.0	-0.88	-0.88	0.22	PEAK
7	23.7	AC	29.0	-1.38	-1.38	0.34	BOWL
8	14.8	AC	24.0	-0.60	-0.60	0.22	BOWL
8	14.8	AC	22.8	-0.50	-0.20	0.32	SMTH
9	12.6	AC	37.0	-1.46	-1.39	0.60	PEAK
11	10.3	AC	42.9	-1.59	-1.48	0.58	PIT
12	12.3	AC	38.0	-0.80	-0.60	0.33	PIT
14	14.7	AC	48.0	-2.07	-0.45	0.98	PIT
16	10.4	AC	69.0	-3.21	-2.71	1.44	PIT
18	8.0	AC	43.1	-1.47	-0.38	0.58	PEAK
19	5.5	AC	106.0	-3.38	-3.33	1.33	PIT
20	4.3	AC	22.9	-0.92	-0.89	0.27	SMTH
21	4.2	AC	30.9	-1.12	-0.53	0.29	SMTH
22	-0.3	AC	39.0	-0.68	-0.35	0.43	PEAK
23	-1.3	AC	47.9	-3.52	-1.97	1.41	PIT
24	-2.5	AC	70.0	-0.92	0.23	0.43	SMTH
25	-3.6	AC	31.0	-2.34	-2.01	0.66	SMTH
26	-5.6	AC	65.0	-1.76	-1.11	0.49	PIT
28	-5.9	AC	45.1	-2.04	-0.81	0.94	PIT
29	-9.5	AC	37.0	-2.40	-2.18	0.60	PEAK
32	-21.8	AC	29.0	-0.83	-0.83	0.24	BOWL
33	-7.6	AC	57.0	-2.36	-2.33	0.79	PIT

0124 J1+001

Callisto

FDS 1642159 01563J1+001

CRATER	LATITUDE	TERR	DIAM(KM)	MAXDEPTH	CENTER DEPTH	RIM HEIGHT	TYPE
1	69.8	AC	36.1	-0.56	-0.06	0.19	PEAK
2	70.0	AC	14.1	-1.03	-1.03	0.29	BOWL
4	66.3	AC	24.0	-2.43	-2.43	0.63	BOWL
5	64.8	AC	55.0	-1.33	0.25	0.76	PIT
6	63.0	AC	36.0	-3.06	-3.06	0.63	BOWL
7	62.6	AC	19.0	-1.52	-1.52	0.43	PIT
8	62.0	AC	31.9	-1.86	-1.60	0.47	PEAK
10	59.6	AC	24.0	-2.22	-2.03	0.74	PEAK
12	56.9	AC	23.0	-1.32	-1.20	0.45	PIT
14	57.8	AC	31.0	-1.53	-0.98	0.44	SMTH
15	53.3	AC	15.9	-0.82	-0.58	0.17	SMTH
16	50.7	AC	30.1	-1.58	-1.58	0.36	PIT
19	50.0	AC	28.9	-1.74	-1.62	0.31	SMTH
22	47.4	AC	20.0	-1.48	-1.48	0.52	SMTH
23	47.4	AC	26.9	-1.07	-0.71	0.35	PEAK
24	48.3	AC	18.1	-1.89	-1.89	0.49	BOWL
25	45.1	AC	25.0	-2.95	-2.77	0.87	PEAK
26	43.9	AC	44.0	-0.73	0.16	0.27	PEAK
30	39.5	AC	55.1	-2.82	-1.72	0.78	PIT
32	39.4	AC	27.1	-3.67	-3.67	0.71	PEAK
33	36.8	AC	27.1	-1.26	-1.26	0.49	SMTH

0156 J1+001

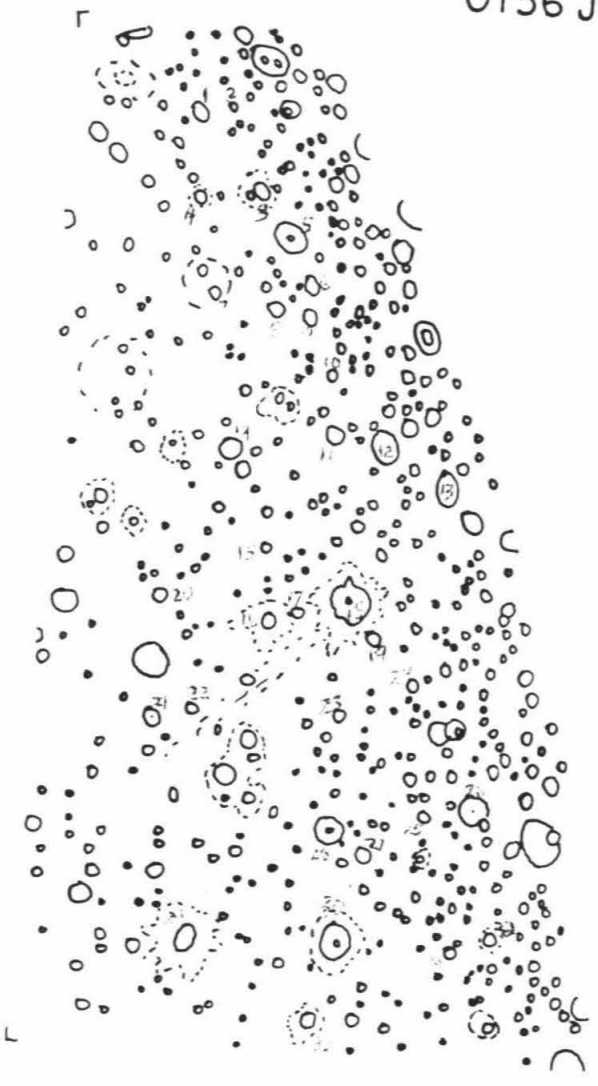

Callisto

FDS 20616641 103452-002

CRATER	LATITUDE	TERR	DIAM(KM)	MAXDEPTH	CENTER DEPTH	RIM HEIGHT	TYPE
1	40.1	AC	41.0	-1.25	-1.25	0.39	PIT
2	41.3	AC	28.9	-0.96	-0.92	0.26	SMTH
3	44.9	AC	42.1	-0.66	-0.41	0.19	SMTH
4	46.0	AC	34.0	-0.74	-0.49	0.40	SMTH
5	46.5	AC	42.1	-1.68	-1.20	0.23	SMTH
6	49.6	AC	119.1	-2.33	-1.63	0.47	PIT
7	49.7	AC	65.0	-2.31	-1.73	0.43	PIT
8	48.2	AC	38.1	-0.62	-0.28	0.24	SMTH
9	48.6	AC	54.1	-0.75	-0.31	0.36	PIT
10	47.4	AC	38.0	-1.04	-0.81	0.38	PEAK
11	50.4	AC	23.1	-1.32	-1.32	0.29	BOWL
12	52.3	AC	29.1	-0.69	-0.65	0.25	BOWL
13	56.5	AC	34.0	-1.10	-0.73	0.41	SMTH
14	58.8	AC	48.9	-2.23	-1.90	0.55	SMTH
15	59.1	AC	58.9	-1.49	-0.83	0.50	SMTH
16	60.3	AC	52.0	-0.62	0.45	0.42	SMTH
17	63.4	AC	21.0	-0.55	-0.55	0.30	BOWL
18	63.6	AC	31.1	-1.10	-1.00	0.30	SMTH
19	63.4	AC	45.0	-1.37	-0.90	0.34	PIT
20	60.3	AC	54.0	-2.70	-2.70	0.73	PIT
21	60.5	AC	44.9	-1.27	-0.43	0.31	SMTH
22	59.0	AC	44.9	-0.69	-0.07	0.33	PIT
23	62.4	AC	112.9	-0.57	0.22	0.44	PIT
24	68.0	AC	21.0	-0.61	-0.40	0.15	PEAK
25	70.8	AC	78.0	-1.94	-0.31	0.97	PIT
26	70.4	AC	22.0	-1.98	-1.98	0.71	BOWL
27	71.7	AC	60.9	-1.09	-0.66	0.37	PIT
28	73.1	AC	36.0	-3.55	-3.55	0.87	BOWL
29	71.5	AC	60.0	-1.69	-0.36	1.21	PIT
30	74.9	AC	30.0	-1.45	-1.45	0.62	PIT
32	79.5	AC	59.9	-1.76	-1.71	0.76	PIT

1034 J2-002

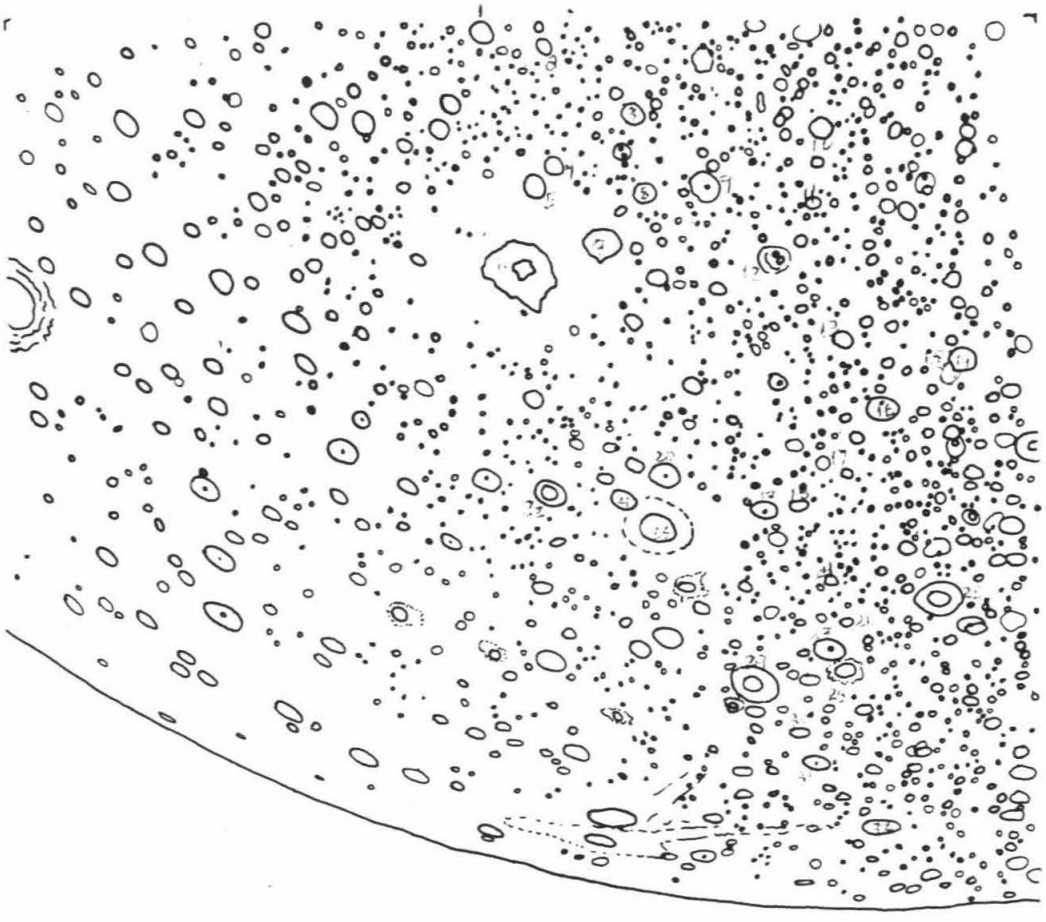

Callisto

FDS 2061657 105032-002

CRATER	LATITUDE	TERR	DIAM(KM)	MAXDEPTH	CENTER DEPTH	RIM HEIGHT	TYPE
1	18.3	AC	34.0	-1.42	-1.42	0.21	PIT
2	19.8	AC	28.0	-0.72	-0.49	0.23	PIT
3	21.1	AC	31.0	-0.86	-0.70	0.26	PIT
4	19.2	AC	50.1	-1.05	-0.63	0.58	PIT
5	22.8	AC	27.9	-2.32	-2.32	0.39	BOWL
6	24.6	AC	34.0	-1.88	-1.88	0.13	PIT
7	27.4	AC	72.1	-1.24	-0.33	0.40	PIT
8	26.6	AC	13.0	-1.31	-1.31	0.15	BOWL
9	25.4	AC	22.1	-1.15	-0.85	0.18	SMTH
10	27.0	AC	38.0	-1.34	-0.78	0.38	PIT
11	25.6	AC	42.0	-1.32	0.10	0.33	SMTH
12	25.7	AC	54.0	-1.36	0.58	0.66	SMTH
13	26.8	AC	34.0	-0.96	-0.49	0.25	SMTH
14	27.8	AC	24.1	-0.71	-0.71	0.24	PEAK
15	32.5	AC	35.9	-1.31	-0.67	0.43	PEAK
16	35.6	AC	34.0	-0.60	-0.31	0.13	PEAK
17	36.5	AC	24.0	-3.24	-3.24	0.50	PEAK
18	34.4	AC	56.0	-0.35	0.53	0.21	SMTH
19	35.6	AC	58.0	-2.06	-1.54	0.84	SMTH
20	35.4	AC	23.0	-0.55	-0.47	0.17	PEAK
21	34.6	AC	25.0	-1.56	-1.56	0.63	PEAK
22	32.8	AC	18.0	-1.23	-1.20	0.13	PEAK
23	31.5	AC	52.1	-0.56	0.0	0.20	SMTH
24	31.0	AC	61.0	-1.04	-0.92	0.36	PIT
25	32.1	AC	36.0	-0.97	0.27	0.25	PEAK
26	35.9	AC	39.9	-1.08	-0.73	0.38	SMTH
27	36.5	AC	28.9	-0.94	-0.94	0.14	SMTH
28	36.6	AC	45.0	-0.53	-0.14	0.32	SMTH
29	35.6	AC	39.9	-1.11	-0.77	0.19	SMTH
30	38.8	AC	40.9	-1.49	-0.48	0.43	PIT
31	39.3	AC	51.9	-0.69	-0.86	0.27	PIT
32	40.1	AC	49.9	-3.18	-3.18	0.81	PIT
33	40.9	AC	31.0	-0.80	-0.72	0.32	SMTH

1050J2-002

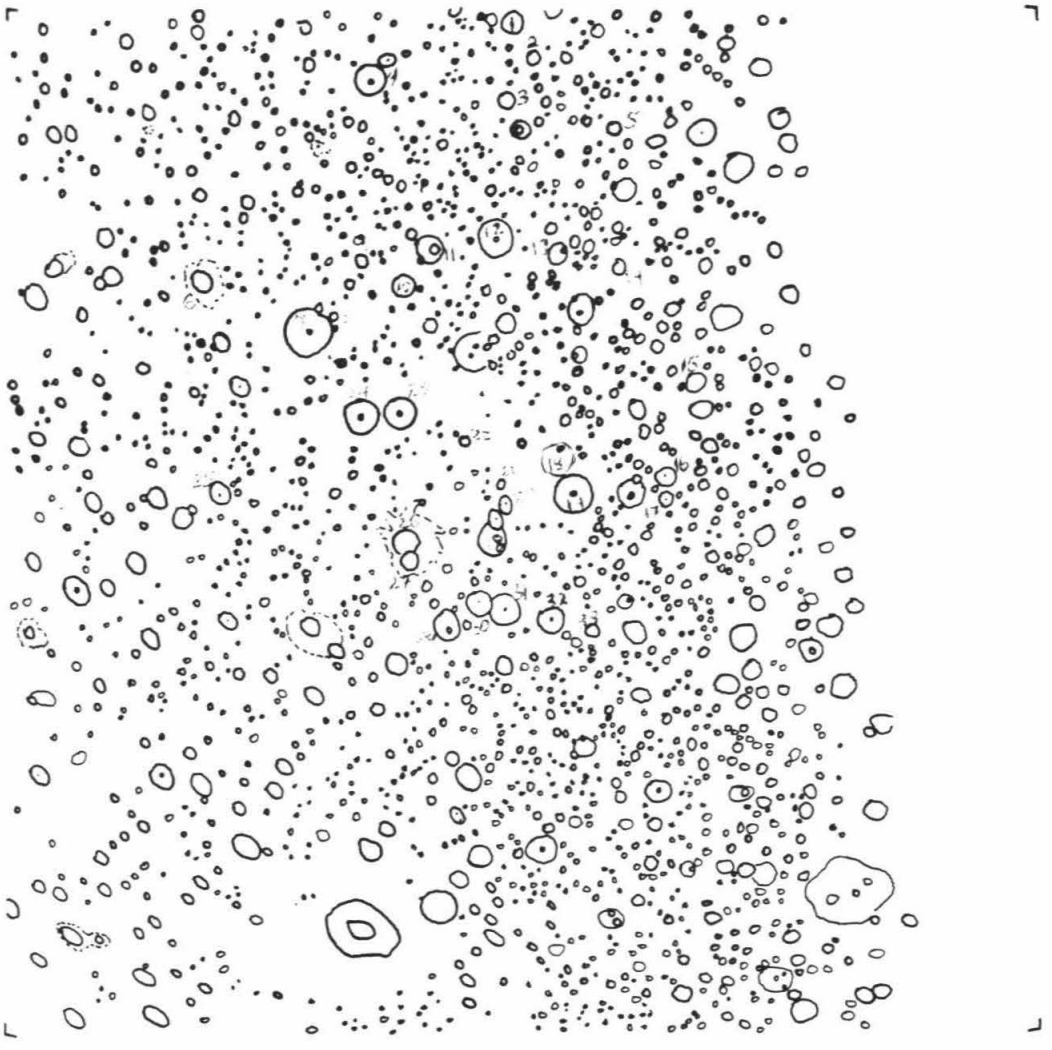

Callisto

FDS 2061725 1078J2-002

CRATER	LATITUDE	TERR	DIAM(KM)	MAXDEPTH	CENTER DEPTH	RIM HEIGHT	TYPE
1	-25.8	AC	44.9	-0.87	-0.43	0.41	SMTH
2	-27.5	AC	34.1	-1.53	-0.10	0.59	PEAK
3	-24.3	AC	35.0	-2.30	-1.87	0.81	SMTH
4	-24.2	AC	43.1	-1.17	-0.80	0.35	SMTH
5	-21.5	AC	54.1	-2.46	-1.90	0.48	PIT
6	-18.4	AC	22.9	-1.55	-1.46	0.34	PEAK
7	-15.3	AC	61.0	-2.54	0.63	0.74	PIT
8	-12.9	AC	34.0	-2.22	-1.66	0.65	PEAK
9	-11.0	AC	76.1	-1.51	-1.43	0.74	PIT
10	-14.8	AC	40.1	-1.34	-0.41	0.26	PIT
11	-13.2	AC	35.0	-0.86	-0.26	0.32	SMTH
12	-7.7	AC	40.0	-2.03	-0.53	1.11	PEAK
13	-4.1	AC	59.0	-1.40	-1.25	0.26	PIT
14	-5.1	AC	83.1	-0.37	0.07	0.20	PIT
15	-2.7	AC	49.9	-1.43	-1.25	0.45	PIT
16	-2.4	AC	35.9	-1.36	-0.86	0.48	SMTH
17	-2.4	AC	38.0	-1.88	-1.88	0.46	BOWL
18	-2.5	AC	21.0	-0.82	-0.68	0.23	PEAK
19	-0.4	AC	32.0	-2.05	-1.95	0.41	SMTH
20	0.4	AC	50.1	-1.09	-0.90	0.37	PIT
21	1.1	AC	31.0	-2.43	-1.87	0.65	PEAK
22	4.2	AC	25.0	-1.78	-1.47	0.53	PIT
23	4.5	AC	27.9	-1.13	-0.97	0.47	PEAK
24	6.4	AC	65.1	-0.83	-0.37	0.37	PIT
25	8.4	AC	76.0	-1.88	-1.19	0.68	PIT
26	9.0	AC	47.0	-1.64	-0.33	0.45	SMTH
27	10.3	AC	32.0	-1.48	-1.25	0.47	SMTH
28	9.7	AC	40.1	-2.95	-2.24	0.39	SMTH
29	8.7	AC	32.1	-1.46	-0.71	0.56	SMTH

1078 J2-002

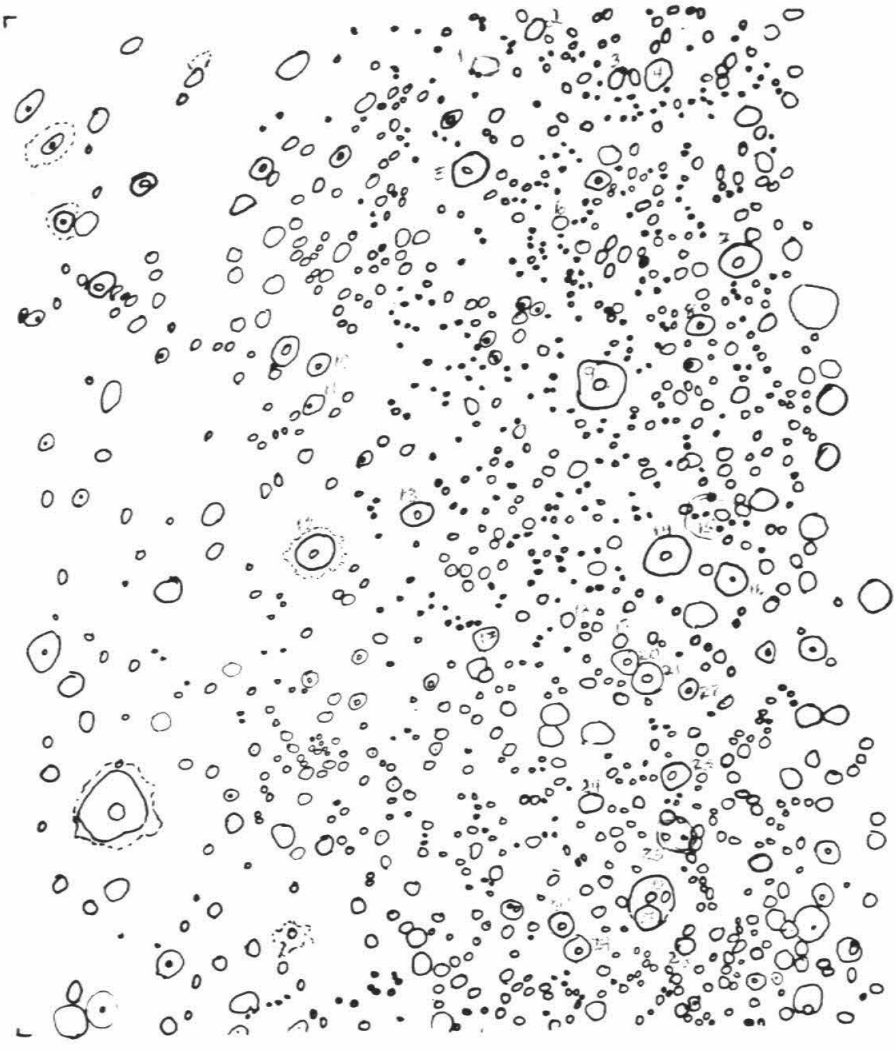

Callisto

FDS 2061741 1094J2-002

CRATER	LATITUDE	TERR	DIAM(KM)	MAXDEPTH	CENTER DEPTH	RIM HEIGHT	TYPE
31	47.2	AC	30.9	-1.32	-1.32	0.37	BOWL
32	48.9	AC	32.0	-3.06	-3.06	0.40	BOWL
33	48.7	AC	34.9	-1.07	-1.07	0.18	BOWL
34	39.2	AC	69.1	-1.98	-1.71	0.41	SMTH
35	43.9	AC	29.1	-0.78	-0.78	0.27	PEAK
36	41.8	AC	52.0	-1.18	-0.38	0.43	SMTH
37	40.0	AC	35.0	-2.14	-2.14	0.78	BOWL
38	36.8	AC	57.9	-1.19	0.15	0.44	PIT
39	35.8	AC	70.9	-0.69	-0.28	0.28	SMTH
40	31.2	AC	80.0	-3.10	-2.81	1.31	SMTH
41	26.4	AC	49.0	-2.98	-0.96	0.90	PEAK
42	27.5	AC	55.0	-1.14	-1.11	0.57	PIT
43	24.1	AC	43.0	-1.09	-1.09	0.45	PIT
44	25.6	AC	55.0	-1.11	-0.92	0.32	PIT
45	25.8	AC	27.0	-0.65	-0.09	0.20	PEAK

1094J2-002

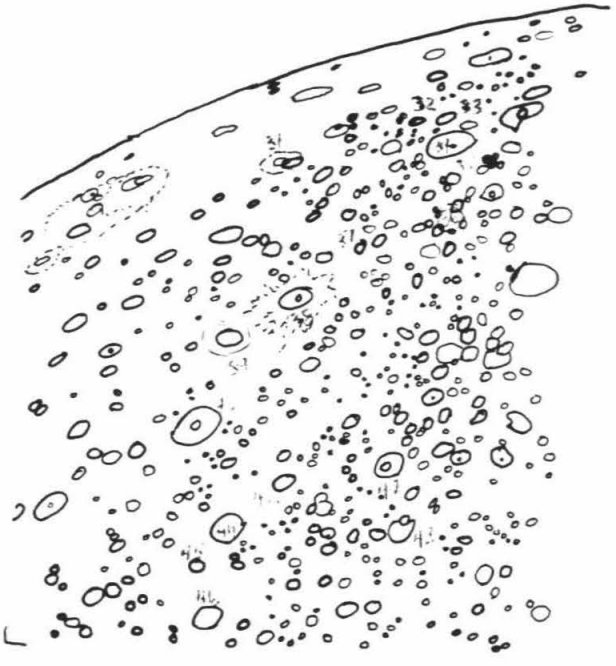

FDS 44004.20 Enceladus

Crater	Diameter	Max Depth (km)	Center Depth	Rim Height
1	19.8	-1.09	-0.66	0.49
2	21.4	-0.51	-0.40	0.18
3	15.5	-1.35	-1.35	0.28
4	11.3	-1.36	-1.36	0.33
5	17.2	-1.03	-0.78	0.38
6	11.6	-0.94	-0.94	0.24
7	19.3	-0.81	-0.21	0.21
8	16.9	-0.44	-0.20	0.22
9	16.2	-0.05	-0.03	0.03
10	13.6	-0.25	-0.11	0.13
11	16.5	-0.24	0.0	0.13
12	7.9	-0.90	-0.90	0.16
13	9.6	-0.66	-0.66	0.16
14	32.4	-0.90	-0.11	0.37
15	34.4	-0.96	-0.58	0.49
16	16.9	-0.42	-0.42	0.17
17	16.2	-1.12	-1.12	0.34
18	19.4	-1.17	-1.14	0.34
19	13.2	-1.52	-1.52	0.34
20	9.6	-0.98	-0.98	0.16
21	10.4	-0.69	-0.69	0.23
22	13.2	-0.58	-0.58	0.34
23	15.3	-1.39	-1.39	0.40
24	14.1	-1.33	-1.22	0.30
25	9.6	-0.91	-0.91	0.24
26	11.9	-1.46	-1.46	0.28
27	13.9	-1.42	-1.42	0.44
28	12.6	-0.77	-0.77	0.29
29	11.3	-0.19	-0.19	0.11
30	10.9	-0.87	-0.87	0.26
31	7.4	-0.25	-0.25	0.15
32	7.9	-0.22	-0.22	0.10
33	11.5	-0.14	0.0	0.09
34	11.3	-0.08	-0.01	0.04
35	10.6	-0.06	-0.02	0.03
36	15.9	-0.88	-0.73	0.24
37	10.0	-1.07	-1.07	0.20
38	17.1	-0.15	-0.05	0.12
39	10.6	-0.06	-0.03	0.03
40	14.6	-0.28	-0.11	0.15
41	11.6	-1.30	-1.30	0.33
42	10.6	-0.82	-0.82	0.16
43	10.3	-0.42	-0.42	0.09
44	26.8	-0.60	-0.09	0.34
45	18.9	-2.57	-2.57	0.33
46	22.7	-1.57	-1.57	0.57
47	12.6	-1.15	-1.15	0.31
48	37.0	-0.15	-0.02	0.08
49	(65.0)	-0.12	-0.04	0.04

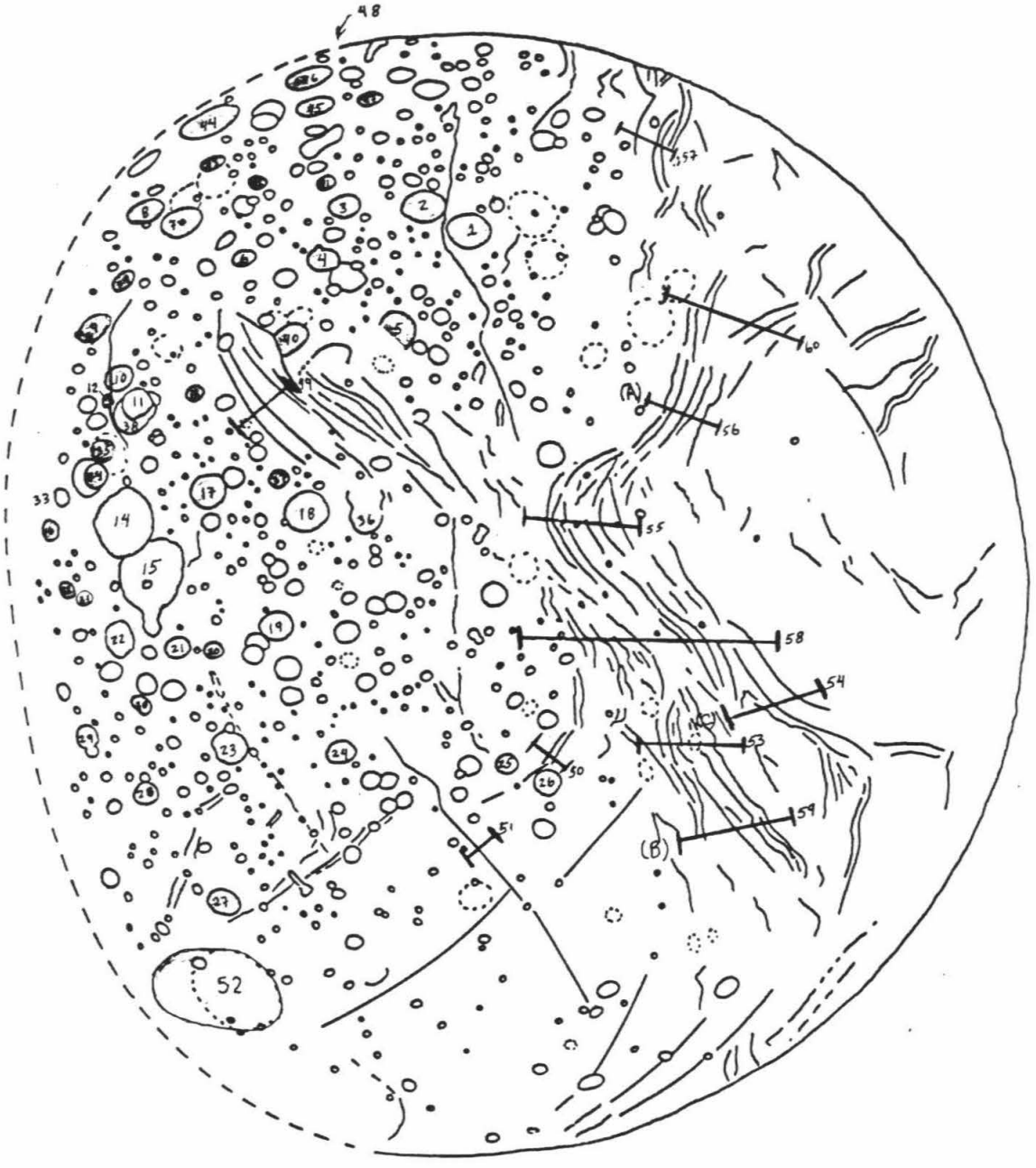
48
57
60
(A)
56
55
58
54
53
59
(B)
50
51
52
14
15
18
17
33